

Torque magnetometry for concurrent acquisitions of magnetostatics &
spin-dynamics

by

Fatemeh Fani Sani

A thesis submitted in partial fulfillment of the requirements for the degree of

Doctor of Philosophy

Department of Physics

University of Alberta

Abstract

To fully utilize magnetic structures, a rich understanding of their physical properties and magnetic interactions is required. As device sizes shrink to the nanoscale, it is also important to acquire characterization information in the presence of inevitable intrinsic pinning sites. Nanomechanical torque magnetometry has been used for capturing the quasi-static magnetization of single, mesoscopic magnetic structures in a non-invasive way. We demonstrate the subtle effects of intrinsic pinning sites on magnetization characterization. Moreover, we study the important role of nanoscale defects by engineering artificial pinning sites on the sample surface. Separated artificial sites can work together to eliminate the effect of intrinsic pinning sites. Additionally, we perform ac magnetic susceptibility studies including the harmonics, from which non-linearities of magnetization response can be inferred.

The ability to simultaneously record the equilibrium magnetic hysteresis and the spin excitations have been an experimental challenge. We demonstrate a down-mixing concept using a nanomechanical torque sensor that enables the concurrent measurements of dc net magnetization and of magnetic resonance spectra, in an individual magnetic structure and at room temperature. A desired magnetic torque component can be measured by adjusting the frequencies of perpendicular RF (or ac) drives in a broad frequency range (dc to GHz). We investigate ferrimagnetic resonances in a yttrium iron garnet (YIG) structure, nearly ideal case study due to its low ferrimagnetic resonance linewidths. An effective gyromagnetic ratio is assigned to some of the resonance modes and the ferromagnetic resonance mode couplings are observed within an individual structure. Together with micromagnetic

simulations, additional physical insights are developed through the spectroscopic map of the YIG structure.

Preface

Some of the research conducted for this thesis are published in peer-reviewed journals in collaboration with groups of Profs. J.P. Davis (University of Alberta); P.E. Barclay (University of Calgary); G.E. Bridges and D.J. Thomson (University of Manitoba); and Drs. W.K. Hiebert and D. Vick at the National Institute for Nanotechnology (NINT). The nanomechanical torque sensors were fabricated at the University of Alberta NanoFab and NINT. More details are below, following the order presented in the thesis.

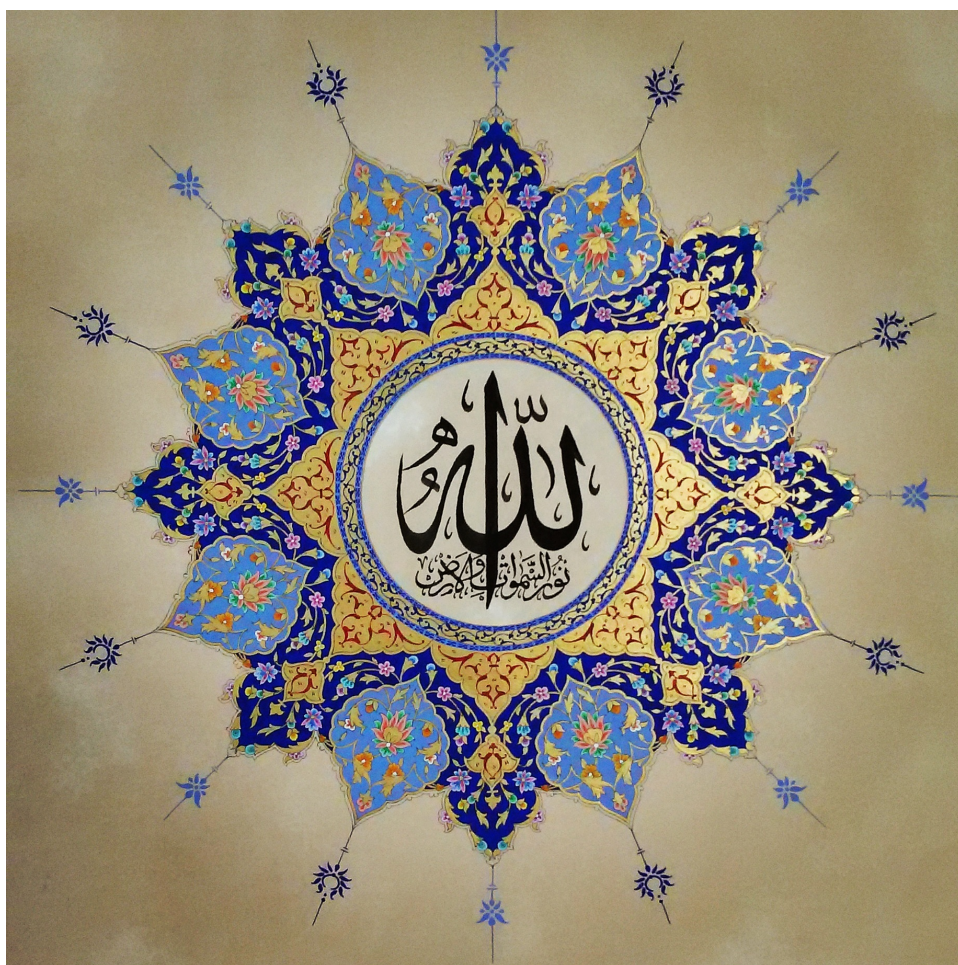
Chapter 2 includes studies about the characterization of magnetic structures in the presence of intrinsic or artificial defects, which act as pinning sites. Our investigations have been published in *Science* **339**, 1051 (2013) with J.A.J. Burgess, A.E. Fraser, D. Vick, B.D. Hauer, J.P. Davis, M.R. Freeman. F.F helped conduct the experiments, collect and analyze data. In addition, part of chapter 2 is taken from published data in the Journal of Applied Physics **17**, 17D131 (2013) with J.E. Losby, Z. Diao, L.C. Parsons, J.A.J. Burgess, D. Vick, W.K. Hiebert, and M.R. Freeman. F.F conducted the experiments, collected data, and performed micromagnetic simulations.

The magnetic susceptibility at Barkhausen steps are investigated in chapter 2 as part of work presented in *Nature Nanotechnology* **12**, 127 (2017) with Marcelo Wu, Nathanael L.-Y. Wu, Tayyaba Firdous, Joseph E. Losby, Mark R. Freeman and Paul E. Barclay. In this paper, F.F. helped analyze data and worked on the theoretical framework for the RF susceptibility mixing scheme in the supplementary material. In addition, F.F. contributed simulations to the manuscript. The work on ac harmonics arising in nonlinear magnetization-field region is adapted from Solid State Commun. **198**, 3 (2014) with J. E. Losby, Z. Diao, D.T. Grandmont, M. Belov, J.A.J Burgess, W.K. Hiebert, and M.R. Freeman. F.F. worked on calculating and analyzing the susceptibility harmonics coefficients.

In chapter 3, part of the presented results (TMRS) are taken from *Science* **339**, 798 (2015) with J.E. Losby., D.T. Grandmont, Z. Diao, M. Belov, J.A.J. Burgess, S.R. Compton, W.K. Hiebert, D. Vick, K. Mohammad, E. Salimi, G. E. Bridges, D. J. Thomson, and M.R. Freeman. In this paper, F.F. conducted the experiments and collected data as well as helped analyze data. Moreover, F.F worked on the theoretical framework of magnetic resonance (the trans-

verse susceptibility) and performed the micromagnetic modelling. The results on spectroscopy of the YIG disk in perpendicular dc bias fields, presented in chapter 3, are in preparation for submission; F.F. performed the experiments and collecting data, micromagnetic simulation, and analyzed the data. In all the co-authored papers, F.F helped writing the manuscript and has the main responsibility when first author.

In Appendix C, there are sections taken from the supplemental materials of *Science* **339**, 798 (2015) with permission. F.F added more information, including instrumentation details, calibrations, thermal investigations, and vector network analysis.



*Allah is the Light of the heavens and the earth. Holy Quran, 24:35
(gilding by A. Hosseinzadeh)*

To my beloved soulmate, Mahdi

“Our imagination is stretched to the utmost, not, as in fiction, to imagine things which are not really there, but just to comprehend those things which are there.”

Richard P. Feynman

The Character of Physical Law (1965)

Acknowledgements

My accomplishments would not have been possible without the presence of special people here at the UofA and a fruitful teamwork in collaboration with various research groups. I feel very fortunate and honored to have such a unique opportunity during the course of my research at the University of Alberta.

First and foremost, my sincerest gratitude goes out to my supervisor Prof. Mark Freeman. It has been an amazing privilege to have met Mark and to work for him. Marks immense knowledge, understanding, and patience added considerably to my graduate experience. From a short daily conversation to ‘aha’ moments of discovering fascinating experimental results, he is the kind of person who motivates you and keeps you pushing forward. Thanks Mark for precious guidance, constructive discussions, constant encouragement, enduring support, and enthusiasm.

I would also like to extend my appreciation to my thesis committee: Prof. Frank Hegmann, Prof. Al Meldrum, Prof. Bruce Sutherland and Prof. Chris Hammel, for their time and valuable challenging discussions.

I would like to convey my thanks to each and everyone of my colleagues, collaborators, and Journal Club crew, in particular: Alastair Fraser, Shawn Compton, Miro Belov, Joe Losby, and Vince Sauer; thanks for the helpful discussions and great times working together in the LAB. Also many thanks to Joe and Vince for being my critical readers. In addition, I would like to express my gratitude to Sandy Hamilton in the Physics General office for helpful assistants; Don Mullin in the Thin Film lab for helping gold deposition in my

samples and in the commemorative gift for Mark's 20th work anniversary at the UofA; and Dave Fortin for the numerous LabView programs.

Thanks to all my wonderful friends with whom I had celebrated many occasions, gathered on Friday nights, met for Wednesday discussions, walked through YEG hiking trails, and shared endless, enjoyable moments together: I am grateful for your friendship, especially Zahra Shahriari, Amir Alizad, Soudeh Zaker, and Leila Zargarzadeh. Also Hossna Gharaee and Negar Reza-jooei, my dear friends at the physics department, thanks for your amazing friendship and extraordinary supports and girlish gatherings. Thanks to Azam Hosseinzadeh for the magnificent handmade gilding (Tazhib) brought on the dedication page and above that our old friendship.

I would like to thank my family for accepting nothing less than excellence from me. Thank you, Maman, Baba, Mohammad, and in the loving memory of my grandmother, for your countless love and support through my entire life. I would also like to express my gratitude to my parents-in-law for their love and supports.

Finally, my deepest gratitude goes to my beloved soulmate, Mahdi. Thank you for your heartfelt love, incentive encouragement, and constant support to experience new things; with you, life is full of colors.

FATEMEH FANI SANI

May 2017

Contents

1	Magnetism	1
1.1	Background	1
1.2	Magnetic ordering	2
1.3	Theoretical framework for magnetism	5
1.4	Experimental backgrounds	8
1.5	Overview of the thesis	11
2	Quasi-static study of magnetic structures in presence of pinning sites	14
2.1	Motivation	14
2.2	Introduction	15
2.3	Magnetic vortex state	18
2.4	Characterization of intrinsic pinning sites	21
2.5	Characterization and control of the energetic landscape using Ga ⁺ ions	23
2.6	Susceptibility at the Barkhausen steps	35
2.7	Measuring ac susceptibility harmonics	42
2.8	Conclusion	49
3	Torque magnetometry for concurrent acquisitions of magneto-statics & spin-dynamics	51
3.1	Motivation	51

3.2	Introduction	52
3.2.1	Gyrotropic modes	53
3.3	Torque-mixing magnetic resonance spectroscopy	57
3.4	Spin resonance spectroscopy of an in-plane magnetized YIG disk	61
3.4.1	Quasi-uniform magnetizations	64
3.4.2	Vortex state	66
3.5	Spin resonances spectroscopy for in-plane magnetized thin Py disks, in the vortex state	73
3.5.1	In the presence of intrinsic pinning sites	73
3.5.2	In the presence of artificial pinning sites	76
3.6	Spin resonances in a perpendicularly magnetized YIG disk . . .	78
3.6.1	Vortex state	78
3.6.2	Uniform magnetization and Kittel-like modes	80
3.6.3	Avoided crossing of confined modes	86
3.6.4	Effective gyromagnetic ratio	90
3.7	Conclusion	91
4	Conclusion & remarks for the future	93
	Appendices	113
A	Micromagnetic simulation - Methods	114
A.1	General parameters	115
A.1.1	Saturation magnetization	116
A.1.2	Exchange constant	116
A.1.3	Magnetic anisotropy	116
A.1.4	Temperature	119
A.1.5	Initial magnetization	120
A.2	Spin dynamics	121
A.2.1	Adjusting the RF pulse excitation	122

A.2.2	Damping factor	124
A.2.3	Fourier transform with windowing process	126
A.3	Sample codes	127
A.3.1	Sample code for hysteresis loop	127
A.3.2	Voronoi tessellation	128
A.3.3	Changing the temperature	129
A.3.4	Magnetic resonance response	129
B	Micromagnetic simulation - Case studies	131
B.1	Experimental insights	131
B.1.1	Artificial pinning potentials in a Py disk	131
B.1.2	Defects in a mushroom-shaped Py structure	137
B.1.3	Gyrotropic frequency in a disk with defects	143
B.1.4	Quasi-static in a thick YIG disk	147
B.1.5	Line defects and magnetic resonances of YIG disk	150
B.1.6	Kittel-like modes in a YIG structure	152
B.2	Future devices	159
B.2.1	YIG spheres with different dimensions	159
B.2.2	Ellipse structure	161
C	Technical Supports	164
C.1	TMRS instrumentation scheme	164
C.1.1	Setup details	166
C.2	Torque sensor	168
C.2.1	Mechanical and spin sensitivities	169
C.2.2	Fabrication a monocrystalline, mesoscopic YIG disk	170
C.3	Design of microwave printed circuit boards (Transmission Lines)	173
C.3.1	Transmission lines calibration	175
C.3.2	Thermal investigations	179
C.4	VNA measurement	181

C.4.1	TLs characterization	182
C.4.2	Gyromagnetic ratios	182

List of Tables

2.1	Torque terms for two sample positions, on- and off-axis.	36
2.2	Harmonics of the ac susceptibility	45
2.3	Harmonics of the ac susceptibility at $H_x = 12.75$ kA/m	48
3.1	Gyromagnetic ratio obtained from linear fits, experiment and simulation.	91
A.1	Magnetization properties of materials used in simulation.	121

List of Figures

1.1	Flowchart of different magnetic ordering	3
2.1	A 3D rendering of a silicon nitride torque sensor	16
2.2	Phase diagram of magnetic state in a magnetic cylinder	18
2.3	Magnetic states in a Py disk at different field values (simulation)	19
2.4	Degenerate magnetic vortex states	20
2.5	Full hysteresis of an as-grown Py disk with 42 nm thickness and 1 μm diameter	21
2.6	Designing the position of artificial pinning sites in a magnetic disk	24
2.7	The core interactions with all the artificial pinning sites	26
2.8	Magnetization response for a 1 μm diameter and ~ 12 nm thick Py disk with one FIB-induced defect	27
2.9	A full minor loops for a 1 μm diameter and ~ 12 nm thick Py disk with one FIB-induced defect	29
2.10	Magnetization response versus in-plane applied field for a 2 μm diameter and ~ 12 nm thick Py disk with three FIB-induced defects	31
2.11	Two different vortex creation and annihilation trajectories in a full hysteresis loop for the disk with three pinning sites	33
2.12	The minor hysteresis loop in a 2- μm diameter Py disk with triple defects before and after HIM	34
2.13	Attain different RF field components via changing the device position on top of the RF coil	36

2.14	M-H characterization of a Py element with enhanced magnetic susceptibility features at Barkhausen steps at room temperature	37
2.15	Low-field M-H curves versus various applied RF drives along with the fitting curves	39
2.16	The extracted experimental susceptibility overlapped for different drive using the presented model	40
2.17	The experimental susceptibility as a function of RF drive amplitude	41
2.18	Instrument schematic for frequency-mixed nanomechanical detection of ac susceptibility	43
2.19	Spectroscopic mapping of higher harmonics of the ac susceptibility	46
2.20	Frequency response of the harmonics at $H_x = 12.75$ kA/m	47
2.21	Magnetization response near vortex creation and the ac susceptibility harmonics	48
3.1	Simulated gyrotropic mode frequencies as a function of thickness in a YIG disk	56
3.2	Schematic of torque-mixing magnetic resonance spectroscopy (TMRS) with a demonstration	60
3.3	The YIG disk structure and its concurrent magnetization and resonance at $f_1 = 100.1000$ MHz	62
3.4	Torque-mixing Magnetic Resonance Spectroscopy of the YIG microdisk	65
3.5	3D rendering of the vortex magnetization at the ground state	67
3.6	Low field TMRS for the YIG disk in the 3D vortex state	68
3.7	Frequency and amplitude modulation of the lowest (first-order) gyrotropic mode in the low-to-high field sweep	69
3.8	2D representation of the first mode magnetic resonance data versus applied field overlapped with the concurrent net magnetization response	70

3.9	Simulation spectroscopic mapping of a YIG disk in a 3D vortex state with shallow imperfections at one disk surface	71
3.10	TRMS map of a thin, polycrystalline Py disk with 2- μm diameter in the presence of intrinsic pinning sites	74
3.11	Magnetic resonance spectra in comparison to micromagnetic simulation	75
3.12	Overlap of the averaged torque of vortex core gyration and net magnetization in the thin, polycrystalline Py disk	76
3.13	TMRS responses in the Py disk with artificial pinning sites . . .	77
3.14	Spectrum of a perpendicularly magnetized thick YIG disk in the vortex state	79
3.15	Experimental measurement of magnetic resonance spectrum in a perpendicular uniform magnetized YIG disk	82
3.16	Micromagnetic simulations of magnetic resonance spectra in perpendicularly magnetized YIG structures	85
3.17	Zoom-in simulated spectrum of tapered disk and selected spatial FFTs	87
3.18	The first two modes in the experimental spectrum with linear fits	88
3.19	Mode-coupling and the Kittel like mode	89
A.1	Simulation of in-plane magnetic field sweeps in a 1.2 μm diameter and 500 nm thick YIG disk with cubic anisotropy	118
A.2	The effect of anisotropy in masked magnetite nanoparticles . . .	119
A.3	Temperature effect on masked nanoparticles without anisotropy	120
A.4	A time-domain pulse and its Fourier transform	123
A.5	Pulse width and the frequency bandwidth investigation	124
A.6	The effect on the gyrotropic frequency of changing the damping factor	125
A.7	The representation of Matlab Hann-windowing function	126

B.1	Single defect characterization in a micron diameter and 12 nm thick Py disk	133
B.2	Simulating the beam misalignment in creating the single defect .	134
B.3	Simulation of the pinning enhancement with three defects	135
B.4	Magnetization characterization in a 2- μ m diameter and 20 nm thick Py disk with three pinning sites	136
B.5	The M-H characterization in a pristine mushroom-shaped Py structure with 40 nm thickness	138
B.6	Characterization of a single pinning site in the mushroom-shaped Py structure at a two-vortex state	139
B.7	The characterization of two pinning sites in the mushroom-shaped Py structure	140
B.8	Investigation of RF susceptibility through the application of a perpendicular dither	141
B.9	The characterizations of magnetization in a grainy Py structure	142
B.10	Geometry-dependent gyrotropic frequencies in Py disks	143
B.11	Simulated magnetic resonances of the vortex core in and out of a single defect	145
B.12	Simulated magnetic resonances of triple defects	146
B.13	The effect of YIG disk dimensions on the magnetic resonance at the ground state	148
B.14	3D Spin Textures of the Mesoscopic YIG disk	149
B.15	Low-field comparison between magnetization responses in a pristine and defected YIG disks	150
B.16	Comparison of magnetic resonance spectra in the YIG disks with and without surface modifications	151
B.17	Resonance spectrum in a perpendicular magnetized thick YIG disk	153

B.18	An investigation into the effect of disk thickness on the resonance spectra of 980-nm diameter YIG disks (field sweep down)	154
B.19	Simulated spectrum of a YIG structure with a step artifact	156
B.20	The cartoon of a tapered disk	157
B.21	The spectra of tapered disks with 980-nm diameter and different tapering angles	158
B.22	Zoom-in spectrum of a tapered YIG disk with tapering angle of $\theta = 11.5^\circ$	159
B.23	Geometry effect on the magneto-static response of YIG spheres with cubic anisotropy	160
B.24	Low-field magnetization profiles for YIG spheres with nano-meter and micro-meter scales	161
B.25	Ground states investigation for various thicknesses in a Py ellipse	162
B.26	The hysteresis loop of a Py ellipse	163
C.1	Instrumental schematic for torque-mixing magnetic resonance spectroscopy	165
C.2	Schematic of setup with extension of frequency bandwidth	166
C.3	Thermomechanical noise calibration of the torque sensor supporting a YIG disk	169
C.4	Fabrication of a mechanical torque sensor housing a FIB-milled single crystal, micromagnetic disk	172
C.5	Microwave TL geometry for generation of orthogonal RF magnetic fields	174
C.6	Simulated RF field profiles to illustrate the variation of RF field strengths and directions if the sample placement is off-center . .	176
C.7	Calibration of Zurich input versus frequency	176
C.8	Calibration of the ENI output versus frequency	177
C.9	Field calibration of TLs versus frequency	178
C.10	The frequency-dependent gain of mini-circuits power amplifier .	179

C.11 Thermal investigation about working frequency range of TLs . .	180
C.12 Thermal scans of the transmission lines at $f= 2.4\text{GHz}$	181
C.13 Calibration of TLs via VNA E5072A	182
C.14 Obtaining a gyromagnetic ratio in a $250\text{-}\mu\text{m}$ YIG sphere	183
C.15 Obtaining gyromagnetic ratio in pieces of original Shin-Etsu wafer	184

List of Abbreviations

2D	Two Dimensions
3D	Three Dimensions
ac	Alternating Current
AF	Anti-Ferromagnets
AFM	Atomic Force Microscopy
BLS	Brillouin Light Scattering Spectroscopy
CCW	Counter Clockwise
Co	Cobalt
COMSOL	Finite Element Multiphysic Modeling
CPU	Central Processing Unit
CW	Clockwise
dc	Direct Current
DPPH	Organic Chemical Compound (2,2-diphenyl-1-picrylhydrazyl), Paramagnetic Salt
DVPM	Deformable Vortex Pinning Model
DW	Domain Wall
ENI	Brand of RF Power Amplifier
EPR	Electron Paramagnetic Resonance
FFT	Fast Fourier Transform
FIB	Focused Ion Beam
FM	Ferromagnets
FMR	Ferromagnetic Resonance
Ga	Gallium

GeForce	A Brand of GPUs designed by Nvidia
GPU	Graphical Processing Unit
GPS	Global Positioning Systems
HeNe	Helium-Neon Laser with $\lambda = 632 \text{ nm}$
HIM	Helium Ion Microscope
HP	Hall Probe (magnetic field sensor)
LAN	Local Area Network
LLG	Landau-Lifshitz-Gilbert
LN2	Liquid Nitrogen
MagPar	Parallel Finite Element Micromagnetics Package
MATLAB	Matrix-Lab, a Programming Platform
MF	Multifrequency
MOD	Modulation option in Zurich Instrument
MRFM	Magnetic Resonance Force Microscopy
MRI	Magnetic Resonance Imaging
Mumax	GPU-accelerated Micromagnetic Simulation
NdFeB	Neodymium Iron Boron permanent magnet
NINT	National Institute for Nanotechnology
NMag	Micromagnetic Simulation Package
NMR	Nuclear Magnetic Resonance
NIST	National Institute of Standards and Technology
NV-center	Nitrogen-vacancy center
OOMMF	Object Oriented Micromagnetic Framework
PD	Photodetector
PLL	Phase-locked Loop
Py	Permalloy ($\text{Ni}_{80}\text{Fe}_{20}$)
RAM	Random Access Memory
RF	Radio Frequency
RKKY	Ruderman Kittel Kasuya Yosida

rms	Root Mean Square
RVM	Rigid Vortex Model
SEM	Scanning Electron Microscopy
SiN	Si ₃ N ₄ , Silicon Nitride
SOI	Silicon on Insulator
SQUID	Superconducting Quantum Interference Device
TL	Transmission Line
TMRS	Torque-mixing Magnetic Resonance Spectroscopy
UHF	UltraHigh Frequency
VNA	Vector Network Analyzer
V-V	Two-Vortex State
VAV	Two-Vortex State with Anti-vortex
YIG	Yttrium Iron Garnet

Nomenclature

- A_{ex} exchange constant, page 81
- $F(t)$ time-dependent excitation force, page 54
- G_0 gyrotropic constant, page 54
- M_s saturation magnetization, page 5
- V volume of the magnetic structure, page 7
- W magnetostatic energy of displaced vortex, page 54
- Δf resonance linewidth, page 58
- α damping parameter, page 5
- \vec{G} gyrovector with an out-of-plane direction, corresponding to polarization, page 54
- \bar{r} displacement of vortex core, page 54
- \mathbf{B} magnetic flux density, page 4
- \mathbf{H} external applied field, page 4
- \mathbf{H}^{RF} RF magnetic field, page 7
- \mathbf{H}^{dc} dc magnetic field, page 7
- \mathbf{H}_0 external dc applied field, page 6

\mathbf{H}_{eff} effective field, page 5

\mathbf{M} net magnetization, page 4

$\boldsymbol{\tau}$ magnetic torque, page 7

\mathbf{m}^{dc} static magnetic response, page 7

\mathbf{m} magnetic moment, page 7

χ_0 baseline low-frequency susceptibility, page 58

χ_0 vortex susceptibility, page 54

χ_0^x dc susceptibility response, page 45

$\chi_{x,y,z}$ scalar components of susceptibility tensor, page 7

χ_n^x susceptibility harmonics, partially derivative of M_x , page 45

$\chi_t(f_1)$ frequency-dependent transverse susceptibility, page 58

γ gyromagnetic ratio, 28.025 GHz/T for electron, page 5

κ parabolicity of the confinement or stiffness coefficient, page 54

λ wavelength, page 15

μ_0 vacuum permeability, page 4

ω angular frequency, page 6

$\omega_{mech}/2\pi$ mechanical resonance frequency, page 10

τ_{χ_x} torques from RF moment, page 35

τ_{m_x} dc torques from x-moment, page 35

τ_{m_z} dc torques from z-moment, page 35

$f_G = \omega_G/2\pi$ gyrotropic resonance frequency, page 54

$f_{1,2}$ RF frequencies, page 58

f_{res} magnetic resonance frequency, page 58

f_{mech} mechanical resonance frequency, page 15

k wave vector, page 81

k_m discrete wave vectors related to radial mode numbers, page 81

l_{ex} exchange length, page 115

$m_y(t) - m_y(0)$ temporal evolution of y component of the magnetic moment,
page 55

p polarization, page 20

χ magnetic susceptibility, page 4

$\chi_{xy} = -\chi_{yx}$ Transverse susceptibility component in Polder notation, page 58

$c_{1,2,3}$ cubic anisotropy axes, page 117

H_z perpendicularly applied field, page 6

H_x^{ac} ac applied field, page 43

L disk thickness, page 54

$N_{x,y,z}$ demagnetization factors, page 6

Chapter 1

Magnetism

1.1 Background

Magnetism factors into many of the most perplexing phenomena in our universe. Migration is one example: scientists have attempted to understand how some species instinctively navigate vast distance across the globe without getting lost. There are many theories as to why this happens, among them is the pull of the Earth magnetic field. Recent studies suggest that some animals have small, natural magnets in their bodies, which react to the Earth's magnetic field. These magneto-receptors work in much the same way that compasses do for humans, as a tool for navigation [1, 2, 3]. Likewise, there is a class of bacteria known as magnetotactic bacteria show reaction to the Earth's magnetic field [4]. There are many other natural phenomena related to magnetism. These include the aurora borealis and magnetars, the latter of which are a type of neutron star with an extremely powerful magnetic field.

An early sign of our relationship with magnetism dates back to Chinese antiquity about 6000 years ago with the discovery of a permanent magnet crafted by nature, lodestone (magnetite, an iron oxide). Chinese inventors polished a brass plate and then put a spoon-like magnetite object on it that could align easily with Earth's field, thus making the first compass (3000 - 2500 BCE)

[5]. William Gilbert, who published a landmark scientific paper, “De Magne” in 1600, found that the Earth was indeed a giant magnet. In 1820, Hans Christian Ørsted accidentally discovered the relationship between electricity and magnetism while demonstrating that an electric current in the wire near a compass changed the direction of compass needle. This breakthrough tied together the separate disciplines of electricity and magnetism. A decade later, Michael Faraday’s monumental demonstration showed the reverse relation – that moving a magnet near a stationary coil of wire induced a current. This paved the way for electric generators. Later in the 19th century, James Clerk Maxwell’s theoretical foundation of the physics of electromagnetism synthesized the results of all the key experimental observations [6] – notably by Charles-Augustin de Coulomb, Hans Christian Ørsted, Carl Friedrich Gauss, Jean-Baptiste Biot, Félix Savart, André-Marie Ampère, and Michael Faraday – and elucidated the nature of light as electromagnetic radiation.

1.2 Magnetic ordering

Why does a magnet very selectively attract materials like iron, cobalt, and steel, but not copper, plastic, or glass? That is because magnetic properties of materials can be sorted in different classifications based on the ordering of unpaired electrons within atoms. In general, if a material does not possess permanent magnetization, it is described colloquially as non-magnetic; the electron magnetic moment cancel each other. Permanent magnets are only the most obvious class of magnetic materials, known in physics as hard ferromagnets. Ferromagnetics exhibit nearest-neighbour alignment and long-range ordering of magnetic moments below a critical temperature known as the Curie point. A kind of flowchart to loosely categorize magnetic properties is shown in Figure 1.1.

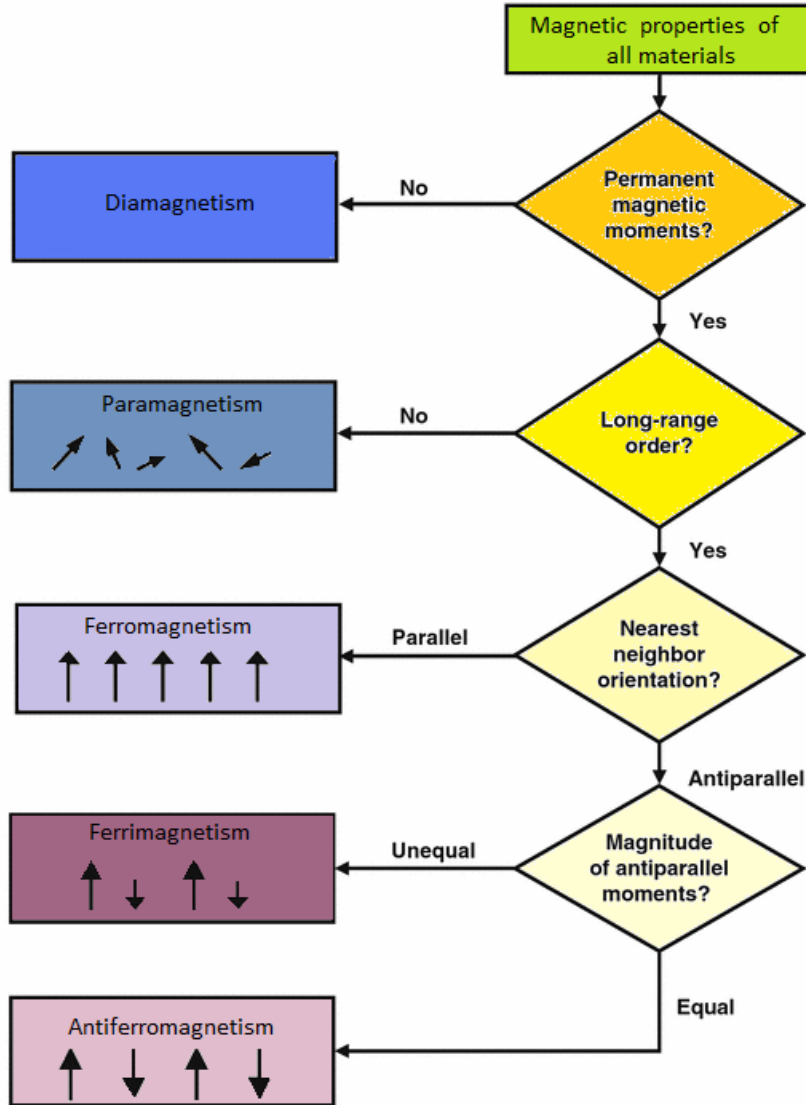


Figure 1.1: Flowchart of different magnetic ordering. Taken from [7].

To reveal, experimentally, a material’s magnetic properties, magnetization (the net magnetic moment divided by volume) has to be measured as a function of the magnetic field and temperature to obtain clues about the type of magnetic ordering and the phase transition. Ferromagnets become paramagnetic above the Curie temperature – because thermal motion destroys the magnetic ordering [8]. Real ferromagnetic specimens characteristically break-up into magnetic domains, to lower the energy embedded in stray magnetic fields out-

side the objects. Weiss suggested that theoretically the energetics would drive the introduction of domains and domain walls, high energy density boundaries between different regions of uniformly aligned spins in ferromagnetic materials (1906).

A magnetic material modifies its inside field, which will be different from the outside applied external magnetic field. Three important vectors can be defined in that regard: the net magnetization (\mathbf{M}), applied field (\mathbf{H}), and magnetic flux density (\mathbf{B}), which are related to each other as presented in Equation 1.1:

$$\mathbf{B} = \mu_0(\mathbf{H} + \mathbf{M}) = \mu_0(1 + \chi)\mathbf{H}, \quad (1.1)$$

in which the μ_0 is the vacuum permeability and the magnetic susceptibility χ is a dimensionless tensor where $\mathbf{M} = \chi\mathbf{H}$. The magnetic field inside a material is related to a tendency of internal magnetic moments to align with the magnetic source, which can be an attractive or repulsive force between the material and magnetic source. The susceptibility tensor is simplified to a scalar, χ , in a linear relationship between net magnetization and the applied field.

The measurement of susceptibility in materials can determine the magnetic ordering. Pierre Curie was the first to examine the thermal properties of magnetic samples. The sign and amplitude of susceptibility determine the attraction and repulsion of the material in response to an applied field. Diamagnetic materials usually have paired electrons. Non-magnetic ions or atoms induce a magnetization opposed to the applied field, which results in small negative values for susceptibility. Therefore, a diamagnet would be pushed weakly by an applied field.

The magnetic moments in the magnetic materials can be due to localized ions on crystal sites in dielectrics and ferromagnetic semiconductors, or partially filled outer shells (like 3d, 4d,5d, or 4f, etc) in metals. The internal moments in this category create a force that causes the material to be attracted

to the external source. Thus, a positive sign is achieved for the susceptibility. In paramagnetic materials this attraction is very weak, but in ferromagnetic materials, it is quite high, which creates larger susceptibilities in ferromagnetic materials.

1.3 Theoretical framework for magnetism

Magnetic ordering happens as a result of quantum mechanical interactions, which cannot be understood in a classical framework. However, for large enough assemblies of atomic and electron moments we can still use classical descriptions like the Landau-Lifshitz equation of magnetization motion for dynamics in a magnetic system. The time-dependent evolution of a ferromagnetic system away from equilibrium as described by Landau and Lifshitz in 1935 [9], is brought in following equation:

$$\frac{d\mathbf{M}}{dt} = -\gamma\mathbf{M} \times \mathbf{H}_{eff} - \frac{\gamma\alpha}{M_s}\mathbf{M} \times (\mathbf{M} \times \mathbf{H}_{eff}) \quad (1.2)$$

where γ , α , M_s and \mathbf{H}_{eff} are the gyromagnetic ratio ($\gamma/2\pi = 28.025$ GHz/T for the electron), damping parameter, and effective field. The \mathbf{H}_{eff} contains a variety of magnetic interactions, including the external field, demagnetizing field, crystalline anisotropy, exchange interaction and so on. The torque created by the effective field leads to a time variation of magnetization: the first term describes the precessional motion around the field. The second term is considered for the damping, which contains the interaction with the surrounding system. The most commonly used form of this equation of motion is that modified by Gilbert in which the damping term depend on the time derivative of the magnetization in the following form (1955), the LLG equation:

$$\frac{d\mathbf{M}}{dt} = -\gamma\mathbf{M} \times \mathbf{H}_{eff} + \alpha\mathbf{M} \times \frac{d\mathbf{M}}{dt}. \quad (1.3)$$

Nuclear and electronic paramagnetic resonances have been extensively studied [10]. The effective field in these resonances contains only an external applied field ($\mathbf{H}_{eff} = \mathbf{H}_0$). As a result the magnetic resonance angular frequency appears as the Larmor relation ($\omega = \gamma H_0$).

In a ferromagnetic system, \mathbf{H}_{eff} contains the demagnetizing and anisotropy fields, which lead to geometry-dependent resonance frequency and $|m_z|$ (Kittel expression) [11]. The Kittel expression for a confined structure in case of perpendicular field orientation is shown here:

$$\omega = \gamma \sqrt{\left(H_z + (N_x - N_z)M_s \right) \left(H_z + (N_y - N_z)M_s \right)}, \quad (1.4)$$

in which H_z is the perpendicularly applied field, M_s the saturation magnetization, and N_x , N_y and N_z are demagnetization (shape-anisotropy) factors. The demagnetization factors are positive, geometry-dependent values that are obtained from the integral formulas [12].

In addition, for other effects like spin transferring in a system, it is required to add related torque terms to the LLG equation. For example, Slonczewski in 1996 introduced a torque term corresponding to spin polarized current flows in magnetic materials [13].

It is also possible to use the classical expression of exerted magnetic torque as $\boldsymbol{\tau} = \mathbf{m} \times \mu_0 \mathbf{H}$, where $\mathbf{m} = \mathbf{M}V$ is the magnetic moment and V is the volume of the magnetic structure. A magnetic moment in presence of a variant magnetic field experiences a torque that creates a new equilibrium moment corresponds to the applied field. With the application of a radio-frequency

(RF) field, the magnetic moment and total applied field can be written as:

$$\begin{aligned}
\mathbf{m} &= \mathbf{m}^{\text{dc}} + V\boldsymbol{\chi}\mathbf{H}^{\text{RF}}, \\
\mathbf{H} &= \mathbf{H}^{\text{dc}} + \mathbf{H}^{\text{RF}}, \\
\boldsymbol{\chi} &= \begin{pmatrix} \chi_x & 0 & 0 \\ 0 & \chi_y & 0 \\ 0 & 0 & \chi_z \end{pmatrix},
\end{aligned} \tag{1.5}$$

where \mathbf{m}^{dc} is the static response to \mathbf{H}^{dc} and $\boldsymbol{\chi}$ is a magnetic susceptibility tensor induced in the presence of RF fields. Therefore, the general torque terms can be rewritten as follow:

$$\begin{aligned}
\boldsymbol{\tau} &= \mathbf{m}^{\text{dc}} \times \mu_0\mathbf{H}^{\text{dc}} + \mathbf{m}^{\text{dc}} \times \mu_0\mathbf{H}^{\text{RF}} \\
&+ \boldsymbol{\chi}V\mathbf{H}^{\text{RF}} \times \mu_0\mathbf{H}^{\text{dc}} + \boldsymbol{\chi}V\mathbf{H}^{\text{RF}} \times \mu_0\mathbf{H}^{\text{RF}}.
\end{aligned} \tag{1.6}$$

A torque sensor is a mechanical paddle to which a magnetic structure is affixed. The magnetic structure in presence of an applied field experiences a torque. That magnetic torque is transferred to the mechanical movements. Then, the mechanical movements are read out accurately using optical interferometry.

Knowing the magnetic torque expression helps us to acquire a desired magnetic moment or the susceptibility terms, experimentally. By adjusting the dc bias and RF drive fields, we can selectively measure specific magnetic terms. A simple geometry is chosen in such a way that the torque sensor is sensitive to the y-direction, τ_y . Thus, H_y^{dc} and H_y^{RF} cannot contribute to the torque terms. The torque terms can be simplified even more if we only consider RF

contributions of torque formula, as shown in following equation:

$$\begin{aligned}
 \tau_y = & -\mu_0 m_x^{\text{dc}} H_z^{\text{RF}} + \mu_0 m_z^{\text{dc}} H_x^{\text{RF}} \\
 & -\mu_0 \chi_x V H_z^{\text{dc}} H_x^{\text{RF}} + \mu_0 \chi_z V H_x^{\text{dc}} H_z^{\text{RF}} \\
 & -\mu_0 (\chi_x - \chi_z) V H_z^{\text{RF}} H_x^{\text{RF}}.
 \end{aligned} \tag{1.7}$$

In the following section, more details will be given about our method, by which we can read a magnetization response, susceptibility harmonics, and magnetic resonances of an individual mesoscopic structure from the mixing technique.

1.4 Experimental backgrounds

Magnetic resonance is a key feature in many spectroscopic analysis techniques to non-invasively study the physical, chemical, and biological properties of matter. In chemistry, it has been utilized to identify different molecules and to characterize their structures. Magnetic resonance has further important applications for medical diagnostics, through magnetic resonance imaging (MRI); and in atomic clocks, without which global positioning systems (GPS) would not work accurately.

The theory of ferromagnetic resonance was developed by Landau and Lifshitz [14], who predicted the existence of the ferromagnetic resonance of the Larmor precession, $\omega = \gamma H_0$, in 1935. In 1936, Gorter predicted the existence of nuclear magnetic resonance (NMR), when he unsuccessfully attempted to detect the NMR phenomenon in lithium fluoride utilizing calorimetric detection [15]. Stimulated by Gorter's work, magnetic resonance spectroscopy began in 1939 with observations based upon the deflection of molecular beams in gradient fields [16]. Zavoisky experimentally discovered the electron paramagnetic resonance (EPR) in 1944 [17], and explored a variety of paramagnets in solids, liquids, and gas phases using calorimetric detection. Purcell et al. [18], and Bloch [19] independently developed NMR for solids and liquids in 1946. Fer-

romagnetic resonance (FMR) was explored by Griffiths in 1946 through the energy lost by a current flowing in ferromagnetic metals, changing the effective permeability [20]. Griffiths showed that the anomalously larger frequency (by factors of about two to six) compare to the Larmor frequency, but he could not explain these numbers. In 1947, Kittel showed that the ferromagnetic resonance frequency is not at all a Larmor resonance; rather it depends essentially on the sample shape [11], as shown in equation 1.4.

The development of an experimental technique for measuring both dc magnetization and the resonance response is highly desirable to probe local effects from variation in the magnetic microstructure such as grain boundaries, vacancies, and other intrinsic or extrinsic inhomogeneities. This method would be a complement to most techniques that can measure one or the other, such as superconducting quantum interference devices (SQUID) [21], and Hall micromagnetometers [22, 23]. SQUID can measure dc magnetization or resonance response with very good sensitivity, but cannot perform the measurement simultaneously. Both SQUID and Hall micromagnetometers are limited to very low temperatures and small fields.

The development of the universally applicable electromagnetic induction method for magnetic resonance detection set the stage for advancing the powerful techniques now used throughout science and medicine. Many complementary methods have emerged over the past six decades, including the non-universal but extraordinarily sensitive EPR and NMR spectroscopies of specific materials via optical or spin-electronic detection. Magnetic resonance force microscopy (MRFM) [24] and scanned diamond nitrogen-vacancy (NV) center probes [25] have measured signals from very small numbers of nuclear spins near surfaces. In MRFM [26, 27, 28], a gradient-dipole interaction between the spin system and a magnetic probe causes a deflection of a micromechanical cantilever, with strong local field gradients leading to very high spin sensitivity and spatial resolution.

The pioneering demonstration of pure mechanical torque detection of spin resonance was reported in 1967 with direct observation of the angular momentum change from resonant RF absorption-induced spin-flips [29]. In 1992 Rugar *et al.* proposed a very sensitive mechanical detection of EPR based on magnetic force microscopy, in which a paramagnetic sample was affixed to a cantilever [30]. A nanomagnet fashioned from the rare-earth permanent magnet (NdFeB) was used to apply a strongly inhomogeneous field parallel to the axis of the cantilever. A signal transduction arises from the magnetic gradient force, responding to the reduction of the longitudinal net moment under magnetic resonance conditions.

A magnetic resonance modulation technique was used to overcome the mismatch between mechanical and magnetic resonance. The modulation has been performed on the dc field, with an additional electromagnet, although the modulation can be performed on amplitude or frequency of the RF source. This approach was also revisited by Ascoli, Alzetta and co-workers in a micromechanical implementation [31] in 1996 with the observation of angular momentum.

In this thesis, we present a complementary approach to MRFM for reading the magnetic resonances along with the concurrent magnetization response based on a torque-mixing technique [32]. The nanomechanical torque sensor magnifies the measurement on its torsional resonance. It is assumed that the net magnetic torque will transfer to the lattice and twist the resonator: mechanical torque (on the torsional resonator) is equal to the net magnetic torque (on the magnetic structure).

The magnetic structures transferred to torque sensors through nano-fabrication processes can be Permalloy (Py) islands, a single crystal yttrium iron garnet (YIG) patterned disk, or even small numbers of iron-oxide nanoparticles [33, 34, 35]. We design our torque sensors to function at the mechanical resonance frequency $\omega_{\text{mech}}/2\pi$ on order of 1-10 MHz and in a specific direction (the

y-direction in this thesis). Moreover, we design ultra-high frequency paddles with the ability to measure torque in two separate directions, at two distinct mechanical frequencies. More detail can be found in Appendix C.

We tackle the mismatch between the mechanical and magnetic resonance frequencies by using two RF sources. One is perpendicular and the other parallel to the dc bias field to excite spin-waves and exert torque terms, respectively, at the mechanical resonance frequency. The magnetic torque that corresponds to the mechanical deflection is read out through optical interferometry (more details in Chapter 3).

1.5 Overview of the thesis

This chapter provided an introduction to magnetism, including magnetic ordering and theoretical and experimental backgrounds. The organization of the rest of the thesis is described below.

Studying magnetization characterization (M-H) curves is very important for acquiring information about the magnetic structure, specifically about the distribution of spin orientations (spin textures). In Chapter 2, we present mainly quasi-static measurements performed using conventional torsional magnetometry on confined disk structures. The effect of pinning sites in magnetic structures, both as-grown intrinsic or fabricated artificial defects, are investigated, while artificial surface modifications are made utilizing focused ion beams.

We present effective measurements of interaction between local energy potential made by inhomogeneities and the spin texture, in an individual system. The study reveals remarkable information about the energy potential of the pinning sites and their dimensions with the help of analytical investigations and micromagnetic simulations. The Barkhausen effect refers to the stochastic jumps in magnetization resulting from the pinning of magnetic domain structures that produce the stick-slip motion of the vortex magnetization texture

[36]. With elaborated engineered pinning sites, it is shown that the effect of intrinsic sites which is usually shown as small jumps on the M-H curve (Barkhausen effects), can be eliminated for a wide field range.

Furthermore, using only one RF coil and changing the sample position on top of the coil, allows us to obtain susceptibility peaks at intrinsic sites on the M-H curve. By using two crossed coils, we gather information about the local non-linearity in magnetization texture transitions by investigating the ac susceptibility harmonics.

In Chapter 3 we describe the torque-mixing technique through experimental showcases, which demonstrate what the method can do. The simultaneous measurements start with the crossed coils, with a limited bandwidth, in polycrystalline Py devices with and without artificial defects. The pinning sites cause the resonance frequency to shift to a higher range. The overlapped magnetization and spin dynamics show the effect of pinning even at a limited bandwidth.

We access a higher range of frequency bandwidth by replacing the coil system with transmission lines designed on a circuit board to produce in-plane and out-of-plane RF fields. A single-crystal YIG ferromagnetic disk fabricated through Ga^+ ions milling is considered for further tests because of its extremely narrow magnetic resonance linewidth.

The YIG structure's frequency-field dispersions have been thoroughly examined for in-plane and out-of-plane uniform magnetizations, and in a vortex state that is a ground state of a cylindrical structure with specific aspect ratios. We present a coupling of two modes (avoided crossing) and an investigation of Kittel-like modes to obtain an effective gyromagnetic ratio. A direct comparison with micromagnetic simulations guides us to extend our understanding about the imperfection made through ion fabrication in the YIG disk, in addition to the geometric implication.

In Chapter 4, the concluding chapter, we suggest some possibilities for fu-

ture research. Appendices are included for further details. In the first two appendices, A and B, we discuss micromagnetic simulation method and case studies, respectively. There are simulated examples of different materials, shapes, and pinning sites in the magnetic structures. These examples enhance our understanding and predict what to expect from the experiments. Appendix C includes the technical supports: a short description of schematics with details about the experimental setups, and devices fabrication of the mechanical sensors and the magnetic sample. There is also a description of designs and calibrations of the transmission lines.

Chapter 2

Quasi-static study of magnetic structures in presence of pinning sites

2.1 Motivation

Studying inhomogeneities and defects in magnetic materials is crucial especially when the size of a structure shrinks down to the nanoscale, which is comparable to the size of the defects. Making point-like defects, pinning potentials, in a magnetic disk with Ga^+ ions provides a great test bench for studying the pinning mechanisms, as well as some insights into the nature of ion damage to the magnetic structure. Although the modifications are limited to small areas on the surface, these artificial pinning sites demonstrate very effective vortex core trappings, which differentiate this work from the earlier studies of controlled pinning of magnetic vortices with hole defects, which create a core-less curled magnetization state.

2.2 Introduction

Nanoscale disorders are intrinsic to most materials used in nanotechnology and can affect both static and dynamic magnetic responses [37, 38]. Understanding the effects of nanoscale inhomogeneities in magnetic systems is of increasing interest, for example in the context of future spintronic devices [39]. The role of intrinsic pinning potentials in polycrystalline disks is always significant but has never been fully characterized previously, particularly in an individual structure [40, 38]. Usually, an array of structures has been used in quasi-static measurements of magnetization in which the magnetization characterization is averaged and manifested as a temperature-dependent residual magnetization (coercive field) [41].

In the present work, the magnetic response of patterned magnetic disks is explored via nanomechanical torque magnetometry in which the magnetic sample is put on top of a mechanical resonator using nanofabrication techniques [42, 43, 33]. From the magnetic torque expression, $\boldsymbol{\tau} = \mathbf{m} \times \mu_0 \mathbf{H}$, the sample can experience a torque as a result of an external magnetic field or a change in the magnetization equilibrium. Since the sample is affixed to the mechanical resonator, the magnetic torque transfers to mechanical torque. This results in a mechanical displacement, which can be read out with red light (HeNe with $\lambda = 632 \text{ nm}$) in a low-finesse Fabry-Perot cavity (optical interferometry).

Figure 2.1 shows the 3D rendering of the torque sensor, in which the mechanical resonator has three paddles. The fundamental torsional resonance frequency, $f_{mech} = 2.81 \text{ MHz}$, has been used in our measurement. In addition, the laser spot was focused on one of the outer paddles, far from the torsional axis to capture the highest deflection. The constructive and destructive patterns guide us to resolve the mechanical deflection and consequently the magnetic torque is obtained.

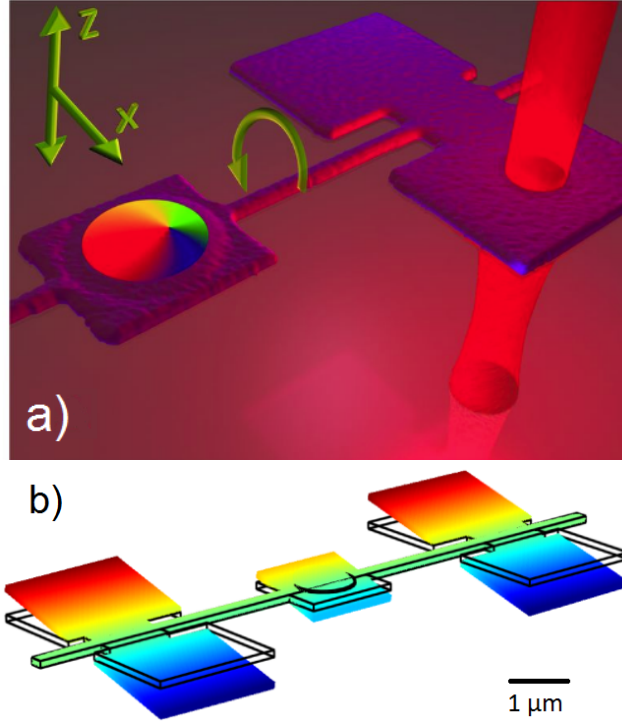


Figure 2.1: A 3D rendering of a silicon nitride torque sensor. a) The mechanical structure is demonstrated with texture generated from scanning electron microscopy (SEM) data and holding a ferromagnetic disk. Magnetic torque arises from applying an out-of-plane (z) RF field in the presence of net in-plane magnetization. The resulting torsional resonance has an amplitude proportional to the magnetization of the affixed structure (Taken from [44]). b) The fundamental torsional mode is obtained via COMSOL finite element modelling, in which all three paddles oscillate in phase (from [43]).

To obtain the magnetic hysteresis loop or the M-H characterization with the torque sensor, we apply a radio frequency (RF) field to the sample via an electric coil perpendicular to the dc bias field. First, from a thermo-mechanical noise measurement, the mechanical resonance is determined for the device at no drive. Then a sinusoidal current with the RF frequency matched to the natural resonance of the torsional paddle is sent out to the RF coil, while the sample is set at the center of the coil to only experiences an out-of-plane component of the RF field. Note that the RF current amplitude should not alter the magnetization equilibrium. For this reason, small RF amplitudes are chosen. The magnetic torque, τ_m , which is proportional to \mathbf{m} , is resolved from reading

the mechanical deflection via a lock-in technique (a Zurich lock-in amplifier has been used [45]). By having the amplitude of the RF drive, \mathbf{H}^{RF} , it is possible to obtain the magnetization \mathbf{m} .

To obtain the hysteresis loops, the position of a permanent magnet (bias field) is changed by translating it on a stepper motor. The new magnet position creates a new magnetization equilibrium in the sample. At a given bias field, the net magnetization \mathbf{m} reaches its equilibrium quite fast in a time frame on the order of a nanosecond (dynamics rates). On the other hand, in the highest speed of the motor around 2500 turns per second (each turn puts the magnet in a new position), it takes around 0.4 ms to put the magnet in a new position, which is still millions of times higher than dynamics rates. Therefore, this capturing of data while moving the magnet is considered a quasi-static measurement.

In this chapter, after introducing the vortex state, we use torque magnetometry to characterize the intrinsic and artificial pinning sites. The ability to deliberately control the magnetic consequences of the inhomogeneities is very important and can be achieved by studying artificial pinning sites. An elegant method of ion manipulation, focused ion beams (FIB), has been used to modify the surface of magnetic disks and create artificial pinning sites. Varying the beam current and exposure time tailor the strength and lateral dimension of the pinning sites.

The magnetic responses of a 42nm thick Permalloy (Py, $\text{Ni}_{80}\text{Fe}_{20}$) disk are shown in the presence of natural (as-grown) inhomogeneities as well as artificial pinning sites made with Ga ions. In addition, a dose-dependent study of artificial inhomogeneities in thin magnetic Py disks (12 nm thickness) is presented. A mapping of local properties provides valuable insights into the nature of ion damage and FIB irradiation on the pinning potentials. Artificial pinning sites can be engineered to change energetic landscapes. These sites provide a basic control mechanism for spintronics devices. The torque magnetometry method

with an analytical model and micromagnetic simulation gives us quantitative understandings of magnetic pinning sites; both the intrinsic magnetic disorder potential responsible for the Barkhausen effects and artificial surface modification.

2.3 Magnetic vortex state

A magnetic vortex is the ground state of low anisotropy magnetic disks with small enough thickness-to-diameter aspect ratios. Figure 2.2 shows the phase diagram of a magnetic disk with respect to diameter and height. The vortex state has a curling in-plane flux-closure magnetization distribution with an out-of-plane point-like core component at the center.

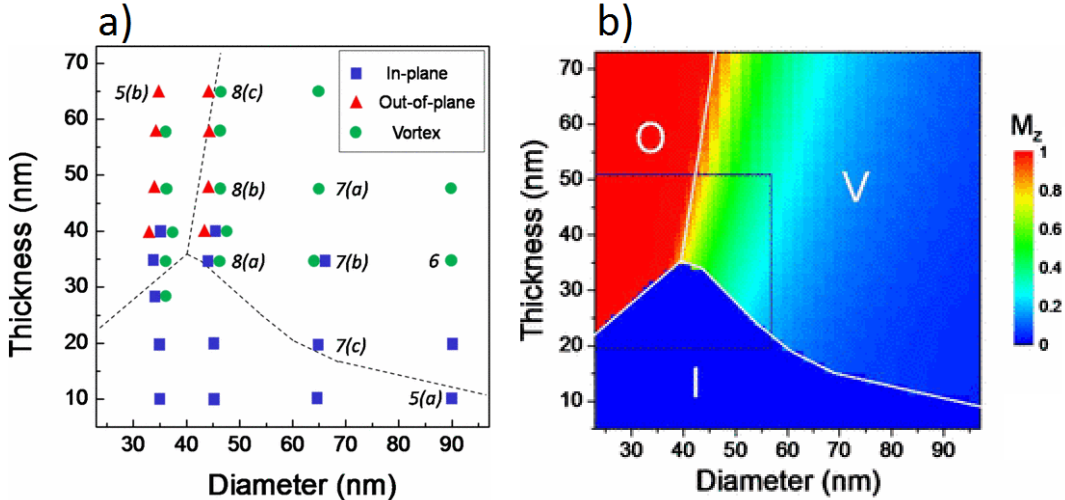


Figure 2.2: Phase diagram of magnetic state (in-plane, out-of-plane, and vortex) in a magnetic cylinder. a) The data points are obtained via scanning electron microscopy with polarization analysis. b) Phase diagram obtained from micromagnetic simulation in the same range of diameter and thickness (OOMMF micromagnetic simulation). At the dashed boundaries a combination of states is predicted. From [46], used with permission.

Through the application of an in-plane external bias field, the vortex core can be moved around inside the disk to reveal the energetic landscape by interacting with intrinsic disorder and other magnetic inhomogeneity. When there

is no external bias field, the vortex core sits nearly at the center of the disk producing zero in-plane magnetization (Figures 2.3a and 2.3d). While the bias field increases slowly, the vortex core will move towards the edge of disk, perpendicular to the field direction (Figure 2.3b). By further increasing the field, the annihilation of the vortex core happens and the single in-plane domain (saturation state) is achieved (Figure 2.3c). Figure 2.3 shows a micromagnetic simulation of a Py disk with $2\ \mu\text{m}$ diameter and $10\ \text{nm}$ thickness to demonstrate magnetization textures.

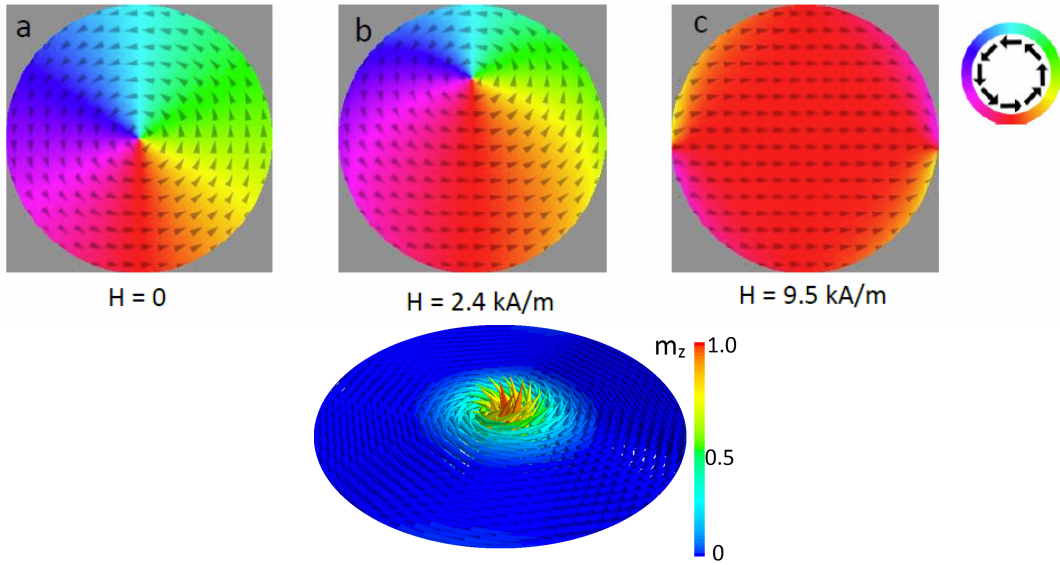


Figure 2.3: Magnetic states in a Py disk at different field values (simulation). a) The vortex state (ground state) at $H_x = 0$, b) the vortex state at a finite in-plane field, and c) uniform magnetization (saturation state). The direction of the applied field corresponds to red in the colour-wheel. d) A 3D rendering of the vortex magnetization at the ground state with colour coding the m_z component ($H_x = 0$).

The magnetic vortex can be described by two independent components: a chirality, which is the direction of in-plane magnetization curling; and a polarization, which is the up or down orientation of the core, as shown in Figure 2.4. The vortex nucleation and annihilation are dominant transitions on the hysteresis loop from a uniform magnetization to a vortex state and reverse. Different chiralities have a dominant effect on the statics appearance

of this transition. The vortex polarization, however, has almost no effect on these static interactions, but it is a leading factor in the dynamics and the vortex core switching.

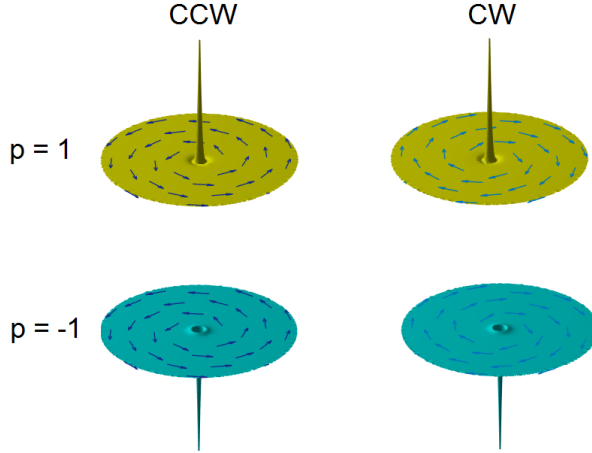


Figure 2.4: Degenerate magnetic vortex states. Four possible cases are presented with two polarities ($p = \pm 1$, up and down) and two chiralities (clockwise (CW) and counter-clockwise (CCW)). The core profiles have been obtained via simulations of a $1 \mu\text{m}$ diameter and 10 nm thick Py disk.

With an in-plane external dc field, the vortex core moves perpendicular to the field towards the edge of the disk to make a new equilibrium position with more net magnetic moment aligned with the external field. While in the perpendicular dc configuration, the size of the core will change. In addition, the vortex core with a diameter on the order of 10 nanometers is a localized region of high demagnetization and exchange energies. Thus a vortex core is a nearly-ideal probe for short-range variations of magnetic properties that can interact with the surface energetic landscapes as the core position is raster-scanned within the disk through the application of external magnetic fields [44, 47, 48].

In the following, the interaction of a vortex with a distribution of nanoscale natural defects is examined directly through the variation in $M(H)$, analogous to the Barkhausen effect familiar from the case of domain wall pinning [49].

2.4 Characterization of intrinsic pinning sites

In a poly-crystalline Py structure, there are intrinsic surface inhomogeneities. The distribution of native nanoscale magnetic inhomogeneities in polycrystalline films with different granularities was mapped through their influence on the gyrotropic frequency of a vortex displaced by a static field throughout the disk. The pinning site was found to depend on the grain size [40, 37]. Albeit in coarse-grained films, the number of magnetic pinning sites that enable to modify the magnetization dynamics is significantly exceeding the number of grains found by atomic force microscopy.

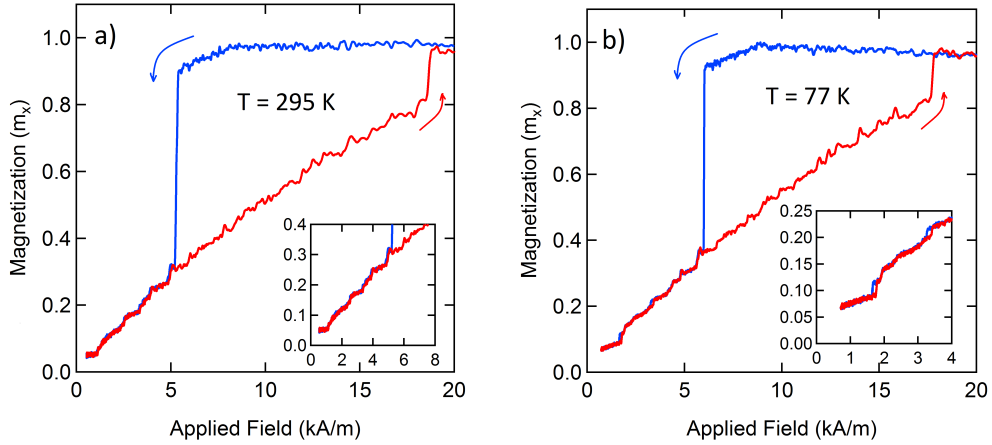


Figure 2.5: Full hysteresis of an as-grown Py disk with 42 nm thickness and 1 μm diameter. a) and b) At room and LN2 temperatures, respectively. The zoom-in of M-H curves is presented in the lower-right insets in each panel. At 77 K, minor hysteresis loops (bistable states) arise between the up (red) and down (blue) sweeps, in contrast to the apparently reversible steps in magnetization in the room temperature measurements.

Quasi-static magnetization measurements of a disk in the vortex state reveal irregular step-like features in the magnetization versus applied field characterization. That reflects the interaction of the point-like vortex core with locally-varying magnetic properties of the disk material. The local variation of the core energy with positions will be manifest as changes in the slope of the M-H curve (dynamic susceptibility), and as hysteric minor loops if the variations

are large enough to produce local pinning sites in the disk and concomitant local irreversibility in the magnetization curve.

The full hysteresis between the magnetic vortex and the quasi-uniform magnetization states of disk-shaped elements has been investigated in great detail, both through measurements which yield the average response of arrays containing many elements [50, 51], via micro-Hall magnetometry [52, 53, 54] and torsional magnetometry [43] of single dots. The sample in this study is a 42 nm thick, 1 μm diameter Py disk on a 100 nm thick silicon nitride torsional resonator. A fine-grained, smooth Py disk is created by electron beam deposition in an ultrahigh vacuum through a stencil mask onto a silicon nitride membrane suspended in a silicon frame. The resonator is cut around the disk using a dual beam focused ion milling system [43].

The hysteresis loop of our device at $T = 295\text{ K}$ and $T = 77\text{ K}$ are presented in Figures 2.5a and 2.5b, respectively. There are two big jumps: in the field sweep down which corresponds to transitions from the quasi-uniform state to the vortex state (vortex nucleation), and in the sweep up from the vortex state to the quasi-uniform state (vortex annihilation). By taking sets of measurements at room temperature, $T = 295\text{ K}$, and at the liquid Nitrogen (LN2) temperature, $T = 77\text{ K}$, we investigate the tiny slope changes in the M-H curve that occurred because of intrinsic pinning sites. The inset shows a zoom-in around a minor loop.

The energy barrier of defects is so small that at room-temperature measurements there is no minor loop, just a stair-like jump in the magnetization, which is related to the thermally activated hopping of the vortex between neighbouring pinning locations. The evidence of energy barriers is shown in the minor loops at the LN2 temperature. Consequently, the energy potential on the order of 1-2 eV has been obtained for the vortex core displacements by using the analytical method deformable vortex pinning model (DVPM) [55].

To obtain the field position of the features independently from the temper-

ature, one can scale the magnetic field to the saturation magnetization ($H_{scaled} = H \times [M_S(T = 0)/MS(T)]$) [51, 54].

2.5 Characterization and control of the energetic landscape using Ga^+ ions

The quantitative understanding of magnetic pinning will allow for further control of both magnetostatic and dynamical processes in future spintronic devices. The locally-varying energy landscape caused by anisotropy, thickness, or saturation magnetization variations can be accessed by introducing artificial defects to amplify the effects [53, 49].

To make artificial surface pinning sites, we introduced single point-like FIB exposures on the order of 10,000 ions for gentle surface modifications and, consequently, an alteration of local magnetic energy landscapes [44, 47]. Through FIB exposure, high-energy Ga^+ ions sputter away some surface atoms and implant into the disk under the exposed area to change the magnetic properties of that region, which is described mainly in terms of the variation in the saturation magnetization and/or exchange strength [56, 57]. The strengths of the pinning sites are tailored via the total Ga dose (beam current \times exposure time), while their lateral width should be dictated by the ion scattering volume in the film (~ 20 nm diameter, larger than the nominal beam focus). Appendix C contains more details about the device fabrication and FIB process.

For a magnetic disk in low field ranges, both the magnetization m_x and the core displacement are linearly proportional to the applied field H_x , as described by the rigid vortex model (RVM), [58]. This corresponds approximately to the core displacements up to half of radius, $R/2$ distance from the disk center. Therefore, we design the position of pinning sites to be in a circle with the radius of $R/2$, as shown by a dashed circle in the schematic of the design in Figure 2.6a.

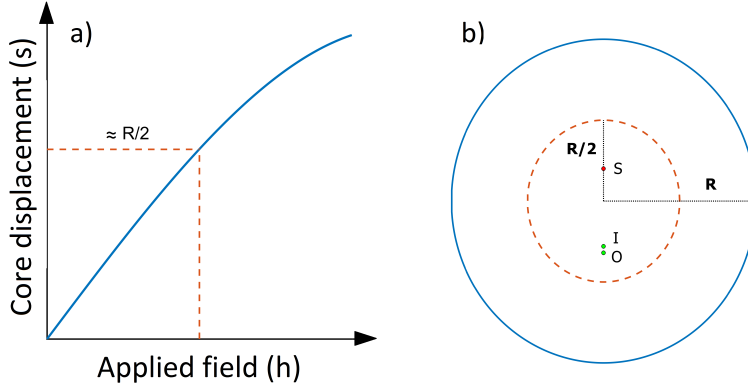


Figure 2.6: Designing the position of artificial pinning sites in a magnetic disk. a) Schematic of idealized vortex core position versus field. The core displacement shows a linear response versus the applied field up to approximately $R/2$ from the center of the disk (R is the disk radius). The presented curve is based on the cubic polynomial in the rigid vortex model ($a\vec{h} - b\vec{h}^3$). b) The layout of the designed site for using the two sides of the disk for exploring a single (S) pinning site, and proximal pairs (inner, I , and outer, O).

The core interactions with the pinning sites, which show the slope changes in the magnetization, are perceptible signatures in the M-H curve in this range. However, for the core position larger than $R/2$, the nonlinearity of the response plays an important role and finding the interaction vortex core with pinning sites would be more complicated.

To investigate an individual site and the effect of coupling between the pinning sites, we consider making a site S (single) on one side and two close pinning sites, I (inner) and O (outer) on the other side of the center line. In the first sample, which is a 42-nm thick Py disk, the disk radius of 550 nm is measured from the SEM imaging. Then, the maximum position limit of $R/2 = 275$ nm is considered for creating the pinning sites. We initially calculated the position to be $S = 0.2R$, $(O,I) = 0.3R \pm$ closest centre-to-centre distance, which is limited to the beam focus, as illustrated in Figure 2.6 b. To consider the uncertainty in the vertical direction, with a concern that defects being too close together, we decided to go with a slightly bigger spacing. Therefore, we selected $0.3R$ for the S site (165 nm from the center) and the paired sites are

centered around $0.4R$ (220 nm), with 50 nm between them (80 nm center-to-center). The I and O sites are at 180 nm and 260 nm, respectively.

In the FIB experiment, fiducial markers on the paddles were created first with 1000 ms exposures, to calibrate the relative Ga/electron beam alignment. Then, we exposed the defined defects in the direction of the torsional rod (y -direction), so by changing only the H_x^{dc} magnetic field the vortex core can interact with all the pinning sites. We measured the positions of artificial sites after introducing point exposures to $\sim 75,000$ Ga^+ ions that sputter away only 2 nm of film material at their centers compared to the AFM dose test [44]. The actual values are around $S = (20, -110)$, $I = (40, 200)$, and $O = (50, 280)$, which have discrepancies from the design values; it seems the beam was tilted from the central line.

Two sets of measurements are presented with opposite in-plane dc field directions in Figure 2.7 top-left inset. The two minor loops (those shaped like a dumbbell) on each experiment are a signature of core pinning/depinning at the single defect in the M-H curve. By rotating the dc magnetic field 180° at “high field”, the other side of the disk with paired defects is not accessible and only chirality of the created vortex changes, but vortex nucleation will occur on the same side.

Compared to the hysteresis loop of the as-fabricated disk presented in Figure 2.5, it is evident that the pinning sites strongly modify the low-field characterization of M-H curve. The pinning sites also have a significant influence upon the process of creating vortex from the quasi-uniform state.

To reach the other side that has the paired sites, we perform the field rotation at a low field, after the vortex nucleation field. Accordingly, by applying more fields, the vortex is pushed further to interact with the paired sites. Three minor loops are seen in the negative field (Figure 2.7), which shows a coupling between the paired pinning sites. If the pinning sites are farther apart, the core can interact with them separately and four minor loops will be created.

However, in this case, while the applied field pushes the vortex core to depin it, the core hops into the second site.

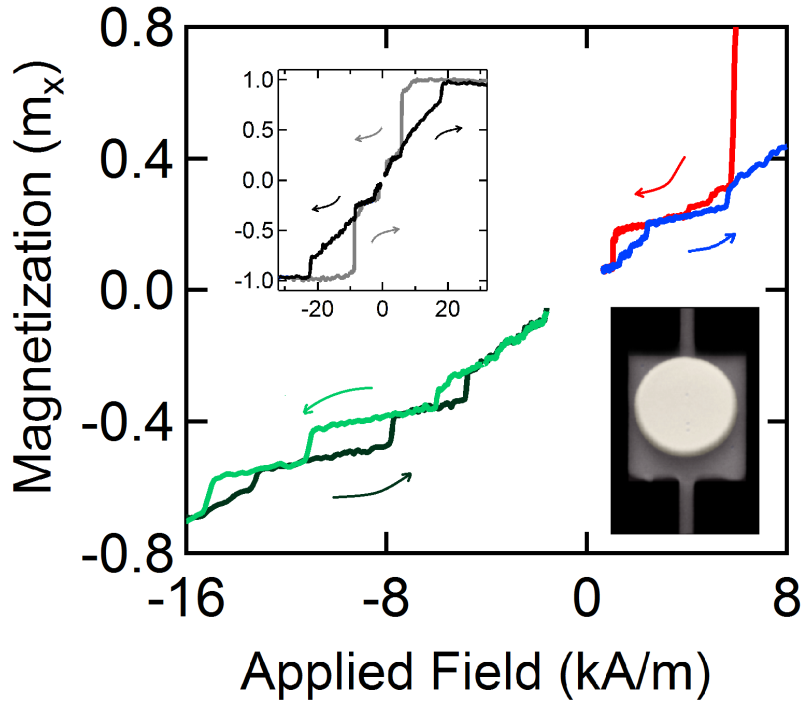


Figure 2.7: The core interactions with all the artificial pinning sites related to minor loops in the M-H curve. The red/blue curves correspond to the single pinning site, while the light/dark green curves show the magnetization responses in the presence of paired pinning sites. The SEM image of the witness Py disk with Ga-made defects (*S* side on top and *I* and *O* in the bottom part of the disk) is presented in the lower-right inset. The top-left inset shows the full hysteresis loop in which, the vortex core has been nucleated with different chiralities but in the same portion of disk that contains the *S* site (with different nucleation absolute field values). The single plateau on the positive field represents the *S* site, while two plateaux on the other side correspond to the paired *I* and *O* pinning sites.

The vortex core can be inside the pinning potential for a large magnetic field range. Due to the presence of artificial defects, the vortex core pinnings are much stronger within an area that has already been characterized in the unaltered condition. This demonstrates, unambiguously, enormous latitude for patterned control of the energetic landscape of the vortex core, for applications for vortex-based devices including memories and oscillators. Using the analytical model, DVPM, the energy potential of the Gaussian pinning sites

was found to be 19 ± 2 eV deep and 42.39 nm wide. However, the positions obtained from the analytical model show large discrepancies, at 110 nm, 215 nm, and 300 nm. That is because the model begins to return fit values larger than the actual positions of the pinning site due to systematics in the model.

An additional study of dose-dependent defects has been performed for thinner Py disks, with the thickness of 12 ± 2 nm. The strengths of pinning sites are characterized for point exposures to 30 keV Ga⁺ ions in doses nominally 1×10^4 , 2×10^4 , and 4×10^4 ions, which provide good ‘pinned vortex susceptibility’ over a wide range of fields. An SEM image of the single site sample created with a Ga beam current is shown in the upper left inset of Figure 2.8.

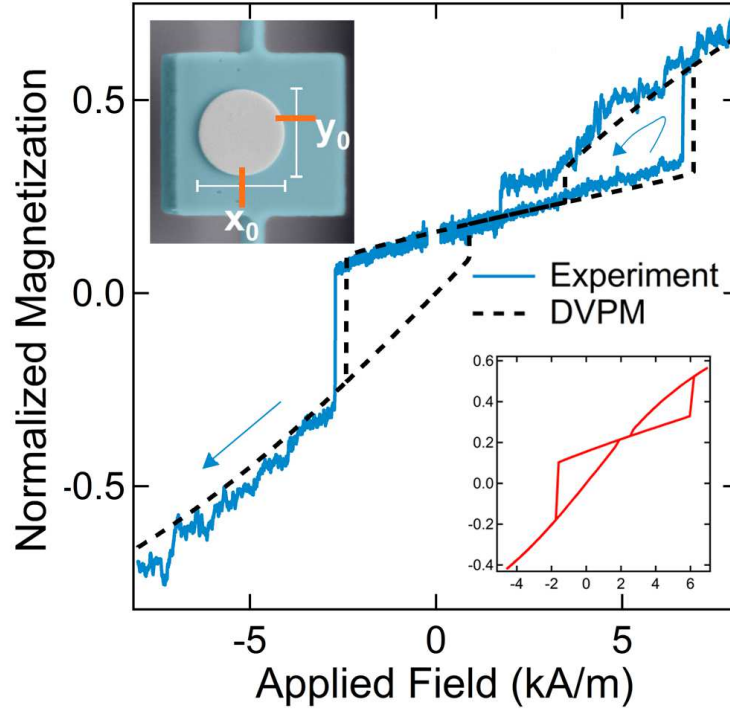


Figure 2.8: A room temperature magnetization response versus in-plane field for a $1 \mu\text{m}$ diameter and ~ 12 nm thick Py disk with one FIB-induced defect. The DVPM fit (dashed line) to a Gaussian pinning potential well yields: disk thickness = 12 nm, defect position = 126 nm, Gaussian width = 29 nm, and pinning potential 9.5 ± 0.5 eV. A numerical simulation result for a $1 \mu\text{m}$ disk with 12 nm thickness and a single defect corresponding to an absence of moment of 4 nm depth is shown in the lower right inset, and displays a similar response.

For a single pinning site, there is an asymmetric dumbbell-shaped hysteresis

response with two jumps each on field sweeps up and down, as shown in Figure 2.8. Even this very small surface alteration overwhelms the regular magnetic response at room temperature. From the two depinning fields, an approximate position of the defect can be estimated, and is found to agree closely with the design location [44, 59]. The effective pinning potential depth for this artificial defect is estimated to be ~ 10 eV by analytical fitting with DVPM, which captures both the flexing and translational response of the core-pinned magnetic vortex texture [55].

After making fiducial markers with 1000 ms exposures, the lowest beam current of 0.15 pA is quickly exposed for 10 ms, ~ 10000 Ga⁺ ions, to induce this very shallow pinning site at the desired location while positional drift remained negligible. The artificial defect is invisible to SEM. So the design position at $x_0 = -43$ nm, $y_0 = +156$ nm from the disk center, relative to the reference marks, is illustrated by means of the orange horizontal and vertical indicators on rulers in the SEM image. The micromagnetic simulation for an off-centered defect with thickness around 5 nm and diameter of ~ 44 nm (circular cross-section) in a micron Py disk with 12 nm thickness demonstrate similar hysteresis loop, as shown in the lower right inset of Figure 2.8.

A full hysteresis loop of a single defect in the micron diameter Py disk is presented in Figure 2.9. The hysteresis loop starts with the pinned vortex at low field, and in sweeping towards the negative high field, the first depinning field is observed. Then in the field sweep up, the vortex is again pinned, and at the positive field, the other depinning event is obtained. There are additional tiny jumps in the minor loops, that we try to qualitatively understand them. By considering that ion beams might be misaligned, then there could be additional rings appeared around the pinning site, very similar to the Airy pattern. In optics, the diffraction patterns of a focused spot of light with a circular aperture are described by the Airy disk and Airy pattern, the bright region in the center and concentric bright rings around it, respectively. The simulation result in the

inset shows wider internal loop for a rectangular ring with 2-cell separation from the pinning site (cell size ~ 5 nm).

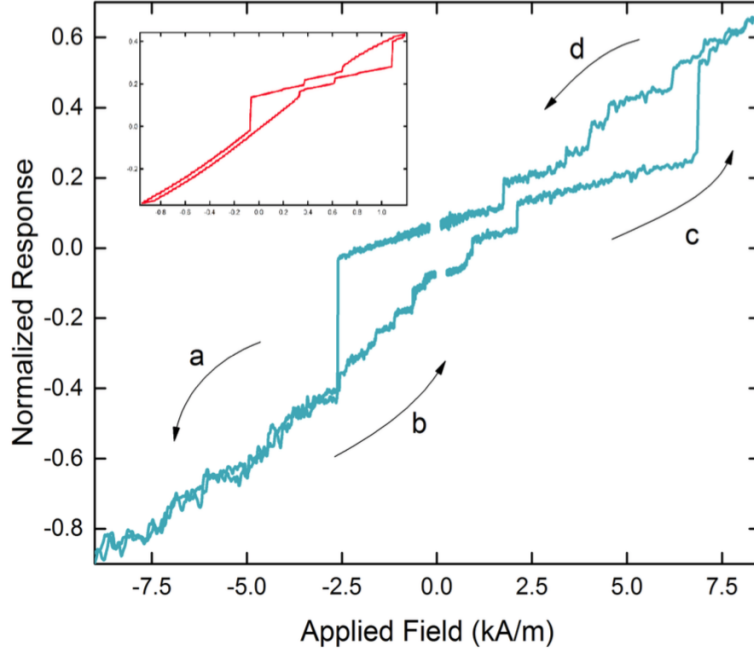


Figure 2.9: A full minor loops for a $1 \mu\text{m}$ diameter and ~ 12 nm thick Py disk with one FIB-induced defect. The labeled arrows show the directions of performing the field sweep. A numerical simulation in the inset obtained for a single defect with a additional rectangular ring with 2-cell separation around the defect.

In our initial study for the 42-nm thick microdisk, the efficacy of magnetic potential well excavation is ~ 0.25 meV per implanted ion (19 eV/75000 ions). However, for the 12-nm thick microdisk, this number is one meV (10 eV/10000 ions), which demonstrates a non-linear response between the number of ions and the potential well energy. It appears that the thinner disk is more responsive to ions and the pinning energy is about three times greater per implanted ion than what is found for the thicker Py disk. The 12-nm film thickness here is well matched to the implantation depth of 30 keV Ga^+ ions. The greater efficacy of the artificial pinning site formation in the latter suggests that ions are disrupting the exchange coupling between grains through the complete film thickness.

The pattern of three off-centered pinning sites in the $2\ \mu\text{m}$ Py disk is shown in the upper-left inset of Figure 2.10, in which site S is at 210 nm from the center and the other sites (I and O) are on the opposite side, at 80 nm and 220 nm. A very small beam current of 0.3 pA and dwell times of 10 ms and 20 ms are used for making single and the pair defects exposures, respectively.

By introducing more than one pinning site, the coupling effect between them can make a remarkable field and magnetization range of “Barkhausen-free” response, as illustrated in Figure 2.10. Additional artificial pinning sites on the $2\ \mu\text{m}$ disk leads to substantially an extension of the net moment change of the disk while the core remains pinned in the first site, unlike the earlier case for a smaller, thicker disk [44], where the sites on two sides behaved independently.

The addition of an extra artificial pinning site makes it even easier energetically for the magnetization to flex in the vicinity of the pinned core at a single site over an applied field range comparable to the vortex annihilation field of the unaltered disk. The net magnetization change without depinning is nearly equal to the saturation moment of the disk. The response is Barkhausen-free as long as the moment changes with the core remaining pinned. With the core trapped at O ($y_0 = -220\ \text{nm}$), when it is driven by the field towards positive y there is much additional flexing of the magnetization texture around I and the depinning event yields vortex annihilation (the core jumps past I and S all the way to $y \geq 1\ \mu\text{m}$). The thinner, larger disk emphasizes the ability of the net moment to change by flexing of the magnetization distribution.

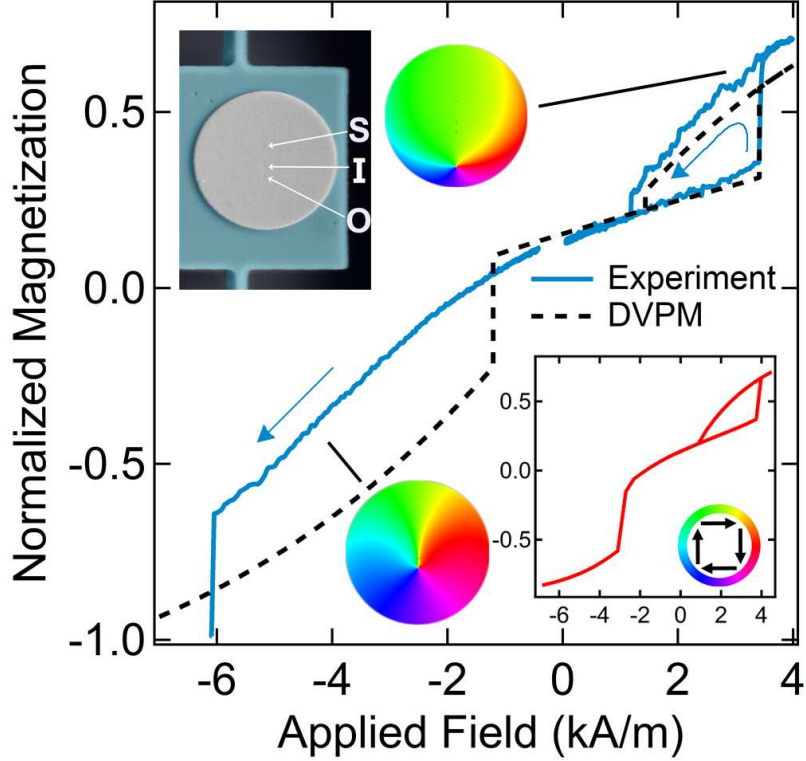


Figure 2.10: Magnetization response versus in-plane applied field for a $2\ \mu\text{m}$ diameter and $\sim 12\ \text{nm}$ thick Py disk with three FIB-induced defects. A FIB exposure of $10\ \text{ms}$ at $0.3\ \text{pA}$ was used for site S (single), $+210\ \text{nm}$ from the center, and $20\ \text{ms}$ exposures created I (inner) at $-85\ \text{nm}$ and O (outer) at $-220\ \text{nm}$. The DVPM fit (dashed line) yields: disk thickness = $11\ \text{nm}$, O site position = $-220\ \text{nm}$, Gaussian width = $29\ \text{nm}$, and pinning potential $10 \pm 1\ \text{eV}$. Lower right inset: simulation result for a $2\ \mu\text{m}$ disk with $10\ \text{nm}$ thickness, and defect depths $2.5\ \text{nm}$ (S), and $5\ \text{nm}$ (I and O).

The DVPM yields a pinning potential depth of $10 \pm 1\ \text{eV}$ from fitting to the minor loop with the half of pinning signature. When the field drives the core towards negative \hat{y} , depinning occurs in a manner well described by DVPM and by simulation. In contrast, both the DVPM and micromagnetic simulation predict that the core will depin much earlier than is measured, for the field sweep down, proving the cooperativity of the O and I sites in effecting the extended Barkhausen-free response in this direction. This remarks that even DVPM be inadequate in describing the flux when there are more than one pinning sites. In addition, we anticipate that the well depth of the single pinning site in the small disk should be half that of the single site in the bigger

disk (nothing to do with the disk diameters, just the exposure being dialled down another factor of two for that last, single pinning site). But on the controversy this is not justified from the DVPM.

Thanks to the high signal-to-noise ratio of nanomechanical torque magnetometry, in the full hysteresis loops shown in Figure 2.11 the Barkhausen/Barkhausen-free regimes are clearly contrasting. It is evident at a glance which are the Barkhausen-free segments of the hysteresis loops and which exhibit the irregular magnetization evolution with field owing to the overlay of intrinsic core pinning resulting from as-grown magnetic disorder in the Py film. The former sections are almost indistinguishable in appearance from numerical simulation lines, when plotted on this scale. A fit using the third-order, susceptibility-corrected rigid vortex model (RVM, dashed line) confirms the disk thickness of 11 nm [51].

The highly confined pinning sites can trap a magnetic vortex core to the extent of suppressing Barkhausen transitions in the magnetization response with an applied field. In addition, because the thinner disks are even more permissive of texture flexing, a cooperative response of two artificial point-like sites arises. This induces Barkhausen-free behaviour over a remarkably large net moment change approaching the saturation moment of the disk.

Introducing more than one defect has led to the presence of different vortex annihilation trajectories. Figure 2.11 exhibits a bistable behaviour of full hysteresis loops for the sample with three defects. If the vortex is created on the S site (the blue curve), it can easily pin into the I site around -0.5 kA/m, independent of how far away the I site may be (magnetization jumps from around -0.2 to about 0.09 , which is corresponding to normalized pinning site positions; $r_S = -0.21$, $r_O = 0.22$, and $r_I = 0.085$).

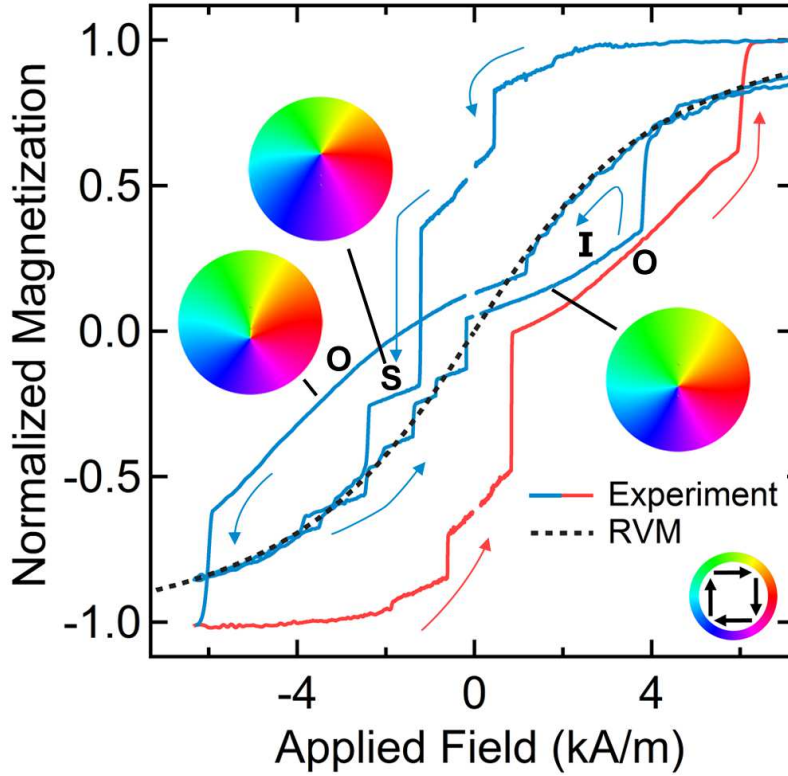


Figure 2.11: Two different vortex creation and annihilation trajectories in a full hysteresis loop for the disk with three pinning sites. Depending on the initial position of the nucleated vortex, the core will interact with either S or O sites. O, being of higher dose, pins the vortex core until annihilation while suppressing Barkhausen signatures (red trace). When the core nucleates on the side of the S site, it depins into I and, upon escaping I, can be brought back into O (blue trace). Paths along which the vortex core is pinned are labeled by site letter and simulation thumbnails. An RVM fit to the unpinned vortex state magnetization is presented with dashed line.

By sweeping up the field, the vortex is pushed towards the edge of the disk on the double defect side, and depinned from the I site at a field around 4 kA/m. In the sweep down on this path, the vortex is pinned in the O site, a strong pinning site, remaining there until the flexing causes vortex annihilation. On the red path, however, the core is nucleated on the (I,O) side and pinned directly into O, remaining pinned until saturation occurs. The I and O defects are strong enough to keep the vortex pinned while the field sweep pushes the vortex towards the S site. The lower dose S defect, on the other hand, releases the core to I comparatively easily.

To reproduce core pinning in simulation, one-quarter and one-half of the disk thickness are set to zero magnetization over an area of 678 nm^2 in order to represent the single and paired sites, respectively. This area corresponds to a circle with a diameter of 29.4 nm chosen closely to beam width of 30 nm . For the remaining region of disk, Py properties at room temperature ($A = 13 \text{ pJ/m}$ and $M_s = 700 \text{ kA/m}$) are used. More details of the investigation about the shape of defect, area, and depth have been brought in Appendix B.

To further this study, the magnetization reduction caused by the He ions were investigated using a helium ion microscope (HIM). It seems that imaging with He^+ ions can extend the pinning strength on the O site as shown in Figure 2.12, which could be related to the interaction of He ion during imaging with the pinning site. Thus the extension pinning loop suggests that even imaging with He ions could modify the surface magnetization.

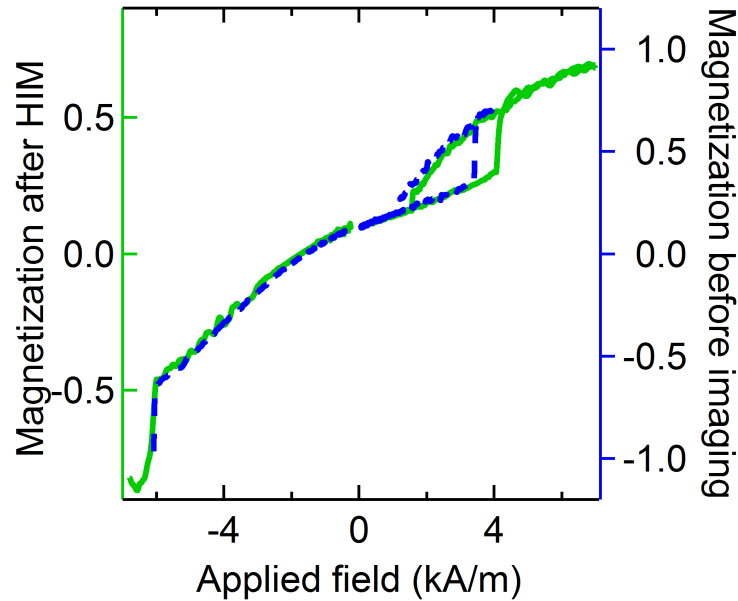


Figure 2.12: The minor hysteresis loop in a $2\text{-}\mu\text{m}$ diameter Py disk with triple defects (made by Ga^+ ions) before and after HIM. The blue dotted line shows the minor loop before imaging with He ions and the solid green curve demonstrates the M-H characterization after imaging.

Although HIM imaging with the sub-nanometer resolution should have pro-

vided us with a better imaging of the pinning sites, we did not obtain a better contrast from all defects compared to the previous use of a traditional SEM. It appears that the currents of 0.54 pA and 0.4 pA have been used for imaging and milling. These currents are considerably larger than what had initially been used to make the pinning site initially. After imaging with He ions, there was an unexplained frequency shift in the mechanical resonance (from 4.39 MHz to 5.24 MHz), and also field dependent. As a result, we used a phased locked loop (PLL) option in the Zurich Instruments lock-in amplifier to obtain the magnetization response.

2.6 Susceptibility at the Barkhausen steps

In a conventional nano-mechanical torque magnetometry, which reads the magnetic moment, one RF drive coil or a dc applied field is required. However, it is possible to obtain susceptibility terms in addition to magnetization with that one coil, which provides new insight into the properties of the pinning processes. Different RF field components are accessible by changing the sample position on top of the coil. To facilitate this process, an additional in-plane component of the RF field (parallel to the nominal dc field direction) is introduced by tuning the device position relative to the center of the RF coil.

The torque in the y-direction can be extracted at the mechanical frequency from Equation 1.7:

$$\tau_y \equiv \tau_{m_x} + \tau_{m_z} + \tau_{\chi_x} = -\mu_0 m_x^{\text{dc}} H_z^{\text{RF}} + \mu_0 m_z^{\text{dc}} H_x^{\text{RF}} - \mu_0 \chi_x V H_z^{\text{dc}} H_x^{\text{RF}}, \quad (2.1)$$

where τ_{m_x} and τ_{m_z} are dc-moment torques, and τ_{χ_x} is the torque generated by the RF moment. When the sample is positioned on the coil axis, it is driven by a pure H_z^{RF} and the torque on the sample is proportional only to m_x^{dc} (χ_z is ignored due to the shape anisotropy inherent in the thin Py island). When

the sample is offset from the coil axis, $H_x^{\text{RF}} \neq 0$ and the in-plane susceptibility χ_x can contribute to the net torque. The relevant torque terms for both cases are summarized in Table 2.1.

Torque terms	On-axis $H_x^{\text{RF}} = 0$	Off-axis $H_x^{\text{RF}} \neq 0$
Magnetization	$-\mu_0 m_x^{\text{dc}} H_z^{\text{RF}}$	$\mu_0 (m_z^{\text{dc}} H_x^{\text{RF}} - m_x^{\text{dc}} H_z^{\text{RF}})$
Susceptibility	-	$-\mu_0 \chi_x V H_z^{\text{dc}} H_x^{\text{RF}}$

Table 2.1: Torque terms for two sample positions, on- and off-axis.

We calculate the RF field distributions of a finite solenoid by numerically integrating over the current source using the Biot-Savart law in Matlab. The resultant simulation of magnetic fields for a solenoid with 3 turns and diameter of 0.49 mm are presented in Figures 2.13b and 2.13c for a current amplitude of 0.24 A.

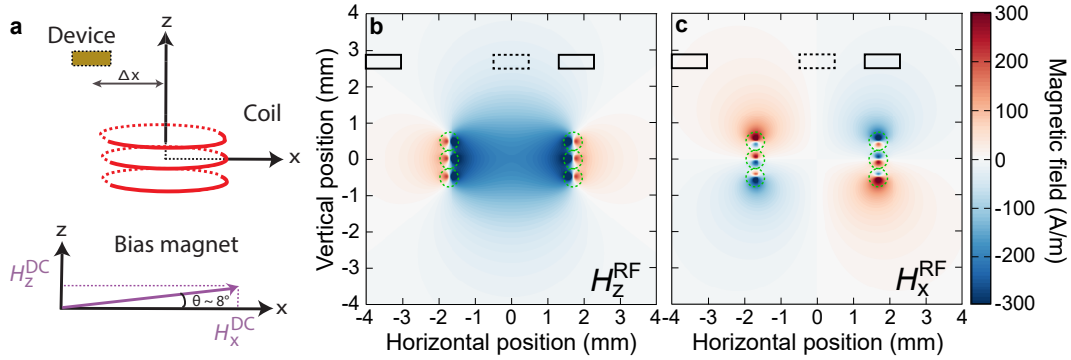


Figure 2.13: Attain different RF field components via changing the device position on top of the RF coil. a) Schematic of the positioning Δx of the device relative to the center of the coil (red). b) and c) H_z^{RF} and H_x^{RF} RF magnetic field simulations of the coil (green dotted circles) at a current of $I = 0.24$ A, respectively. The approximate positions of the device for experiments are shown by the dashed boxes. After supplemental information of Nat. Nanotech. Advanced Online publication (31 Oct. 2016).

When the chip is centered ($\Delta x = 0$ mm, about 2 mm above coils), H_z^{RF} is at its strongest point while H_x^{RF} is approximately zero due to symmetry. For

the observations of RF susceptibility requiring a non-zero in-plane component of \mathbf{H}^{RF} , the chip was positioned with offsets of $\Delta x = -3.6$ and 1.9 mm relative to the center of the coil as depicted in Figure 2.13a. It is found from Figures 2.13b and 2.13c that both x and z-components have comparable amplitudes, $H_x^{\text{RF}} = H_z^{\text{RF}} = H^{\text{RF}}$ for $\Delta x = 1.9$ mm. For the other offset to the left at $\Delta x = -3.6$ mm, we obtain $H_x^{\text{RF}} \approx -6H_z^{\text{RF}}$.

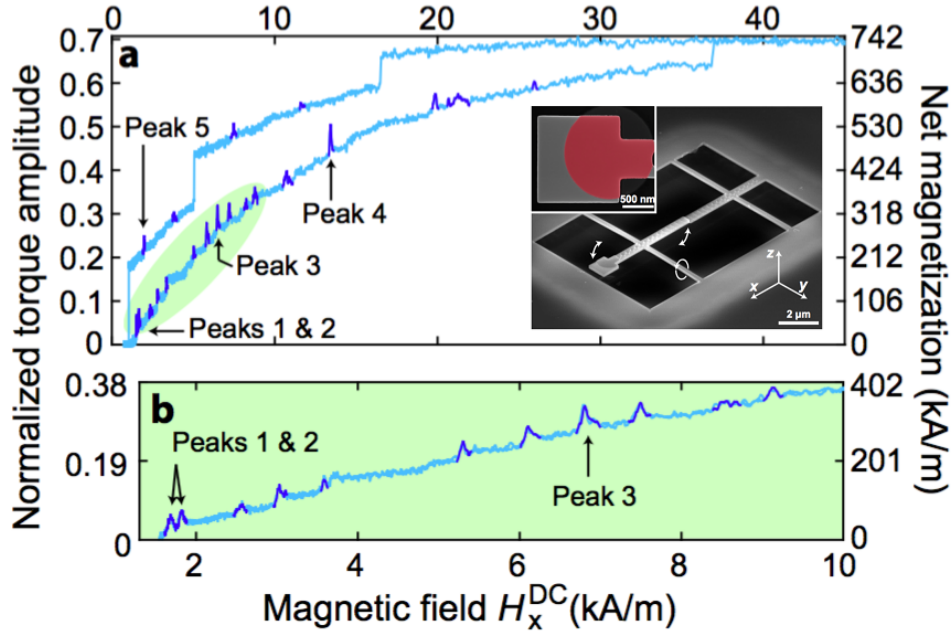


Figure 2.14: *M-H* characterization of a Py element with enhanced magnetic susceptibility features at Barkhausen steps at room temperature. Hysteresis sweep of the Py structure is captured at the coil position with $H_x^{\text{RF}} = H_z^{\text{RF}} = 35$ A/m. The upward peaks have been highlighted in dark blue to show the contribution to torque from susceptibility. The tilted SEM inset shows a torque sensor device (split-beam cavity optomechanic) with highlighted magnetic element in red. b) The low field H_x^{dc} field sweep up. After supplemental information of Nat. Nanotech. Advanced Online publication (31 Oct. 2016).

Figure 2.14a shows the full hysteresis loops for $H_x^{\text{RF}} = H_z^{\text{RF}} = H^{\text{RF}}$ field orientations ($\phi = 45^\circ$). The green highlighted region corresponding to the low-field responses is brought in 2.14b. The torque values remain normalized to the 90° orientation in the presence of only H_z^{RF} . The other useful way to readout the data is to normalize it to saturation magnetization, as presented on the

right axis of panels a and b in Figure 2.14. The magnetometry for this device is performed using the high quality factor cavity for readout the deflection of mechanical resonator. The inset in Figure 2.14 shows the mushroom-like device integrated in a cavity optomechanics.

Key features here are the RF susceptibility signatures, which contribute to the peaks in presence of in-plane RF field component. The phase between RF field components is related to sign of susceptibility terms that can appear as a peak or dip on top of the magnetization response (here only peaks are presented). The larger transitions, which correspond to changes in magnetization states in the main loop are irreversible and therefore exhibit no accompanying RF susceptibility features. When the energy barrier between neighbouring pinning sites is small enough, the in-plane RF field is able to drive the core synchronously back-and-forth (the Barkhausen effect). Given the already important role of thermally-driven rapid hopping in eliminating observed minor hysteresis at Barkhausen steps [44], the synchronization must be thermally-assisted.

Numerical estimates of χ_x at each peak is achieved in the following. By considering the ratio of the torques generated by the RF and dc magnetization at Barkhausen step from Equation 2.1,

$$\frac{\tau_{\chi_x}}{\tau_{m_x}} = \frac{\mu_0 \chi_x V H_z^{\text{dc}} H_x^{\text{RF}}}{\mu_0 m_x^{\text{dc}} H_z^{\text{RF}}}, \quad (2.2)$$

one can simplify it to the following:

$$\chi_x = \frac{m_x^{\text{dc}} H_z^{\text{RF}}}{V H_z^{\text{dc}} H_x^{\text{RF}}} \frac{\tau_{\chi_x}}{\tau_{m_x}}. \quad (2.3)$$

where $|\tau_{\chi_x}|$ is the size of the peak overshoot (or undershoot) and τ_{m_x} is the torque from the dc magnetic moment. For $|H_x^{\text{RF}}| = |H_z^{\text{RF}}|$, the peak suscepti-

bility is expressed as

$$\chi_x^{\text{peak}} = \frac{m_x^{\text{dc}}}{V H_z^{\text{dc}}} \left| \frac{\tau_{\chi_x}}{\tau_{m_x}} \right|. \quad (2.4)$$

The normalization scale set by the saturation moment of the film, which is a multiplication of the sample volume and the saturation magnetization of Py ($V M_s$) and the definition of the net magnetization, $m_x^{\text{dc}}/V \equiv M_x^{\text{dc}}$ allow us to obtain χ_x from the experimental data based on the following:

$$\chi_x^{\text{peak}} = \frac{M_x^{\text{dc}}}{H_z^{\text{dc}}} \left| \frac{\tau_{\chi_x}}{\tau_{m_x}} \right|. \quad (2.5)$$

We investigate the effect of the RF drive on the susceptibility. In Figure 2.15, a set of torque response (dc and susceptibility peaks) are considered for the case of $|H_x^{\text{RF}}| = |H_z^{\text{RF}}|$. At each drive, the amount of torque being generated by the susceptibility term is proportional to the peak height.

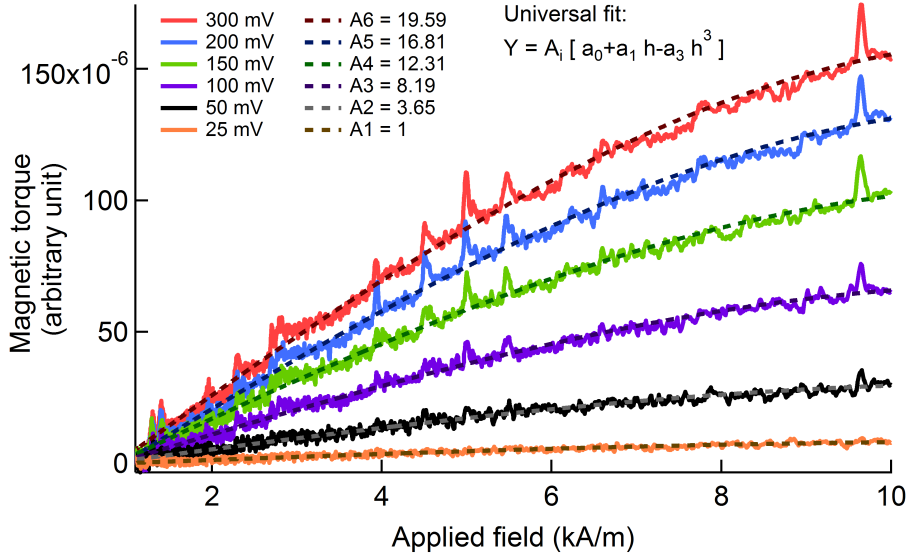


Figure 2.15: Low-field M - H curves versus various applied RF drives along with the fitting curves. The drive has been increased from 25 mV to 300 mV in various steps. The universal fit to each curve is shown in the dotted curve, which is only varied in the scalar factors, A_i .

Then the different heights for a given peak can all be measured with the same ruler to see how the effective susceptibility for that peak varies with drive, and in addition the only scaling parameter between different peaks will be: $M_x^{\text{dc}}/H_z^{\text{dc}}$. So if one put the different drives on equal footing, the trend of susceptibility at each field position can be determined from the peak values.

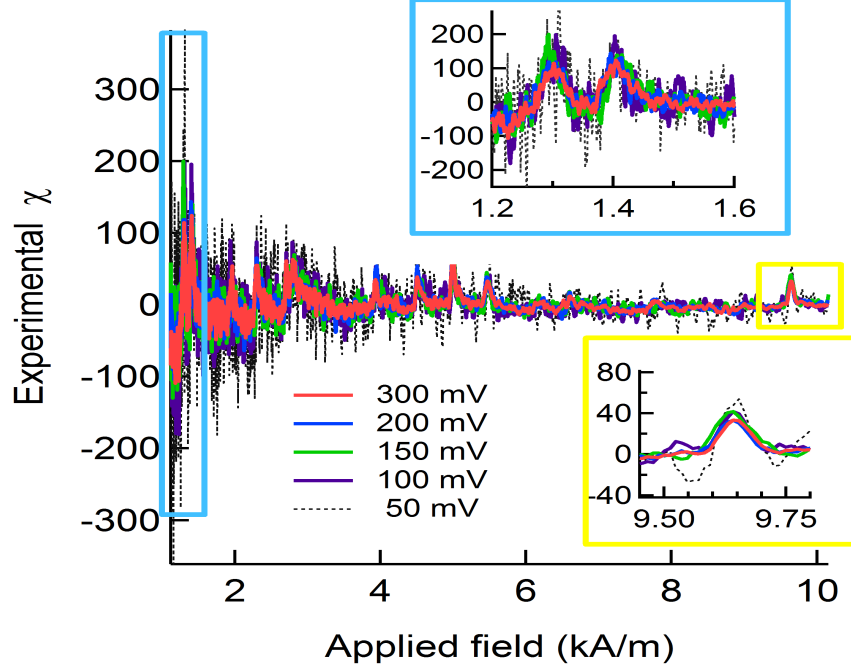


Figure 2.16: The extracted experimental susceptibility overlapped for different drive using the presented model. The two blue and yellow panels show the zoom in of the measured susceptibility. It is clear that susceptibility values depend on the dc bias field and also the RF drive, as one could predict from the model.

We start with rescaling the family of the low-field curves measured for different drive amplitudes with a “universal fit” so that they can all be plotted together. The universal fit, $Y = A_i[a_0 + a_1 h - a_3 h^3]$ is intended to find a fit function with only one free variable A_i , as a scale factor; and other fixed values: a_0 as offset, and a_1 and a_3 in the cubic model for the vortex displacement in a given applied field ($a_1 h - a_3 h^3$). Scaling the curves enables them to overlap all one another. In addition, the saturation torque in all cases corresponds to the saturation moment of the element times the H_z^{RF} field. Our model of the

system predicts that the signal amplitude response to H_z^{RF} increases should be linear. The differences would be limited to Barkhausen-y features with an added component of H_x^{RF} .

After subtracting the fit (normalized curves), what remains is the magnetic torque related to susceptibility peaks that are still normalized to saturation magnetization, as shown in Figure 2.16. Now refer to the expression for the susceptibility contribution in Equation 2.5, and considering the tilt angle of the permanent magnet, which introduces the H_z^{dc} , the unit-less susceptibility terms are obtained.

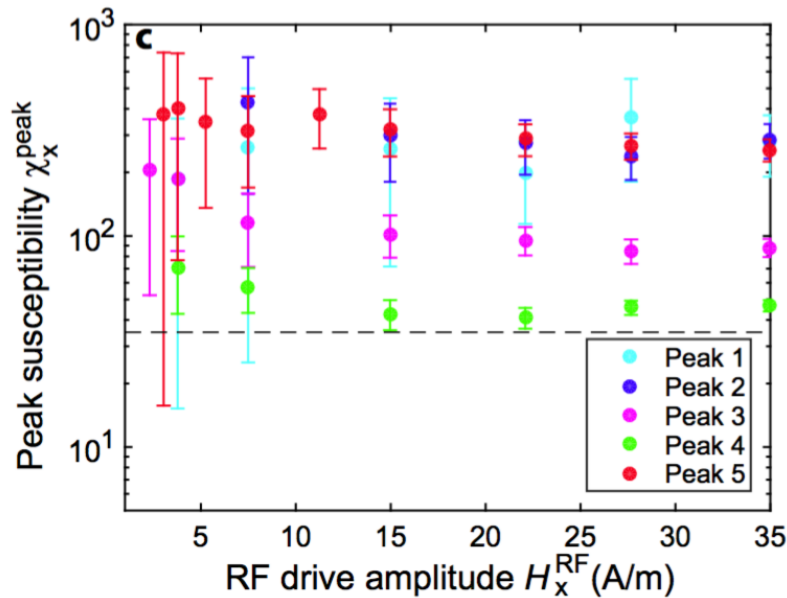


Figure 2.17: The experimental susceptibility as a function of RF drive amplitude. For selected peaks (peak 1 to 5 in Figure 2.14) the susceptibility terms have been extracted and presented for various RF drive. The dotted line shows the low-field quasi-static susceptibility that is determined from the lower branch in the absence of pinning. After supplemental information of Nat. Nanotech. Advanced Online publication (31 Oct. 2016).

The extracted values of χ_x^{peak} at some selected peaks (the peak numbers are presented in Figure 2.14), are illustrated as a function of RF drive amplitude in Figure 2.17. The susceptibility values range between 40 - 400, depending on the peak. The maximum value of χ_x^{peak} is ~ 10 times larger than the quasi-static

low field susceptibility in absence of pinning (unattainable in practice). On the other hand, the enhancement is ~ 25 times larger than a typical susceptibility with the core pinned. Observed enhancements of up to 25 times over the susceptibilities while the core is pinned suggest applications to RF susceptibility engineering in applications such as field-sensing magnetometry and detecting small volumes of magnetic material.

Moreover, a two-coil implementation provides independent control of RF field components, which enables quantitative separation of the susceptibility and magnetometry components through π phase shifts of individual RF drives; without changing anything else. That will provide further confirmation of the phenomena reported above, where different susceptibility components of the pinning events are detected. Finally, m_z^{dc} is small on account of the shape anisotropy of the Py island, but should be resolvable in future experiments if back-to-back measurements can be performed at different relative phases of H_x^{RF} and H_z^{RF} while keeping all magnitudes constant.

2.7 Measuring ac susceptibility harmonics

The measurement of ac magnetic susceptibility is an important tool, which makes it possible to probe the hysteresis characterization and dynamics of many materials including the bulk magnetic materials and superconductors. Our technique can be easily extended to detect the harmonics of ac susceptibility at low-frequency ranges by using two orthogonal fields, here through a Helmholtz coil assembly (H_x^{ac}) and single coil (H_z^{RF}), as shown in Figure 2.18. The ac coil makes a small in-plane dither field with a low frequency at around 400 Hz. The operating bandwidth of the ac coil, which is hundreds of Hz, will not disturb the magnetization and keep it remain in quasi-static equilibrium with the dc field at all times.

The slope change and/or the minor loops associated with Barkhausen tran-

sitions in the the M-H characterization can strongly influence and complicate the RF susceptibility [44]. We select a short cylinder of a single-crystalline yttrium iron garnet (YIG), which is fabricated from an epitaxial thick film using FIB and is nano-manipulated *in-situ* onto a prefabricated torsional resonator [34]. The YIG sample provides a Barkhausen-free platform to simplify the interpretation of the susceptibility signals in absence of nanoscale imperfections such as grain boundaries in polycrystalline materials. The SEM of the Si mechanical paddle with the affixed YIG disk on top is shown in the upper left inset.

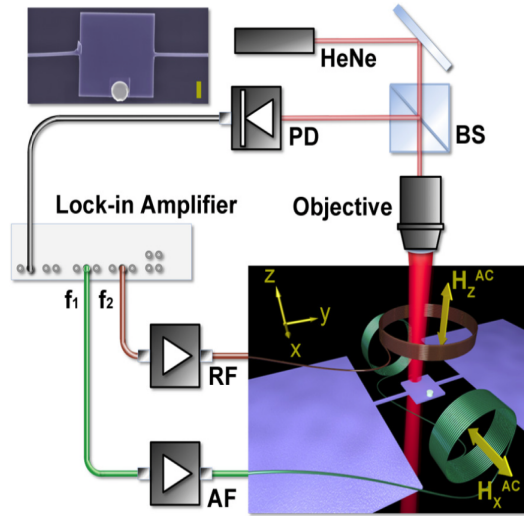


Figure 2.18: Instrument schematic for frequency-mixed nanomechanical detection of ac susceptibility. Two orthogonal ac and RF fields are used through a Helmholtz coil assembly (H_x^{ac}) and single coil (H_z^{ac}), taken from *Solid State Commun.* **198**, 3 (2014).

The ac susceptibility harmonics arise when the magnetization response is nonlinear in the field, e.g., near the vortex nucleation or annihilation (the major transitions in a typical magnetic disk hysteresis loop). We can describe the magnetization by a polynomial series in field,

$$M_x = a_1 H_x + a_2 H_x^2 + a_3 H_x^3 + a_4 H_x^4 + a_5 H_x^5 + a_6 H_x^6 + a_7 H_x^7 + \dots, \quad (2.6)$$

where M_x is the density of magnetic moment such that $m_x = \iiint_{Volume} M_x dv$, and $H_x = H_x^{dc} + H_x^{ac} \cos(2\pi f_1 t)$. By considering M_x expression from Equation 2.6, with the assumption of uniform magnetic moment density over the structure volume (V), the torque terms can be obtained in presence of RF field $\mathbf{H}_z^{RF} = H_z^{RF} \cos(2\pi f_2 t)$ as follows:

$$\begin{aligned} \tau_y &= M_x V \times \mu_0 H_z^{RF} \\ &= V \mu_0 \sum_{n=1}^{\infty} a_n \left(H_x^{dc} + H_x^{ac} \cos(2\pi f_1 t) \right)^n H_z^{RF} \cos(2\pi f_2 t), \end{aligned} \quad (2.7)$$

The nonlinearity response leads to the multiple harmonics of f_1 in the torque terms. By simplifying the series as $\sum_{n=1}^{\infty} A_n \left(1 + (H_x^{ac}/H_x^{dc}) \cos(2\pi f_1 t) \right)^n$, where $A_n = V \mu_0 a_n (H_x^{dc})^n H_z^{RF} \cos(2\pi f_2 t)$ and then by considering the binomial series, the n -th term in the series simplifies to an internal series of $\cos^k(2\pi f_1 t)$:

$$A_n \left(1 + \frac{H_x^{ac}}{H_x^{dc}} \cos(2\pi f_1 t) \right)^n = A_n \sum_{k=0}^n \binom{n}{k} \left(\frac{H_x^{ac}}{H_x^{dc}} \right)^k \cos^k(2\pi f_1 t). \quad (2.8)$$

Moreover, the power-reduction formulas are used to make the $\cos^k(\theta)$ in terms of $\cos(n\theta)$, and $n = 1, 2, 3, \dots, k$. The power-reduction formulas for the power of cosine functions, up to $n = 6$, are brought as follow:

$$\begin{aligned} \cos^2(\theta) &= \frac{1 + \cos 2\theta}{2}, \\ \cos^3(\theta) &= \frac{3 \cos \theta + \cos 3\theta}{4}, \\ \cos^4(\theta) &= \frac{3 + 4 \cos 2\theta + \cos 4\theta}{8}, \\ \cos^5(\theta) &= \frac{10 \cos \theta + 5 \cos 3\theta + \cos 5\theta}{16}, \\ \cos^6(\theta) &= \frac{10 + 15 \cos 2\theta + 6 \cos 4\theta + \cos 6\theta}{32}, \\ \cos^7(\theta) &= \frac{35 \cos \theta + 21 \cos 3\theta + 7 \cos 5\theta + \cos 7\theta}{64}, \\ &\dots \end{aligned} \quad (2.9)$$

Therefore, the n -th term contains multiplications of $[\cos((2n)\pi f_1 t) \times \cos(2\pi f_2 t)]$, which is mixing frequencies; the multiplication of two tones results in tones at sum and difference frequencies, $f_2 \pm n f_1$. This suggests it is possible to tune the frequencies to match the natural resonance frequency of the torque sensor, allowing the sensor to function with a background-free signal that is related to the susceptibilities. On the other hand, one can consider a Fourier sum for the susceptibility harmonics,

$$\begin{aligned}\chi_x(H_x) &= \sum_{n=-\infty}^{\infty} \chi_n^x(H_x) e^{-i(2\pi n f_1)t} \\ &= \chi_0^x + 2 \sum_{n=1}^{\infty} \chi_n^x(H_x) \cos(2\pi n f_1),\end{aligned}\tag{2.10}$$

in which χ_0^x is the dc response in the x-direction and $\chi_n^x(H_x) = d^n(M_x)/d(H_x)^n$ is a partially derivative of M_x .

Table 2.2: Harmonics of the ac susceptibility

$f_2 \pm n f_1$	Amplitude coefficients	related to
$f_2 + 0$	$a_1 h_0 + a_2 [h_0^2 + \frac{1}{2}] + a_3 [h_0^3 + \frac{3}{2} h_0]$ $+ a_4 [h_0^4 + 3h_0^2 + \frac{3}{8}]$ $+ a_5 [h_0^5 + 5h_0^3 + \frac{15}{8} h_0]$ $+ a_6 [h_0^6 + \frac{15}{2} h_0^4 + \frac{45}{8} h_0^2 + \frac{5}{16}]$ $+ a_7 [\frac{35}{16} h_0 + \frac{105}{8} h_0^3 + \frac{21}{2} h_0^5 + h_0^7]$	$\chi_0^x(H_x)$
$f_2 \pm f_1$	$a_1 + 2a_2 h_0 + a_3 [3h_0^2 + \frac{3}{4}] + a_4 [4h_0^3 + 3h_0]$ $+ a_5 [5h_0^4 + \frac{15}{2} h_0^2 + \frac{5}{8}]$ $+ a_6 [6h_0^5 + 15h_0^3 + \frac{15}{4} h_0]$ $+ a_7 [\frac{35}{64} + \frac{210}{16} h_0^2 + \frac{105}{4} h_0^4 + 7h_0^6] - \frac{dM_z}{dH_z} _{h_0}$	$\chi_1^x(H_x)$
$f_2 \pm 2f_1$	$\frac{1}{2} a_2 + \frac{3}{2} a_3 h_0 + a_4 [3h_0^2 + \frac{1}{2}] + a_5 [5h_0^3 + \frac{5}{2} h_0]$ $+ a_6 [\frac{15}{2} h_0^4 + \frac{15}{2} h_0^2 + \frac{15}{32}] + a_7 [\frac{105}{32} h_0 + \frac{35}{2} h_0^3 + \frac{21}{2} h_0^5]$	$\chi_2^x(H_x)$
$f_2 \pm 3f_1$	$\frac{1}{4} a_3 + a_4 h_0 + a_5 [\frac{5}{2} h_0^2 + \frac{5}{16}]$ $+ a_6 [5h_0^3 + \frac{15}{8} h_0] + a_7 [\frac{21}{64} + \frac{105}{16} h_0^2 + \frac{35}{4} h_0^4]$	$\chi_3^x(H_x)$
$f_2 \pm 4f_1$	$\frac{1}{8} a_4 + \frac{5}{8} a_5 h_0 + a_6 [\frac{15}{8} h_0^2 + \frac{3}{16}] + a_7 [\frac{21}{16} h_0 + \frac{35}{8} h_0^3]$	$\chi_4^x(H_x)$
$f_2 \pm 5f_1$	$\frac{1}{16} a_5 + \frac{3}{8} a_6 h_0 + a_7 [\frac{7}{64} + \frac{21}{16} h_0^2]$	$\chi_5^x(H_x)$
$f_2 \pm 6f_1$	$\frac{1}{32} a_6 + \frac{7}{32} a_7 h_0$	$\chi_6^x(H_x)$
$f_2 \pm 7f_1$	$\frac{1}{64} a_7$	$\chi_7^x(H_x)$

Then the amplitude coefficients for the first seven entries in the susceptibility harmonic representation are calculated using the power-reduction formulas as shown in Table 2.2. Once the $a_i, i = 1, 2, 3, \dots$ are obtained with a polynomial fit to the M-H curve, from Equation 2.6, the corresponding χ_n^x terms can be distinguished at a specific $h_0 = H_x^{dc}$ and considering $H_x^{ac} = 1A/m$.

A spectroscopic frequency-versus-field mapping of high order ac susceptibilities for the YIG disk is shown in Figure 2.19 for a field sweep-down from 31 to 4 kA/m. Here the frequency response was recorded at each magnetic field step while keeping both f_1 (H_x^{ac}) and f_2 (H_z^{RF}) constant (400 Hz and 1.8092 MHz, respectively). The torque response corresponding to the susceptibility term is normalized to its maximum value.

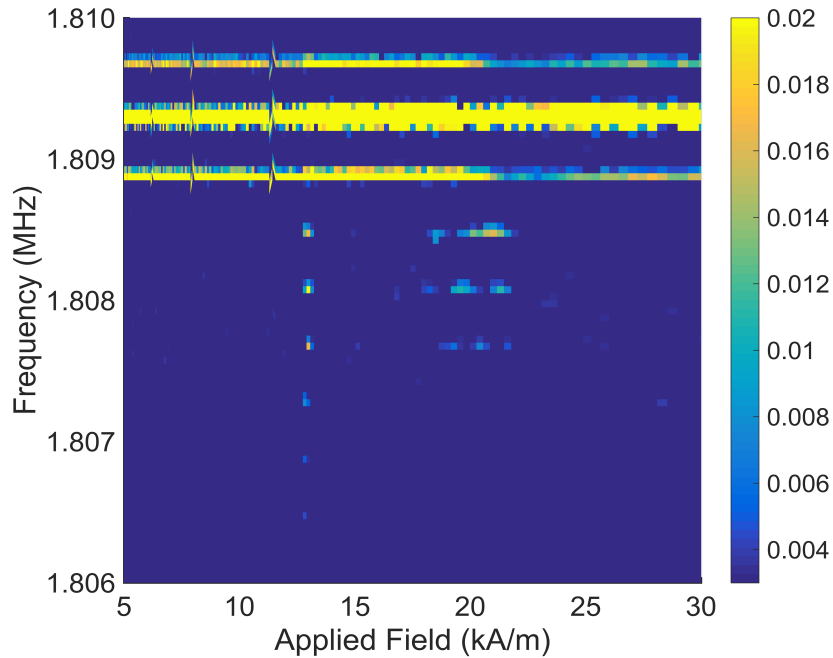


Figure 2.19: Spectroscopic mapping of higher harmonics of the ac susceptibility. The band of highest intensity is the demodulation of f_2 , with the successive bands representing the harmonics of ac susceptibility, $f_2 \pm n f_1$. A line-scan thorough the high susceptibility peaks is shown in the bottom left, showing up to the $n=7$ harmonic. The original normalized intensity scale was cropped (from 0.003 to 0.02) to show the highest order signals.

The colorbar shows part of normalized signal to highlight the ac suscepti-

bility harmonics in Figure 2.19. The f_2 drive was shifted from the resonance frequency (1.808 MHz) to allow for more susceptibility harmonics to be recorded within the mechanical resonance line-width. The brightest band is the demodulation of the f_2 drive, while the subsequent bands represent the harmonics of the magnetic susceptibility. The reason that f_2 and the sidebands are bright through the field range is that they fall under the mechanical resonance peak, with a mechanical linewidth around 1.5 kHz.

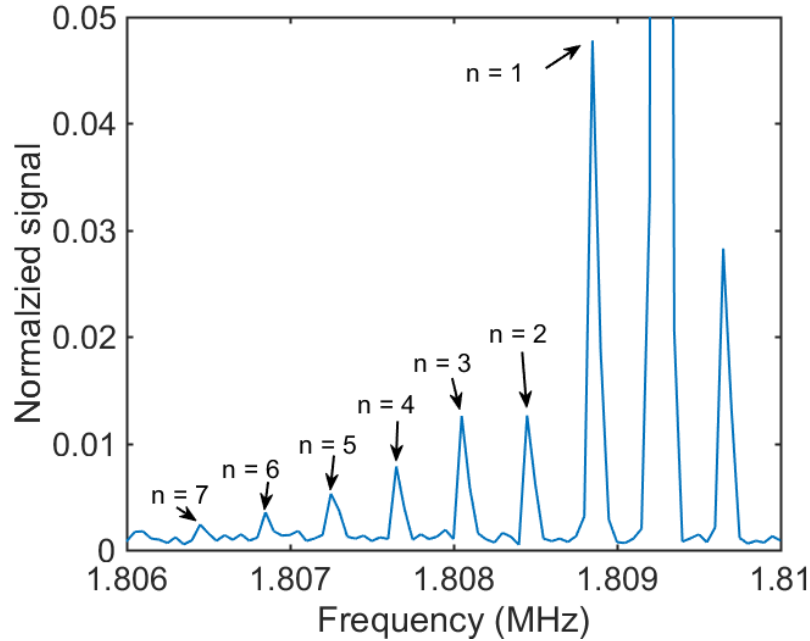


Figure 2.20: Frequency response of the harmonics at $H_x = 12.75$ kA/m. The frequency difference between peaks is 400 Hz.

Figure 2.20 shows the susceptibility peaks at $H_x = 12.75$ kA/m, which is the onset of vortex nucleation. The susceptibility peak values are reported in Table 2.3. By having the amplitude of multiple harmonics, we can locally reconstruct magnetization. In a recursive method $a_i, i = 1, 2, 3, \dots, 7$ are obtained from the susceptibility harmonics (Table 2.3). Then, by inserting a_i in Equation 2.6 at the bias field, the magnetization is determined.

The reconstructed magnetization around the vortex nucleation is presented in Figure 2.21a with only the first six magnetization coefficients, a_i . Including

Table 2.3: Harmonics of the ac susceptibility at $H_x = 12.75$ kA/m

χ_1^x	χ_2^x	χ_3^x	χ_4^x	χ_5^x	χ_6^x	χ_7^x
0.0478	0.01263	0.0126	0.0078	0.0053	0.0035	0.0024

the seventh term changes the reconstructed magnetization coefficients slightly, e.g., normalized a_6 changes from $4e^{-7}$ to $5e^{-7}$ by including χ_7^x in the calculations.

The accompanying magnetization was not recorded for this experiment, since finding the susceptibility harmonics was our first trial for read-out using the mixing technique. The magnetization response presented in Figure 2.21b, is obtained in a separate experiment.

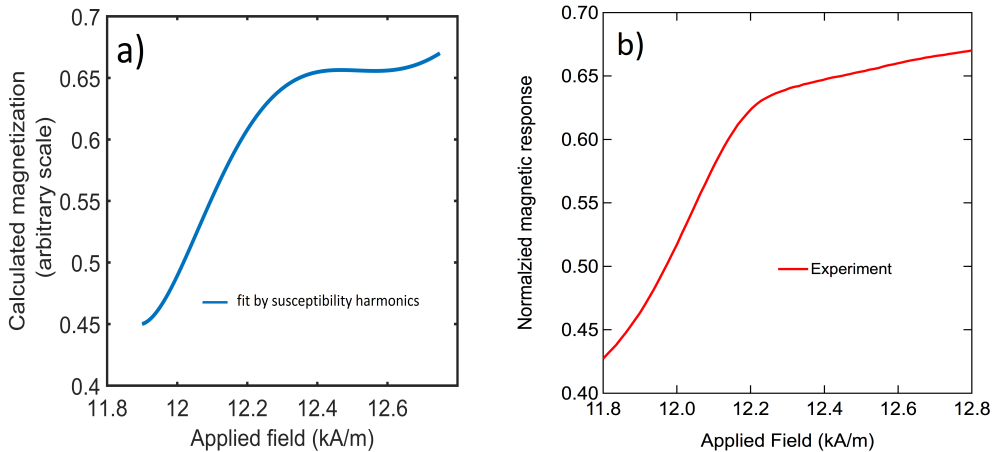


Figure 2.21: Magnetization response near vortex creation and the ac susceptibility harmonics. a) Reconstructed magnetization response from the susceptibility harmonics in the non-linear Equation 2.6. b) The experimental result of the magnetization response in the vicinity of the vortex creation.

The fit is in close agreement with the magnetization signal. Also, the susceptibility harmonic fit works locally, and we could not determine the entire magnetization curve based on the current peak values. It is possible to go in the reverse direction, and from the magnetization response and non-linear fit find the susceptibility harmonics value at a specific bias field range. Moreover,

the scale of magnetization is presented as an arbitrary unit because the amplitudes of the ac and RF drives are represented as currents and not calculated as field values.

We demonstrate the ac harmonics of susceptibility using a very small operating bandwidth for f_1 (a few hundred Hz, using a large Helmholtz coil outside the chamber). For the next chapter, we use transmission lines produce two perpendicular RF fields to probe the magnetic resonance spectroscopy measurements. In principle, this will enable very broadband measurements of frequency-dependent susceptibility to consistently benefit from resonantly enhanced detection, simply by arranging the sum or difference frequency to line up with a torsional mode.

2.8 Conclusion

The local magnetic patterning of nanoscale pinning potentials in ferromagnetic Py disks was achieved using focused ion beam irradiation. As a result of artificial surface pinning sites induced in thin Py disks by point exposure to as few as 10000 ions from a focused Ga^+ beam, a first order change appears in the magnetization response of the disk. We can measure the low-field susceptibility in this instance (defect with the size comparable to vortex core diameter) corresponding to the susceptibility of a pinned-core, which could unlock the mysterious nature of the small slope of the magnetization curve found at the low field for the non-perforated disk.

Making point-like defects in the disk, which is invisible to SEM tool but still demonstrates very effective pinning sites, differentiates this work from earlier studies of controlled pinning of magnetic vortices. We present a mapping of local properties (dose-dependent artificial inhomogeneities in thin films) on very short length scales in two dimensions. This represents a powerful, quantitative tool. From the artificial pinning sites made in these three disks with different

doses, we learned much about the basic control mechanics of pinning sites as well as modeling and engineering the pinning effects. Using these structures, we showed that several widely separated sites can work together to keep the core pinned in one place while the Barkhausen effect is eliminated from the magnetization curve over a range approaching the saturation moment of the disk. This represents a new regime of artificial control over the micromagnetic response.

Measuring the susceptibility in addition to magnetization helps us to unlock some more information about the magnetic structure. In this case we need two perpendicular ac (or RF) fields to be able to read the susceptibility terms on the torsional resonance, using a mixing technique. Using only one coil, by displacing the sample on top of it to have in-plane and out-of-plane field components, we measure the in-plane susceptibility term at the Barkhausen steps. In addition, we present the susceptibility harmonics, from which we can construct the magnetization locally in the non-linear range using a two-crossed coil configuration.

Chapter 3

Torque magnetometry for concurrent acquisitions of magnetostatics & spin-dynamics

3.1 Motivation

Magnetic disks have been extensively studied since the late 20th century, because many applications relies on them. Among these applications are magnetic memory elements. To fully utilize magnetic elements, a rich understanding of their physical properties is required. In addition, it is important to acquire characterization information in the presence of intrinsic pinning sites, which are indispensable parts of a nanoscale structure and can affect both spin dynamics and magnetization response.

Directly correlating spin dynamics with the complementary information obtained from the net equilibrium magnetization (hysteresis curve) has been an experimental challenge. Nanomechanical torque magnetometry, due to its exceptional sensitivity, has been used widely to capture the quasi-static magnetization of single, mesoscopic magnetic structures in a non-invasive way. Moreover, we demonstrated a down-mixing concept, torque-mixing magnetic reso-

nance spectroscopy (TMRS), which makes it possible to concurrently measure dc magnetization and magnetic resonance spectroscopy in an individual magnetic structure using nanomechanical torque sensors. The simultaneous measurement of magnetization and related broadband spin resonances can enrich the understanding of pinning mechanism in magnetic structures.

3.2 Introduction

Nanostructures display distinctive magnetizing-demagnetizing fingerprints on account of unavoidable imperfections arising during their fabrication, usually, a blur-out in measurements of arrays of nominally identical objects. Chapter 2 includes quantitative information of magnetic pinning obtained by studying the quasi-static (Barkhausen) response of the magnetic vortex core interacting with the local energetic landscape. Studies have shown that a Ga^+ focused ion beam (FIB) has a significant effect on the magnetization of mesoscopic structures [47, 44]. The local modifications of the magnetization with FIB occur through the interaction mechanism between the FIB and a magnetic system. That mechanism is still not well understood [56, 60]. The FIB-induced regions have been utilized to act as pinning sites for the high energy vortex core ends [47, 44], and for domain walls [61].

It is necessary to study individual structures to probe the local effects caused by variations in the magnetic structure due to grain boundaries, vacancies, and other intrinsic or extrinsic inhomogeneities. This is even more crucial as the size of a structure shrinks down to the nanoscale, which is comparable to the size of the defects. The local variations can affect both static and dynamic magnetic responses. Therefore, it is highly desirable to develop an experimental technique to measure both the dc and dynamic responses of magnetization.

We had demonstrated that nanomechanical torque magnetometry has an exceptional sensitivity (the magnetic moment resolution is approaching 10^{-19}

Am^2 at room temperature) with the ability to non-invasively measure single, mesoscopic elements [44, 34]. This is the reason that existing nanomechanical torque sensors with zepto-Newton-meter (10^{-21} Nm) sensitivity are capable of resolving 10^6 spins in the presence of the Earth's magnetic field (20-60 μT).

We built up on torque sensor a complementary broadband mechanical approach with greater generality, TMRS, which enables direct readout of the transverse components of precessing magnetization in a geometrically confined nanostructure [32]. That is directly analogous to how inductive detection of spin resonance is usually implemented and is much more versatile for many applications.

The main part of Chapter 3 is to study magnetic resonance in disk structures. A short description to low-frequency dynamics (gyrotropic frequencies) at the vortex state is presented with considering the geometric effects. Afterwards, with the TMRS demonstration for detecting magnetic resonances, we show the effects of surface modifications and pinning sites (intrinsic and artificial) on the magnetic resonance spectra. Chapter 3 includes detailed experimental studies in a single-crystalline yttrium iron garnet (YIG) disk in two cases of in-plane and out-of-plane bias field orientations. In addition, polycrystalline Permalloy (Py) structures in the case of in-plane bias field are discussed. Compared the experimental resonance spectra with micromagnetic simulations reveals more insights into the modes as well as the shape of specimens.

3.2.1 Gyrotropic modes

A magnetic vortex is a ground state of a magnetic disk with low anisotropy and a small enough aspect ratio, as described in detail in Chapter 2. The fundamental magnetic resonance of a vortex texture is a translational mode or gyrotropic mode, in which the vortex core circulates around its equilibrium position.

To excite the gyrotropic modes an in-plane radio-frequency (RF) field or a

pulse are used. In this case, the vortex core is moved away from its equilibrium position perpendicularly to the applied field direction, e.g., on the rising and falling edges of pulse transitions. Subsequently, the vortex core starts gyration. The pulse width should be selected wisely. A short discussion on the pulse width is provided in Appendix A, where we used pulse excitation for finding the magnetic resonance spectrum in a magnetic structure. In linear excitations with small RF drives, the gyrotropic mode is well studied experimentally and analytically [62, 63, 64, 65]. The drives with higher amplitude put the vortex gyration in nonlinear dynamics such as deformation of a vortex, which can lead to a core reversal [38].

The Thiele’s equation is a general theoretical approach that could simplify dynamics of magnetic domains. Likewise, the magnetic resonance frequency can be calculated in a vortex state, which is analytically described by the Thiele’s equation of motion [66], as follows:

$$\vec{G} \times \frac{d\vec{r}}{dt} - \nabla W(r) = \vec{F}(t), \quad (3.1)$$

in which, $\vec{G} = -pG_0\hat{z}$ is the gyrovector with an out-of-plane direction corresponding to the sign of the polarization p and with the constant $G_0 = 2\pi L \frac{M_s}{\gamma}$ (L is the disk thickness, M_s is the saturation magnetization, and γ is the gyromagnetic ratio), $W(r)$ is the magnetostatic energy of the displaced vortex, $\vec{F}(t)$ is a time-dependent excitation force, and \vec{r} is the displacement of the vortex core from its equilibrium position. For the vortex state, the magnetostatic energy is isotropic in the disk plane and can be written as a quadratic function, $W(r) = W(0) + \frac{1}{2}\kappa r^2$, where κ is the parabolicity of the confinement or stiffness coefficient.

The resonant gyrotropic solution of Equation 3.1 is obtained as $\omega_G = 2\pi f_G = \kappa/G_0$. From the “pole-free” or two-vortex model of Guslienko [67], the stiffness coefficient which depends on the boundary condition is calculated for the vortex at the center: $\kappa = (2/3M_s)^2\pi L/\chi_0$, where χ_0 is the vortex sus-

ceptibility. As a result, the gyrotropic resonance frequency, typically on the order of a sub-GHz frequency, is related dominantly to the geometry of a disk and initial dc susceptibility. One can insert the dissipation term that contains the Gilbert damping α_G to the Equation 3.1; however, the damping term would not come into play in calculating the resonance frequency. Moreover, the core polarization, $p = \pm 1$, determines the direction of gyration [68, 69].

In a thin disk, the core can be considered as a rigid column of an out-of-plane magnetization. The dominant gyrotropic mode seen in thin disks is associated with the zero-order (uniform) gyrotropic mode, where the vortex core precesses uniformly through the disk thickness with in-phase core ends on the top and bottom surfaces. The existence of higher spatial order gyrotropic modes is a function of the thickness of the disk [70, 71]. The higher order gyrotropic modes appear in disks with higher aspect ratios, e.g., the one-node (first-order) gyrotropic mode, in which the vortex core high-energy ends precess out of phase. Depending on the aspect ratio, a first-order gyrotropic mode can be the lowest excited mode.

To examine the effect of disk thickness on the gyrotropic modes, we perform micromagnetic simulations. Constant diameter (980 nm) YIG disks with thickness variations from 50 nm to 450 nm are considered. For each disk at the ground state (vortex state at the disk center), we excite the dynamics by applying a 1.43-ns width magnetic pulse in the y-direction. Then, the gyrotropic modes are extracted through Fourier transform of the temporal response of the in-plane component of magnetization, $[m_y(t) - m_y(0)]$ (more details in Appendix A). Figure 3.1 shows the nonlinear dependence of the disk thickness on the gyrotropic resonances.

As the disk thickness increases, the zero-order mode crosses over into a higher frequency band at 200 nm. The real “cross-over” does not occur, as it is forbidden. Instead, a mode repulsion, which is a characterizing of dynamical modes happens, as shown in Figure 3.1. Panels a and b show two core

profiles (spatial Fourier transform) after the cross-over region at the thickness of 250 nm: the zero-order gyrotropic mode at $f = 345$ MHz and first-order gyrotropic mode at $f = 134$ MHz, respectively.

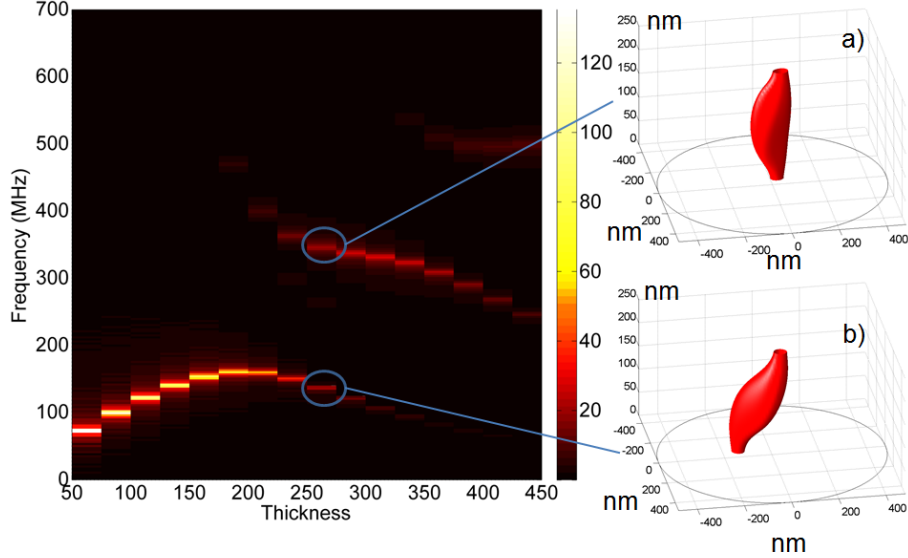


Figure 3.1: Simulated gyrotropic mode frequencies as a function of thickness in a 980nm-diameter YIG disk. Panels a and b represent the core profile of the dynamics acquired with micromagnetic simulation for a 250-nm thick disk.

Inhomogeneities in real materials influence the vortex dynamics profoundly. When a vortex is pinned by a defect, the gyrotropic frequency increases and the amplitude approaches zero [72, 73, 74]. The effect of pinning on the structure can cause changes in the energy potential and consequently on the susceptibility. As a result, the gyromagnetic frequency shifts to the higher range. To study the effect of pinning sites, Chen *et al.*, added a Gaussian modification to the quadratic energy function in the Thiele's equation of motion, which has a local minimum and vanishes for large r . Accordingly, the equation of motion became a 2D nonlinear system with explicit time dependence, which can be solved numerically. The threshold for RF amplitude to depin the vortex from the grain-boundary disorders has also been studied [38]. It has been anticipated that pinning sites in a thin disk would dramatically shift the gyrotropic frequencies to a higher range. In a similar manner, Zaspel calculated what the

magnetostatic and exchange energy contributions to take into account surface pinning in the Thiele's equation; he solved the Euler-Lagrange equation from a variational method in the case of a disorder on one side of the disk surface. The frequency shift would be much smaller for thick disks [75].

In the following sections, we experimentally and through simulation examine the effects of impurities and pinning sites on the magnetic resonance. Section 3.4 focuses on the study of surface modification in a mono-crystalline YIG thick disk fabricated through Ga⁺ ions. Section 3.5 shows the polycrystalline Py structures with intrinsic and artificial pinning site investigations.

3.3 Torque-mixing magnetic resonance spectroscopy

The TMRS technique builds on a torque measurement of ac susceptibility at 400 Hz, presented in the previous chapter [34]. Our torque sensors are sensitive to torque along their torsional rods, which are considered along y-direction in this thesis. By having RF fields along \hat{y} and \hat{z} directions, via transmission lines, the only net moment term that produces direct torque is m_x . The magnetic torque expression is brought in following:

$$\tau_y \hat{y} = m_x \hat{x} \times \mu_0 H_z^{RF} \hat{z}. \quad (3.2)$$

A tensor notation for the magnetic permeability of ferrites is formalized by considering the anisotropic characterization in presence of magnetic field, usually in high fields, known as the Polder tensor [76]. For a material magnetized in the z-direction as illustrated in Figure 3.2A, the in-plane RF-driven moments are related to RF field, $\mathbf{H}_y^{RF} = H_y^{RF} \cos(2\pi f_1 t)$, in the Polder tensor notation

as [77]:

$$\begin{pmatrix} m_x \\ m_y \end{pmatrix} = V \begin{pmatrix} \chi_{xx} & \chi_{xy} \\ \chi_{yx} & \chi_{yy} \end{pmatrix} \begin{pmatrix} 0 \\ H_y^{RF} \cos(2\pi f_1 t) \end{pmatrix}, \quad (3.3)$$

in which the $\chi_{xy} = -\chi_{yx} = -i\chi_t(f_1)$. By solving the Bloch equation and assuming $H_y^{RF} \ll H_0$ [78], the transverse susceptibility, $\chi_t(f_1)$, is obtained with a Lorentzian profile [79] in terms of the magnetic resonance frequency, f_{res} , the resonance linewidth, Δf , and the baseline low-frequency susceptibility, χ_0 :

$$\chi_t(f_1) = \frac{\chi_0 f_{\text{res}}}{\left((f_{\text{res}} - f_1)^2 + \left(\frac{\Delta f}{2}\right)^2 \right)^{1/2}}. \quad (3.4)$$

It is convenient to describe the transverse moment amplitude, $m_x(f_1)$, via an experimental transverse susceptibility, $\chi_t(f_1)$. This RF transverse moment is ideally suited to nominally background-free mechanical torque detection, mimicking the original crossed-coil concept for inductive detection [80]. Therefore, by inserting the m_x term from Equations 3.3 and 3.4 into Equation 3.2 and noting that $\mathbf{H}_z^{RF} = H_z^{RF} \cos(2\pi f_2 t)$, the torque becomes

$$\begin{aligned} \tau_y &= - \left(-iV\chi_t(f_1)H_y^{RF} \cos(2\pi f_1 t) \right) \left(\mu_0 H_z^{RF} \cos(2\pi f_2 t) \right) \\ &= i \frac{\mu_0 V H_y^{RF} H_z^{RF}}{2} \chi_t(f_1) \left(\cos(2\pi(f_1 - f_2)t) + \cos(2\pi(f_1 + f_2)t) \right). \end{aligned} \quad (3.5)$$

The key is exposing the sinusoidally-varying moment to a second, orthogonal RF tone H_z^{RF} at frequency f_2 . The two sinusoids then cooperatively generate RF magnetic torques at sum and difference frequencies, $f_1 \pm f_2$. Then, the phase-sensitive detection at $f_{\text{mech}} = f_1 - f_2$, where the frequency offset f_{mech} corresponds to a torsion resonance of the mechanical sensor, enables sensitive detection of a ‘mixing torque’ proportional to the susceptibility in Equation 3.4:

$$\tau_y(f_{\text{mech}}) = \frac{\mu_0 V H_1 H_2}{2} \chi_t(f_1). \quad (3.6)$$

This simple analysis assumes the spin-lattice relaxation time of the specimen to be shorter than the oscillation period of the torque sensor (allowing for magnetic-to-mechanical torque conversion), but otherwise, the choice of f_{mech} is unconstrained by sample properties ($f_{\text{res}}, \Delta f$). The torsional motion of the resonator also induces fields, which should be included in a full analysis. At the peak angular speeds of the torque sensor (~ 3000 rad/s with $f_{\text{mech}} = 2$ MHz and angular displacement of $\theta = 3.5 \times 10^{-4}$ rad), the effective magnetic field via the Larmor theorem is on the order of 0.01 A/m, several orders of magnitude lower than the smallest RF fields applied for the measurements.

In a second motional mechanism, the magnetic anisotropies of the specimen (shape and magnetocrystalline) drag the spin texture out of alignment with the external field by an amount up to (in the limiting case) the angular amplitude of the mechanical oscillation, θ . In the mechanical resonator coordinate, the effective field equals $H_0 \sin(\theta)$. By using the small angle approximation, the field simplifies to $H_0 \theta$. In a strong magnetic resonance, e.g. at $f_{\text{res}} = 500$ MHz, the required bias field is obtained from the Larmor theorem around $H_0 = 14$ kA/m. Consequently, the resulting effective field could reach amplitudes on the order of 1 A/m. This also is small enough to neglect for present purposes, but approaches the range where one can begin to conceive of measurements designed to look for this effect via a transverse RF moment driven by this field mixing with the H_z^{RF} tone to create an internal torque that would modify the spin resonance amplitude (akin to a back-action or radiation damping). Higher-order effects will arise when the effective magnetic fields due to mechanical rotation become non-negligible, at much larger peak angular speeds of the torque sensor.

Detail of our experiment is illustrated in Figure 3.2A, a schematic of the applied RF excitation and demodulation field geometry in the context of a nanotorsional resonator-supported magnetic specimen. A net moment m_0 is induced by a dc magnetic field H_0 , applied *perpendicular* to the torsion axis (z -

direction). The magnetic resonance is driven by an RF magnetic field applied transverse to the dc field with amplitude $H_1=H_y^{RF}$ at frequency f_1 , shown aligned with the torsion rod (y -direction), while another perpendicular RF field $H_2=H_z^{RF}$ is presented at frequency f_2 . In this arrangement, an RF magnetic moment, orthogonal to both H_0 and H_1 , arises from spin precession at magnetic resonances.

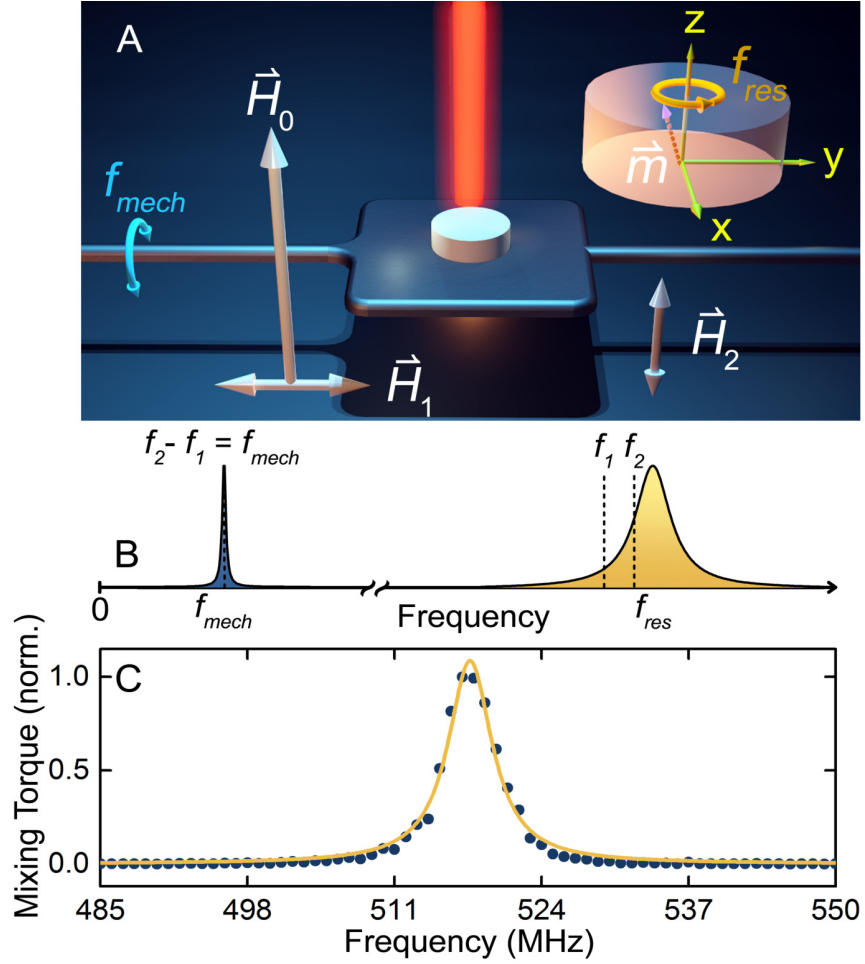


Figure 3.2: Schematic of torque-mixing magnetic resonance spectroscopy (TMRS) with a demonstration. A) Applied field and torque sensor geometry for TMRS. A spin system (illustrated as a micromagnetic disk), supported by the sensor with mechanical resonance at f_{mech} , is biased in an applied field H_0 (direction arrows not to scale). H_y^{RF} (at f_1) is applied to drive the transverse component of magnetic resonance, f_{res} (inset), accompanied by H_z^{RF} (at f_2) such that $f_1 - f_2 = f_{mech}$. B) Frequency-space representation of the downconversion scheme. C) Torque detection of magnetic resonance at $H_0 = 70.5$ kA/m. H_y^{RF} and H_z^{RF} were driven with peak-to-peak field amplitudes of 78 A/m and 190 A/m, respectively.

The amplitude of the resulting mechanical oscillation is measured by optical interferometry with lock-in amplification at f_{mech} . Spectroscopy is performed by sweeping f_1 through f_{res} while keeping the frequency offset of f_2 constant at f_{mech} , as illustrated by Figure 3.2B.

There is no requirement for f_1 and f_2 to be separated by more than the resonance linewidth. In situations where H_2 also drives spin resonances, the mixing torque remains zero because H_1 is parallel to the torsion axis. RF fields are applied using transmission lines on a custom, multilayer circuit board. All RF tones are generated using an ultrahigh multifrequency lock-in amplifier [45], when the spectrum bandwidth of 500 MHz is a desire. For higher frequency ranges, up to 2.1 GHz, we use signal generators with power amplifiers.

Figure 3.2C shows the mixing torque signal from an $f_{\text{res}} = 517$ MHz FMR mode of a microscopic disk of YIG in an applied field $H_0 = 70.5$ kA/m. The field geometry for the resonance mode in Figure 3.2C (shown in Figure 3.2A) is the same as for NMR and electron paramagnetic resonance, but the $f(H)$ dependence is nonlinear, modified by the strong dipolar fields in the ferrimagnet [11]. The full resonance linewidth at half maximum, 4.76 MHz, is obtained by fitting the Lorentzian presented in Equation 3.4 to the normalized data.

3.4 Spin resonance spectroscopy of an in-plane magnetized YIG disk

TMRS enables direct readout of the transverse RF components of the precessing magnetization and thereby introduces much more versatility for applications of pure torque detection of spin resonances like FMR, which is not restricted to uniform applied fields. FMR is the common expression for EPR in materials with spontaneous magnetic order yielding a net moment [14, 20].

The ferrimagnetic insulator YIG is an ideal material for TMRS. YIG has the narrowest known ferro/ferri-magnetic resonance line and in the form of a

mesoscopic structure has a rich resonance spectrum. The magnetic hysteresis exhibited by YIG permits demonstration of the simultaneous capability to measure the net moment of the sample while performing resonance spectroscopy in a microfabricated device. This is of immediate interest in the context of the resurgence of YIG for spin-based device applications [81, 82, 83, 84, 85].

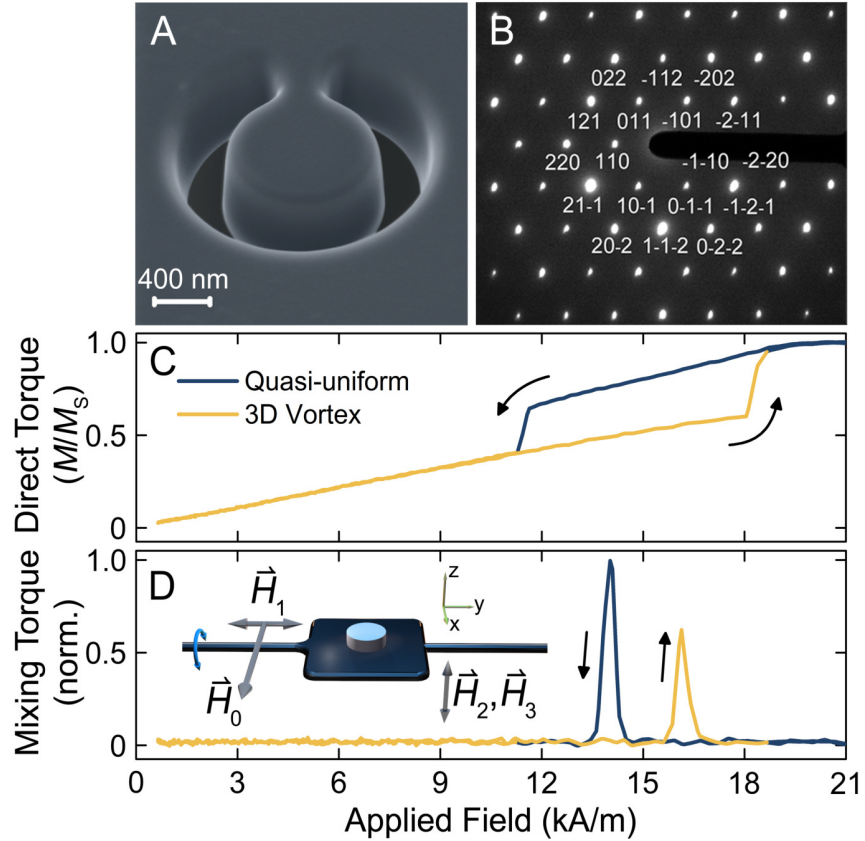


Figure 3.3: The YIG disk structure and its concurrent magnetization and resonance at $f_1 = 100.1000\text{MHz}$. A) FIB-defined microdisk in a bulk YIG crystal prior to nanomanipulation onto a torsional mechanical resonator (see Fabrication chapter for fabrication procedure, Appendix C). B) Electron diffraction pattern of a reference YIG lamella milled from the same crystal. C,D) Simultaneous acquisition of net moment and dynamic response hysteresis loops. The net moment signal (C) was captured by supplying and lock-in demodulating a small RF drive ($H_3 = 23\text{ A/m}$ peak-to-peak) off the mechanical resonance peak, $f_3 = 1.8031\text{ MHz}$, in the z -direction while H_0 was swept in the x -direction. The field configuration is shown schematically in the inset of (D). The sweep in (D) is demodulated at $f_{\text{mech}} = 1.8037\text{ MHz}$ while $H_1 = 78\text{ A/m}$ peak-to-peak amplitude was driven at $f_1 = 100.1000\text{ MHz}$ and $H_2 = 190\text{ A/m}$ at $f_2 = 101.9037\text{ MHz}$. The two colors represent different spin textures, quasi-uniform (dark blue) and 3D vortex (gold).

The monocrystalline YIG disk is sculpted from a thick-film epitaxial starting crystal [86], using a FIB milling procedure designed to minimize ion beam modification of the magnetism of the material. The final structure is 450 ± 10 nm thick and has a radius of 550 ± 30 nm on account of the slightly tapered side-walls imprinted by the intensity profile of the ion beam. An electron micrograph taken at the penultimate step of disk fabrication is seen in Figure 3.3A. Details of the fabrication procedure are included in the Appendix C. The monocrystalline nature of the FIB-sculpted mesoscopic YIG is confirmed by 300 kV electron diffraction from a YIG reference lamella FIB-milled from the same bulk substrate (Figure 3.3B). The hexagonal Laue pattern represents a cubic structure in the (111) crystal orientation. After mounting to the mechanical resonator, the crystal (110) orientation is along \hat{x} , perpendicular to the torsion bar axis. The (h,k,l) crystal plane indices are indicated, consistent with the (111) orientation (the zone axis normal to the disk surface). The configuration of magnetization within a mesoscopic magnet is a spatially nonuniform but well-defined spin texture. The mesoscopic disk has a fully demagnetized ground state at $H_0 = 0$, a circularly-symmetric magnetic vortex texture [87, 88]. As a function of the magnetic field H_0 , there are abrupt, hysteretic (irreversible) transitions between vortex textures and quasi-uniform states, as one or the other configuration becomes favoured energetically. Some spin textures, between vortex and quasi-uniform states, are discussed further in Appendix B.

The magnetizing/demagnetizing behavior of the YIG disk as a function of H_0 along \hat{x} is shown in Figure 3.3C. Because H_0 is *not* parallel to the torsion axis, the net moment can be recorded simultaneously through torque generated by an additional magnetic tone along \hat{z} : H_3 (see Figure 3.3D inset), at a frequency f_3 slightly detuned from f_{mech} but still intersecting the mechanical resonance peak. The two steep transitions in the measured net moment of the disk are magnetic vortex nucleation field at 11.5 kA/m during the field sweep-down, and vortex annihilation field happens at 18 kA/m during the

field-increasing half of the measurement (reminiscent of the two-dimensional vortex behaviour of thin Py disks [87, 88]). The YIG disk is always in a three-dimensional (3D) vortex state below the nucleation field.

Magnetic resonance spectroscopy often is performed at fixed frequency, sweeping the strength of H_0 . An example of fixed-frequency TMRS is shown in Figure 3.3D, where the frequency $f_1 = 100.1000$ MHz of the RF drive field H_1 is chosen such that the vortex and quasi-uniform textures both exhibit a resonance (at different values of H_0). The simultaneous dc moment acquisition distinguishes unambiguously the magnetic resonances of the two different spin textures.

3.4.1 Quasi-uniform magnetizations

A spectroscopic map of spin resonances is presented in Figure 3.4 for H_0 along \hat{x} , corresponding to the upper branch of Figure 3.3C (sweeping the field from high to low). A ladder of modal oscillations is observed [89], akin to a standing-wave resonance hierarchy wherein each new mode adds a node. The field strength steps down in 26.5 A/m increments during this measurement, and at each field step, the frequency is swept from low to high. The data of Figure 3.4A exhibits decreasing mode amplitudes towards the higher field and higher mode number. Two factors contribute to this trend: as the texture becomes more uniform, a smaller effective volume from each mode contributes to the torque; and higher order modes have less net coupling to a spatially uniform H_1 drive field. The rich experimental phase diagram provides many features that may be exploited with complementary numerical simulation. For instance, the slope changes common to all ladder modes in Figure 3.4A near 16 kA/m indicates a metastable intermediate spin texture involved in the vortex nucleation process. In simulations, all modes show a similar, although more abrupt (hysteretic), a pair of jumps where the texture transitions from the quasi-uniform state to a metastable two-vortex state before the creation of the single-vortex state.

The complex nature of nucleation processes presents an experimental challenge. However, simultaneous monitoring of the net magnetic moment of the sample is a powerful advantage of the TMRS method. Figures 3.4B and 3.4C show individual pixels of the field vs. frequency map in the vicinity of the vortex nucleation transition, from both torque amplitude channels: the mixing torque (from H_1 and H_2 , the transverse RF susceptibility) and the direct torque (from H_3 , net moment), respectively.

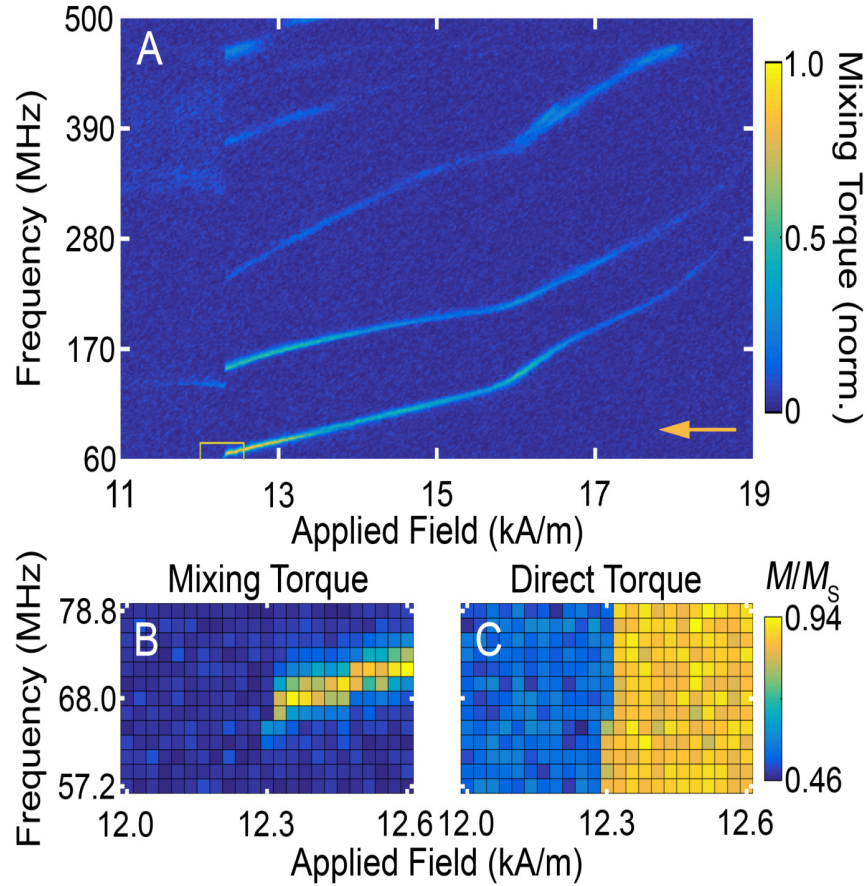


Figure 3.4: Torque-mixing Magnetic Resonance Spectroscopy of the YIG microdisk. A) The spectrum is acquired while sweeping the field from high to low, with $H_y^{RF} = 78$ A/m and $H_z^{RF} = 190$ A/m as in Figure 3.3C. The field and frequency step sizes are 30 A/m and 1.8 MHz, respectively. The arrow represents the direction of the field sweep. B) Zoom-in of region outlined in (A). Each pixel represents a data point. C) The simultaneously acquired net magnetic moment measured with $H_3 = 23$ A/m. The abrupt transitions in both the mixing torque (B) and direct torque (C) signals between the fifth and sixth frequency steps from the bottom at field $H_0 = 12.3$ kA/m, represents the resonantly-assisted vortex nucleation event.

Upon the transition to the 3D vortex state (12.3 kA/m), the quasi-uniform spin texture resonances abruptly end and those corresponding to the new configuration appear. Vortex state nucleation is triggered as f_1 steps up onto the first resonance mode, in this instance. This is a reproducible occurrence, showing that the method is a natural tool for the study of resonantly-assisted transitions in mesoscopic magnets [90, 91]. Beyond the use of the exquisite mode fingerprint and the simultaneous dynamic and static capabilities of TMRS to study coarse transitions, the sensitivity of the technique also lends itself to study of extremely small effects.

3.4.2 Vortex state

FIB offers unique possibilities for nanofabrication of monocrystalline objects but still suffers in comparison with lithographic methods in terms of dimensional accuracy. Utilizing Ga^+ FIB, an epitaxially-grown single-crystalline YIG film is milled out to form a disk. The dimensions have been inferred with a comparison to simulation to be 980 nm in diameter and 250 nm in thickness. In addition, the interaction of Ga^+ ions reduces the magnetic properties of the YIG disk and creates a magnetically dead shell around the disk. We present a study of gyrotropic resonances in the FIB-fabricated YIG disk and the effect of surface roughness on the magnetic resonances as a function of in-plane magnetic field using TMRS.

In contrast to two-dimensional thin magnetic disk, higher spatial-order gyrotropic modes exist in a three-dimensional (3D) YIG disk. The disk has a great effective stiffness for the core to be straight-up-and-down and to remain uniformly magnetized in the z (thickness) direction. In a 3D vortex state [92], the core diameter increased towards the middle of the disk, lowering the core's energy density. An illustration of magnetization at its ground state is shown in Figure 3.5 with the top and bottom cross sections demonstrating the in-plane magnetization direction (the color-wheel) and the perpendicular plane showing

the m_z intensity (color-bar).

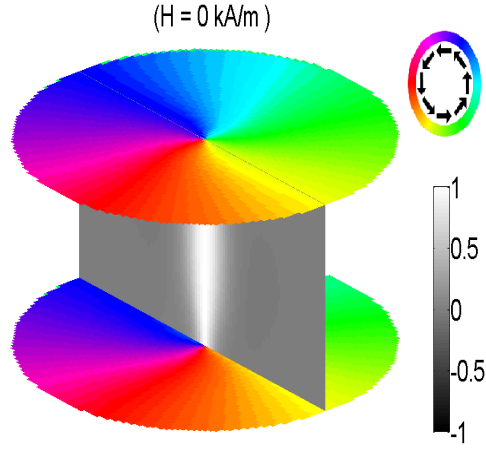


Figure 3.5: 3D rendering of the vortex magnetization at the ground state. Top and bottom surfaces show the angle of in-plane curling magnetization vertical. The vertical plane shows the cross-section of m_z magnetization and the gray color-bar shows the intensity (simulation of 1- μ m diameter and 250-nm thick YIG disk).

There is a rich resonance spectrum for a confined magnetic structure like a disk in the presence of RF actuations. The TMRS map of fundamental modes of the 3D vortex texture in the single-crystalline YIG disk, which involves gyrations of the core is shown in 3.6A. The in-plane dc bias field swept from ground state to high field to obtain the field dispersion of resonances in the vortex state. The first two modes presented in the spectrum are the gyrotropic modes. It is shown from the simulation of YIG disk with 250-nm thickness, presented in Figure 3.1, that lowest frequency mode of the thick YIG disk is a first-order spatial mode. In this mode, the vortex core interacts with the disk surface while the high-energy ends are precessing out of phase at the top and bottom surfaces.

Monitoring simultaneously the net magnetic moment of the sample with the related resonance spectrum is a powerful advantage of TMRS. Figures 3.6B and 3.6C show individual pixels of the field versus frequency map in the vicinity of the vortex core annihilation transition, from both torque amplitude channels: the transverse RF susceptibility torque and the net moment torque,

respectively. Upon the transition to the quasi-uniform spin (~ 18.4 kA/m), the 3D vortex texture resonances abruptly end and those corresponding to the new configuration appear. The vortex core annihilation is reproducibly triggered as f_1 steps close to the first resonance mode. Recognizing this, however, is also a realization that the method is a natural tool for the study of resonantly-assisted transitions in mesoscopic magnets [90, 91].

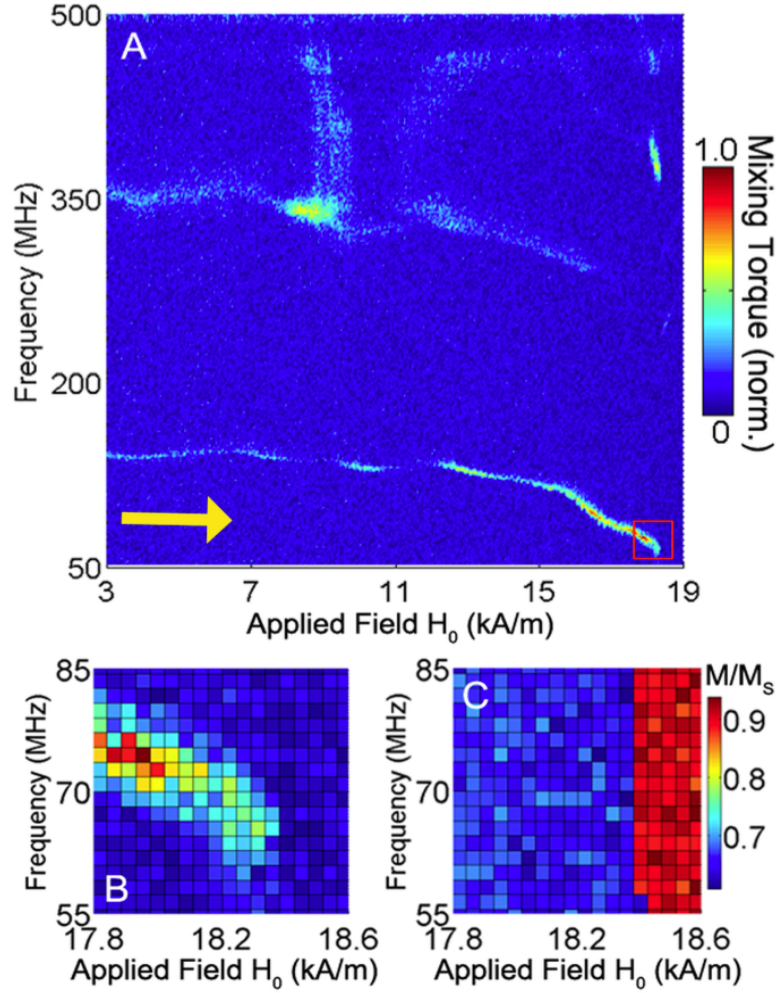


Figure 3.6: Low field TMRS for the YIG disk in the 3D vortex state. The resonances correspond to the first-order (lowest) and zero-order (second) vortex core gyrations. The frequency step size is 1.8 MHz and the field steps are 45 A/m. The arrow indicates the field sweep direction. The RF drive amplitudes are $H_1 = 78$ A/m and $H_2 = 190$ A/m.

In Figure 3.7, clearly visible amplitude and frequency modulations of the

lowest mode reveal the imperfections in the disk. The modulations could be attributed to the FIB-induced magnetic roughness, in which the gyrotropic modes for the pinned core are slightly modified.

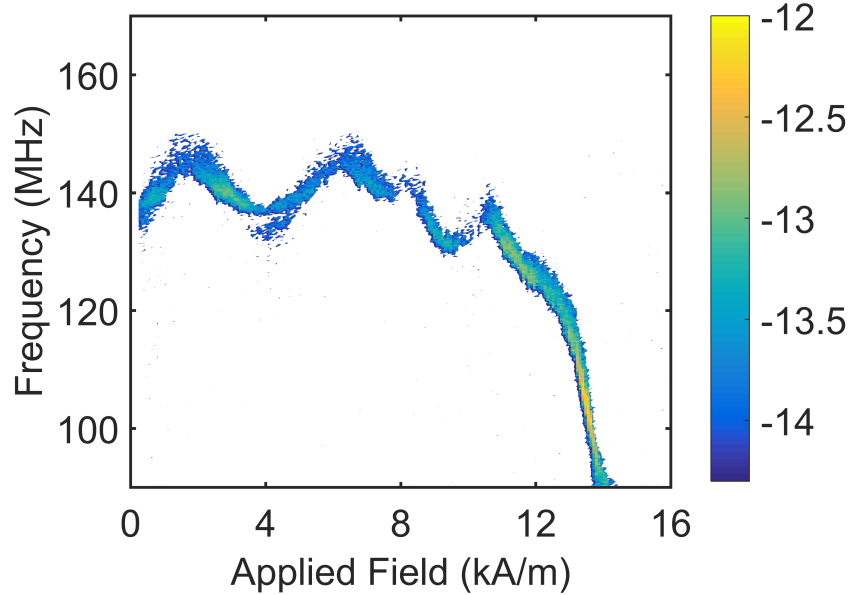


Figure 3.7: Frequency and amplitude modulation of the lowest (first-order) gyrotropic mode in the low-to-high field sweep. The spectrum is obtained via a crossed coil configuration. For highlighting the mode, part of the color bar, in a log format, is presented (white background).

When the dc external field is applied (increasing along \hat{x}), the equilibrium position of the precessing vortex core is translated in the \hat{y} direction towards the edge of the disk while interacting with the imperfections.

To obtain frequency and amplitude variations, we extracted information about the first resonance peak using an averaging box with a 9-MHz width around the peak at each field. Figure 3.8 shows a rendering of the simultaneously measured information of the mixing torque averaged around the first resonance mode and plotted together with net moment versus field (averaged over the full frequency range).

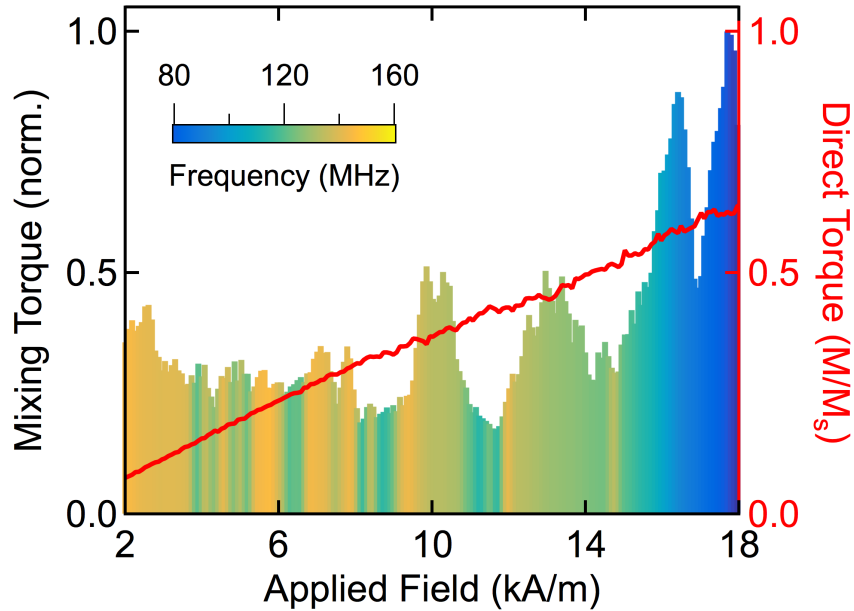


Figure 3.8: 2D representation of the first mode magnetic resonance data versus applied field overlapped with the concurrent net magnetization response. The averaged mixing torque around the lowest mode in Figure 3.6A is plotted on the left axis. The colors of the underfills represent the peak frequencies of the resonance (see inset color bar). The simultaneously acquired net magnetic moment is shown on the right axis averaged over the full spectrum in Figure 3.6C.

The value of the peak amplitude corresponds to the left axis of Figure 3.8, while the frequency of the peak signal is represented by the underfill colour. The gyrotropic frequency variability is on the order of 10 percent as the field changes by a few kA/m ; this is believed to be imperfection-related. An even larger relative variation of modal amplitude supports this interpretation. At the same time, the YIG magnetizing curve exhibits only subtle slope (differential susceptibility) variations, near the resolution of the present measurements, as shown in the red curve in Figure 3.8.

The other trend, the red-shift of resonance frequencies as the annihilation field is approached, is a separate effect, not related to disorder [68]. The quasi-uniform spin modes presented in the previous section, in contrast, are more ‘internal’ to their respective textures and are not significantly affected by roughness as they do not exhibit energy densities highly localized at the

surface.

The qualitative variations in mode amplitude, frequency, and differential susceptibility are reproduced in the simulation through the introduction of shallow defects at one surface. The FIB milling can cause the surface modifications as during the milling of the undercut creating the lamella, the bottom surface of the YIG structure was heavily exposed to the FIB. Moreover, a very small system drift may create nanoscale corrugated features along the direction of the FIB as well.

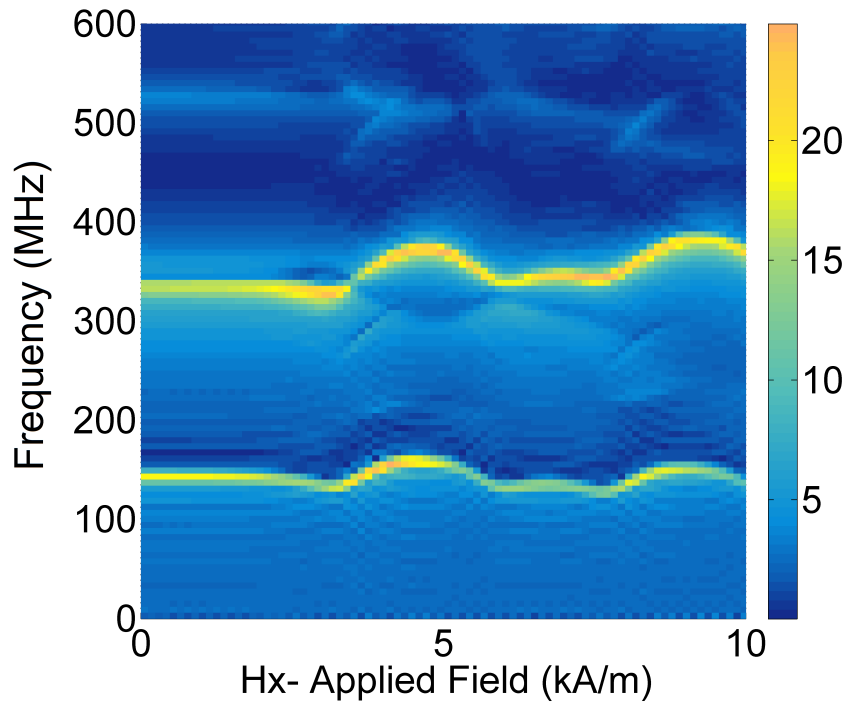


Figure 3.9: Simulation spectroscopic mapping of a YIG disk in a 3D vortex state with shallow imperfections at one disk surface. The three linear surface defects (shown in inset) were applied as vacancies in the simulation grid that are 9.8 nm wide 6.25 nm deep. As the applied field increases, the core begins to translate toward the edge of the disk, and interact with the imperfections. Two significant modes are clearly visible with the qualitatively similar amplitude and frequency modulations.

In the micromagnetic simulation, three very narrow magnetic linear vacancies (9.8 nm wide and 6.25 nm deep) were introduced in the simulation grid on the bottom layer of the disk (more detail in Appendix B). The vacancies are

placed in the direction of the FIB beam during fabrication and perpendicular to the path of vortex translation at 100, 200, and 350 nm from the center of the disk.

The simulated dynamic spectrum is presented in Figure 3.9 with the application of an RF pulse (400 A/m amplitude and 10.34 ns pulse width) in the \hat{x} direction at each applied field step. More so than symmetric defects, asymmetric defects modify the transition fields between textures in simulation. For that reason, asymmetric defects are used for better comparison to the smooth-faced disk in the simulation. Before quantitative simulations of magnetic hysteresis can be performed, it is necessary to complete a detailed characterization of the magnetic interface.

A modulation of amplitude and frequency of the resonances is also observed in the simulated spectrum for a 980 nm diameter and 250 nm thick YIG disk with line imperfections. As the core on the bottom surface of the disk approaches the defect it becomes pinned, while the core on the top surface is free to precess at an increased frequency. However, the wider modulations of the simulated frequencies, compared to experiment, are believed to be due to creation of larger pinning sites in the simulation than exist in the experimental YIG disk. A 6.25 nm deep for the imperfections was the limit imposed by the minimum grid size of the simulation. The observation of vortex core pinning through the interaction of resonant dynamics with nanoscale imperfections is not directly evident in the dc magnetization response. More simulation discussions are found in Appendix B.

3.5 Spin resonances spectroscopy for in-plane magnetized thin Py disks, in the vortex state

TMRS measurements yield more insight into phenomena such as vortex core pinning in an individual magnetic structure. For thin film disk, the magnetic structure can be considered as a 2D system and consequently the vortex core gyration excited with an in-plane RF field would be the zero-node mode. The Py structures with a thickness of 14 ± 4 nm were deposited directly onto an array of torque resonators using the lithographic method described in [33]. In this section, we study the polycrystalline thin Py disks, in which the grainy structures have intrinsic pinning sites. A case with artificial pinning sites is also investigated. Here, we use two perpendicular coils with 100-Hz bandwidths, which limit the working frequency range of the TMRS.

3.5.1 In the presence of intrinsic pinning sites

Figures 3.10A and 3.10C show torque spectroscopy of the gyrotropic resonances in a two-micron diameter Py disk with intrinsic pinning sites for an in-plane bias field sweep and two H_x^{RF} drives of 140 mV and 180 mV, respectively. The precessing core undergoes pinning potentials as it is pushed towards the disk edge with an applied field. For the higher drive, the mixing torque in Figure 3.10C shows mode-splitting as well as signal drop-out because of core pinning. The discontinuity of the resonance signal with applied field is associated with the suppression of gyration, as the translating vortex core interacts with magnetic disorders. There is a drive threshold for each pinning site that depends on the pinning potential energy, below which the resonance frequency is suppressed. Using a higher drive amplitude could help to depin the vortex by making the core gyrate at larger amplitude orbits. However, at a large ampli-

tude nonlinear dynamics (e.g., the mode splitting of the resonance) can also appear.

The simultaneously acquired magnetization and gyrotropic responses make it possible to directly correlate the suppression of the dynamic modes with vortex core pinning events. The accompanying net dc magnetizations are shown in Figures 3.10B and 3.10D for $H_x^{RF} = 140$ mV and $H_x^{RF} = 180$ mV, respectively. These magnetizations demonstrate very similar features, which confirm that the higher drive could not overcome the pinning potential in regions with the corresponding signal drop-out.

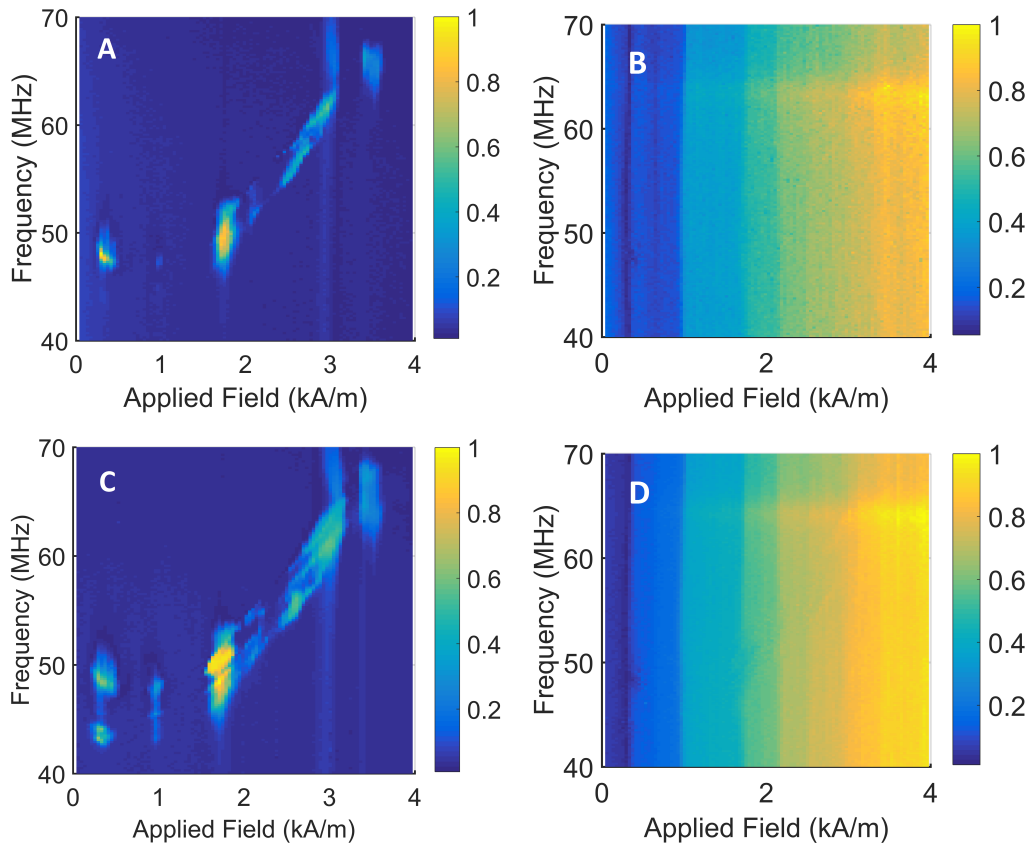


Figure 3.10: TRMS map of a thin, polycrystalline Py disk with 2- μ m diameter in the presence of intrinsic pinning sites. The vortex core gyrotropic mode with the concurrent magnetization is investigated for two values of in-plane RF drives: $H_x^{RF} = 140$ mV (A and B) and $H_x^{RF} = 180$ mV (C and D).

The higher drive provides larger splitting of the resonances. Figure 3.11

shows the different spectrum obtained from subtracting spectra in Figures 3.10A and 3.10C. The hot (red) part of the colorbar shows modes at the $H_x^{RF} = 180$ mV drive, while the cold (blue) part shows the resonance at $H_x^{RF} = 140$ mV. In addition, the micromagnetic simulation result for a 15-nm thick, 2- μ m diameter Py disk follows closely with experiment as shown in grey line with circles.

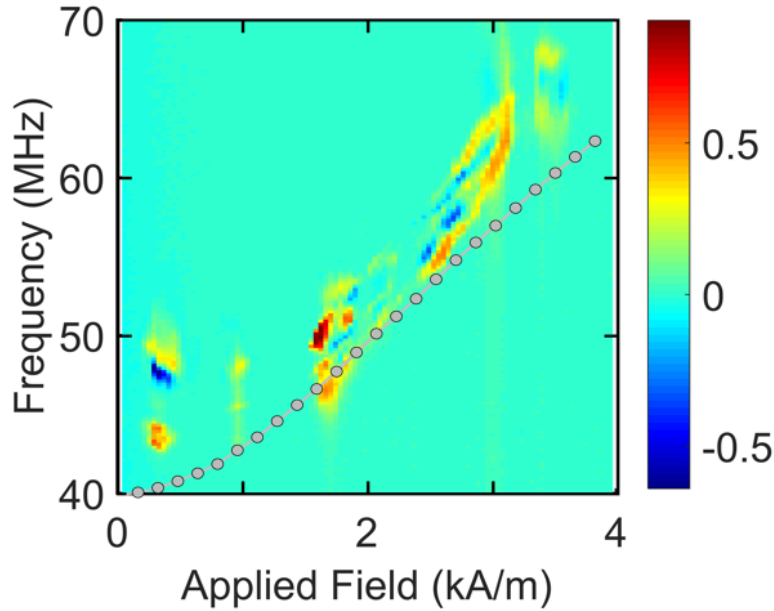


Figure 3.11: Magnetic resonance spectra in comparison to micromagnetic simulation. Through a subtraction operation, the two RF drives spectra are overlapped and accompanied by micromagnetic simulation. In simulation bulk Py parameters are used: $M_S = 680$ kA/m, $A_{ex} = 10.5$ pJ/m, and the resonance frequencies are extracted by fitting the temporal response of the m_y component to an analytical form of Thiele's equation.

Figure 3.12 shows an average of the mixing torque (left axis) overlapped with the simultaneously acquired net magnetic moment (right axis) for the 2- μ m Py disk. A box with a width of 9-MHz is considered to perform averaging around a resonance peak at each field in the spectrum of the lower RF drive (Figure 3.10). However, for the accompanying magnetization, the averaging is performed with the integration over a full frequency range. The step-like Barkhausen transitions in the magnetization response (right axis) represent

the interaction of the vortex core with disorders, as it is pushed towards the edge of the disk with the increasing dc applied field. The drop-outs of the resonance signal correlate with plateaus of reduced differential susceptibility that occur while the vortex core is pinned by the grain boundary along its pathway. Between these regions, the core is free to precess, as correlated with the spin dynamic response.

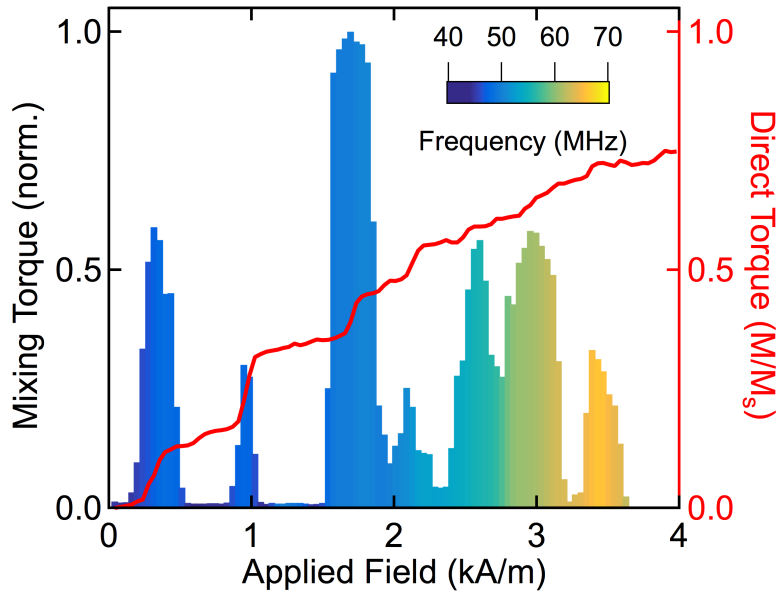


Figure 3.12: Overlap of the averaged torque of vortex core gyration and net magnetization in the thin, polycrystalline Py disk. The integrated dynamic and simultaneously acquired net dc magnetic moment responses are presented in the left and right axes, respectively.

3.5.2 In the presence of artificial pinning sites

The Ga^+ ions have been used to make three artificial pinning sites in a $2\text{-}\mu\text{m}$ Py disk. A gentle surface modification using FIB exposures has been used to make pinning sites: a single site 210 nm from the center, and paired sites 85 nm and 220 nm from the center on the opposite side. The quasi-static study of a Py disk with three artificial pinning sites has been presented in Chapter 2. We use the same disk to investigate magnetic resonances.

The magnetic resonance spectrum of the disk is presented in Figure 3.13a. The field sweep is chosen from high to low to push a free vortex toward the pinning sites. The spectrum is very quiet, which might be because of the pinning effect that shifts the resonance frequencies to an even higher range. However, it appears that there is narrow field dependence in the mixing signal, and the resonance frequency has a similar range of resonance in comparison to the unmodified Py disk. Because of the limited bandwidth of the crossed-coil configuration, the pinned gyrotropic mode of the vortex core could not be captured. Future investigation with the transmission lines would be very helpful to understand more about the pinning mechanism and its effect on the resonance spectra, as discussed in Appendix B.

The sharp transition near 2.87 kA/m in Figure 3.13b is a vortex pinning and actually appears to be more dependent on the frequency sweeps of the RF field rather than the dc field sweep. The RF field helps the vortex to get pinned, while in Chapter 2 similar vortex pinning phenomena seems to be caught at lower field.

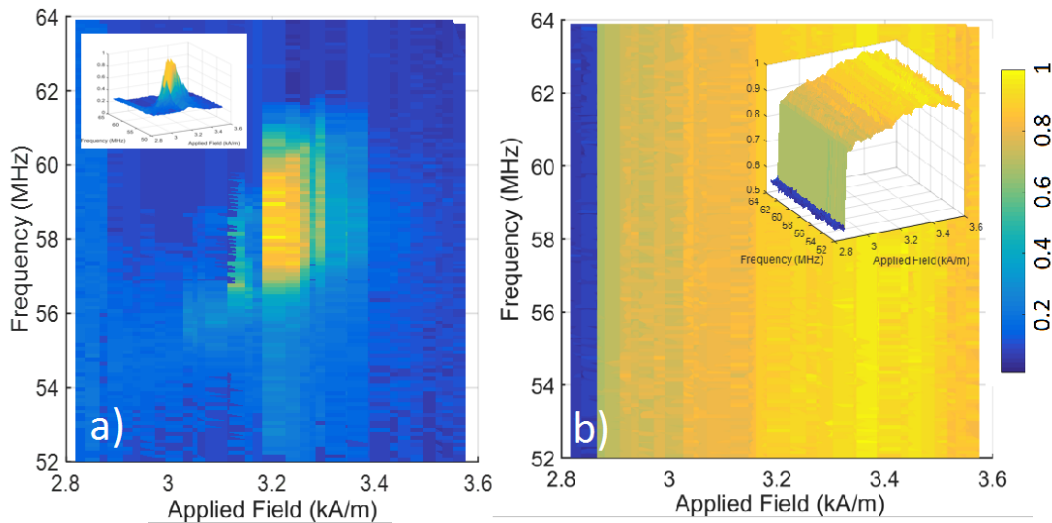


Figure 3.13: TMRS responses in the Py disk with artificial pinning sites. a) At high field, the vortex is free to gyrate. In a field sweep down, the vortex approaches the artificial pinning site and gets pinned at $H_x^{dc} = 2.87$ kA/m. b) The spectrum and magnetization responses are normalized to 1. A 3D view of the responses shown in the insets.

3.6 Spin resonances in a perpendicularly magnetized YIG disk

In this section, we consider the spectrum of the YIG structure in the presence of a bias field in the \hat{z} direction; there is an option in the LabView program that could automatically rotate the permanent magnet in the experimental setup to achieve the external field in \hat{x} or \hat{z} . By having a perpendicularly applied field, obtaining the magnetization would be a challenge. Because of transmission-line orientation, the torque sensor is sensitive to only in-plane dc magnetization, m_x . However, increasing the applied field from the low values in the z-direction only changes the m_z , and will not significantly modify the in-plane components. In a perpendicular applied field, the vortex state would still be the ground state. In addition, after the vortex annihilation that occurs at a higher field compared to in-plane dc field orientation, the in-plane magnetization component is completely ignorable.

One solution to this challenge that is left for future work is to measure dc susceptibility instead of magnetization in the perpendicular orientation. dc susceptibility not only reveals similar features in the hysteresis loop (e.g., state changes), it is sensitive to the small transitions like the pinning/depinning effects. The additional coil in the x-direction is also helpful for measuring the out-of-plane component.

3.6.1 Vortex state

Figure 3.14 shows the spectrum of modes in the field sweep starting from the low field, at the vortex state, up to ~ 65 kA/m. A piecewise spectrum is made out of four separate spectra to capture the modes in appropriate time slots and avoid signal drift. The vortex annihilation clearly happens around 59 kA/m, which is related to a slope change signature for resonance modes. Below the annihilation field, there are two dominant modes related to the gyrotropic

modes; Section 3.4 showed that a thick YIG disk provides higher gyrotropic modes. There are some amplitude/frequency modulations for the resonance mode that are believed to be related to the surface modification of the YIG disk studied in Section 3.4.

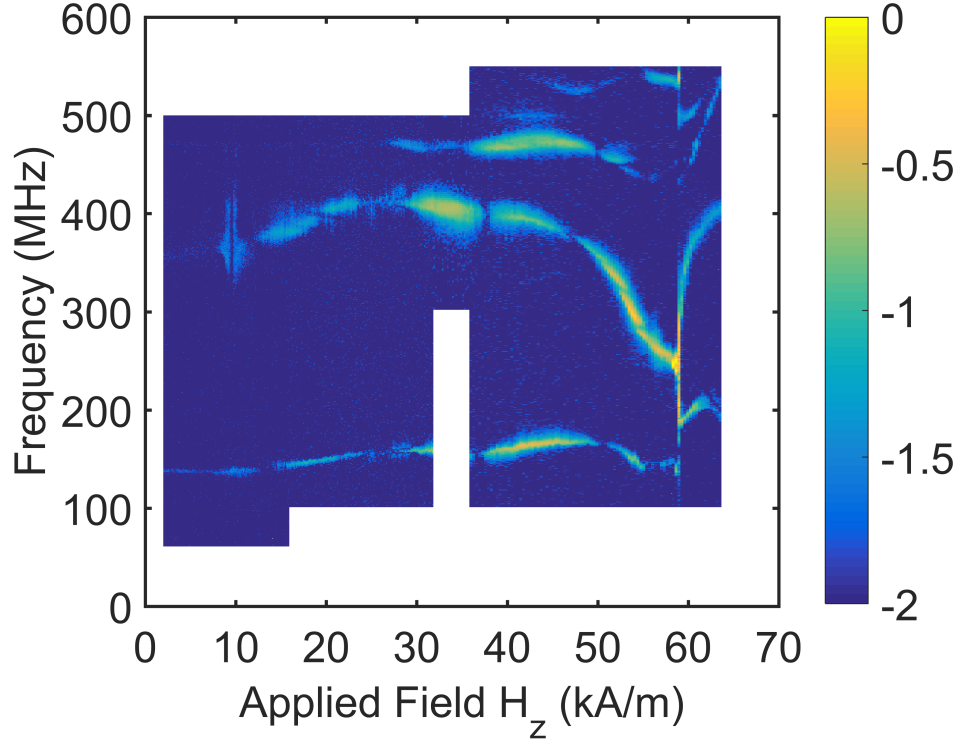


Figure 3.14: Spectrum of a perpendicularly magnetized thick YIG disk in the vortex state. In the field sweep up, there are gyrotropic modes of a vortex state in the YIG disk. The RF fields are provided through a Zurich lock-in amplifier and power amplifiers. There is a 550 MHz bandwidth limit constrain associated with the Zurich instrument.

For the initial adjustments, we use a small H_x offset to identify the in-plane component. The vortex annihilation strongly depends on this additional in-plane field offset. The small offset in the field can also shift the resonance modes in the spectrum.

3.6.2 Uniform magnetization and Kittel-like modes

The Kittel expression for ferromagnetic resonance is a gold standard for determining fundamental properties of magnetic films, owing to the weak dependence of Kittel modes on *film* geometry. The Kittel mode, a uniform precession of spins, has a magnetic resonance frequency that depends on the field intensity as well as the field orientation. The Kittel formula has been modified by additional terms for specific geometries such as an ellipsoid. The simple analytical Kittel expression determined the frequency-field dispersion for a confined structure in the case where a perpendicular field orientation is brought into the Equation 3.7:

$$\omega = \gamma \sqrt{\left(H_z + (N_x - N_z)M_s\right)\left(H_z + (N_y - N_z)M_s\right)}, \quad (3.7)$$

in which γ is the gyromagnetic ratio, H_z is the perpendicularly applied field, M_s the saturation magnetization, and N_x , N_y and N_z are shape-anisotropy or demagnetization factors. The demagnetization factors are positive geometry-dependent values that are obtained from the integral formulas [12]. In the case of a cylindrical disk where $N_x = N_y$, the Kittel expression is simplified to a linear relation between frequency and applied field:

$$\omega = \gamma \left|H_z + (N_x - N_z)M_s\right|. \quad (3.8)$$

This equation allows us to directly obtain fundamental magnetic properties of a magnetic disk such as an effective g-factor that corresponds to the gyromagnetic ratio and can be acquired from the slope. In addition, the absolute-value function in the Equation 3.8 has a slope change feature at its root; from that aspect, we can anticipate that the resonance frequency would reach very close to zero values. By knowing the field in which the root happens, one can determine other fundamental magnetic properties such as the saturation mag-

netization and demagnetization factors. Note that the intercept could contain more terms if one includes the crystalline anisotropy, an exchange term including the wave vector and maybe a couple of more related energy terms to the Kittel expression articulated in Equation 3.7, [11, 93].

For a magnet, the dispersion relation converges to a single mode, Kittel mode. However, for a confined magnetic structure like a disk, there is a rich spin resonance spectrum, which appears because of disk boundary conditions. The theoretical analysis suggests that the resonance modes in a perpendicularly magnetized disk, because of cylindrical symmetry, would be Bessel functions in the radial direction and standing waves along the thickness. Finding the mode numbering, associated with the zeros of the Bessel and sine functions, is more complicated in the case of a thick disk.

Multi-resonance modes in an unrestricted in-plane magnetic film are quantitatively described using a dipole-exchange theory of spin waves [94], which considers not only dipole-dipole but also exchange interactions. If the disk thickness is lower than the exchange length, then a 2D system is considered with constant mode profiles along the thickness. With some modifications, the dipole-exchange theory for the film can be used for a thin disk with discrete in-plane wave vectors (radial mode number) [95].

$$\omega_k = \gamma \sqrt{\left(H_{eff} + \frac{2A_{ex}}{M_s} k^2\right) \left(H_{eff} + \frac{2A_{ex}}{M_s} k^2 + M_s f(kL)\right)}, \quad (3.9)$$

where H_{eff} is the effective internal bias field including the external field, demagnetizing factors, and perpendicular anisotropy field; A_{ex} is the exchange constant; wave vectors $k \rightarrow k_m$ are discrete values related to radial mode numbers; and $f(kL) = 1 - \frac{1 - \exp(-kL)}{kL}$ is the dipole-dipole interaction matrix element for a perpendicularly magnetized disk, in which L is the film thickness.

The obtaining of the mode numbering for thin disks from simulations is presented in reference [96]. The confined modes can exhibit the non-monotonic

evolution of frequency with a field familiar from Kittel modes [97]. The downside is that only specific dimensions are considered (close to 2D structure) and the anisotropy term is not considered. For instance, in YIG disk, there is a cubic anisotropy that could not be ignored, and the 3Dness of the structure makes the identifying of modes even harder.

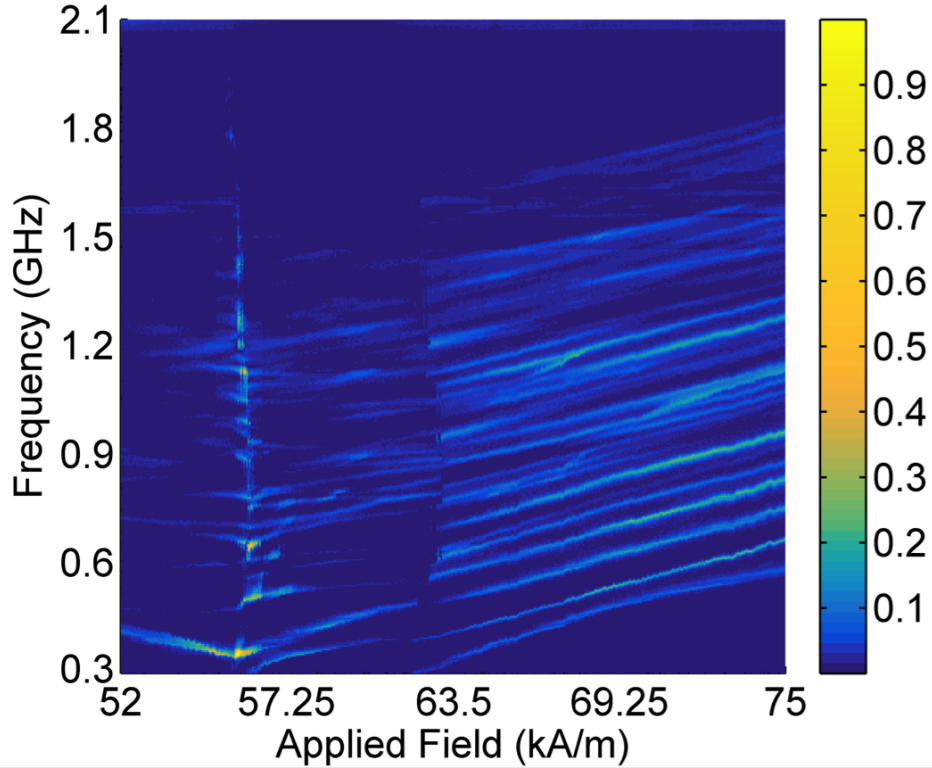


Figure 3.15: Experimental measurement of magnetic resonance spectrum in a perpendicular uniform magnetized YIG disk. The field is swept from high to low-field. The field calibration is performed by finding the resonance of a 250- μm YIG sphere with VNA. field sweep direction is from high to low field.

Fig. 3.15 shows the 2D map of frequency-field dispersion of the perpendicularly magnetized YIG structure obtained with torque-mixing magnetic resonance spectroscopy (TMRS) technique. We extend the frequency bandwidth to 2.1 GHz using signal generators. TMRS enables us to capture subtle details with very fine resolution in the spectrum, with a frequency step of $\Delta f = 5$ MHz, and field step of $\Delta H = 40$ A/m shown in Fig. 3.15.

At the high field, $H_z \sim 75$ kA/m, there are around 28 modes with some interactions between the modes while some modes are brighter than the other ones. This is the highest number of modes one can achieve via magnetometry, with fine field and frequency resolution.

There are two striking features in Figure 3.15: a V-shape feature in which slopes of the resonances are reversed before and after and a ladder of modes at uniform state (high fields). The location of the V-shape corresponds to a transition from the uniform state to the vortex state, where the frequency of resonance modes reduces to a minimum value and it appears mainly because of a vortex nucleation. The number of modes reduces after vortex nucleation around $H_z = 57$ kA/m in a field sweep from high to low direction.

The Kittel expression in Equation 3.8, anticipates another V-shape corresponding to the slope change at the root of the absolute value function. That case would be of interest to obtain directly the saturation magnetization or the demagnetization factors. However, this V-shape feature would not relate to the vortex nucleation, where a softening of the magnetic texture causes a red shift in the resonance frequencies. It is worth mentioning that the Kittel equation is valid only when the magnetization is oriented approximately in the direction of applied field. By nucleating a vortex, the uniform magnetization condition would not be satisfied anymore, and as a result, the Kittel expression could not be used for the lower field.

In the spectrum, numerous modes are visible in two distinct regions of uniform and vortex states in a high-to-low field sweep. Furthermore, there are some mode coupling, anti-crossings between modes, which are not well understood. The ladder of modes at the high field has appeared because of the standing waves created by the disk boundary conditions. In addition to the different slope, the number of modes is slightly lower in the vortex state. This decrease in number of modes could be related to the different nature of modes. It is mentioned that for a thin disk there should be a bijective relationship

between the number of modes in the vortex state and uniform state; however, due to the symmetry, some modes might have degeneracy [96] and also this higher thickness would add more complexity to the spectrum.

Note that the field calibration has been performed based on the Kittel expression as well. A single-crystalline, $250\mu\text{m}$ -diameter YIG sphere is replaced rather than the sample on top of transmission lines. The corresponding fields are obtained from frequency read out via a vector network analyzer (VNA E5072A). The field axis is calibrated based on a known linear relation between ferromagnetic resonance frequencies and corresponding applied magnetic fields for a magnetic sphere: $\omega = \gamma H$, which is independent of demagnetizing factors and considering $\gamma = 28.025 \text{ GHz/T}$. The field calibration is obtained based on the Kittel expression as well.

Furthermore, the micromagnetic simulation has been used to obtain a more qualitative understanding of the spectrum. During the thinning process of the lamella thickness through FIB fabrication (one step before making a disk out of the YIG film), a normal-incidence dose is used. The wings of the ion beam (approximately Gaussian shape) could taper the dead-layer in the thickness direction.

It is shown that ion exposure that could make a magnetically rough surface with a surface corrugation less than 5 nm has an impact on the resonance modes in the vortex state, as presented in Section 3.4.2. However, the uniform magnetization state is more internal and the surface roughness effects are less significant. The disk dimensions have been obtained via a close comparison between the spectrum of the YIG disk with an in-plane magnetization and simulation results to be with 980 nm diameter and 250 nm thickness.

Therefore, similar dimensions are used for the perpendicularly magnetized disk and the spectrum is presented in Figure 3.16a. There are two similar signatures in the simulation: a change in the slope of modes at the V-shape softening point (at the vortex nucleation) and a bunch of linear modes before

the vortex nucleation (at uniform state). The mode profiles of 250 nm YIG disk, obtained from spatial Fast Fourier transform (FFT), are presented in Appendix B, Figure B.17.

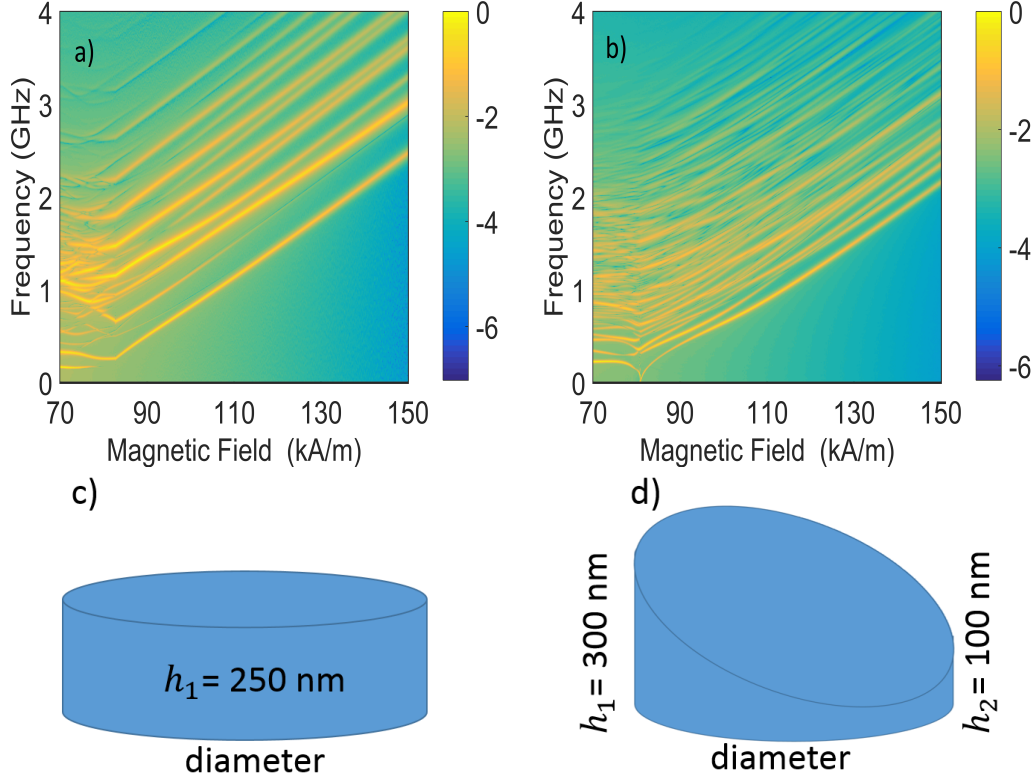


Figure 3.16: Micromagnetic simulations of magnetic resonance spectra in perpendicularly magnetized YIG structures. a) The spectrum of 980nm diameter and 250nm thick YIG disk is presented. The disk simulations show very similar features compared to experimental results presented in Figure 3.15, but specifically at the saturation, the modes in the simulation have the higher slope and there is lower number of modes. b) The mapping of the resonance spectrum for a tapered YIG disk with 980nm diameter and thickness taper of 100-300 nm is depicted. The spectrum qualitatively shows more similarity to the experiment. Scale bars are presented in log scale. c) and d) are illustrations of a 250-nm thick disk and a tapered disk with tapering of 100 nm to 300 nm in the thickness.

The slope of modes in the uniform states is larger and the number of modes is lower in comparison to the experiment. As a result, based on the fabrication insight, a tapered disk is considered in simulation and its simulated spectrum is shown in Figure 3.16b. The depictions of a tapered disk is illustrated in

Figure 3.16d. The vertical cross-section of a tapered disk is considered as a right trapezoid with the base of 980 nm and two thicknesses of 100 nm and 300 nm, which corresponds to a tapering angle of 11.5° . In term of magnetization volume, the tapered disk is equivalent to a disk with 200 nm thickness and 980 nm diameter. Note that the spectrum of the 200-nm thick disk is very similar to the 250-nm thick disk, but in the former, the modes shifted to the lower frequencies. The tapering of the disk thickness breaks the circular symmetry and non-degenerate modes can appear. As a result, the thickness modification of the YIG disk has a huge impact on the number of modes and their brightness. The spectrum of the tapered disk has more similarities in terms of increased number of modes, the interaction of modes like the mode couplings, and the closer slope of modes to experimental data in comparison to the simulated disk spectra. Thus, the actual geometry is more like a tapered disk inferred from the simulation insights. For all the simulation, the following magnetic parameters are used: $M_s = 140$ kA/m, $A_{ex} = 12$ pJ/m, and $K_c = -610$ J/m³. More simulated spectra and details have been presented in Appendix B.

3.6.3 Avoided crossing of confined modes

It has been shown that for sufficiently thick disks in the ground state, the lowest resonance mode is not the uniform gyration, but instead there is a crossover between the two first gyrotropic modes as discussed previously in Chapter 3. Likewise, similar mode crossings may occur between the Kittel mode and first spin-wave mode in the thick magnetic disk at the uniform state (for more information see Appendix B, Section B.1.6).

The zoom in the spectrum of the tapered disk with the mode profiles is presented in Figure 3.17. The mode profiles are obtained through spatially resolved FFT analysis of the time-evolution magnetization in each cell of the tapered disk. From micromagnetic simulation for the tapered YIG disk, however, the first mode at high field resembles Kittel-like mode with uniform mode

profile, shown in Figure 3.17c. Interestingly, the mode profiles of the first mode at the lower field ($H_z = 87$ kA/m) and the second mode at the higher field ($H_z = 103$ kA/m), presented in Figures 3.17a and 3.17d, are very similar. One explanation would be that there is a mode crossing, while the Kittel mode smoothly evolves through the softening of the texture at the beginning of vortex nucleation.

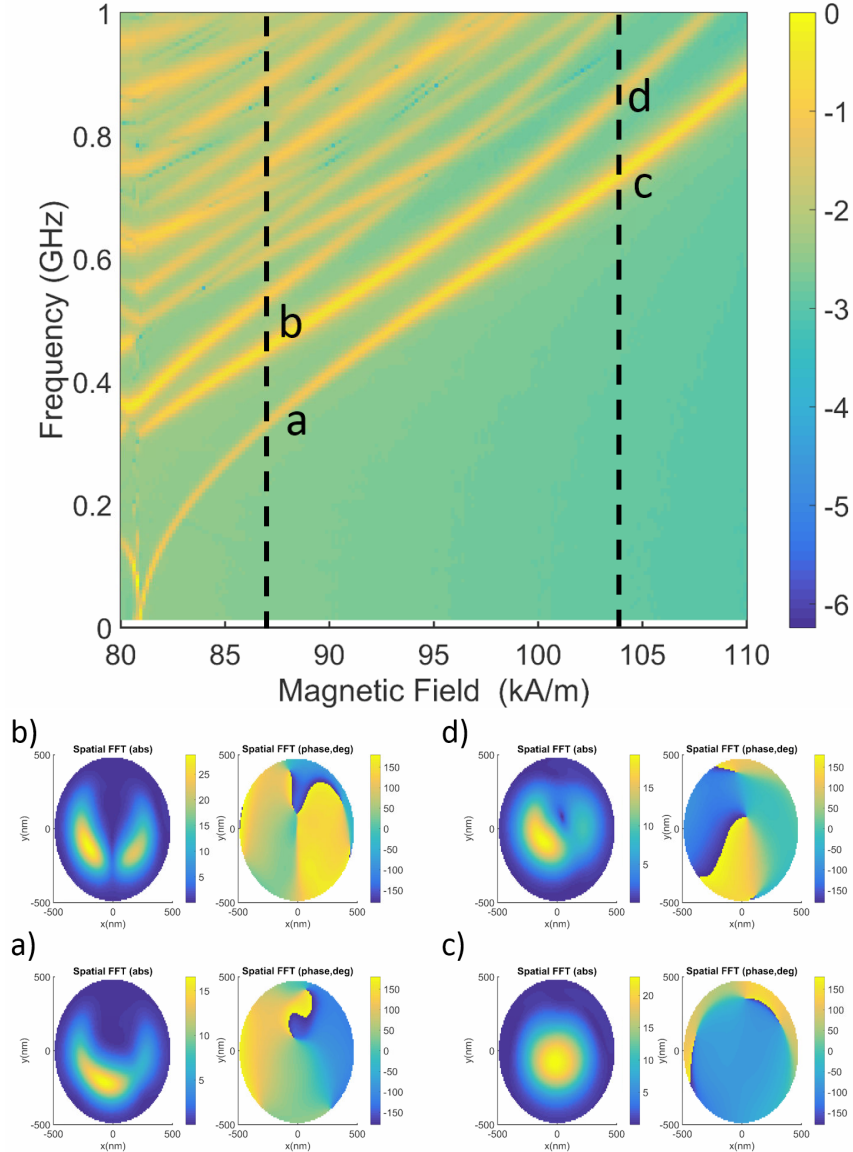


Figure 3.17: Zoom-in simulated spectrum of tapered disk and selected spatial FFTs. The spectrum with selected fields highlighted with the dashed lines is shown. The FFT mode profiles at $H_z = 87$ kA/m (a and b), and at $H_z = 103$ kA/m (c and d) are shown in amplitude and phase of the bottom layer of the tapered disk.

The frequency-field dispersions obtained from the simulations suggest that the structure geometry will affect the slope. In addition, it appears that the magnetic texture will affect the slope of mode in an intermediate field range.

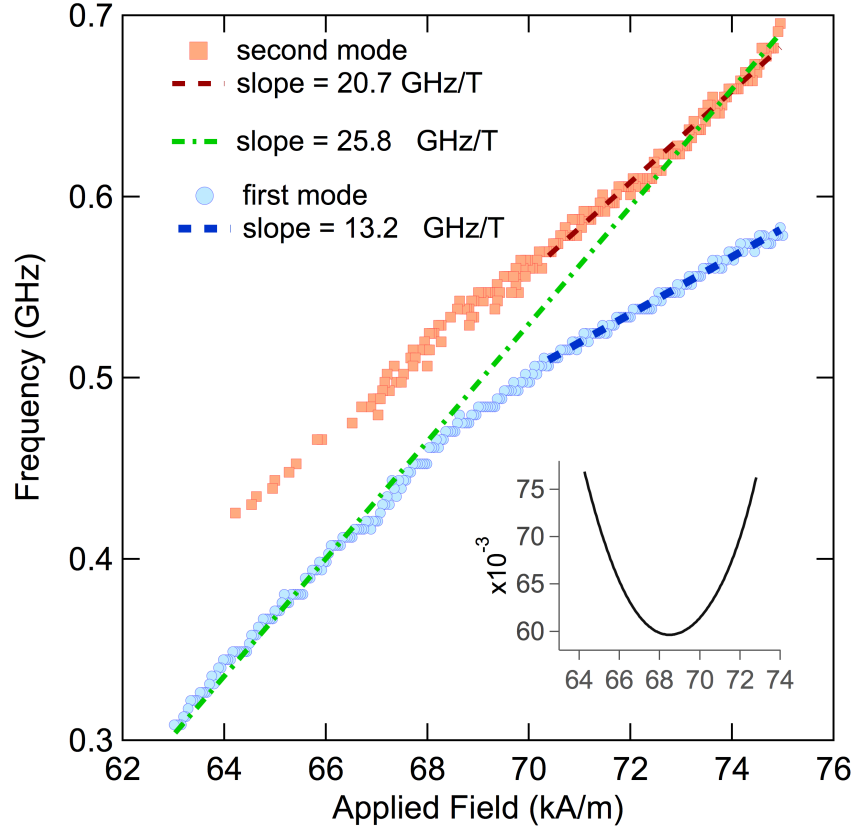


Figure 3.18: The first two modes in the experimental spectrum with linear fits. The inset shows the subtraction of two modes with the vertex position at $H_z = 68.5$ kA/m with the gap of 60 MHz.

We consider the first two modes in the experimental spectrum through a script Matlab that finds the high peaks. The accuracy of script can be changed, but may not be sufficient when there are mode couplings, or avoided crossing modes. In Figure 3.18, the two modes and their interestingly avoided crossing are presented. The subtraction of two modes shown in the inset demonstrates a parabola shape. Therefore, the two modes would not continue the linear slope for a full given field range. We used a polynomial fitting for each mode to perform the subtraction. The gap is determined at $H_z = 68.5$ kA/m, where

the parabola has the lowest value, as shown in Figure 3.18 inset.

We also attempt a fitting with a hyperbola containing two crossing lines to find the coupling strength of the two first modes. Figure 3.19 demonstrates a preliminary fit to an avoided level crossing, superposed on an image of data. The hyperbolas fit is obtained from determining the two straight lines, which intersect near the middle of the gap. An estimate of the coupling strength is obtained around 60 MHz at the intersect $H_z = 69.14$ kA/m. That is in close agreement with the results obtained from the other method presented in Figure 3.18 inset, in which the coupling strength is determined at the vertex of modes difference.

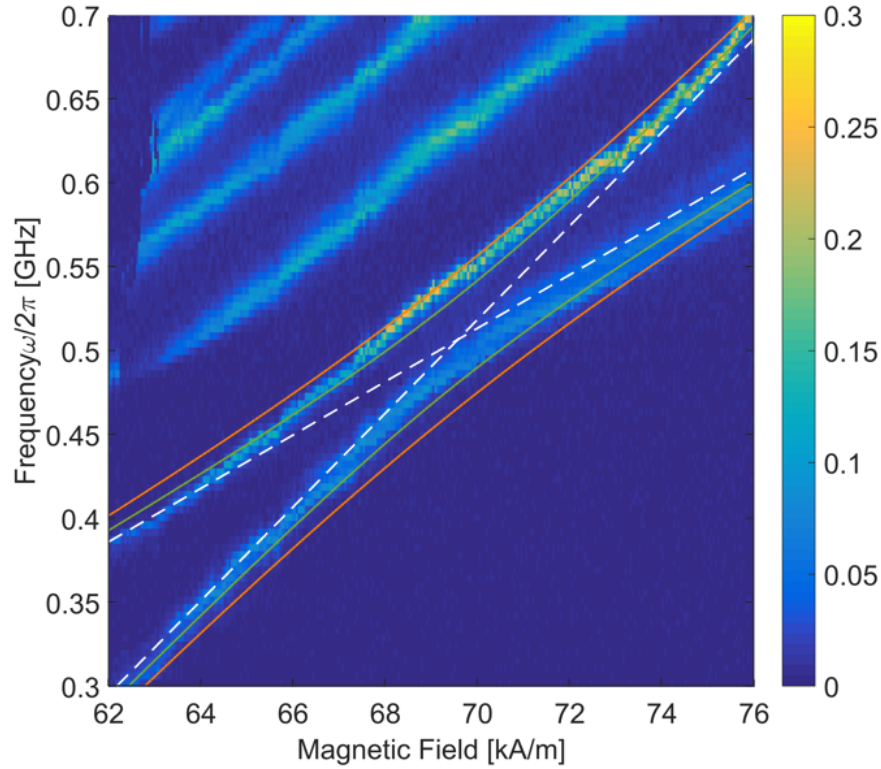


Figure 3.19: Mode-coupling and the Kittel like mode. To investigate the mode coupling, Figure 3.15 is zoomed in around the first two modes at high field. The Kittel-like mode Experimental measurement of magnetic resonance spectrum in a perpendicular magnetized YIG disk.

The overall shape of curves deviates from the hyperbolas. It is partly due

to a limited experimental field range used for fitting. We first estimate the asymptotic lines, although the linear fit might not overlap on the measurements, then hyperbolas would be fitted on the data. The two asymptotic lines used here have slopes of 12.6 GHz/T and 22.2 GHz/T.

3.6.4 Effective gyromagnetic ratio

To further our understanding of the magnetic properties of the structure, we perform analysis such as the linear fitting to obtain an effective γ , or the gyromagnetic ratio. The Kittel expression anticipates a linear relation between frequency and applied field, in which the slope corresponds to the gyromagnetic ratio. The Kittel mode, with uniform precession, is usually the lowest excited mode in the uniform state.

Thus, we consider linear fitting for the field range higher than the vertex of the parabola, as shown in Figure 3.18. The slopes found from the linear fits beyond the avoided-crossing region are 13.2 GHz/T and 20.7 GHz/T for the first and second modes, respectively. Although both values are different from the accepted gyromagnetic ratio value for an electron, $\gamma_{ref(sim)} = 28.025$ GHz/T, the slope of the first mode is even less than half of the gyrotropic value.

The original single-crystalline film we started with for the fabrication of the YIG disk has 1% Bismuth doping, and it could account for the lower initial gyromagnetic value. Using a VNA measurement, we obtained the gyromagnetic ratio of a piece of unmodified Shin-Etsu YIG, the original wafer, $\gamma_{ref(exp)} = 25.8$ GHz/T as a reference value. As a result, the normalized experimental values are $\gamma_{1,exp} = 0.51 \gamma_{ref,exp}$ and $\gamma_{2,exp} = 0.80 \gamma_{ref,exp}$.

Also, the Ga ion disruption may cause the doping of Ga in the crystal structure. Moreover, the uniform magnetization is an initial assumption in deriving the Kittel expression, which does not satisfy for confined structure because of the boundary conditions specifically for the intermediate fields. The Quasi-uniform state could be a perturbation from Kittel expression that leads

to an effective gyromagnetic factor.

We perform similar linear fit procedures for the simulation spectra for the first mode and by considering $\gamma_{ref(sim)} = 28.025$ GHz/T as a reference. The normalized value for the gyromagnetic ratios are obtained as follows: $\gamma_{disk} = 0.94 \gamma_{ref,sim}$ and $\gamma_{tapereddisk} = 0.82 \gamma_{ref(sim)}$.

The normalized experimental values for the gyromagnetic ratio for the second mode are very close to the normalized gyromagnetic ratio obtained from simulation. A summary of the gyromagnetic values appears in the following table.

Experiment	$\gamma_{ref,exp} = 25.8$ GHz/T	$\frac{\gamma_{1,exp}}{\gamma_{ref,exp}} = 0.51$	$\frac{\gamma_{2,exp}}{\gamma_{ref,exp}} = 0.80$
Simulation	$\gamma_{ref,sim} = 28.025$ GHz/T	$\frac{\gamma_{disk}}{\gamma_{ref,sim}} = 0.94$	$\frac{\gamma_{tapered}}{\gamma_{ref,sim}} = 0.82$

Table 3.1: Gyromagnetic ratio obtained from linear fits, experiment and simulation.

The experimentally limited field range is a challenge to obtain more accurate gyromagnetic ratio values. We will manage to use a higher magnetic field range for future investigation for a more uniform magnetization consideration.

3.7 Conclusion

The direct correlation of spin dynamics with complementary information in the magnetization hysteresis curves typically has been an experimental challenge; most techniques yield nice observations of one *or* the other. TMRS provides the capabilities of simultaneous monitoring of equilibrium net magnetization and detecting of the transverse RF moment in an individual magnetic structure. With an excellent coupling to small specimens, TMRS results in high spin sensitivities. On one hand, the simplicity of the technique is owed to the recent development of multi-UHF lock-in instrumentation [45], and to the natural compatibility of RF transmission line actuators with on-chip nanomechanical torque sensors. On the other hand, straightforward processing to integrate

samples onto sensors [33, 34] opens TMRS to a wide variety of materials. The approach is fully broadband, is massively scalable through microfabrication, and has the intriguing potential for low-frequency work where induction signals become very small, per Faraday's law. However, the amplitude of the TMRS torque is frequency-independent.

TMRS provides tantalizing possibilities to study a single (misshaped), low-damping element, broadband frequency response with fine frequency resolution. Using the nanofabrication processes, we can design the shape of a magnetic structure to study the shape anisotropy, engineer the magnetic properties, and introduce shallow pinning sites on the surface. We experimentally examined the modifications of magnetic resonance dynamics due to impurities and pinning sites effects. We obtained great insights about the pinning mechanism by making artificially fabricated surface modifications to the magnetic Py structures by utilizing focused ion beams.

We presented the spectra obtained through TMRS measurements, which shows fine physics, with very good resolution in comparison to time domain and even frequency domain techniques. The spectra of spin resonances in a single crystalline YIG disk were shown in two cases of in-plane and perpendicular field orientations. In the last case, the frequency range extended to 2.1 GHz. As a result, we examined the effect of surface roughness on the magnetic resonance and obtained the effective gyromagnetic ratio γ at a given field range from the Kittel expression. This study, with the help of micromagnetic simulation, allows us to elucidate the effect of geometry on γ , which produces an effective value and provides promising new possibilities for engineering new devices based on the modification of geometry.

Chapter 4

Conclusion & remarks for the future

In this thesis, we presented demonstrations of the torque-mixing technique in which the concurrent measurement of a single mesoscopic element's magnetostatics and spin dynamics is achieved, based on torque sensing. TMRS affords very high sensitivity with excellent coupling to small specimens. A desired magnetic torque component can be measured using a mechanical resonance by adjusting the frequencies of perpendicular RF (or ac) drives. Using TMRS, we have studied magnetic phenomena including quasi-static responses, magnetic susceptibilities, and magnetic resonances with a very broad frequency range (dc to GHz) at room temperature.

Using nanofabrication processes, a variety of magnetic materials can be affixed to the mechanical resonator. Moreover, we can engineer artificial pinning sites on the sample surface, and design shape anisotropies to study the important role of nanoscale defects. This is possible by using a FIB to mill and surface modify the magnetic structures. Point-like defects are created in Py disks. These point-like defects are not visible using SEM imaging, but are still very effective pinning sites. They differentiate this work from earlier studies that examined the controlled pinning of magnetic vortices. The local surface

modification in a thin Py disk is achieved with a point exposure with as few as ~ 10000 Ga⁺ ions.

The vortex core, with its high energy density, is an exceptional probe to determine small-scale imperfections at disk surfaces. The vortex core can be moved around the surface by using the in-plane bias field. Using that, we have demonstrated the elaborate mapping of local properties of intrinsic and dose-dependent artificial inhomogeneities in thin disks. The diameters of artificial pinning sites in this study are comparable to the vortex core diameter. Therefore, a first order change corresponding to the susceptibility of a pinned core appears in the magnetization response of the disks.

Engineering adjacent pinning sites enhances the “Barkhausen-free” range. In addition, it gives rise to a completely different trajectory for vortex annihilation. We have shown that several widely separated sites can work together to keep the core pinned in one place, while the Barkhausen effect is eliminated from the magnetization curve over a range approaching the saturation moment of the disk. This is a new regime for the artificial control of the magnetic response. Additionally, we performed studies to measure susceptibility terms on Barkhausen jumps along with the ac harmonics of susceptibility. From the latter result, one gets more information about buckling, a non-linearity in the vortex nucleation/annihilation.

Thin-film polycrystalline Py disks provide dramatic examples for demonstrating the TMRS technique with intrinsic magnetic disorders (which are grain boundary dominated). To eliminate the effect of grain boundaries, FIB milling is used to sculpt a thick disk from a single crystalline YIG film. This was an ideal TMRS case study due to the absence of intrinsic pinning sites, and due to YIG having one of the lowest ferromagnetic resonance linewidths.

The ability to record both the equilibrium magnetic responses and the spin excitations allow for the development of a complete understanding of magnetic devices. We investigate RF-assisted transitions related to ferromagnetic

resonances in the YIG structure. We have demonstrated that the nucleation (annihilation) transition is tuned to occur at a higher (lower) bias field, using the magnetization response, and it was characterized as a function of the RF amplitude in the vicinity of the lowest frequency resonance of the spin texture. In combination with micromagnetic simulations, slight (nm-amplitude) corrugations at the surface of a disk can be induced during fabrication. The geometric insights are developed using the spectroscopic map of the YIG structure when it is magnetized perpendicularly. Finally, we are able to study Kittel-like modes, which allowed us to measure an effective gyromagnetic ratio, and the ferromagnetic resonance mode coupling of an individual structure.

Using magnetic resonance as a tool to study magnetic properties in an individual nanoscale gemstone, where impurities have a significant impact, is very important. The study of periodic artificial defects can be essential in investigating the effect that defects have in a material; the nano-scale defects will become significant components of the sample, as the device shrinks down to a size comparable with the size of defects. More complicated pinning patterns tailored by ion irradiations can lead to magnonic devices with bandgaps for spin-waves. It is possible to design a magnonic-cavity integrated with cavity optomechanics [98], and this could reveal more information about the spin (magnon), photon, and phonon interactions. In fact, by using cavity optomechanics, the sensitivity of the TMRS method can be increased [99]. Torque spectroscopy, in combination with optomechanical devices, will be most likely used to explore novel phenomena in emerging spin-mechanical physics [100, 101].

Measurements of other materials (e.g., paramagnets, solutions) will illuminate the next question to be answered by TMRS: how does the whole-body torque on the mechanical resonator cascade from magnetic torques on the individual spins? As a litmus test, large samples such as ferri-spheres could be used to measure the Gilbert damping to confirm that shape anisotropy has no (or a very little) effect on the TMRS measurement. DPPH, the organic

chemical compound (2,2-diphenyl-1-picrylhydrazyl) is a standard material for electron paramagnetic resonance (EPR) studies and can also be considered as an option.

The spin-lattice relaxation time has been studied extensively in nuclear and electronic paramagnetic resonances [10], where the effective field contains only the external applied field ($\mathbf{H}_{eff} = \mathbf{H}_0$) and as a result the Larmor frequency relation ($\omega = \gamma H_0$). Moreover, there are some investigations of spin-lattice relaxation in ferromagnetic materials as a function of high-level microwave power, but only the upper limit for T_1 is presented [102, 103, 104]. In a ferromagnetic system, \mathbf{H}_{eff} contains the demagnetizing and anisotropy fields, which lead to a geometry-dependent resonance frequency and $|m_z|$ (Kittel expression) [11]. Consequently, heating up the spin system should be done in a different way. One suggestion to overcome the geometry dependent relations in ferromagnets is to use spherical samples, in which the Kittel expression is simplified to the Larmor expression.

In conclusion, with its ability to simultaneously measure static magnetization, and dynamic responses in an individual structure, TMRS opens up new avenues for further research on magnetic materials. Broadband TMRS forms a foundation for nanomagnetism lab-on-a-chip applications for highly sensitive, non-invasive, and rapid prototyping of individual mesoscopic elements. It presents another functional method to create and detect dynamic spin-based devices.

Bibliography

- [1] S. Johnsen and K.J. Lohmann. The physics and neurobiology of magnetoreception. *Nature Rev. Neurosci.*, 6:703–712, September 2005. URL <http://dx.doi.org/10.1038/nrn1745>.
- [2] Ki. Maeda, K.B. Henbest, F. Cintolesi, I. Kuprov, C.T. Rodgers, P.A. Liddell, D. Gust, C.R. Timmel, and P. J. Hore. Quantum biology. *Nature*, 453:387–390, May 2008. URL <http://dx.doi.org/10.1038/nature06834>.
- [3] N. Lambert, Y. Chen, Y. Cheng, C. Li, G. Chen, and F. Nori. Quantum biology. *Nature Phys.*, 9:10–18, January 2013. URL <http://dx.doi.org/10.1038/nphys2474>.
- [4] R Blakemore. Magnetotactic bacteria. *Science*, 190(4212):377–379, 1975. ISSN 0036-8075. doi: 10.1126/science.170679. URL <http://science.sciencemag.org/content/190/4212/377>.
- [5] D. Mattis. *The Theory of Magnetism Made Simple*. World Scientific Publishing Company, 2006.
- [6] J.C. Maxwell. On physical lines of force. *Philosophical Magazine*, 90 (sup1):11–23, 1861. doi: 10.1080/14786431003659180. URL <http://dx.doi.org/10.1080/14786431003659180>.
- [7] D.D Stancil and A. Prabhakar. *Spin Waves: Theory and Applications*.

Springer, Berlin, 2009. ISBN 978-0-387-77864-8 (Print) 978-0-387-77865-5 (Online).

- [8] P. Curie. Proprietes magnetiques des corps à diverses temperatures. *Ann. Chim. Phys.*, 5(7):289, 1895.
- [9] L. D. Landau and E. M. Lifshitz. Theory of the dispersion of magnetic permeability in ferromagnetic bodies. *Phys. Zeitsch. der Sowjetunion*, 8: 153–169, 1935.
- [10] N. Bloembergen, E. M. Purcell, and R. V. Pound. Relaxation effects in nuclear magnetic resonance absorption. *Phys. Rev.*, 73:679–712, Apr 1948. doi: 10.1103/PhysRev.73.679. URL <http://link.aps.org/doi/10.1103/PhysRev.73.679>.
- [11] Charles Kittel. Interpretation of anomalous larmor frequencies in ferromagnetic resonance experiment. *Phys. Rev.*, 71:270–271, Feb 1947. doi: 10.1103/PhysRev.71.270.2. URL <http://link.aps.org/doi/10.1103/PhysRev.71.270.2>.
- [12] J. A. Osborn. Demagnetizing factors of the general ellipsoid. *Phys. Rev.*, 67:351–357, Jun 1945. doi: 10.1103/PhysRev.67.351. URL <https://link.aps.org/doi/10.1103/PhysRev.67.351>.
- [13] J.C. Slonczewski. Current-driven excitation of magnetic multilayers. *Journal of Magnetism and Magnetic Materials*, 159(1):L1 – L7, 1996. ISSN 0304-8853. doi: [http://dx.doi.org/10.1016/0304-8853\(96\)00062-5](http://dx.doi.org/10.1016/0304-8853(96)00062-5). URL <http://www.sciencedirect.com/science/article/pii/0304885396000625>.
- [14] L. D. Landau and E. M. Lifshitz. Theory of the dispersion of magnetic permeability in ferromagnetic bodies. *Phys. Zeitsch. der Sow.*, 8:153, 1935.

- [15] C.J. Gorter. Negative result of an attempt to detect nuclear magnetic spins. *Physica*, 3(9):995–998, 1936. URL <http://www.sciencedirect.com/science/article/pii/S0031891436803243>.
- [16] I. I. Rabi, S. Millman, P. Kusch, and J. R. Zacharias. The molecular beam resonance method for measuring nuclear magnetic resonance. *Phys. Rev.*, 55:526, 1939.
- [17] E. Zavoisky. Paramagnetic relaxation of liquid solutions for perpendicular fields. *J. Phys. U.S.S.R.*, 9:211, 245, 1945.
- [18] E. M. Purcell, H. C. Torrey, and R. V. Pound. Resonance absorption by nuclear magnetic moments in a solid. *Phys. Rev.*, 69:37, 1946.
- [19] F. Bloch. Nuclear induction. *Phys. Rev.*, 70:460, 1946.
- [20] J. H. E. Griffiths. Anomalous high-frequency resistance of ferromagnetic metals. *Nature*, 158:670, 1946.
- [21] W. Wernsdorfer, B. Doudin, D. Maily, K. Hasselbach, A. Benoit, J. Meier, J. Ph. Ansermet, and B. Barbara. Nucleation of magnetization reversal in individual nanosized nickel wires. *Phys. Rev. Lett.*, 77:1873–1876, Aug 1996. doi: 10.1103/PhysRevLett.77.1873. URL <http://link.aps.org/doi/10.1103/PhysRevLett.77.1873>.
- [22] K. S. Novoselov, A. K. Geim, S. V. Dubonos, E. W. Hill, and I. V. Grigorieva. Subatomic movements of a domain wall in the peierls potential. *Nature*, 426(6968):812–816, Dec. 2003. URL <http://dx.doi.org/10.1038/nature02180>.
- [23] A. K. Geim, S. V. Dubonos, J. G. S. Lok, I. V. Grigorieva, J. C. Maan, L. Theil Hansen, and P. E. Lindelof. Ballistic hall micromagnetometry. *Applied Physics Letters*, 71(16):2379–2381, 1997. doi: 10.1063/1.120034. URL <http://dx.doi.org/10.1063/1.120034>.

- [24] H. J. Mamin, T. H. Oosterkamp, M. Poggio, C. L. Degen, C. T. Rettner, and D. Rugar. Isotope-selective detection and imaging of organic nanolayers. *Nano. Lett.*, 9:3020, 2009.
- [25] D. Rugar, H. J. Mamin, M. H. Sherwood, M. Kim, C. T. Rettner, K. Ohno, and D. D. Awschalom. Proton magnetic resonance imaging with a nitrogen-vacancy spin sensor. *Nat. Nanotechnol.*, 10:120, 2015.
- [26] J. A. Sidles, J. L. Garbini, K. J. Bruland, D. Rugar, O. Zuger, S. Hoen, and C. S. Yannoni. Magnetic resonance force microscopy. *Rev. Mod. Phys.*, 67:249, 1995.
- [27] D. Rugar, O. Zuger, S. Hoen, Yannoni, C.S., H.-M. Vieth, and R. D. Kendrick. Force detection of nuclear magnetic resonance. *Science*, 264:1560, 1994.
- [28] Z. Zhang, P. C. Hammel, M. Midzor, M. L. Roukes, and J. R. Childress. Ferromagnetic resonance force microscopy on microscopic cobalt single layer films. *Appl. Phys. Lett.*, 73:2036, 1998.
- [29] G. Alzetta, E. Arimondo, C. Ascoli, and A. Gozzini. Paramagnetic resonance experiments at low fields with angular-momentum detection. *Il Nuovo Cimento*, 52:392, 1967.
- [30] D. Rugar, C. S. Yannoni, and J. A. Sidles. Mechanical detection of magnetic resonance. *Nature*, 360:563, 1992.
- [31] C. Ascoli, P. Baschieri, C. Frediani, L. Lenci, M. Martinelli, G. Alzetta, R. M. Celli, and L. Pardi. Micromechanical detection of magnetic resonance by angular momentum absorption. *Appl. Phys. Lett.*, 69:3920, 1996.
- [32] J. E. Losby, F. Fani Sani, D. T. Grandmont, Z. Diao, M. Belov, J. A. J. Burgess, S. R. Compton, W. K. Hiebert, D. Vick, K. Moham-

- mad, E. Salimi, G. E. Bridges, D. J. Thomson, and M. R. Freeman. Torque-mixing magnetic resonance spectroscopy. *Science*, 350(6262):798–801, 2015. ISSN 0036-8075. doi: 10.1126/science.aad2449. URL <http://science.sciencemag.org/content/350/6262/798>.
- [33] Z. Diao, J. E. Losby, J. A. J. Burgess, V. T. K. Sauer, W. K. Hiebert, and M. R. Freeman. Stiction-free fabrication of lithographic nanostructures on resist-supported nanomechanical resonators. *J. Vac. Sci. Technol. B.*, 31:051805, 2013.
- [34] J. E. Losby, Z. Diao, F. Fani Sani, D. T. Grandmont, M. Belov, J. A. J. Burgess, W. K. Hiebert, and M. R. Freeman. Nanomechanical ac susceptibility of an individual mesoscopic ferrimagnet. *Solid State Commun.*, 198:3, 2014.
- [35] T. Firdous, D. Vick, M. Belov, F. Fani Sani, A. McDermott, J. E. Losby, D. A. Bazylinski, T. Prozorov, D. K. Potter, and M. R. Freeman. Nanomechanical torque magnetometry of an individual aggregate of 350 nanoparticles. *Can. J. Phys.*, 93:1–5, 2015.
- [36] H. Barkhausen. *Phys. Z.*, 20:401, 1919.
- [37] T. Y. Chen, M. J. Erickson, and P. A. Crowell. Surface roughness dominated pinning mechanism of magnetic vortices in soft ferromagnetic films. *Phys. Rev. Lett.*, 109:097202, 2012.
- [38] T. Y. Chen, A. T. Galkiewicz, and P. A. Crowell. Phase diagram of magnetic vortex dynamics. *Phys. Rev. B*, 85:180406, May 2012. doi: 10.1103/PhysRevB.85.180406. URL <http://link.aps.org/doi/10.1103/PhysRevB.85.180406>.
- [39] Stuart S. P. Parkin, Masamitsu Hayashi, and Luc Thomas. Magnetic domain-wall racetrack memory. *Science*, 320(5873):190–194, 2008.

ISSN 0036-8075. doi: 10.1126/science.1145799. URL <http://science.sciencemag.org/content/320/5873/190>.

- [40] R. L. Compton and P. A. Crowell. Dynamics of a pinned magnetic vortex. *Phys. Rev. Lett.*, 97(137202), 2006.
- [41] H. Shima, V. Novosad, Y. Otani, K. Fukamichi, N. Kikuchi, O. Kitakamai, and Y. Shimada. Pinning of magnetic vortices in microfabricated permalloy dot arrays. *J. Appl. Phys.*, 92:1473, 2002.
- [42] John Moreland. Micromechanical instruments for ferromagnetic measurements. *Journal of Physics D: Applied Physics*, 36(5):R39, 2003. URL <http://stacks.iop.org/0022-3727/36/i=5/a=201>.
- [43] J P Davis, D Vick, J A J Burgess, D C Fortin, P Li, V Sauer, W K Hiebert, and M R Freeman. Observation of magnetic supercooling of the transition to the vortex state. *New Journal of Physics*, 12(9):093033, 2010. URL <http://stacks.iop.org/1367-2630/12/i=9/a=093033>.
- [44] J. A. J. Burgess, A. E. Fraser, F. Fani Sani, D. Vick, B. D.. Hauer, J. P. Davis, and M. R. Freeman. Quantitative magneto-mechanical detection and control of the barkhausen effect. *Science*, 339:1051, 2013.
- [45] Zurich Instruments model UHF lock-in amplifier with MF and MOD options (<http://www.zhinst.com>).
- [46] S.-H. Chung, R. D. McMichael, D. T. Pierce, and J. Unguris. Phase diagram of magnetic nanodisks measured by scanning electron microscopy with polarization analysis. *Phys. Rev. B*, 81:024410, Jan 2010. doi: 10.1103/PhysRevB.81.024410. URL <http://link.aps.org/doi/10.1103/PhysRevB.81.024410>.
- [47] F. Fani Sani, J. E. Losby, Z. Diao, L. C. Parsons, J. A. J. Burgess, D. Vick, and M. R. Hiebert, W. K. and Freeman. Strong vortex core pinning and

- barkhausen-free magnetization response in thin permalloy disks induced by implantation of 1×10^4 ga^+ ions. *J. Appl. Phys.*, 115:17D131, 2014.
- [48] A. Wachowiak, J. Wiebe, M. Bode, O. Pietzsch, M. Morgenstern, and R. Wiesendanger. Direct observation of internal spin structure of magnetic vortex cores. *Science*, 298(5593):577–580, 2002. ISSN 0036-8075. doi: 10.1126/science.1075302. URL <http://science.sciencemag.org/content/298/5593/577>.
- [49] Thomas Uhlig, M. Rahm, Christian Dietrich, Rainer Höllinger, Martin Heumann, Dieter Weiss, and Josef Zweck. Shifting and pinning of a magnetic vortex core in a permalloy dot by a magnetic field. *Phys. Rev. Lett.*, 95:237205, Nov 2005. doi: 10.1103/PhysRevLett.95.237205. URL <http://link.aps.org/doi/10.1103/PhysRevLett.95.237205>.
- [50] R. P. Cowburn, D. K. Koltsov, A. O. Adeyeye, and M. E. Welland. Designing nanostructured magnetic materials by symmetry. *EPL (Europhysics Letters)*, 48(2):221, 1999. URL <http://stacks.iop.org/0295-5075/48/i=2/a=221>.
- [51] J. A. J. Burgess, D. C. Fortin, J. E. Losby, D. Grombacher, J. P. Davis, and M. R. Freeman. Thermally activated decay of magnetic vortices. *Phys. Rev. B*, 82:144403, 2010.
- [52] M Rahm, R Höllinger, V Umanski, and Dieter Weiss. Influence of point defects on magnetic vortex structures. *Journal of Applied Physics*, 95:6708, 2004. URL <http://epub.uni-regensburg.de/7927/>.
- [53] M. Rahm, J. Stahl, W. Wegscheider, and D. Weiss. Multistable switching due to magnetic vortices pinned at artificial pinning sites. *Applied Physics Letters*, 85(9):1553–1555, 2004. doi: <http://dx.doi.org/10.1063/1.1785281>. URL <http://scitation.aip.org/content/aip/journal/apl/85/9/10.1063/1.1785281>.

- [54] G. Mihajlović, M. S. Patrick, J. E. Pearson, V. Novosad, S. D. Bader, M. Field, G. J. Sullivan, and A. Hoffmann. Temperature dependent nucleation and annihilation of individual magnetic vortices. *Applied Physics Letters*, 96(11):112501, 2010. doi: <http://dx.doi.org/10.1063/1.3360841>. URL <http://scitation.aip.org/content/aip/journal/apl/96/11/10.1063/1.3360841>.
- [55] J. A. J. Burgess, J. E. Losby, and M. R. Freeman. An analytical model for vortex core pinning in a micromagnetic disk. *J. Magn. Magn. Mater.*, 361:140, 2014.
- [56] J. Fassbender and J. McCord. Magnetic patterning by means of ion irradiation and implantation. *Journal of Magnetism and Magnetic Materials*, 320:579, 2008.
- [57] A. Vogel, S. Wintz, T. Gerhardt, L. Bocklage, T. Strache, M.-Y. Im, P. Fischer, J. Fassbender, J. McCord, and G. Meier. Field- and current-induced domain-wall motion in permalloy nanowires with magnetic soft spots. *Appl. Phys. Lett.*, 98:202501, 2011.
- [58] N.A. Usov and S.E. Peschany. Magnetization curling in a fine cylindrical particle. *Journal of Magnetism and Magnetic Materials*, 118(3):L290 – L294, 1993. ISSN 0304-8853. doi: [http://dx.doi.org/10.1016/0304-8853\(93\)90428-5](http://dx.doi.org/10.1016/0304-8853(93)90428-5). URL <http://www.sciencedirect.com/science/article/pii/0304885393904285>.
- [59] A. Hubert and R. Schäfer. *Magnetic Domains: The Analysis of Magnetic Microstructures*. Springer, 1998.
- [60] T. Devolder and H. Bernas. Magnetic properties and ion beams: Why and how. *Topics in Applied Physics*, 116:227, 2010.
- [61] J. H. Franken, H. J. M. Swagten, and B. Koopmans. Shift registers based

on magnetic domain wall ratchets with perpendicular anisotropy. *Nat. Nanotechnol.*, 7:499, 2012.

- [62] J. P. Park, P. Eames, D. M. Engebretson, J. Berezovsky, and P. A. Crowell. Imaging of spin dynamics in closure domain and vortex structures. *Phys. Rev. B*, 67:020403, 2003.
- [63] J. P. Park and P. A. Crowell. Interactions of spin waves with a magnetic vortex. *Phys. Rev. Lett.*, 95:167201, Oct 2005. doi: 10.1103/PhysRevLett.95.167201. URL <http://link.aps.org/doi/10.1103/PhysRevLett.95.167201>.
- [64] V. Novosad, F. Y. Fradin, P. E. Roy, K. S. Buchanan, K. Yu. Guslienko, and S. D. Bader. Magnetic vortex resonance in patterned ferromagnetic dots. *Phys. Rev. B*, 72:024455, Jul 2005. doi: 10.1103/PhysRevB.72.024455. URL <http://link.aps.org/doi/10.1103/PhysRevB.72.024455>.
- [65] C. E. Zaspel, B. A. Ivanov, J. P. Park, and P. A. Crowell. Excitations in vortex-state permalloy dots. *Phys. Rev. B*, 72:024427, Jul 2005. doi: 10.1103/PhysRevB.72.024427. URL <http://link.aps.org/doi/10.1103/PhysRevB.72.024427>.
- [66] A. A. Thiele. Steady-state motion of magnetic domains. *Phys. Rev. Lett.*, 30:230–233, Feb 1973. doi: 10.1103/PhysRevLett.30.230. URL <http://link.aps.org/doi/10.1103/PhysRevLett.30.230>.
- [67] K. Yu. Guslienko, B. A. Ivanov, V. Novosad, Y. Otani, H. Shima, and K. Fukamichi. Eigenfrequencies of vortex state excitations in magnetic submicron-size disks. *Journal of Applied Physics*, 91(10):8037–8039, 2002. doi: <http://dx.doi.org/10.1063/1.1450816>. URL <http://scitation.aip.org/content/aip/journal/jap/91/10/10.1063/1.1450816>.

- [68] O. V. Sukhostavets, B. Pigeau, S. Sangiao, G. de Loubens, V. V. Naletov, O. Klein, K. Mitsuzuka, S. Andrieu, F. Montaigne, and K. Y. Guslienko. Probing the anharmonicity of the potential well for a magnetic vortex core in a nanodot. *Phys. Rev. Lett.*, 111:247601, 2013.
- [69] S.-B. Choe, Y. Acremann, A. Scholl, A. Bauer, A. Doran, J. Stöhr, and H. A. Padmore. Vortex core-driven magnetization dynamics. *Science*, 304(5669):420–422, 2004. ISSN 0036-8075. doi: 10.1126/science.1095068. URL <http://science.sciencemag.org/content/304/5669/420>.
- [70] T. Y. Chen. *Magnetic vortex dynamics: non-linear dynamics, pinning mechanisms, and dimensionality crossover*. PhD thesis, University of Minnesota, 2012.
- [71] J. Ding, G. N. Kakazei, X. M. Liu, K. Y. Guslienko, and A. O. Adeyeye. Intensity inversion of vortex gyrotropic modes in thick ferromagnetic nanodots. *Appl. Phys. Lett.*, 105:192405, 2014.
- [72] A. Dussaux, B. Georges, J. Grollier, V. Cros, A. V. Khvalkovskiy, A. Fukushima, M. Konoto, H. Kubota, K. Yakushiji, S. Yuasa, K. A. Zvezdin, K. Ando, and A. Fert. Large microwave generation from current-driven magnetic vortex oscillators in magnetic tunnel junctions. *Nature Commun.*, 1:8, Apr 2010. URL <http://dx.doi.org/10.1038/ncomms1006>.
- [73] V. S. Pribiag, I. N. Krivorotov, G. D. Fuchs, P. M. Braganca, O. Ozatay, J. C. Sankey, D. C. Ralph, and R. A. Buhrman. Magnetic vortex oscillator driven by d.c. spin-polarized current. *Nature Phys.*, 3(7):498–503, Jul 2007. ISSN 1745-2473. doi: 10.1038/nphys619. URL <http://dx.doi.org/10.1038/nphys619>.
- [74] R. L. Compton, T. Y. Chen, and P. A. Crowell. Magnetic vortex dynamics in the presence of pinning. *Phys. Rev. B*, 81:144412, Apr 2010. doi: 10.

1103/PhysRevB.81.144412. URL <http://link.aps.org/doi/10.1103/PhysRevB.81.144412>.

- [75] C. E. Zaspel. Gyrotropic frequencies of pinned vortices in magnetic nanodisks. *Phys. Rev. B*, 87:134425, Apr 2013. doi: 10.1103/PhysRevB.87.134425. URL <http://link.aps.org/doi/10.1103/PhysRevB.87.134425>.
- [76] Polder, D. On the theory of ferromagnetic resonance. *Phil. Mag.*, 40:99, 1949.
- [77] C. E. Patton. *Magnetic Oxides*. Wiley, 1975.
- [78] C. P Slichter. *Principles of Magnetic Resonance*. Springer-Verlag, 2 edition, 1980.
- [79] S. S. Kalarickal, P. Krivosik, M. Wu, C. E. Patton, M. L. Kabos P. Schneider, T. J. Silva, and J. P. Nibarger. Ferromagnetic resonance linewidth in metallic thin films: Comparison of measurement method. *J. Appl. Phys.*, 99:093909, 2006.
- [80] F. Bloch, W. W. Hansen, and W. Packard. The nuclear induction experiment. *Phys. Rev.*, 70:474, 1946.
- [81] T. Kikkawa, K. Uchida, Y. Shiomi, Z. Qiu, D. Hou, D. Tian, H. Nakayama, X. F. Jin, and Saitoh. Longitudinal spin seebeck effect free from the proximity nernst effect. *Phys. Rev. Lett.*, 110:067207, 2013.
- [82] B. Heinrich, C. Burrowes, E. Montoya, B. Kardasz, E. Girt, Y-Y. Song, Y. Sun, and M. Wu. Spin pumping at the magnetic insulator (yig)/normal metal (au) interfaces. *Phys. Rev. Lett.*, 107:066604, 2011.
- [83] J. Flipse, F. L. Bakker, A. Slachter, F. K. Dejene, and B. J. van Wees. Direct observation of the spin-dependent peltier effect. *Nat. Nanotechnol.*, 7:166, 2013.

- [84] C. Hahn, G. de Loubens, M. Viret, O. Klein, V. V. Naletov, and J. Ben Youssef. Detection of microwave spin pumping using the inverse spin hall effect. *Phys. Rev. Lett.*, 111:217204, 2013.
- [85] A. A. Serga, A. V. Chumak, and B. Hillebrands. Yig magnonics. *J. Phys. D: Appl. Phys.*, 4:264002, 2010.
- [86] Shin Etsu Chemical Corporation Lot Number SEW-3571.
- [87] R. P. Cowburn, D. K. Koltsov, A. O. Adeyeye, M. E. Welland, and D. M. Tricker. Single-domain circular nanomagnets. *Phys. Rev. Lett.*, 83:1042, 1999.
- [88] M. Rahm, M. Schneider, J. Biberger, R. Pulwey, J. Zweck, D. Weiss, and Umansky V. Vortex nucleation in submicrometer ferromagnetic disks. *Appl. Phys. Lett.*, 82:4110, 2003.
- [89] F. Guo, L. M. Belova, and R. D. McMichael. Spectroscopy and imaging of edge modes in permalloy nanodisks. *Phys. Rev. Lett.*, 110:017601, 2013.
- [90] G. Woltersdorf and C. H. Back. Microwave assisted switching of single domain ni(80)fe(20) elements. *Phys. Rev. Lett.*, 99:227207, 2007.
- [91] Y. Nozaki, M. Ohta, S. Taharazako, K. Tateishi, S. Yoshimura, and K. Matsuyama. Magnetic force microscopy study of microwave-assisted magnetization reversal in submicron-scale ferromagnetic particles. *Appl. Phys. Lett.*, 91:082510, 2007.
- [92] S. Wintz, C. Bunce, A. Neudert, M. K'orner, T. Strache, M. Buhl, A. Erbe, S. Gemming, J. Raabe, Quitmann, C., and J. Fassbender. Topology and origin of effective spin meron pairs in ferromagnetic multilayer elements. *Phys. Rev. Lett.*, 110:177201, 2013.
- [93] C. Kittel. On the theory of ferromagnetic resonance absorption. *Phys. Rev.*, 73:155, 1948.

- [94] B A Kalinikos and A N Slavin. Theory of dipole-exchange spin wave spectrum for ferromagnetic films with mixed exchange boundary conditions. *Journal of Physics C: Solid State Physics*, 19(35):7013, 1986. URL <http://stacks.iop.org/0022-3719/19/i=35/a=014>.
- [95] G. N. Kakazei, P.E. Wigen, K. Yu. Guslienko, V. Novosad, A.N. Slavin, V.O. Golub, N.A. Lesnik, and Y. Otani. Spin-wave spectra of perpendicularly magnetized circular submicron dot arrays. *Appl. Phys. Lett.*, 85:443, 2016.
- [96] B. Taurel, T. Valet, V. V. Naletov, N. Vukadinovic, G. de Loubens, and O. Klein. Complete mapping of the spin-wave spectrum in a vortex-state nanodisk. *Phys. Rev. B*, 93:184427, May 2016. doi: 10.1103/PhysRevB.93.184427. URL <http://link.aps.org/doi/10.1103/PhysRevB.93.184427>.
- [97] V. Castel, J. Ben Youssef, F. Boust, R. Weil, B. Pigeau, G. de Loubens, V. V. Naletov, O. Klein, and N. Vukadinovic. Perpendicular ferromagnetic resonance in soft cylindrical elements: Vortex and saturated states. *Phys. Rev. B*, 85:184419, May 2012. doi: 10.1103/PhysRevB.85.184419. URL <http://link.aps.org/doi/10.1103/PhysRevB.85.184419>.
- [98] Xufeng Zhang, Chang-Ling Zou, Liang Jiang, and Hong X. Tang. Cavity magnomechanics. *Science Advances*, 2(3), 2016. doi: 10.1126/sciadv.1501286. URL <http://advances.sciencemag.org/content/2/3/e1501286>.
- [99] Marcelo Wu, Nathanael L. Y. Wu, Tayyaba Firdous, Fatemeh Fani Sani, Joseph E. Losby, Mark R. Freeman, and Paul E. Barclay. Nanocavity optomechanical torque magnetometry and radiofrequency susceptometry. *Nat. Nano.*, 12:127–131, 2017.

- [100] S-H. Lim, A. Imtiaz, T. M. Wallis, S. Russek, P. Kabos, L. Cai, and E. M. Chudnovsky. Magneto-mechanical investigation of spin dynamics in magnetic multilayers. *Europhys. Lett.*, 105:37009, 2014.
- [101] S.T.B. Goennenwein, S. Maekawa, G.E.W. Bauer, and Eds. Spin mechanics. *Solid State Commun.*, 198, 2014. Special Issue: Spin Mechanics.
- [102] N. Bloembergen and R. W. Damon. Relaxation effects in ferromagnetic resonance. *Phys. Rev.*, 85:699–699, Feb 1952. doi: 10.1103/PhysRev.85.699. URL <http://link.aps.org/doi/10.1103/PhysRev.85.699>.
- [103] R. W. Damon. Relaxation effects in the ferromagnetic resonance. *Rev. Mod. Phys.*, 25:239–245, Jan 1953. doi: 10.1103/RevModPhys.25.239. URL <http://link.aps.org/doi/10.1103/RevModPhys.25.239>.
- [104] N. Bloembergen and S. Wang. Relaxation effects in para- and ferromagnetic resonance. *Phys. Rev.*, 93:72–83, Jan 1954. doi: 10.1103/PhysRev.93.72. URL <http://link.aps.org/doi/10.1103/PhysRev.93.72>.
- [105] M. R. Scheinfein. Llg micromagnetic simulator version 2.46 (llgmicro@mindspring.com).
- [106] M. J. Donahue and D. G. Porter. Oommf user’s guide, version 1.0. inter-agency report nistir 6376, national institute of standards and technology, gaithersburg, md. 1999.
- [107] A. Vansteenkiste, J. Leliaert, M. Dvornik, M. Helsen, F. Garcia-Sanchez, and B. Van de Wiele. The design and verification of mumax3. *AIP Adv.*, 4:107133, 2014.
- [108] W. Scholz, J. Fidler, T. Schre, D. Suess, R. Dittrich, H. Forster, and V. Tsiantos. Scalable parallel micromagnetic solvers for magnetic nanostructures. *Comput. Mater. Sci.*, 23:366, 2003. URL <http://www.magpar.net>.

- [109] T. Fischbacher, M. Franchin, G. Bordignon, and H. Fangohr. A systematic approach to multiphysics extensions of finite-element-based micromagnetic simulations: Nmag. *IEEE Transactions On Magnetics*, 43: 2896–2898, 2007.
- [110] The go programming language,. 2009. URL <http://golang.org>.
- [111] A. V. Oppenheim, R. W. Schaffer, and J. R. Buck. *Discrete-Time Signal Processing*. Prentice Hall, Inc., Upper Saddle River, NJ, 1999.
- [112] G. F. Dionne. *Magnetic Oxides*. Springer, New York, 2009.
- [113] J. Losby, J.A.J. Burgess, Z. Diao, D.C. Fortin, W.K. Hiebert, and M.R. Freeman. Thermo-mechanical sensitivity calibration of nanotorsional magnetometers. *Journal of Applied Physics*, 111(7):07D305, 2012. doi: 10.1063/1.3676231. URL <http://dx.doi.org/10.1063/1.3676231>.
- [114] W. W. Clegg, N. A. E. Heyes, E. W. Hill, and C. D. Wright. Development of a scanning laser microscope for magneto-optic studies of thin magnetic films. *J. Magn. Magn. Mater.*, 95:49, 1991.
- [115] A. Banholzer, R. Narkowicz, C. Hassel, R. Meckenstock, S. Stienen, O. Posth, D. Suter, M. Farle, and J. Lindner. Visualization of spin dynamics in single magnetic elements. *Nanotechnology*, 22:295713, 2011.
- [116] P. H. Kim, C. Doolin, B. D. Hauer, A. J. R. MacDonald, M. R. Freeman, P. E. Barclay, and Davis. Nanoscale torsional op. *Appl. Phys. Lett.*, 102: 053102, 2013.
- [117] M. Wu, A. C. Hryciw, C. Healey, J. Harishankar, M. R. Freeman, J. P. Davis, and P. E. Barclay. Dissipative and dispersive optomechanics in a nanocavity torque sensor. *Phys. Rev. X*, 4:021052, 2014.
- [118] S. Khizroev and D. Litvinov. Focused-ion-beam-based rapid prototyping of nanoscale magnetic devices. *Nanotechnology*, 15:R7, 2004.

- [119] A. E. Fraser. Focus ion beam milled magnetic cantilevers. Master's thesis, University of Alberta, 2010.
- [120] J. H. Van Vleck. Primitive theory of ferrimagnetic resonance frequencies in rare-earth iron garnets. *Phys. Rev.*, 123:58–62, Jul 1961. doi: 10.1103/PhysRev.123.58. URL <https://link.aps.org/doi/10.1103/PhysRev.123.58>.
- [121] Wilhelm H. Von Aulock. *Handbook of Microwave Ferrite Materials*. Academic Press Inc., New York and London, 1965.
- [122] J. Fassbender and J. McCord. Control of saturation magnetization, anisotropy, and damping due to ni implantation in thin ni81fe19 layers. *Applied Physics Letters*, 88(25):252501, 2006. doi: 10.1063/1.2213948. URL <http://dx.doi.org/10.1063/1.2213948>.
- [123] L. Yaohai, X. Feng, X. Zhang, Y. Shen, and D. Wang. Effects of bi doping on structural and magnetic properties of double perovskite oxides sr2femoo6. *Physics Letters A*, 380(37):2962 – 2967, 2016. ISSN 0375-9601. doi: <http://doi.org/10.1016/j.physleta.2016.06.057>. URL <http://www.sciencedirect.com/science/article/pii/S0375960116303966>.

Appendices

Appendix A

Micromagnetic simulation - Methods

We performed micromagnetic simulations to identify the equilibrium magnetization configurations (spin textures) and spin-dynamical modes in magnetic structures. There are several platforms for micromagnetic simulations such as the LLG micromagnetic simulator, developed by M.R. Scheinfein [105]; NIST open source code, object oriented micromagnetic framework (OOMMF) [106]; mumax, a GPU-accelerated micromagnetic simulation program developed at Ghent University [107]; MagPar, Parallel Finite Element Micromagnetics Package [108]; and Nmag, suitable for non-cuboidal structures [109].

In 2012 I started working with LLG micromagnetic simulator (version 2.46) developed by M.R. Scheinfein. A couple of months later I began working with mumax version 2. The speed of simulation runs on mumax was extraordinary, at least 100 times faster than the former CPU-based platform. Moreover, memory usage has been optimized in mumax in such a way that the software can handle about 16 million cells within 2GB of GPU RAM. In this thesis, mumax has been dominantly used for micromagnetic simulations, including all the results presented in this chapter. mumax is run on an nVIDIA GeForce GTX TITAN with double-precision floating-point format.

All the micromagnetic simulation techniques have similar principles, which are based on the dynamic integration of the Landau-Lifshitz-Gilbert (LLG) equation of motion [9]. The LLG equation is a finite difference time domain problem. A magnetic structure is divided into discrete cells with constant magnetization and a given direction is considered at the center of each cell. The coupling quantities such as the exchange constant are updated in a neighbouring approach on the faces between the cells, so at each time every cell is updated from the initial condition, and each cell is independent from the far cells; that is why it is possible to run these simulations on the GPU system for faster results.

In the following sections, general parameters in simulation are presented, usually with the simulation representatives. Some case studies are described to provide a detailed understanding of related experimental investigations. The chapter concludes with sample codes to show how to execute the program.

A.1 General parameters

In mumax, a Go programming language scripting[110] has been used to describe simple to complicated simulations. The first parameters to consider are the geometry-related parameters including the discretization factor or cell size and the total number of cells. The cells can be orthorhombics in a 3D structure. For accurate results, the cell size must be smaller than the exchange length, $l_{ex} = \sqrt{\frac{2A_{ex}}{\mu_0 M_s^2}}$, in which the A_{ex} is the exchange constant and M_s is the saturation magnetization (SI units). Although any combination can be used for the total number of cells, to speed up the computing time, the total number should contain one prime number multiplied by powers of two such as 1×2^n , 3×2^n , 5×2^n . The dimensions in simulation that are obtained should be justified by the total cell number multiplied by the the cell size.

In the case of Cartesian meshing, there is a staircase instead of a smooth

boundary for a magnetic structure. In some cases, the staircase boundaries add unwanted pinning sites to the structure that would make it difficult find the equilibrium magnetization and calculate the dynamical modes. There is a command in mumax that smooths the boundary

A.1.1 Saturation magnetization

Saturation magnetization is a material-related property and its value for a specific magnetic material is usually obtained from experimental measurements such as torque magnetometry or Brillouin light scattering (BLS) experiments, and is usually tabulated. This value is used to determine the maximum moment aligned with the external field. Beyond the corresponding field the magnetization cannot be increased. Furthermore, saturation magnetization is a temperature-dependent function, and for a specific temperature, the Currie temperature, reaches zero.

A.1.2 Exchange constant

The exchange constant, A_{ex} , is considered as a positive value for ferromagnets (FM) and negative value for anti-ferromagnets (AF), besides Ruderman-Kittel-Kasuya-Yosida (RKKY) interaction. For AF, atomic resolution is needed, but resolution lower than the exchange length is sufficient for FM (exchange length $l_{ex} = \sqrt{\frac{2A_{ex}}{\mu_0 M_s^2}}$). For instance, in Py material the exchange length at room temperature ($M_s = 780$ kA/m) is calculated to be 5.72 nm, and in YIG material the exchange length is around 12 nm.

A.1.3 Magnetic anisotropy

The magnetic anisotropy can be manifested through the directional dependence of magnetic crystalline with the applied field. That means the magnetization aligns along some easy axes that are energetically more favourable. In a case

of no anisotropy, the equilibrium magnetization will always be aligned with the applied field. Another anisotropy term is the shape anisotropy, which is quite different. The shape anisotropy is usually considered by calculating demagnetization factors (dipolar effect).

In Py structures the crystalline anisotropy is neglected because of small values. However, in a YIG disk, we consider the cubic anisotropy with three axes. Because the anisotropy constant is negative for YIG, the axes are hard axes. Moreover, because the axes are obtained from a cross-product relationship, a determination of only two axes out of three is sufficient. Note that in mumax, we always insert the easy axis.

To investigate the effect of in-plane field rotation and the directional dependence of magnetization, we selected a YIG disk with cubic anisotropy. The simulations started from the ground state (3D vortex), and then the applied in-plane magnetic field in a specific direction was swept from zero to high field to annihilate the vortex state. The simulation parameters for a YIG disk are: the cell size $6.25\text{nm} \times 6.25\text{nm} \times 6.25\text{nm}$, $M_s = 140 \text{ kA/m}$ and $A_{ex} = 2 \text{ p(J/m)}$, and the cubic anisotropy with $K_c = -610 \text{ J/m}^3$. The hard axes are determined in such a way to make the easy axis in a z-direction: $c_1 = (-0.4085, 0.7075, 0.5774)$, $c_2 = (-0.8165, 0.7075, 0.5774)$, and $c_3 = c_1 \times c_2$.

Figure A.1 shows a high field responses (close to vortex annihilation) with groupings in similar directions. It is very hard to see the similarities of the grouped traces; therefore a subtraction of a linear fit is considered to highlight the differences at each field angle. The residuals of the linear fit are plotted on a polar graph in Figure A.1 and show a directional dependent of magnetization versus an in-plane angle of the applied field.

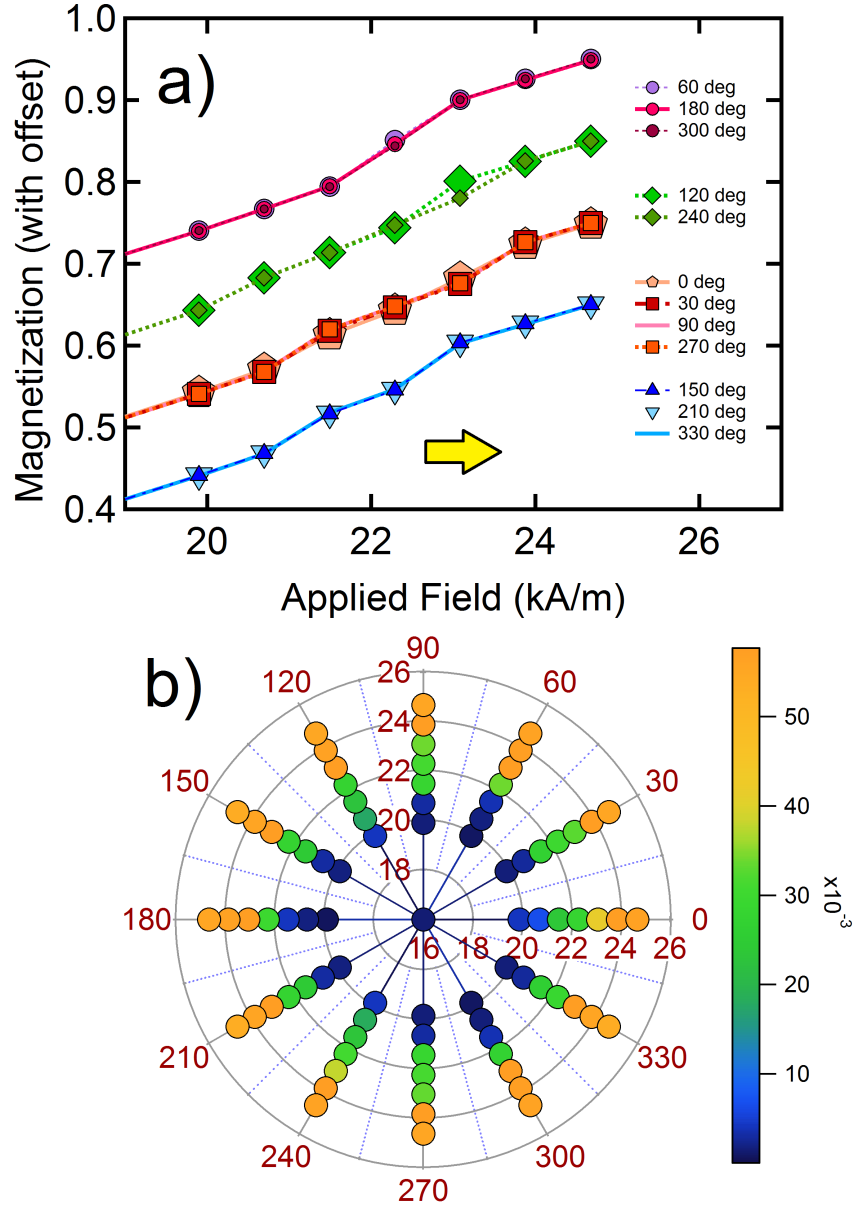


Figure A.1: Simulation of in-plane magnetic field sweeps in a $1.2 \mu\text{m}$ diameter and 500 nm thick YIG disk with cubic anisotropy. a) The magnetization responses are shown for the in-plane field angle with steps of 30° , which are grouped based on similarities. The field sweep is performed from a low field with the 3D vortex state (ground state) to obtain the vortex annihilation, and the sweep direction is shown with the yellow arrow. b) The subtracted magnetization responses from a linear fit are presented in polar diagram with field range of 16-26 kA/m.

In the other example, we show the effect of uniform anisotropy in magnetite nanoparticles. The mask is obtained from a SEM image of a device with

aggregated magnetite nanoparticles deposited on an Si_3N_4 membrane. The simulation parameters are cell size $3\text{nm} \times 3\text{nm} \times 3\text{nm}$, $M_s = 480 \text{ kA/m}$ and $A_{ex} = 13.3 \text{ pJ/m}$. Increasing the anisotropy shows a tendency for magnetization to be in specific direction, and as a result creates a bigger loop. In comparison to experimental data, the case without any anisotropy is a better match.

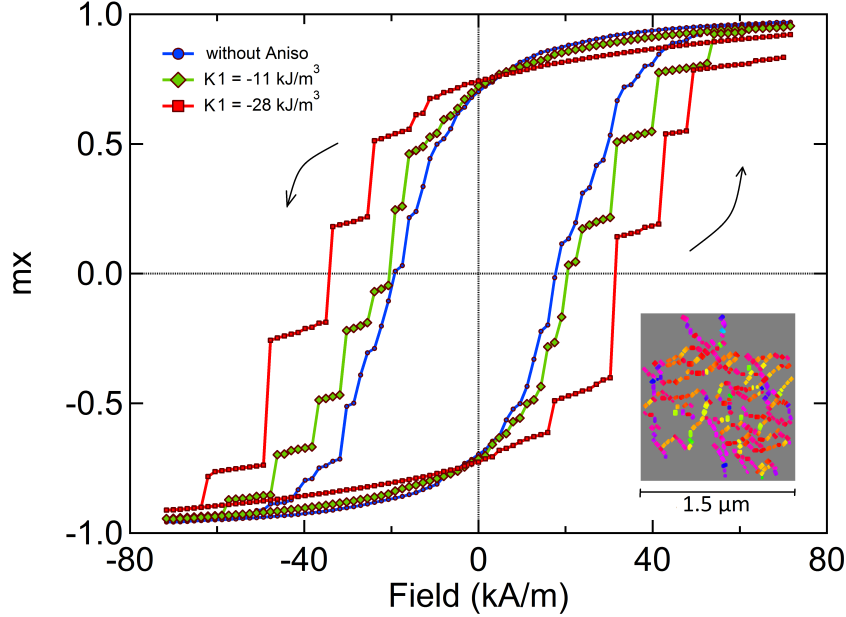


Figure A.2: The effect of anisotropy in a masked magnetite nanoparticles. The hysteresis loops of a structure with two uniaxial anisotropy values (red and green curves) are shown along with a response of the same structure without any anisotropy (blue curve). The lower left inset shows the magnetization profile of magnetite nanoparticles at $H_x = 0$ in a field sweep down.

A.1.4 Temperature

One option to make the simulation result more closely resemble the experiment is to consider the finite temperature in the system. The random thermal fluctuations are not included in the LLG equation. However, in mumax a finite temperature is provided by considering the fluctuating thermal field, which is related to the square root of the temperature. The default value for the temperature in mumax is $T = 0 \text{ K}$. Therefore the thermal field is zero. The option

to use finite temperature in mumax comes with a constraint of selecting the proper solver like Euler or Heun . Either of which enables using the fixed time steps, usually 1-10 fs.

An example of the temperature effect in the nanoparticle system is considered here, as shown in Figure A.3. The high temperature, washed out the jumps in the magnetization response creating a smoother curve for the magnetization characterization.

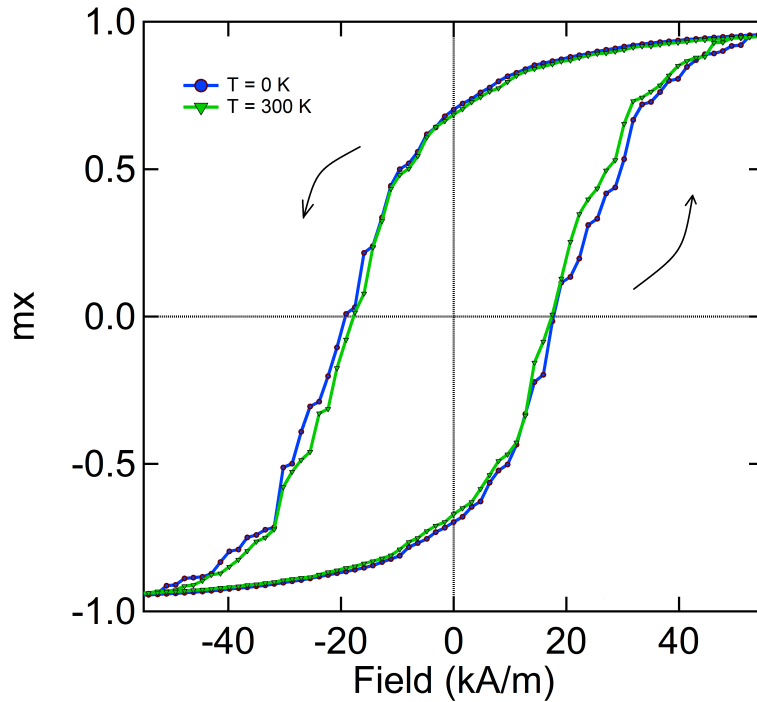


Figure A.3: Temperature effect on masked nanoparticles without anisotropy. Two temperatures of $T = 0\text{ K}$ (default) and $T = 300\text{ K}$, corresponding to the experimental condition, are presented.

A.1.5 Initial magnetization

Selecting an initial magnetization is very important to obtain the correct results – sometimes there are multiple ground states or local minimum potentials which can mislead the system into choosing the incorrect state. Depending on the shape and geometry of a structure and the applied field, some well-known

initial conditions exist. These include uniform, vortex, two domain, random magnetization, vortex wall, bloch-skyrmion, Néel-skyrmion.

When the magnetization equilibrium is disturbed because of a change in the external field or temperature, a torque term tries to align the magnetization to the new equilibrium state. There are different convergence criteria in simulation. One is to set the running time as a large number, about nano-second scale, to make sure all the ring-downs are settled. Another is to establish a maximum torque limit, which is more accurate in many cases. The latter is usually used to find quasi-static responses as in states in a hysteresis loop. The former is used when it is necessary to obtain spin dynamics in the magnetic structure.

The magnetic parameters for some magnetic materials that have been used in simulation are summarized in the following table.

Magnetic Material	Saturation Magnetization	Exchange Constant	Exchange Length	Anisotropy Constant
	M_s , kA/m	A_{ex} , pJ/m	l_{ex} , nm	K, J/m ³
Py	850	13	5.35	~ 0
YIG	140	2	12.74	-610
Magnetite (nParticles)	480	13.3	9.59	0

Table A.1: Magnetization properties of materials used in simulation.

A.2 Spin dynamics

To obtain the dynamical response, one can apply a time-variant magnetic field to a magnetic structure. The field can be spatially confined too, but we ignore it for now because in our experimental setup a uniform radio-frequency (RF) field is provided.

We utilize a time-domain approach in simulation, although in the laboratory we capture the spectrum of resonance response directly in frequency domain by sweeping the RF frequencies at a constant external field. In the time-domain approach, an RF pulse with a specific width. The frequency bandwidth of the pulse is inversely related to the pulse width. Then the magnetic spectrum at a given external dc field can be obtained from a Fast Fourier transform (FFT) of the time evolution of magnetization, normalized to that of the applied pulse.

Two main time-domain parameters that affect the frequency domain results are the total time span and sampling rate. The frequency resolution comes from the total time, $\Delta f = 1/t_{total}$. In contrast to the experiment, in which the frequency resolution can be decreased to less than 1 MHz, in simulation a long evolution of time is needed to achieve such a fine frequency resolution.

The total time span of 1 μ sec makes the frequency resolution around 1 MHz. One of the fine frequency/field resolution spectrum presented in Chapter 3 was taken at around two days. However, in simulation it took around two weeks to obtain the result with similar resolutions, even with running fast GPUs. One might think that a time span of 1 μ sec in simulation should not take that long, but the time sampling is chosen at around 10^{-12} second.

Another important variable is the total sample equal to total time/sampling rate. In the FFT procedure, the total sample should be rounded to the next power of 2. The more samples that are collected, the more accurate the spectrum will be.

A.2.1 Adjusting the RF pulse excitation

The Fourier transform of any rectangular pulse is a sinc function ($sinc(\theta) = \frac{\sin \theta}{\theta}$, with θ in radians), in which there are periodic nodes corresponding to the nodes of the sinusoidal function. The node positions in frequency domain are inversely related to the pulse width, as shown in Figure A.4. Therefore, the pulse width should be chosen in such a way as to cover experimentally

accessible frequency ranges.

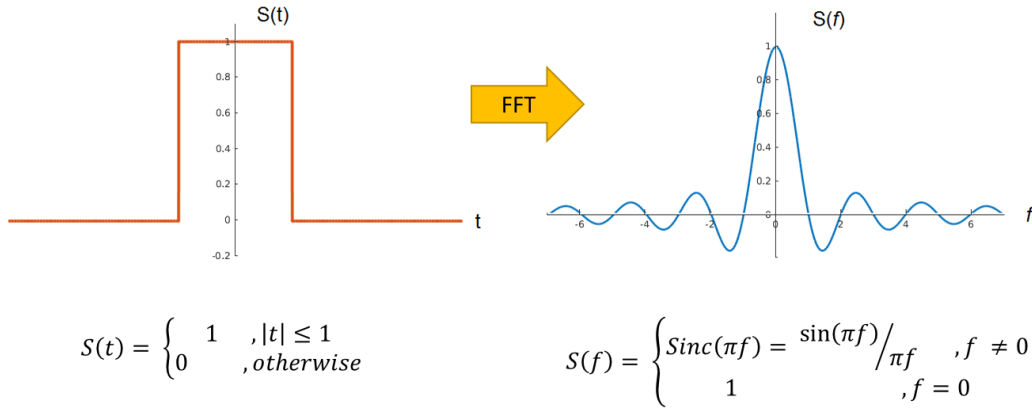


Figure A.4: A time-domain pulse and its Fourier transform. The frequency domain response corresponds to a Sinc function, in which the nodes' positions are related to the pulse width T .

The drive bandwidth of a pulse has an inverse relation with the pulse width ($1/t_{width}$, corresponds to the frequency of the first node). The pulse width of 1.43 ns provides a frequency range of dc to 700 MHz; for the higher frequency range, a lower pulse width should be chosen.

The pulse width can be considered as a relative phase of tones, at which the constructive or destructive interference can be applied. For instance, for a specific tone, if the relative phase between the rising and falling edges is zero or multiple integers of 2π , the excitement has been suppressed for that tone.

In Figure A.5, we present the time evolution of two oscillations at frequencies 100 MHz and 600 MHz. The oscillations are described by adding two phase-shifted sinusoids, as brought in the equation:

$$A\sqrt{1 + B^2 + 2B \cos(\omega t + C)}, \quad (\text{A.1})$$

at which $A = 0.68$, $B = 0.93$, $C = \pi$.

For the higher frequency, the first smallest amplitude corresponds to a relative phase of 2π at $t = 1.67 \times 10^{-9}$ second. It is best to choose the pulse width at which all the frequency tones will oscillate below reaching their rela-

tive phase of 2π , e.g., the pulse width of 1.43 ns, as shown in a time stamp on Figure A.5.

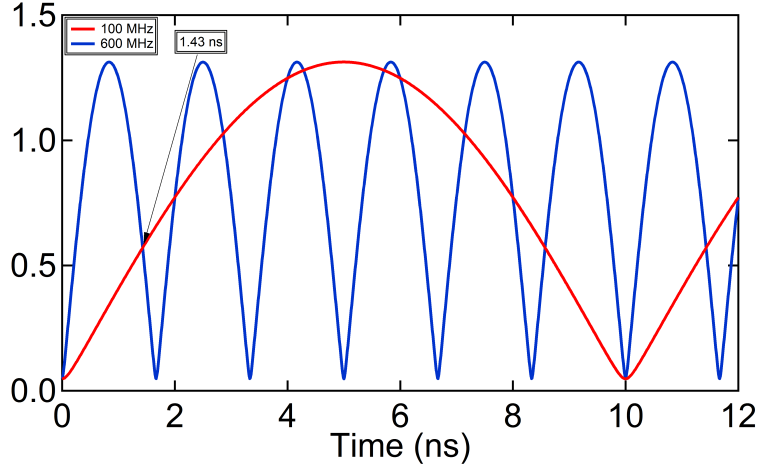


Figure A.5: Pulse width and the frequency bandwidth investigation. This figure shows the time evolution of two phase-shifted sinusoidal functions with frequencies of 100 and 600 MHz. The time stamp $t = 1.43$ ns is shown as a sample point, at which both the waves will not reach their first relative phase of 2π in time domain.

The pulse amplitude is crucial as well. It should be neither too small nor too high. In the case of small amplitude, the response sampling in simulation might not be captured. In the case of high drive, the magnetization will be disturbed and might cause a non-linear response, which is not of interested for this thesis.

A.2.2 Damping factor

The LLG equation contains a dimensionless constant that corresponds to damping in the magnetic system. Depending on the statics or dynamics, the damping factor, α , is considered with different values: α equal or greater than 1 is set for relaxation and lower than 1 is considered for dynamics. In the case of dynamics ($0 < \alpha < 1$), α should be selected as a small value to make the results more accurate. However, selecting a small damping factor like $\alpha = 0.0001$ will slow the convergence; this value corresponds to a lowest experimental value for YIG

material. For YIG simulations, however, we use a larger value obtained from the linewidth of magnetic resonance in our experimental results, $\alpha = 0.008$.

Here, we show that the value of α should not play a significant role in finding the resonance frequencies, just in the linewidth of the resonances. Figure A.6 shows a simulation of gyrotropic frequencies in a micron diameter and 10 nm thick Py disk for two damping factors.

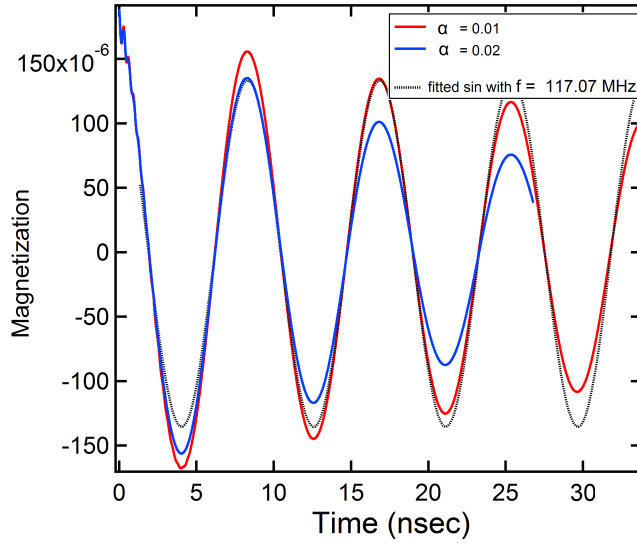


Figure A.6: The effect on the gyrotropic frequency of changing the damping factor. The simulations of core gyrations in the vortex state are presented for two damping factors, $\alpha = 0.01$, and 0.02 in a $1 \mu\text{m}$ diameter and 10 nm thick Py disk. In addition, the dotted black line represents the fitted sinusoidal function and shows identical resonance frequencies for the two damping factors.

The magnetic properties are $M_s = 700 \text{ kA/m}$, $A_{ex} = 13 \text{ pJ/m}$, and cell size $5.21 \text{ nm} \times 5.21 \text{ nm} \times 5 \text{ nm}$. To make the vortex core begin to gyrate, a step ($H_x = 1 \text{ Oe}$) is applied to the disk at its ground state. Shown here is the y-component of the magnetization, which reaches zero at the new equilibrium. The resonance frequencies are obtained via sinusoidal fitting, the same for two cases, and the decay rates are obtained from the exponential fits. It takes longer for the system with the lower damping factor to reach its equilibrium.

A.2.3 Fourier transform with windowing process

To obtain frequency information about the time-domain simulations, we use FFT algorithm in Matlab. The time-domain parameters, such as the sampling and running times, should be considered very accurately to produce very nice resolution field-frequency dispersions. For instance, it is good to select the total number of samples in the power of 2, an input in the FFT function in Matlab.

Moreover, when a pulse is applied to the system, usually there are some high frequency excitations included in the response. Therefore, to overcome the transient response and obtain only the desired dynamics, we use the FFT with a windowing process. Here, the Hann windowing in Matlab is described with the following equation [111]:

$$w(n) = 0.5 \left(1 - \cos\left(2\pi \frac{n}{N}\right) \right), \quad 0 \leq n \leq N, \quad (\text{A.2})$$

in which n is the sample, N total number of samples, and the window length L is equal to $N+1$. Figure A.7 shows the time domain and Fourier transform of a Hann window with $L = 64$.

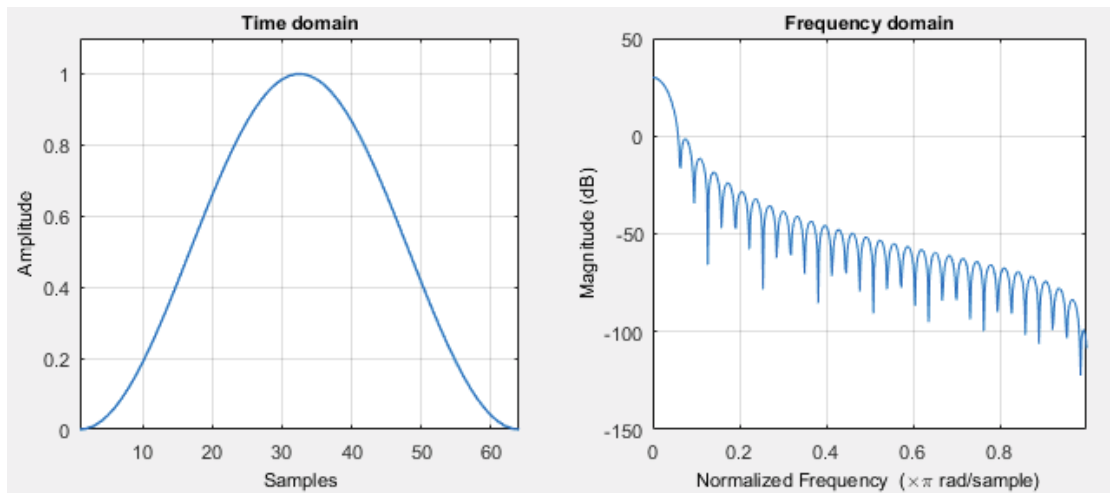


Figure A.7: The representation of Matlab Hann-windowing function. The time domain representation of the Hann function with a selected window of $L = 64$ is shown in the left panel and the corresponding FFT response is presented in the right panel.

We use a modified Hann function so that half of the time domain data has been used to reduce just the initial transition, but the resonance will continue ringing. First a Hann function with twice the length of time data is selected. Then, the time-domain data is multiplied by the modified Hann function (time-domain) with the same length, and the FFT function is applied to this new vector.

A.3 Sample codes

An example of a complete code for obtaining a hysteresis loop in a cuboid is presented following by part of codes for Voronoi tessellation and non-zero temperature.

When a text code is ready, a mumax executable file can be run in the terminal. There is a browser-based user interface that allows the user to run a simulation or modify the code.

A.3.1 Sample code for hysteresis loop

```
1 /* ..... Geometry ..... */
2
3 SetGridsize(64, 64, 64)
4 SetCellsize(1e-9, 1e-9, 1e-9)
5
6 setgeom(cuboid(50e-9, 50e-9, 50e-9))
7
8 /* ..... Input parameters ..... */
9
10 Msat = 480e3           // Saturation magnetization in A/m
11 Aex  = 1.33e-11       // Exchange stiffness in J/m
12 alpha = 1.0           // Gilbert damping constant
13 save(Msat)
14
```

```

15 m = uniform(0,0,1)      // Initial magnetization
16 saveas(m, "m_initial")
17
18 anisU = vector(1, 1, 1) // uniaxial anisotropy vector
19 Kul   = -2.8e4 // uniaxial anisotropy constant in (J/m3)
20 save(anisU)
21 save(Kul)
22
23 // time, magnetization, and applied fields are the
24 tableadd(E_total)
25 tableadd(E_anis)
26
27 // increasing field in a loop
28 for Bi:=0; Bi < 100; Bi+=5{
29     B_ext = vector(Bi*1e-4,0,0)
30     print(Bi)
31     RunWhile(MaxTorque > 1e-3) // relax
32     tablesave()
33     save(m)
34     print(B_ext) }

```

A.3.2 Voronoi tessellation

```

1 // define grains with region number 0-255 (maximum number of
   regions 256 in mumax)
2 grainSize := 40e-9 // m
3 randomSeed := 1234567
4 maxRegion := 255
5 ext_makegrains(grainSize, maxRegion, randomSeed) % built-in
   function using Voronoi tessellation
6
7 defregion(256, Mask.inverse()) // region 256 is outside, not
   really needed
8 Msat = 700e3 // saturation magnetization (A/m)

```

```

9 Aex    = 13e-12 // exchange constant (J/m)
10 alpha  = 1 // damping factor
11
12 // set random parameters per region
13 for i :=0; i<maxRegion; i++){
14     // random 30
15     MS := 700e3
16     Msat.SetRegion(i, MS + randNorm() * 0.1 * MS) // 10%
           saturation magnetization variation
17 }
18
19 snapshot(Msat)
20
21 for i :=0; i <maxRegion; i++){
22     for j :=i+1; j <maxRegion; i++){
23         ext_ScaleExchange(i, j, 0.9) // reduce exchange coupling
           between grains by 10%
24     }
25 }

```

A.3.3 Changing the temperature

```

1 setsolver (1)
2 fixdt = 1e-14
3 thermalseed (1)
4 Temp = 300
5 thermalseed (0)

```

A.3.4 Magnetic resonance response

```

1 for Bi := 1000; Bi > 0; Bi--=5{
2
3     alpha = 1 // Set the damping factor for relaxation
4     B_ext = vector(0,0,Bi*1e-4)

```

```
5   relax()
6   tablesave()
7   save(m)
8
9   t = 0          // reset the time to zero for FFT calculation
10  alpha = .008 // Set the damping factor for resonance
11  B_ext = vector(0,.005 * (1-heaviside(t-7.34e-9)),Bi*1e-4)
12  tableautosave(10e-12)
13  Run(100e-9)   // run for 100 ns
14  t = 0
15
16 }
```

Appendix B

Micromagnetic simulation - Case studies

Many general problems have been simulated for magnetic structures, as well as various interesting case studies with the experimental insights and future devices. Among them are the disk structures with different magnetic materials (YIG, Py, Co), Py ellipse and complicated structures such as a mushroom Py shape. A concise summary of these case studies is presented in the following sections, in the same order presented in the main thesis chapters.

B.1 Experimental insights

B.1.1 Artificial pinning potentials in a Py disk

We study about the effect of the pinning sites on the magnetization characterization, mainly to control the Barkhausen free path in multigrain structures such as Py disks. Engineering the position of the pinning sites results a larger pinned characterization. In the experiment, we introduce the point-like pinning sites with the help of a beam of Ga^+ ions. The Gaussian beam-width makes a circular cross-section at the surface of magnetic material. Some surface molecules

are sputtered away with a dead-layer around the defect. Consequently, the pinning sites will not annihilate the vortex, but will keep the core pinned with the signature of slope change in the magnetization characterization.

Based on Cartesian meshing in simulation, we design defects with cross-like shape areas resembling circle intersections. In order to make pinning sites, in simulation we set the designed area with a selected depth to be not magnetic. This is a simplified version of finding the equivalent regions that correspond to the defects made using different approaches. These approaches include decreases in the saturation magnetization and/or exchange constant. Moreover, various shapes with combinations of area and height could be considered: e.g., instead of a pillar for a defect region, one can consider a Ziggurat pattern for the height. Many different cases are tested, but to be concise we are reporting only the results of simple cases, in which defects are pillars with no magnetic properties.

Figure B.1 shows an investigation into how size and dimension affect off-centered defects for a single pinning site in a 1- μm diameter and 12-nm thickness Py disk. A dumbbell feature in the hysteresis loop shown in the inset is a signature of the interaction of the vortex core with a pinning site, getting pinned and depinned in two field sweeps up and down. For each depth and area, only one of the minor loops is presented with an estimated position obtained from the experiment, at 126 nm in the y-direction. However, the magnetization (M-H) curve of a defect with 4 nm depth, 86 nm^2 area, and at a slightly shifted position is plotted in full. The areas of 86 nm^2 and 125 nm^2 are considered as 11 and 16 cells in a square shape orientation with the cell size of 7.8125 nm.

The width of the minor loops corresponds to the strength of pinning site, which depends on both the area and depth of the defect. However, the defect depth has a more significant effect on the size of minor loops.

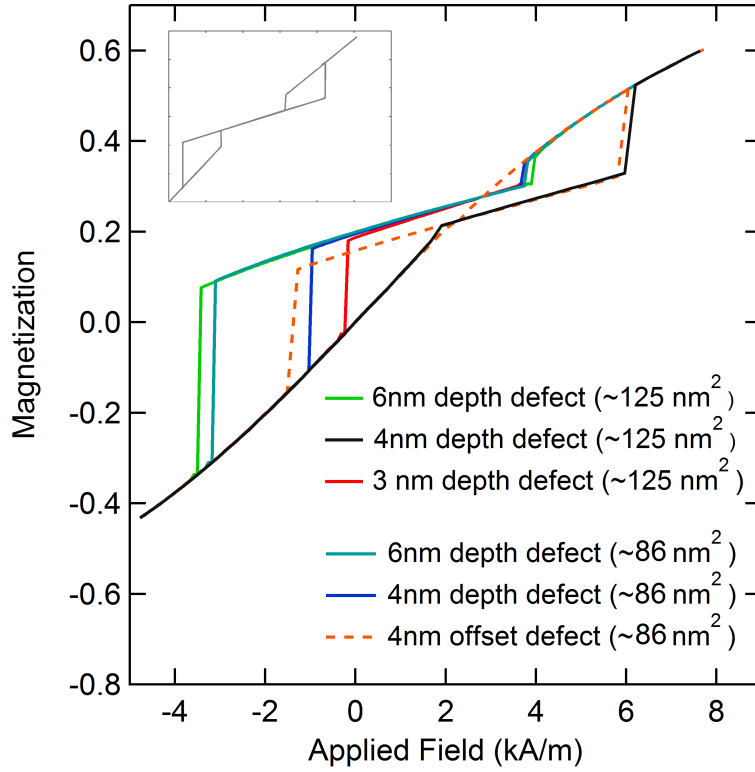


Figure B.1: Single defect characterization in a micron diameter and 12 nm thick Py disk. The M-H curves are obtained for some variation of defect depth and area. The depth of the defect is more effective in the pinning characterization. The top-left inset shows a cartoon of a full dumbbell-shape hysteresis loop.

An estimate of the effective vortex core size can be determined by running simulations for the same defect “depth”, and just changing the pinning site as a function of the area. The width of minor loops at first should grow with the area (when the site area is less than the core area, the energy depth is still growing), and then “saturate” (when the pinning site is so large that the core falls into a flat-bottomed potential well, is propelled across by field, and later depins). But it would be better to mimic the pinning potential with a variation of M_s and/or exchange constant for a big study.

We also investigated another condition using insights gained from the experiment: a single pinning site and an additional ring around the defect in a micron Py disk. This ring could have appeared because of a misalignment of

the Ga beam and it could be analogous to adding a faint shoulder to the defect.

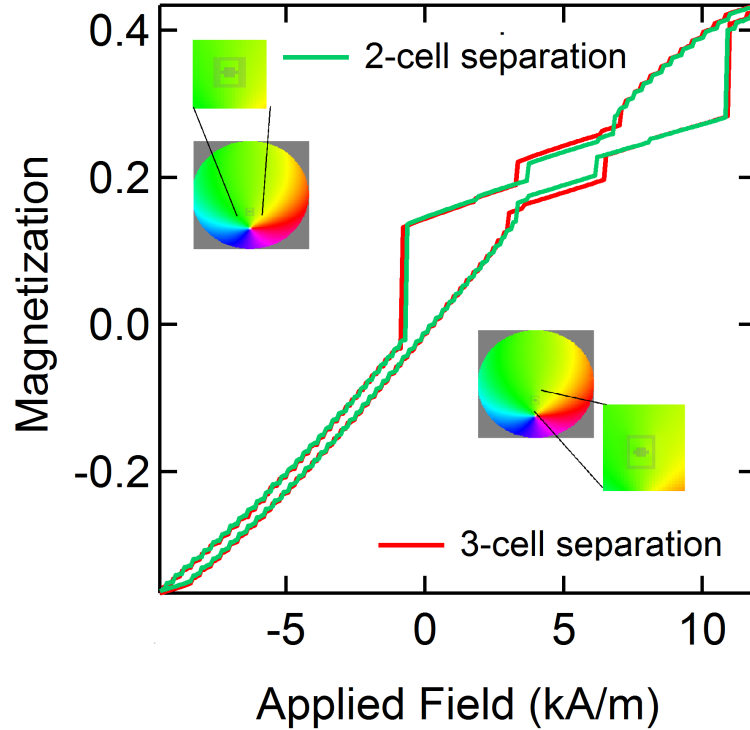


Figure B.2: Simulating the beam misalignment in creating the single defect. This figure shows the hysteresis loop characterization in a micron diameter and 12 nm thick Py disk with a rectangular ring around the single defect. The defect was made with 3×3 cells with two additional cells on the top and bottom. The insets show additional information about the mask of rings in two cases of two-cell and three-cell separations.

In a simulation we chose a rectangular ring because of the simplicity. Two cases are considered: two-cell and three-cell separations between the pinning site and the ring in the vortex movement direction. The related hysteresis loops are presented in Figure B.2 with the corresponding simulation snapshots in the insets. It seems that the ring should be closer to the defect in our sample to produce similar result compared to the experiment.

The magnetization characterization for a Py disk with three surface pinning sites is shown in Figure B.3. The position of the pinning sites was taken from SEM images of Py devices at 210 nm (single site, S), -85 nm (inner site, I), and

-220 nm (outer site, O).

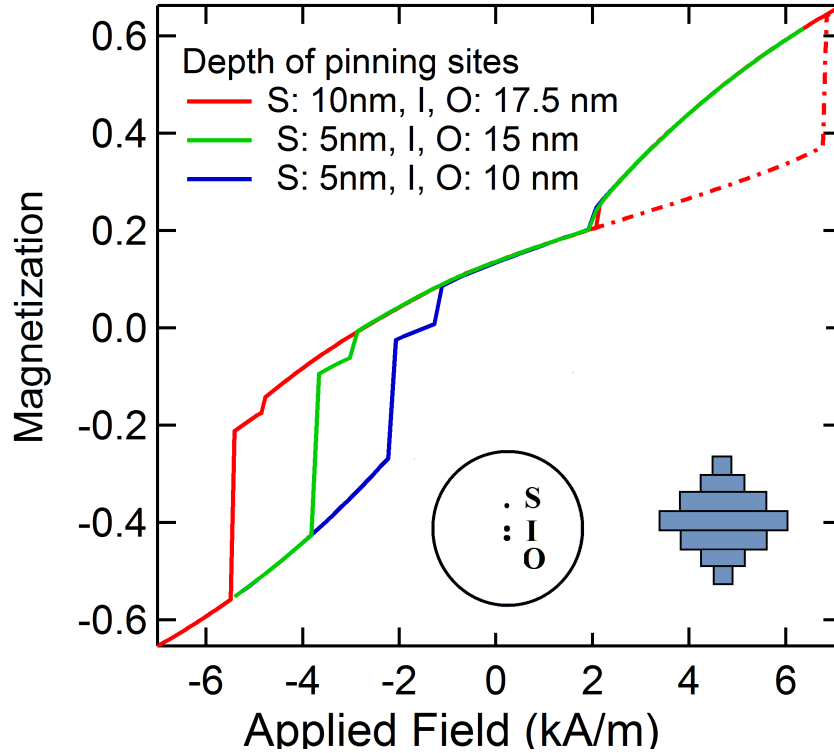


Figure B.3: Simulation of the pinning enhancement with three defects in a 2- μm diameter and 20 nm thick Py disk. The magnetization response with a variation of defect depths and areas is presented. The pinning positions are obtained from the experiment, single (S) site at 210 nm, inner (I) site at -85 nm, and outer (O) site at -220 nm, as shown in the lower-right schematic.

A cross section with an area of 678 nm² shown in the inset has been chosen so that the area will be close to the area of a circle with 30 nm diameter. Some variations of defect depth are considered, while the defect areas are kept the same.

The hysteresis loop starts from a free vortex close to the S side of disk. With the applied field, the vortex is pushed towards the S site and pinned there; the corresponding field is very close in all the cases. The presence of other sites keeps the vortex further in the S site, while the in-plane magnetization flex creates a domain wall (DW) that is extended to all three defects. After the DW connects the three defects, with a hop (small transition in the hysteresis

curves) the vortex moves to the I site. Depending on the depth of the pinning site, the pinned field range can be extended to vortex annihilation, which is not the case here, but was in the experimental result.

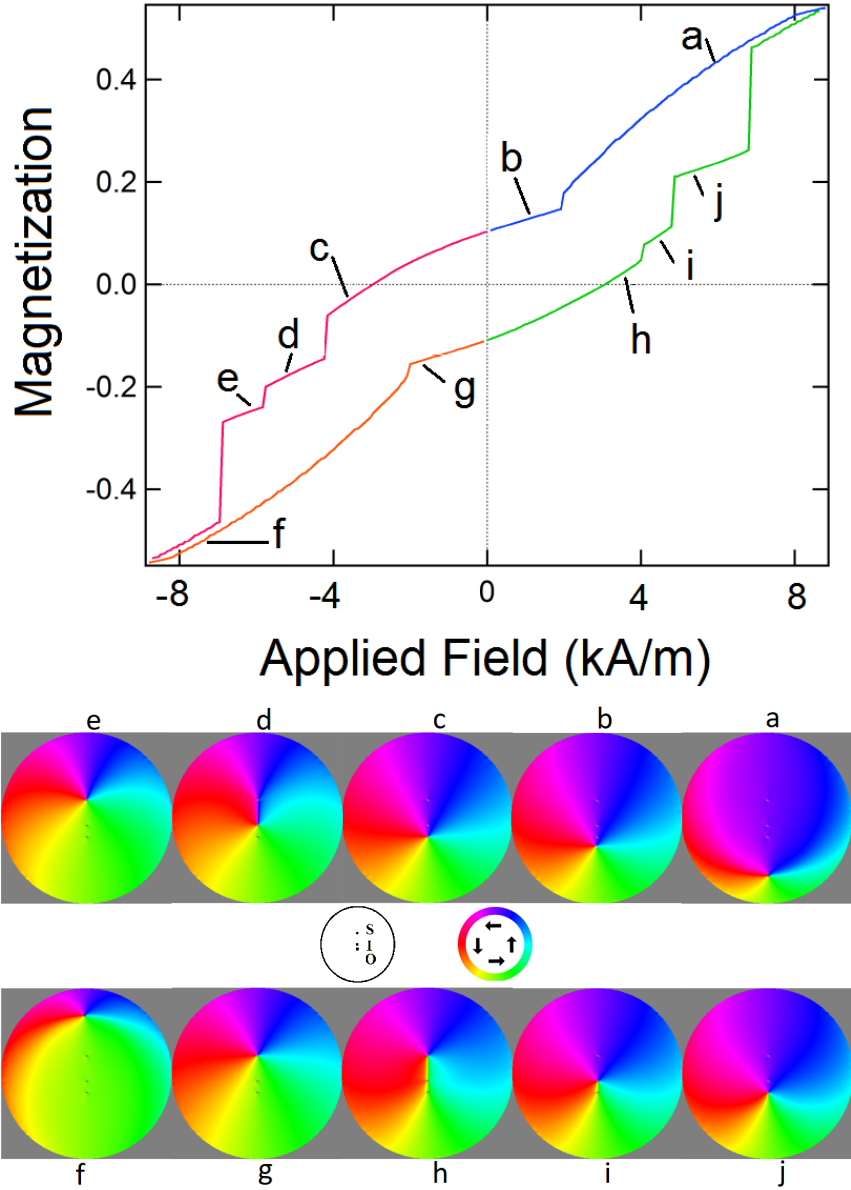


Figure B.4: Magnetization characterization in a 2- μm diameter and 20 nm thick Py disk with three pinning sites. The characterization is performed for in-plane applied fields with a free vortex state. Some magnetic profiles are presented with the corresponding labels in the hysteresis. The color-wheel shows the direction of in-plane magnetization with related colors.

Based on the selected dose during FIB, the initial defect depths were selected as 4 nm for a single defect in a micron Py, and 8 nm (S site) and 16 nm (I and O sites) in a 2- μm diameter and 20 nm thick Py disk. However, the selection of 10 nm and 17.5 nm depths for the S, and I,O, respectively, generate results that are more closely related to that from the experiment.

In addition, we select smaller defect areas, 20-nm diameter circles, which make a larger pinning enhancement with additional transition to O site. Figure B.4 shows a full hysteresis loop with the corresponding magnetization profiles for a Py disk with a defect in smaller areas. The presence of more than one pinning site makes it possible to into the disk a completely different “trajectory” for vortex annihilation. The touchstone is that the magnetization changes its sign, a big energetic cost, without jumping to the second defects, through “flexing”, which can enhance the “Barkhausen free” range.

B.1.2 Defects in a mushroom-shaped Py structure

In the simulation, a mushroom structure supports different ground states depending on the orientation of applied bias fields. The M-H characterizations of field sweep-up for two initial ground states are shown in Figure B.5.

The two-vortex state (V-V) with different chiralities and two-vortex (the same chiralities) with the anti-vortex (VAV) are shown in red and blue curves, respectively. The subtle difference between the two initial states is the big jump at the intermediate field due to the annihilation of the anti-vortex. There are other subtle tiny jumps which are related to the annihilation of the vortex in the stem. In addition, a field sweep down from a uniform magnetization is shown as a black trace. The jumps are transitions to a single vortex in the mushroom cap, and the initialization of a two-vortex state. The nucleation of an additional vortex in the stem happens in the negative fields, which is not shown here.

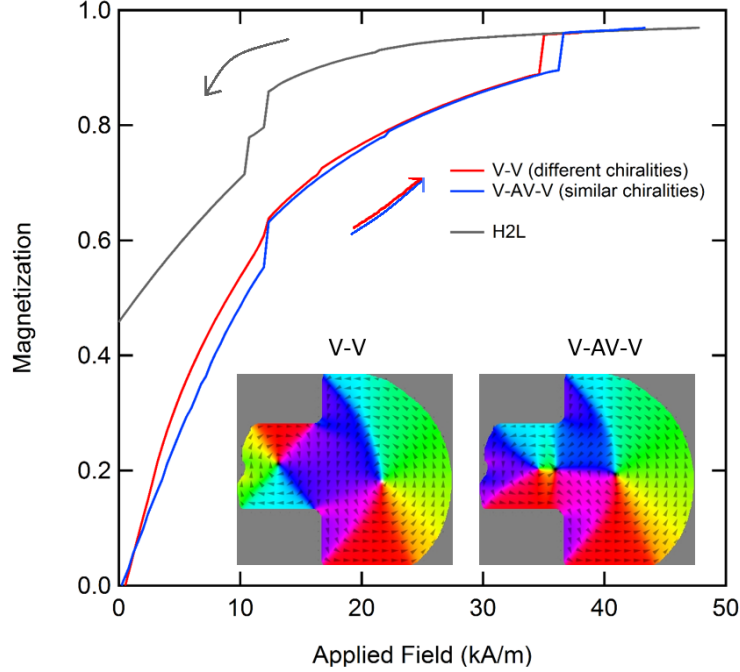


Figure B.5: The M - H characterization in a pristine mushroom-shaped Py structure with 40 nm thickness. Two colored curves show the field sweep up with the specified initial states, the two-vortex state (V-V, red curve) and vortex-anti-vortex-vortex state (V-AV-V, blue curve) as shown in the insets. The black curve shows the field sweep down from uniform magnetized structure.

The main focus of this section is to investigate the interaction of the two-vortex state with defects. First, we introduce a single pinning site in the mushroom cap and then add an additional pinning site to the stem. The defect positions are determined from the core trajectories calculated in a structure without pinning sites. Finally, we use the Voronoi tessellation to simulate random defect distributions (grainy-like Py structure) and obtain the susceptibility term.

Figure B.6 shows the in-plane magnetization versus applied field, in which the core depinning happens from a single pinning site. The pinning site has a diameter of 32 nm and thickness of 10 nm at (220 nm, 0 nm). The cores' displacements shown in the lower-right inset demonstrate that the two vortices are somehow coupled. When one is pinned, the movement of other is also restricted. As a result, the overall in-plane flex demonstrates a lower slope

while one of the core is pinned.

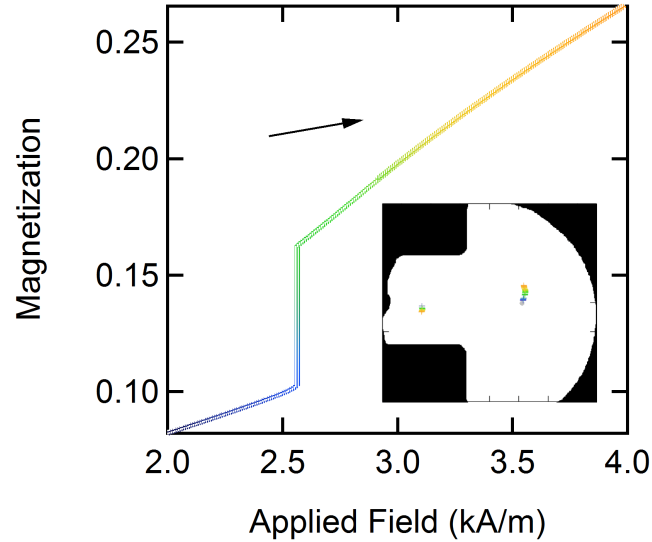


Figure B.6: Characterization of a single pinning site in the mushroom-shaped Py structure at a two-vortex state. The vortex depinning from a pinned core is presented with the corresponding core displacements in the inset.

To study the effect of the additional pinning site to the stem in the mushroom-shape structure, we established a weaker defect while keeping the cap defect the same as in the previous case. The weaker defect is considered in two cases: as squares with dimensions of 8 nm and 12 nm at (-461 nm, -22 nm), and a height of 10 nm. A cartoon of the pinning position is presented in the top-left inset of Figure B.7; the weaker pinning site is barely visible.

In addition, the initial core polarities have been chosen to be parallel or antiparallel, making it possible to overlap the magnetization. Figure B.7 shows the hysteresis loops of in-plane and out-of-plane magnetization components. The two-jump signature in both directions (sweep-up and sweep-down) shows the effect of two pinning sites. Moreover, the jump height in m_z magnetization in the nine-cell defect M-H curve is twice as the four-cell defect curve.

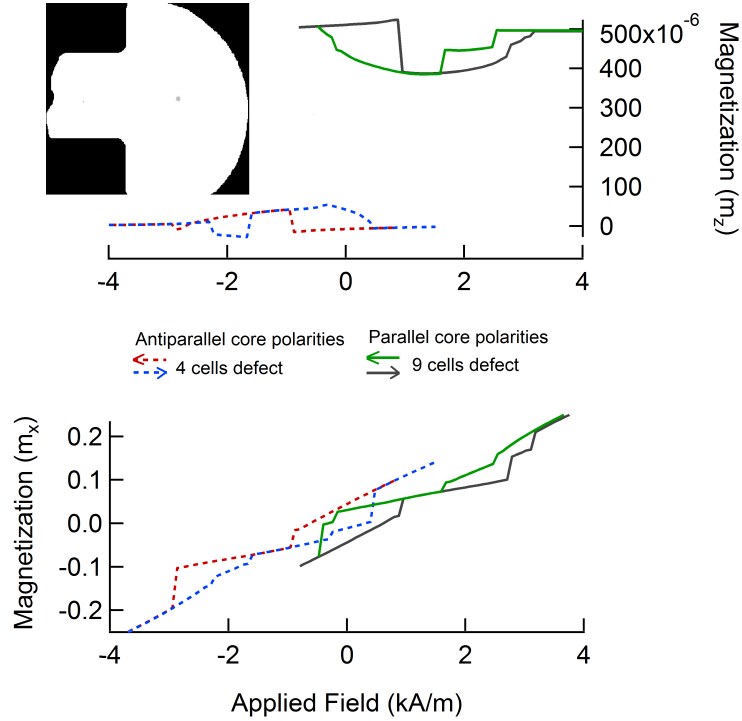


Figure B.7: The characterization of two pinning sites in the mushroom-shaped Py structure, one defect in the cap and the other in the stem. The magnetization responses, m_x and m_z components, versus applied field are presented for two cases: the cap defect is kept the same and the other defect is considered with surface removal of 4 cells and 9 cells (cell size ~ 4 nm). The device mask is shown in the top-left inset.

In the experimental data, there are some transitions in the M-H characterization due to the local pinning sites. To reproduce the pinning sites, a grainy Py structure is presented in simulation by using the Voronoi tessellations in mumax. Part of the code in which we make the grain regions and determine the magnetic parameters in each grain (the saturation magnetization of Py with 10% change and the exchange coupling reduced to 10% between the grains), is presented at the end of this previous chapter. Only 256 regions can be defined in mumax.

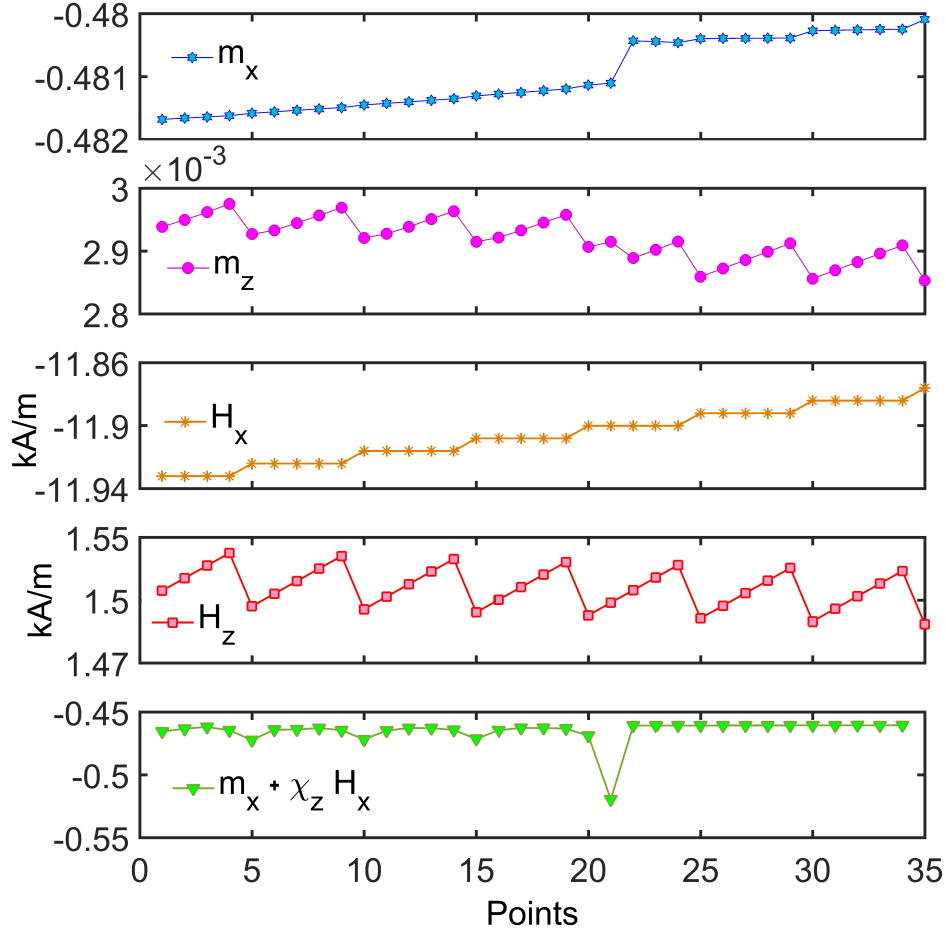


Figure B.8: Investigation of RF susceptibility through application of a perpendicular dither. The magnetization components, m_x and m_z , the applied fields, H_x and H_z , and the term including the susceptibility, $m_x + \chi_z H_x$, are presented versus sampling points. The m_z magnetization shows an irregular pattern on the m_x jump due to the depinning process, which corresponds to the susceptibility peaks.

To enable a close comparison with the experimental data and to study the effect of the susceptibility term, we included a sawtooth waveform as a perpendicular RF field, resembling an RF sine-function in the experiment, along with the dc sweeping bias field, H_x . Figure B.8 shows the magnetization and field components, as well as the torque term, $m_x + \chi_z H_x$. The m_z component is modulated with the H_z . Except the vortex pinning/depinning transition signature happens at the point = 21 in the magnetization components, the mean

value of m_z remains very close to the value for m_z before introducing a dither.

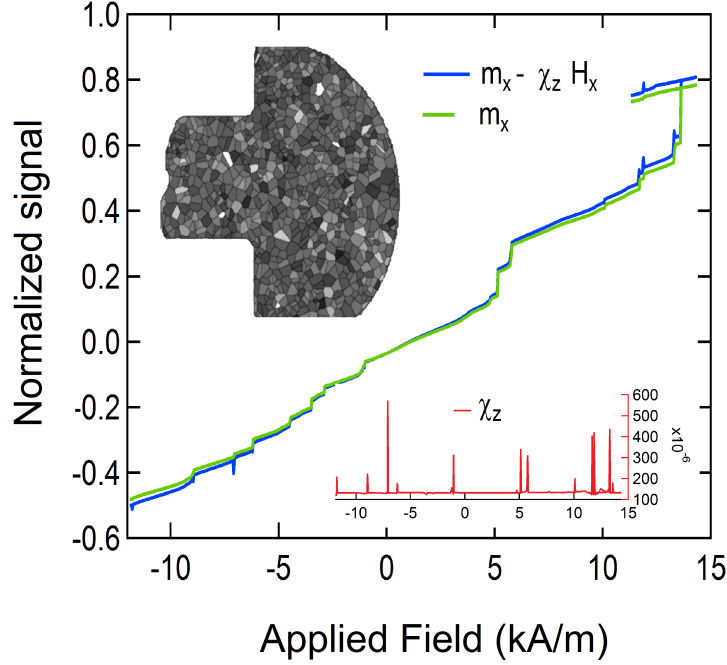


Figure B.9: The characterizations of magnetization in a grainy Py structure. The green curve is the magnetization response versus the applied field. The blue trace demonstrates additional peaks at the pinning/ depinning events, which are due to the out-of-plane susceptibility term. The top-left inset shows the grainy structures obtained via Voronoi tessellation and the bottom-right inset (red trace) shows the susceptibility peaks versus the applied field.

In a constant H_x bias field, a sine-like dither with a sawtooth function with six points is applied to the system. We selected the sawtooth with a positive slope for the first five points in a row. As a result, the calculated susceptibility based on $\chi_z = \frac{dm_z}{dH_z}$, is always a positive value for those points. At the sixth point that the slope becomes negative, the transition in all terms is ignored in final calculations.

The corrected hysteresis loop obtained from the susceptibility term is shown in Figure B.9. Those small jumps in the signal occur because of the core hops from one site to the other site – the size of the jump depends on the nearby favourable site in which the core jumps (spatial position). Note that the data processing has been done in Matlab, and here the differentiate or numerical

derivative function is used.

B.1.3 Gyrotropic frequency in a disk with defects

The gyrotropic frequency, which is the fundamental resonance mode in the vortex state, is tightly dependent on the structural geometry and magnetization. Figure B.10 shows the effect of three Py disks with different aspect ratios. The gyrotropic frequency is inversely related to the aspect ratio at the ground state. The magnetic resonances are obtained from the Thiele equation.

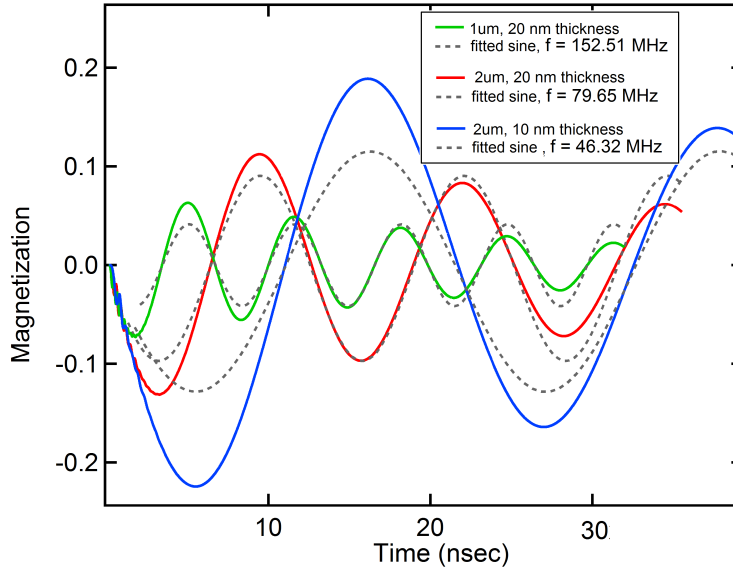


Figure B.10: Geometry-dependent gyrotropic frequencies in Py disks. The effect of aspect-ratio (diameter/thickness) in three Py disks at the ground state is presented: disks with $1\mu\text{m}$ diameter and 20 nm thickness (green trace with $f_0 = 152.51\text{ MHz}$), $2\mu\text{m}$ diameter and 20 nm thickness (red trace with $f_0 = 79.65\text{ MHz}$), and $2\mu\text{m}$ diameter and 10 nm thickness (blue trace with $f_0 = 46.32\text{ MHz}$).

While the gyrotropic frequency can be excited with a pulse at a given applied field (pulse properties discussed in the other section), there are two options for obtaining the resonances. One method is to use FFT, and the other is to use a fit function to a temporal magnetization. The latter fit function is obtained from the Thiele's equation of motion and it has the form of $\exp(\alpha t) \cos(2\pi f_{res} t)$. This fit can be used for only one mode, usually the fundamental mode. How-

ever, in the thicker structure that will be discussed in the next section, there are more gyrotropic modes. So FFT would be a more accurate way to resolve all the modes.

In this section, we investigate the pinning effect on gyrotropic frequency in thin disks with pinning sites. We consider a Py disk with a single defect, and obtain its spectrum in a field sweep up from a free vortex at the ground state towards the pinning site. A single defect with 30 nm diameter area is set at 210 nm in the y-direction (off-centered in the way of the vortex trajectory). The spectra of two separate defects with depths of 5 nm and 2.5 nm are presented in Figures B.11a and B.11b, respectively. The overlapped static magnetizations are shown in Figure B.11c. Although there is a slight difference in the magnetization responses for the two cases, the spectra are very different in the pinned regions. The disk with a 2.5nm-depth pinning site shows a lower pinned resonance frequency.

Moreover, we consider the disk with three defects. The defects have been chosen at the same depth of 5 nm and an area around 706 nm^2 (a circle with diameter of 30 nm), at the spatial positions of -220 nm, -85 nm and 210 nm.

To initiate the dynamical response, a step (instead of pulse) with 80 A/m amplitude is applied to a relaxed equilibrium magnetization state with $\alpha = 0.01$. The total time evolution of 100 ns is considered, which corresponds to a 10-MHz frequency resolution, for each field with increments of 160 A/m. The time evolution of the magnetization shows a normal gyration while the vortex is free, but when the core gets pinned, the gyration jumps to a higher resonance frequencies with a smaller amplitude gyration inside the pinning site.

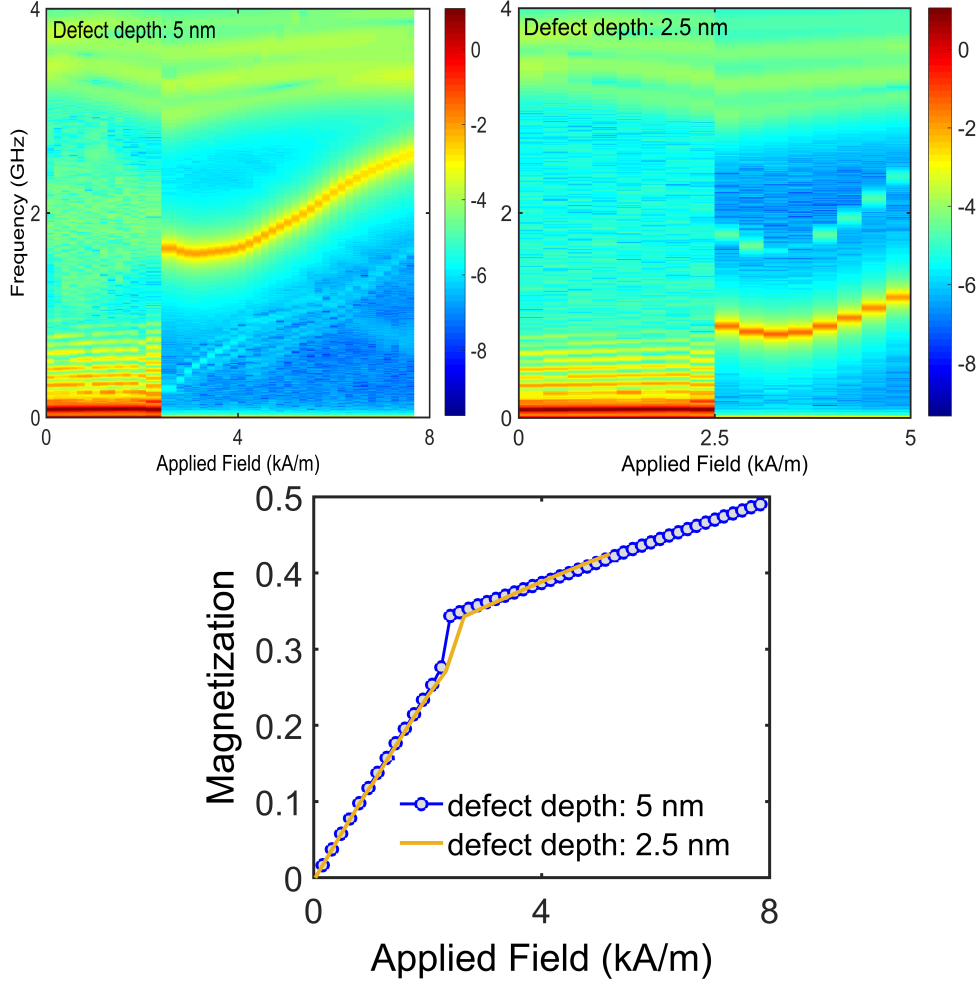


Figure B.11: Simulated magnetic resonances of vortex core in and out of a single defect. a) and b) The magnetic resonance spectra are presented before and after the vortex pinning in a single defect with depth of 5 nm and 2.5 nm, respectively. The defects are considered in a 1- μm diameter and 10 nm thick Py disk. c) The magnetization responses in the two cases are overlapped.

There is a significant difference between responses at the positive and negative fields, which is due to the pinning positions. In the positive side, there is only one pinning site, and the chosen position of defect is in the linear regime of core movement with an applied field (less than 250 nm). This position is strong enough that not only can it keep the vortex for a large field range, but also the depinning field causes the core to be annihilated (assisted annihilation). However, on the negative side, there are two pinning sites, one of which is closer to the center. As a result, the core gets pinned while the depinning field

pushes the vortex core to around a -370 nm position, out of the reach the outer defect. As a result, there is a spectrum of free vortex until the usual vortex annihilation field at $H_x = -17.5$ kA/m. Moreover, the spectrum experiences a very large meandering, around 1 GHz, while the vortex core is pinned.

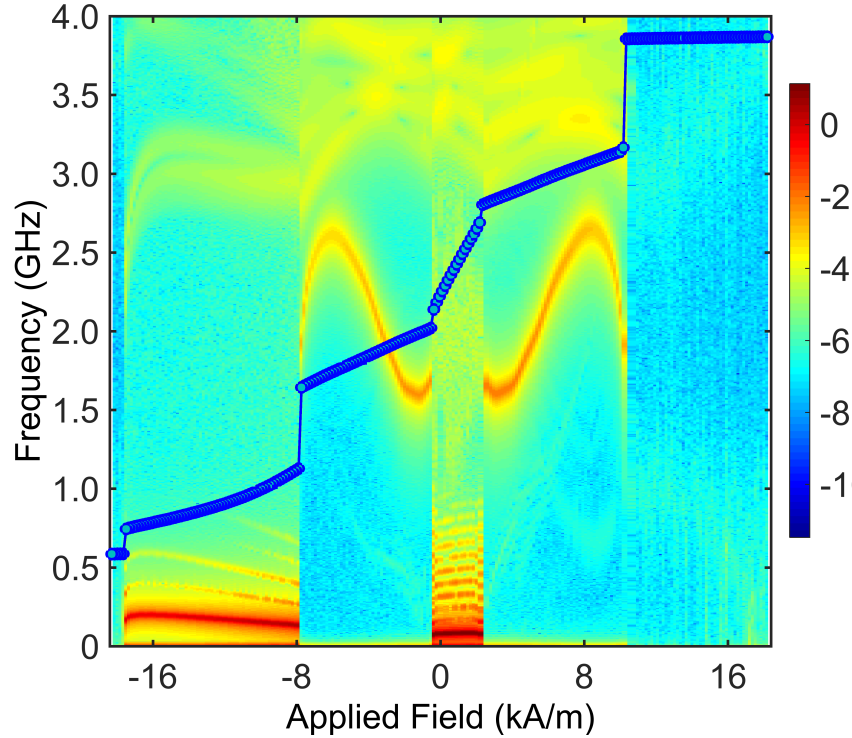


Figure B.12: Simulated magnetic resonances of triple defects in a 1- μ m diameter and 10 nm thick Py disk. The spectrum is obtained via overlapping of two individual simulations from zero field to high positive and negative field values. The static response overlaps on top of the spectrum.

The spectrum would be different if the field sweep had been started from the high field, independent of which side of the disk the vortex core was created. Then the pinning positions of 210 nm and -220 nm create a roughly symmetric situation for a vortex: the free vortex sees only one pinning site (does not matter if it is the outer of the paired ones, or just the single one). But there is a middle ground between having the defects behave as if they are fully independent (where the core would depin, then reside unpinned in the disk before dropping into the next pinning site), and having the defects interact but with a more

dramatic dependence on separation – the domain wall opens a “conductance channel” from one pinning site to the next.

B.1.4 Quasi-static in a thick YIG disk

The FIB fabrication offers unique possibilities for nanofabrication of individual, monocrystalline nano-objects. We use FIB to mill a thick disk from a single-crystalline YIG film. However, the disruption by Ga^+ ions reduces the magnetic properties of YIG crystal near the surface and creates a magnetically dead shell encapsulating the magnetic core of the resultant structure. To obtain a qualitative understanding of the device spectrum, dimensions of a YIG magnetic disk are determined from SEM images of the device. The shell diameter is obtained from the last step, disk milling, $550 \pm 30\text{nm}$, but due to a symmetric dead-layer consideration in the radial direction, the diameter of 980 nm is set in simulation. The thickness of 250 nm is empirically determined from the experimental resonance frequencies for in-plane magnetizations with a direct comparison to simulation.

The gyrotropic frequency versus disk thickness is obtained in YIG disks at the ground state with three diameters, as shown in Figure B.13. The Thiele’s expression is used to find the resonance frequencies. Up to 100 nm thickness, all three disks have shown similar linear trends of increasing gyrotropic frequency. However, at around 200 nm thickness, there is a plateau corresponding to mode cross over, at which the FFT is more reliable to find all modes, as shown in Figure 3.1.

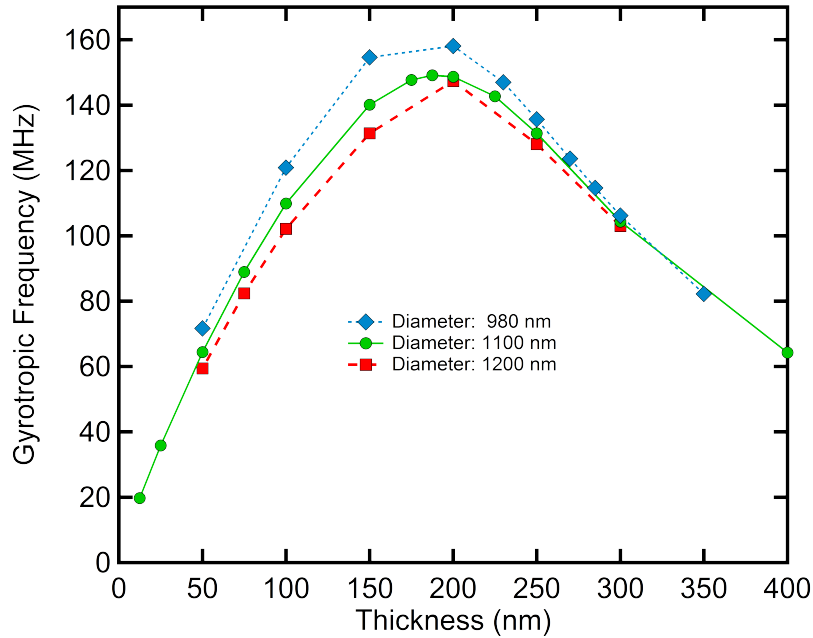


Figure B.13: The effect of YIG disk dimensions on the magnetic resonance at the ground state. Three different disk diameters (980 nm, 1100 nm, and 1200 nm) have been used to obtain the relationship between the gyrotropic frequencies and disk thickness (without considering the anisotropy). Compared to the experimental data, the disk with 980-nm diameter produces closer resonance at 250 nm thickness.

The hysteresis loop shown in Figure B.14, is obtained for a 250-nm thick YIG disk with 980-nm diameter for an in-plane applied field in the x-direction with a resolution of 800 A/m, from zero to 23 kA/m and returning back to zero field (the hysteresis loop is shown up to 21 kA/m). The color contrast of the hysteresis loop represents the regions where the spin texture exists as a three-dimensional vortex (yellow green) or quasi-uniform (dark blue) states. The hysteresis loop with the vortex annihilation at ~ 18 kA/m and nucleation of a three-dimensional vortex state at the transition ~ 14 kA/m is consistent with the results of the experiment. The corresponding labeled spin textures are shown as thumbnails in Figures B.14A-E insets, with in-plane magnetization direction represented as a color-wheel for the bottom and top disk surfaces. m_z magnetization is shown in a gray scale-bar at the plane passing the center.

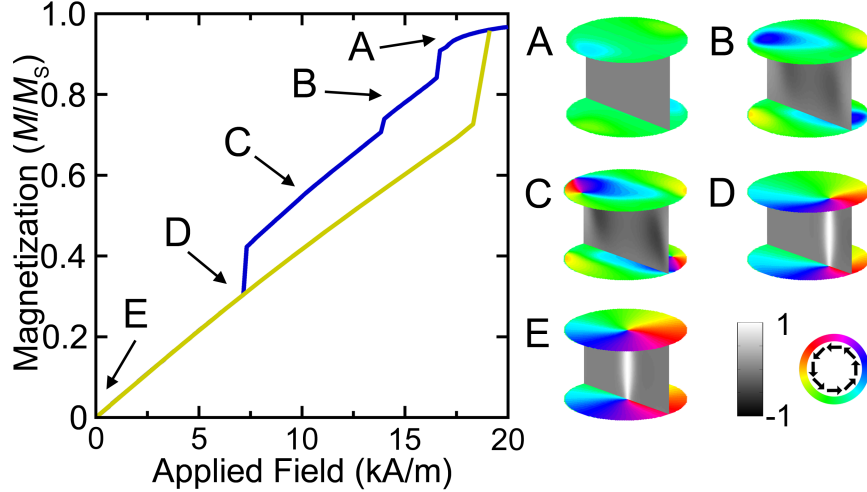


Figure B.14: 3D Spin Textures of the Mesoscopic YIG disk. The hysteresis loop for a 980-nm diameter and 250-nm thick YIG disk is presented. The insets (A to E) illustrate the spin textures (in-plane and m_z) at the corresponding fields. The in-plane magnetization directions (for the top and bottom surfaces of the disk) with the accompanying color wheel and the m_z components through a plane intersecting the center of the disk are shown in grayscale. The spin textures (in-plane direction and m_z) for vortex and quasi-uniform states corresponding to 0 and 19 kA/m applied fields are shown in the bottom-right and top-left insets, respectively.

The aspect ratio of the YIG disk permits variation of the spin texture with the \hat{z} position. Figure B.14E shows the ground-state of the structure as a three-dimensional vortex for which the core sits at the disk center at zero field. As the applied field is increased, the core is translated towards the edge of the disk, and annihilated. Figure B.14A shows the quasi-uniform state at 19 kA/m shows a major magnetization along \hat{x} direction and small non-uniformity near the edges.

Room-temperature bulk properties of YIG were used as the input parameters to the simulations [112]: exchange stiffness constant $A_{ex} = 2$ pJ/m, $M_s = 140$ kA/m, and anisotropy constant $k_{c1} = -610$ J/m³ with the anisotropy axes oriented such that one of the easy axis is along the cylinder axis (as in experiment). The calculated exchange length for YIG is 12.7 nm, so a cell size of $9.8 \times 9.8 \times 6.25$ nm³ for the 3D simulations. The lower size in the z direction for the cell size was chosen to obtain a more accurate result, and it will be

explained in the ‘shallow imperfection’ section.

B.1.5 Line defects and magnetic resonances of YIG disk

Through FIB fabrication, ion exposure makes a rough surface with a surface corrugation less than five nm, which has an impact on the resonance modes in the vortex state. Qualitative micromagnetic comparisons are performed for a pristine YIG disk and a disk with six shallow grooves on the bottom layer. The observation of the vortex core pinning through the interaction of resonant dynamics with nanoscale imperfections is not directly evident in the net moment (dc magnetization) response in both measurement and micromagnetic simulations.

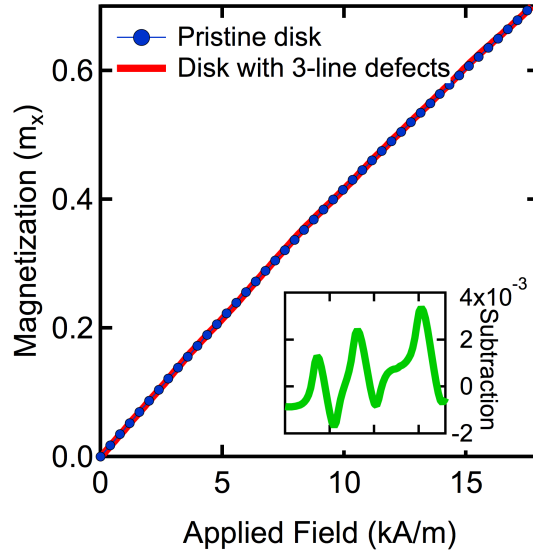


Figure B.15: Low-field comparison between magnetization responses in a pristine and defected YIG disks. The subtraction of two M - H curves shows a slight change, three peaks corresponding to three surface defects, as demonstrated in the lower-right inset.

Figure B.15 shows the simulated magnetization responses for both cases, with no defects and with imperfections, in which the disk with imperfections shows a very slight wobble as the core interacts with the defects. The subtraction of two magnetization responses in Figure B.15 inset shows a very small

difference (smaller than the experiment sensitivity).

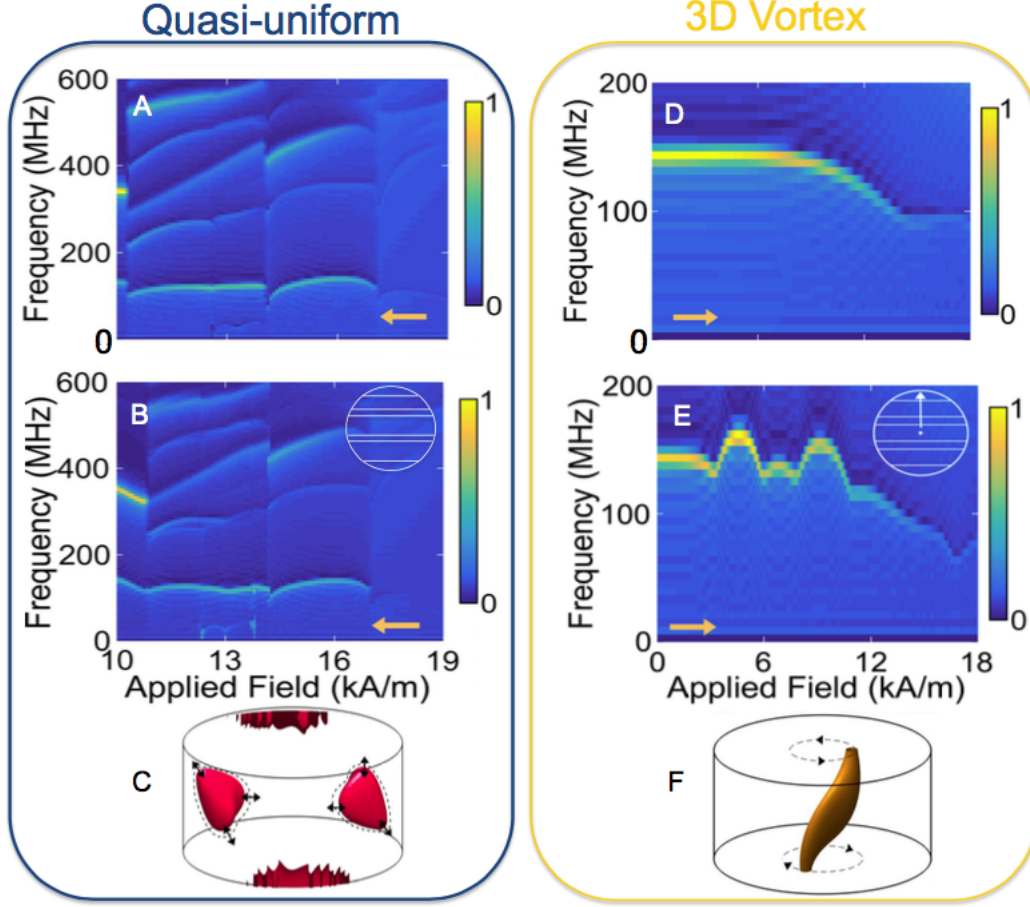


Figure B.16: Comparison of magnetic resonance spectra in the YIG disks with and without surface modifications. A) and B) The quasi-uniform in YIG disks with and without surface modifications, respectively. D) and E) The vortex state spectra in the YIG disks with and without surface modifications, respectively. The arrow indicates the direction of the field sweep (low-to-high direction for vortex state and high-to-low for quasi-uniform state). The surface modifications have a higher impact on the spectrum of the vortex state than on the spectrum of the quasi-uniform state. C) Iso-surface of the $m_z = 0.35$ component of magnetization is presented at $H_0 = 12$ kA/m and $f_{res} = 116$ MHz. The dashed lines and arrows depict a breathing mode of the two-vortex state. F) Mode profile of the gyrating magnetic vortex (iso-surface $m_z = 0.5$) is illustrated at $H = 0$ kA/m and $f_{res} = 140$ MHz. The core ends at the top and bottom of the disk circle out-of-phase about the center (the state illustrated corresponds to zero applied field).

The resonance frequencies are extracted through FFT of the temporal response of $m_y(t) - m_y(0)$ and shown for the cases of a pristine disk and disk

with surface modification (six line defects), in Figure B.16. The insets in Figure B.16B and B.16E illustrate the pattern of linear surface defects. The dynamics were excited by applying a square pulse (400 A/m amplitude, 1.43 ns width) at each field step upon the convergence of the spin texture to an equilibrium state with LLG α was set to 0.008.

In the quasi-uniform spin textures, because the state is more internal the surface roughness has little influence on the modes (compare Figures B.16A and B.16B). The resonance frequencies are slightly higher in the presence of roughness, but the field-frequency variations are the same as for the pristine disk. That is because the high field spin modes are more ‘internal’ to their respective textures, as illustrated in Figure B.16C.

This is in contrast to the case for the vortex texture (shown in Figures B.16D and B.16E), where a clear qualitative difference between the simulated spectra of the gyrotropic modes is seen by comparing the disk with roughness and the pristine disk. When a vortex core end (the highest energy density region of the spin texture) interacts with a defect, the resonance frequency and amplitude are strongly modulated. As the core on the bottom surface of the disk approaches the defect it becomes pinned, while the core on the top surface is free to precess at an increased frequency. The first mode gyration in the pristine disk is illustrated in Figure B.16F. The wider modulation of the simulated frequencies, compared to the experiment, are believed to be due to the imperfections in the simulation creating larger pinning sites than what exist in the experimental YIG disk (a limit imposed by the minimum grid size of the simulation).

B.1.6 Kittel-like modes in a YIG structure

Knowing an accurate geometry of the disk is crucial for understanding the modes. From our previous study of an in-plane magnetized disk, an estimate of 250 nm was found for the YIG disk thickness. Having the resonance spec-

trum for out-of-plane field direction helped show that the overall shape has an asymmetric thickness, like a trapezoid in a side view. For that reason, the simulation investigations about the adjusted shape are presented here in a step-by-step procedure.

First, we selected a disk with the same dimension as obtained in the previous section, 980-nm diameter and 250-nm thickness. Then, we obtained the resonance frequencies at $H_z = 2000$ Oe, which we selected to be higher than the saturation magnetization in YIG ($M_s = 1780$ Oe) and which is sufficient to make the structure uniformly magnetized in the z -direction. Figure B.17 shows the frequency responses at this perpendicular field, accompanied by spatial FFTs (both spatial amplitude and phase) for the first five modes. The first mode in 250-nm thick YIG disk has two nodes along the thickness, which does not correspond to the uniform response.

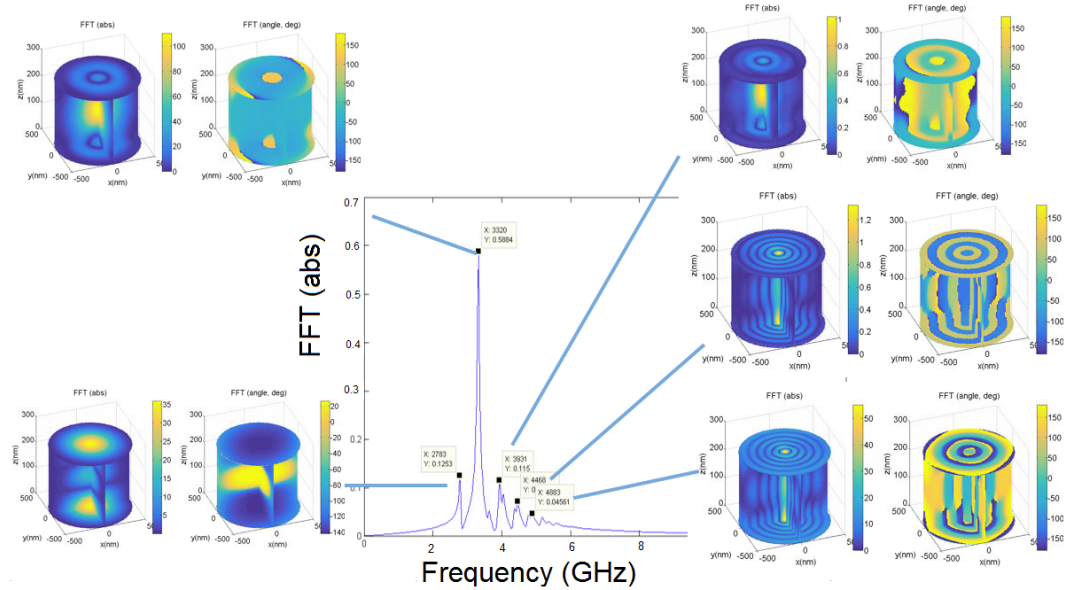


Figure B.17: Resonance spectrum in a 250-nm thick YIG disk at $H_z = 2000$ Oe = 159.2 kA/m. The related amplitude and phase profiles are presented for the five first resonance modes.

However, the second mode with the highest amplitude in the frequency spectrum displays a more uniform response internally. This is very similar to

the 'crossover' that occurs for the gyrotropic modes in the thick YIG disk. The nodes along z are another manifestation of the crossover behaviour as a function of thickness, which means the lowest frequency mode doesn't have the minimum number of nodes. Moreover, the radial nodes increase with the mode number, after the second mode.

Then, the larger spectra of perpendicular magnetized YIG disks with three different thicknesses – 200 nm, 250 nm, and 400 nm – are presented in Figures B.18 a, B.18b, and B.18c, respectively. The field sweep-down starts from $H_z = 2000 \text{ Oe} = 159 \text{ kA/m}$ in a uniform magnetization towards a vortex state.

There are two similar signatures in the simulations: a change in the slope of modes at the softening point (which corresponds to the vortex nucleation, a V-shape feature) and a bunch of linear modes before the vortex nucleation (at the uniform state). There are around 10 bright modes in the saturation magnetization, and there is a coupling between the second and third modes. By increasing the thickness, that coupling occurs at higher frequencies, but there is no mode crossing or joining as seen in the experiment.

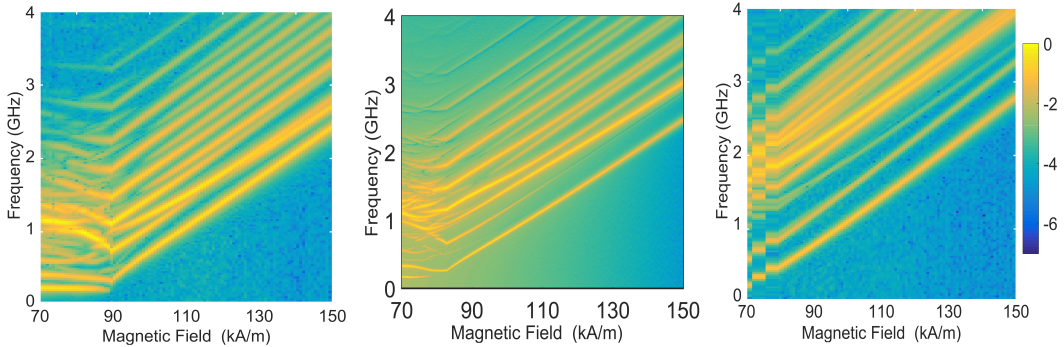


Figure B.18: An investigation into the effect of disk thickness on the resonance spectra of 980-nm diameter YIG disks (field sweep down). a) The spectrum of a 200-nm thick disk is presented with a field step of $10 \text{ Oe} = 796 \text{ A/m}$ and frequency steps = 24.41 MHz (total running time = 40.96 ns). b) The simulation spectrum of a 250-nm disk with a field step of $2 \text{ Oe} = 159 \text{ A/m}$ and frequency steps = 6.1 MHz (total running time = 163.84 ns) is illustrated. c) A disk with a 400 nm thickness field step = $10 \text{ Oe} = 796 \text{ A/m}$, frequency steps = 24.41 MHz (total running time = 40.96 ns).

Because 250-nm thickness has been confirmed from the previous discussion,

finer resolutions in the field and frequency are considered for Figure B.18 b with the field step of $2 \text{ Oe} = 159 \text{ A/m}$ and frequency steps = 6.1 MHz (total running time = 163.84 ns).

On the other hand, the field at which the V-shape occurs depends on the disk dimensions: for instance, in a thinner disk, that feature will be pushed towards a higher field, while in a thicker disk the vortex nucleation happens at lower field. Compared to the experiment presented in Figure 3.15, the V-shape field, slope of modes in the uniform states and the number of modes in the disk spectra are not in good agreement. We also investigate the effect of the in-plane field offset on the spectra. It appears that the additional in-plane bias field will shift the whole spectrum at a uniform state, but in the vortex state resonance modes, the modes are less sensitive to the additional in-plane field. Moreover, this additional field will change the spin texture, the vortex creation, annihilation fields and so on.

During the thinning process of the lamella thickness (one step before making a disk), a normal-incidence dose is used. The wings of the ion beam (approximately Gaussian shape) can taper the dead-layer in the thickness direction. One possibility for increasing the number of modes in the uniform state is to break the symmetry in the structure, since some modes can be coupled because of cylindrical symmetry. Therefore, in a first trial, we partially cut one side of the structure in the thickness to make a step. In Figure B.19, the spectrum of a deformed structure is shown with the schematic of the structure in the inset.

The initial structure is considered as a YIG disk with 980-nm diameter and 400-nm thickness. Then a cuboid with dimension of $135 \text{ nm} \times 980 \text{ nm} \times 150 \text{ nm}$ is removed from the top – as if a D-shape has been removed from the structure. Compared to the disk spectrum, there are more modes in a given frequency range. However, breaking the symmetry in a discontinuous way will not provide a good agreement with the experiment. Our investigation also shows that a smaller deformation will not significantly disturb the spectrum of

the disk.

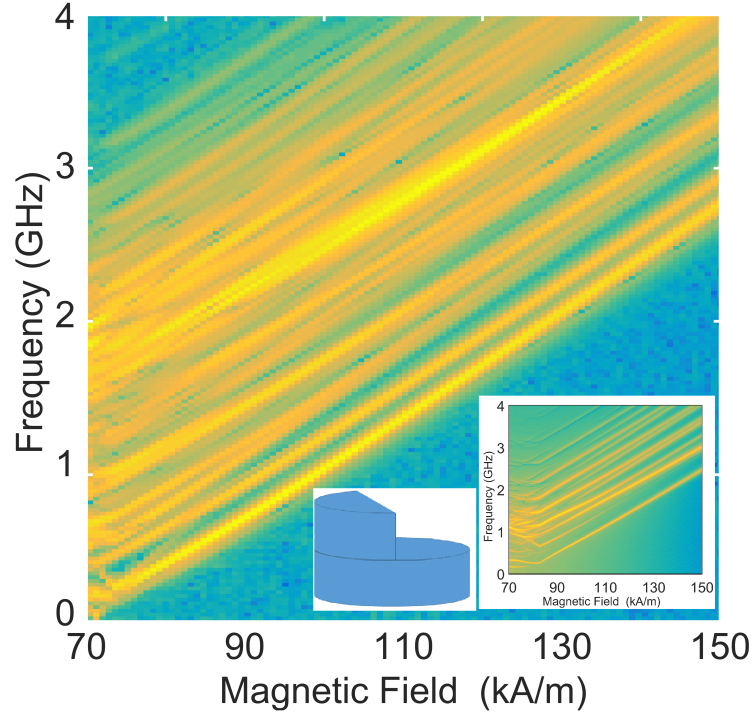


Figure B.19: Simulated spectrum of a YIG structure with a step artifact. In right inset the spectrum of the YIG disk (Figure B.18) is presented, while a schematic of the structure is shown in the left inset.

For the next step, we consider making a tapered disk, in which the height is modified on a gradient. The tapering of the disk thickness breaks the circular symmetry and accordingly, degenerate modes can appear. The schematic of the tapered disk in 3D and side views is illustrated in Figure B.20. The vertical cross-section of a tapered disk is considered as a right trapezoid with the base of 980 nm. Two thicknesses, h_1 and h_2 , correspond to the tapering angle. In terms of the magnetization volume, the tapered disk is equivalent to a disk with 980-nm diameter and equivalent thickness of $(h_1 + h_2)/2$.

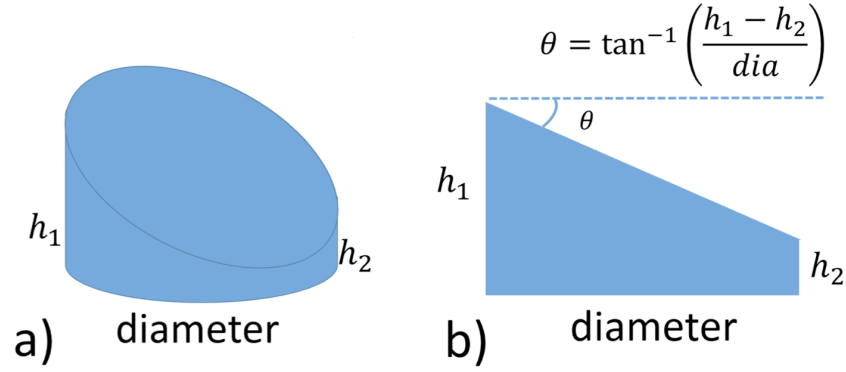


Figure B.20: The cartoon of a tapered disk. a) and b) 3D view and side view are presented, respectively. On the side view, from the trapezoid cross-section, the angle of the tilt plane is obtained. The tapered disk in terms of a magnetic volume is equivalent to a disk with $h = (h_1 + h_2)/2$.

Figure B.21 shows the spectra of various tapering angles. The thickness modification of the YIG core disk has a huge impact on the number of modes and their brightness. Among all the panels presented in Figure B.21, Panel a with $h_1 = 300$ nm and $h_2 = 100$ nm ($\theta = 11.5^\circ$), has a spectrum closer to that of the perpendicular magnetized YIG structure in the experiment. For all the simulations, the following magnetic parameters are used: $M_s = 140$ kA/M, $A_{ex} = 12$ pJ/m, $K_c = -610$ J/m³. To obtain the spectrum, the time-domain pulse width of 50 ps is chosen. This width provides an accurate excitement of modes up to 20 GHz bandwidth. Qualitatively, compared to the simulated disk spectra the spectrum of the tapered disk has more similarities in terms of an increased number of modes, interaction of the modes and also the slope of modes to the experimental data. So it is inferred that the actual geometry is more or less like a tapered disk.

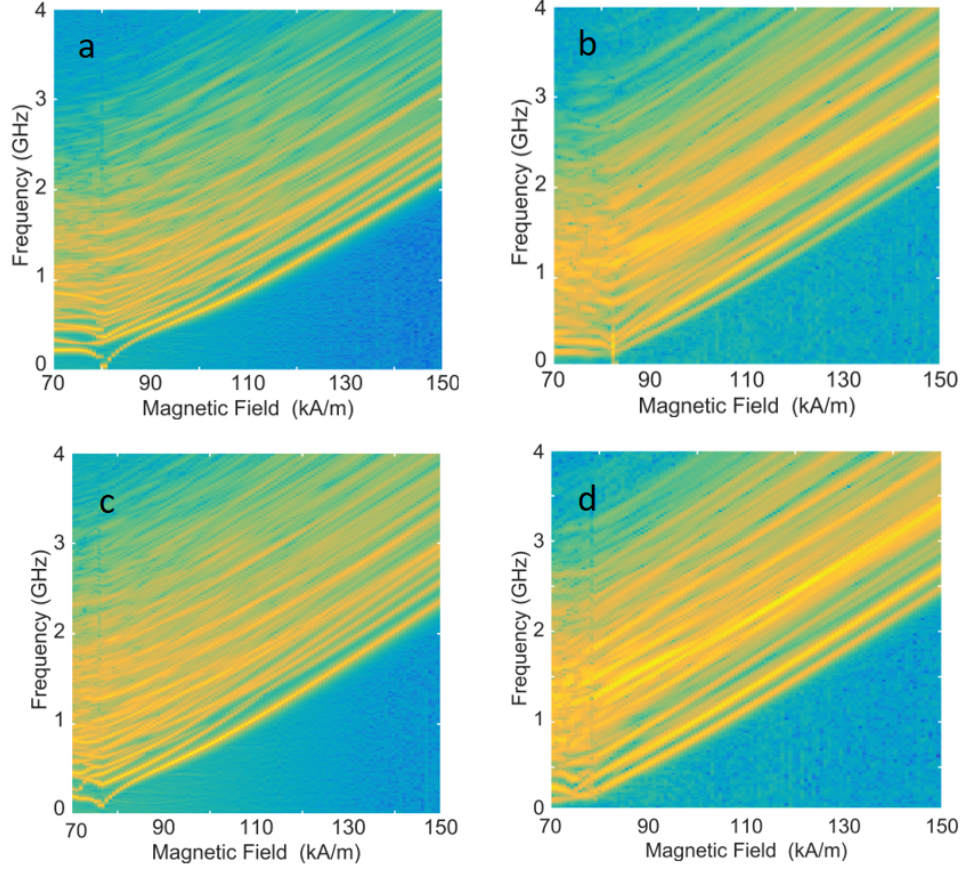


Figure B.21: The spectra of tapered disks with 980-nm diameter and different tapering angles. The tapered disk with a) $h_1 = 300$ nm and $h_2 = 100$ nm ($\theta = 11.5^\circ$), b) $h_1 = 300$ nm and $h_2 = 200$ nm ($\theta = 5.8^\circ$), c), $h_1 = 400$ nm and $h_2 = 100$ nm ($\theta = 17^\circ$), and d), $h_1 = 400$ nm and $h_2 = 200$ nm ($\theta = 11.5^\circ$). The other simulation parameters are kept the same and total running time = 40.96 ns (frequency steps = 24.41 MHz) is considered for b) and d), while the total running time = 163.84 ns (frequency steps = 6.1 MHz) is used for a) and c).

The finer resolution of panel a in Figure B.21 is presented in Figure B.22. Figure 3.17 shows more investigations, including the mode profiles of the first two modes at two fields.

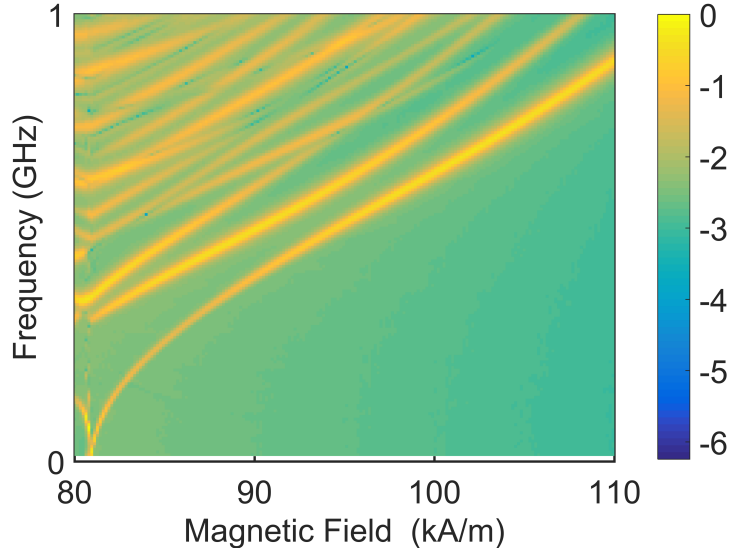


Figure B.22: Zoom-in spectrum of a tapered YIG disk with $h_1 = 300$ nm and $h_2 = 100$ nm ($\theta = 11.5^\circ$). The field steps of 2 Oe = 159 A/m and frequency steps of 6.1 MHz (total running time = 163.84 ns) are used to obtain the spectrum.

B.2 Future devices

B.2.1 YIG spheres with different dimensions

Magnetic spheres are a good test bench to obtain and study the Kittel expression. Because of the spheres' symmetry, the Kittel formula simplifies to $\omega = \gamma H$, which does not depend on the saturation magnetization and the anisotropy. However, to find the lowest possible FMR frequency in a YIG sphere, we should have a good estimate of the lowest field at which the structure is still in uniform magnetization.

The commercial YIG spheres have diameters as low as 250 μm . So, for a reference, we first simulate a 250 -nm diameter YIG sphere, where the exchange is still important. The 7.8125 -nm cell size is chosen to be smaller than the exchange length of 12.7 nm. Afterwards, a 250 - μm sphere (1000 times larger in diameter) is simulated with different (bigger) cell sizes. To obtain a faster result bigger cell sizes are chosen.

The M-H characterizations of spheres with two sizes are presented in Figure B.23 for field sweep-down. The smaller sphere keeps the uniform magnetization down to 18 kA/m, while the 250- μm sphere has a transition to a complicated state at 44 kA/m.

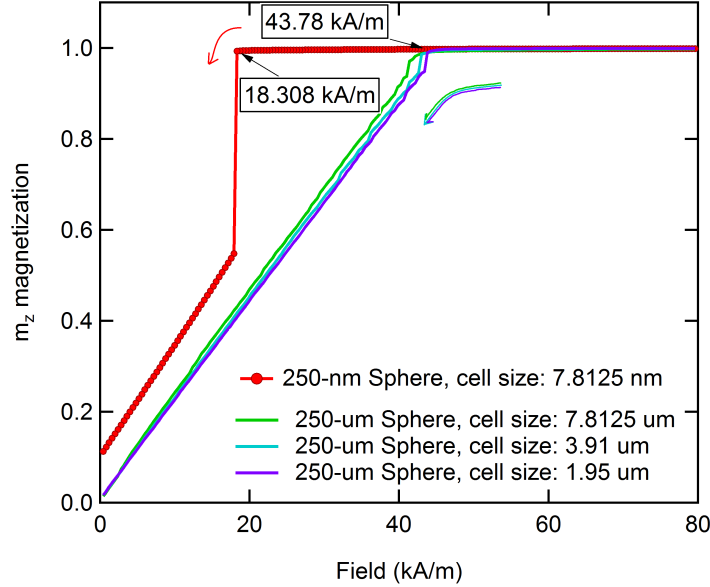


Figure B.23: Geometry effect on the magneto-static response of YIG spheres with cubic anisotropy (easy axis along z-direction). The M-H curves with the field sweep-down (H_z), from uniform magnetized spheres to low field, are presented. For the 250- μm sphere, the cell sizes bigger than the exchange length of YIG have been used: 1.95 μm , 3.91 μm , and 7.8125 μm . The M-H curves with different cell sizes show very similar results.

For cubic anisotropy, we need to determine at least two out of the three anisotropy vectors (axes). For the case of a negative anisotropy constant, we select the two hard axes in such a way that the crystalline easy axis (111) will be in the z-direction.

The magnetization profiles for m_z and m_x components are demonstrated in 250-nm and 250- μm diameter spheres, in Figure B.24. In the smaller sphere, the ground state is a vortex state with the core component pointing up at low field ($H_z = 0.4$ kA/m). However, the ground state in a bigger sphere is more complicated. To plot the profiles, some sample cuts of the spheres are

shown. By considering the constant $\gamma = 2.8 \text{ MHz/Oe} = 35.176 \text{ MHz/(kA/m)}$, the nanoscale sphere has a minimum limit of an FMR signal at 644 MHz, while for the larger sphere this limit is at 1.54 GHz.

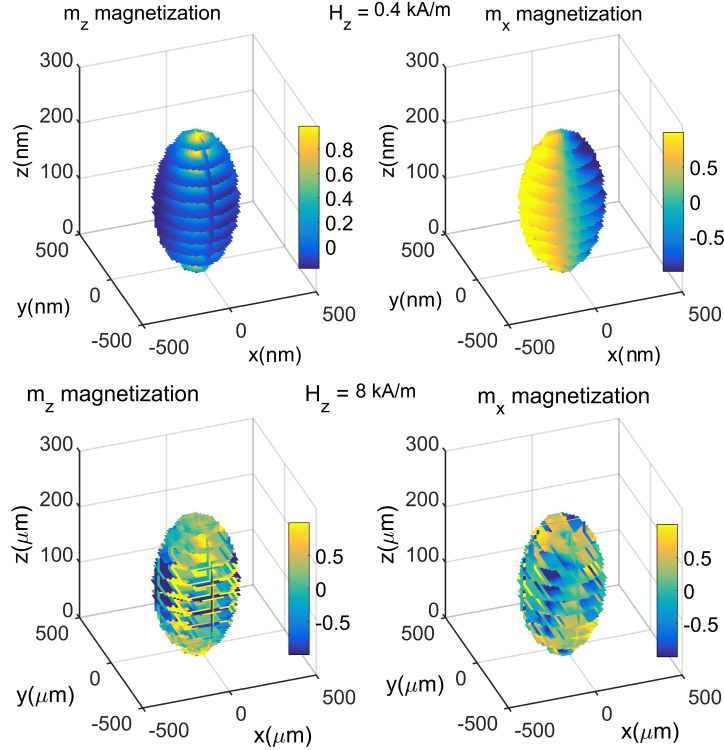


Figure B.24: Low-field magnetization profiles for YIG spheres with nano-meter and micro-meter scales. A vortex state in a 250-nm YIG sphere is shown at $H_z = 0.4 \text{ kA/m}$ with the m_z and m_x components presented in a) and b), respectively. A more complicated state in a 250- μm YIG sphere is demonstrated at $H_z = 8 \text{ kA/m}$ with the magnetization components m_z and m_x shown in c) and d), respectively.

B.2.2 Ellipse structure

Magnetic ellipses are interesting structures with the future possibilities, e.g. to study of a two-vortex state and the coupling between the cores. In this thesis, only the ground-state investigations are presented in Py ellipses with a minor-to-major axes ratio of one-half. Figure B.25 shows the possible ground states in Py ellipses with different thicknesses for an in-plane H_x^{dc} applied field. It seems the two-vortex state happens in 30 nm and higher thicknesses. The highest

thickness provides the two-vortex state is not investigated. The two-vortex states in a 40-nm thick Py ellipse are shown in Figure B.25.

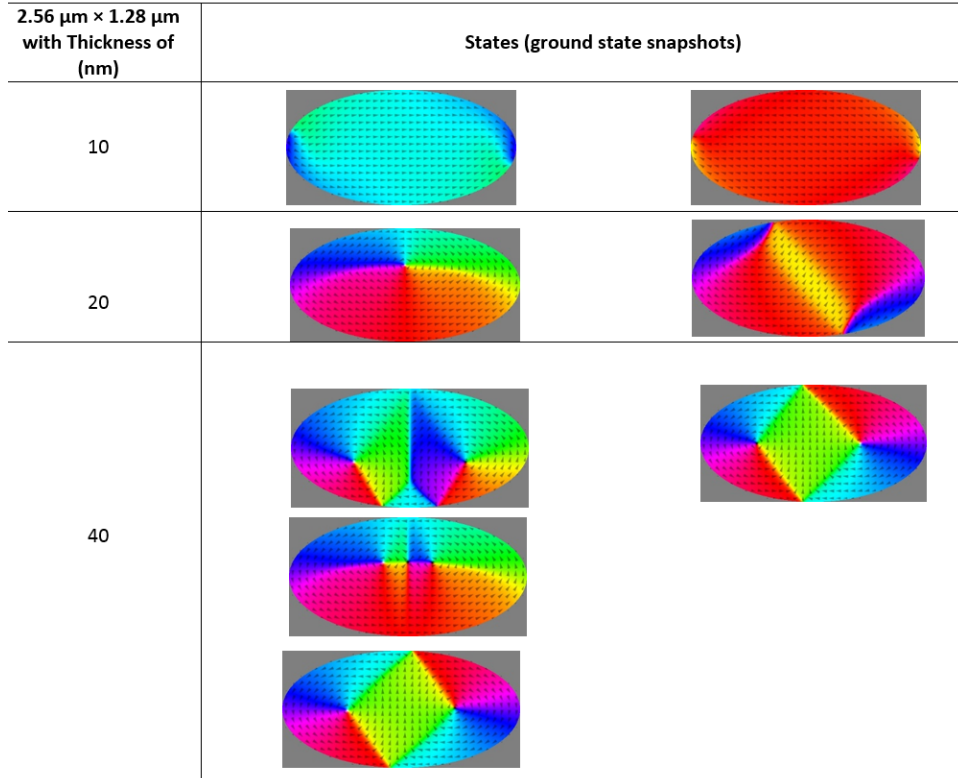


Figure B.25: Ground states investigation for various thicknesses in a Py ellipse with major axis of 2.56 μm and minor axis of 1.28 μm . For 10-nm thickness there is only a single domain along the major axis direction. For 20-nm thickness, it depends on the field direction: the magnetic field along the major axis supports a vortex state, while in the other direction only modifications of a single domain exist. Jumping to 40-nm thickness, there are varieties of two-vortex states as the ground state.

In the lowest thickness (10 nm), the shape anisotropy causes the system to have variations of only a single domain state. However, in the 40-nm thickness, there are combinations of two-vortex states. If the two vortices have the same chirality, there should be a domain wall or anti-vortex to keep the system stable. The hysteresis loops starting from variant ground states at 40-nm thickness might be very similar. However, the additional tiny jumps in the hysteresis loop, which could be related to annihilations, are significant changes. We obtain these different ground states by manually inserting the desired state in the

system and applying additional small fields to keep the local energy minimum. As a rule of thumb, similar field orientations can be used in the experiment, by having H_y^{dc} offset along the H_x^{dc} most of the time, to have the ground state be a two-vortex state with different chiralities in a 40 nm thick ellipse.

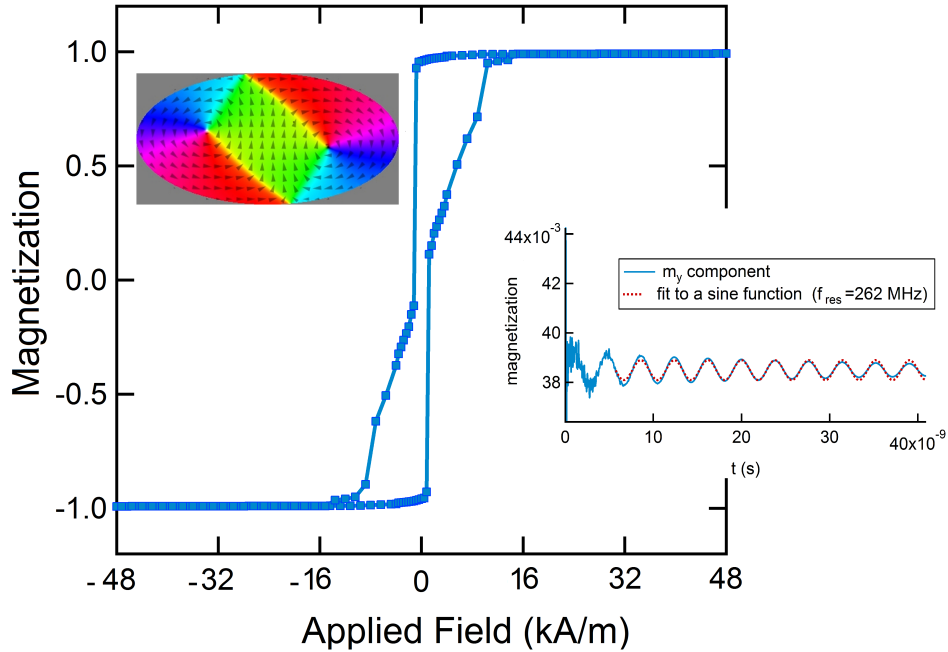


Figure B.26: The hysteresis loop of a Py ellipse with $2.01 \mu\text{m}$ major axis and $1.04 \mu\text{m}$ minor axis. The ellipse supports a two-vortex state with opposite chiralities at the low magnetic field. The top left inset shows the magnetization profile at $H_x = 1.2$ kA/m. The time evolution of the gyrotropic frequency at the two-vortex state is shown in the lower-right inset. A sinusoidal fitting (part of Thiele’s equation) has been used to obtain the resonance frequencies, $f = 262$ MHz.

The static characterization in a Py ellipse with 40-nm thickness and a minor-to-major axes ratio of one-half is presented in Figure B.26. The resonance frequency of the two-vortex state at $H_x = 1.2$ kA/m is also obtained with a pulse excitation. The lower-right inset shows the 40-ns run oscillation with the fitted sine function with a resonance frequency of ~ 262 MHz. The full spectrum of the ellipse will give us some hints about the two-vortex coupling and engineering the pinning site for two cores, as well as the boundary modifications for controlling the resonance of the two cores.

Appendix C

Technical Supports

C.1 TMRS instrumentation scheme

The instrumentation schematic for torque-mixing magnetic resonance spectroscopy is shown in Figure C.1. The RF fields (\mathbf{H}_1 and \mathbf{H}_2 , in y and z direction, respectively) are produced at the Zurich UHF lock-in amplifier reference (multifrequency (MF) and frequency modulation (MOD) options are installed, [45]) and each output to separate RF power amplifiers (ENI 510L with 45 dB gain and 1.7 MHz to 500 MHz bandwidth).

Both signals are sent through microwave transmission line (TL) geometries designed to produce local orthogonal RF fields at the region of the device chip housing the torque sensor (described in the next section). Device motion is detected using optical interferometry, with the torque sensor and substrate forming the interferometric cavity. The reflected intensity signal from the photodetector is demodulated at the difference frequency ($f_2 - f_1 = f_{\text{mech}}$) to acquire the dynamic response of magnetization, where f_{mech} is the torsional resonance frequency of the torque sensor. Accompanying $H_2 = 190$ A/m is a small RF field $H_3 = 23$ A/m. H_3 is oriented along the z-axis and monitors the net magnetic moment using torque magnetometry at a frequency slightly off the f_{mech} resonance peak.

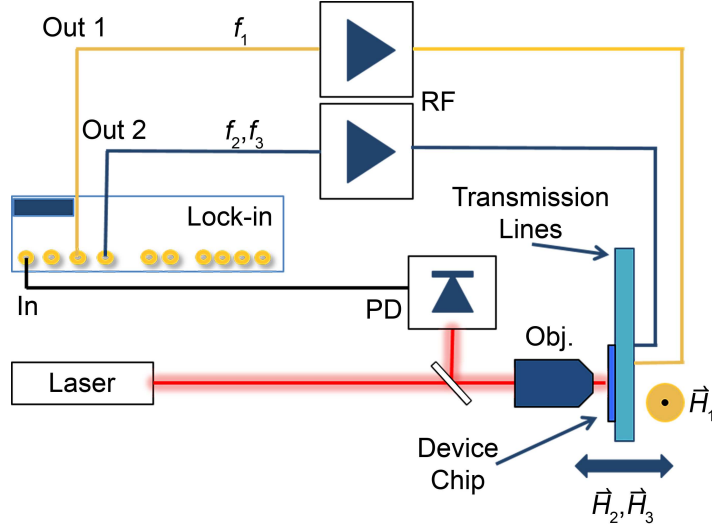


Figure C.1: Instrumental schematic for torque-mixing magnetic resonance spectroscopy. RF signals f_1 and f_2 are generated at the lock-in and power-amplified. A small signal f_3 can also be applied and demodulated to measure the net magnetization simultaneously with the dynamic response. The signals are sent to a microwave transmission line-printed circuit board (blue-green) designed to generate orthogonal RF fields \mathbf{H}_1 and \mathbf{H}_2 (and \mathbf{H}_3 , if desired) at the location of the torque sensors (which are housed on a SOI chip). The deflection of the sensor is detected interferometrically using a laser source focused through a microscope objective (obj.) and the modulated reflected light is detected with a fast photodetector (PD).

For spectroscopy, f_1 and f_2 are concurrently swept while maintaining the f_{mech} frequency difference, using the internal capabilities of the Zurich lock-in. The dc applied field \mathbf{H}_0 is provided by a permanent magnet housed on motorized linear positioner. Computer control is through LabView programming with data read directly from the lock-in through a high-speed LAN interface. The measurements are conducted at room temperature in a home-built vacuum chamber at a pressure of $\sim 10^{-4}$ mTorr.

For extending frequency ranges to the Gigahertz, we utilize an SRS signal generator (SG396 with a 6-GHz frequency bandwidth) followed by amplifiers (MiniCircuits with frequency ranges between 200 MHz-2.8 GHz). The power amplifiers because of having the lower bandwidth put the experimental bandwidth limits. A Zurich 10-MHz internal clock source synchronizes two signal generators, as shown in Figure C.2. The amplified tones are sent to transmis-

sion lines (TLs), which are producing in-plane and out-of-plane RF magnetic fields. Through LabView programming, we adjust the frequencies of SRSs so that the two tones have a frequency difference of f_{mech} .

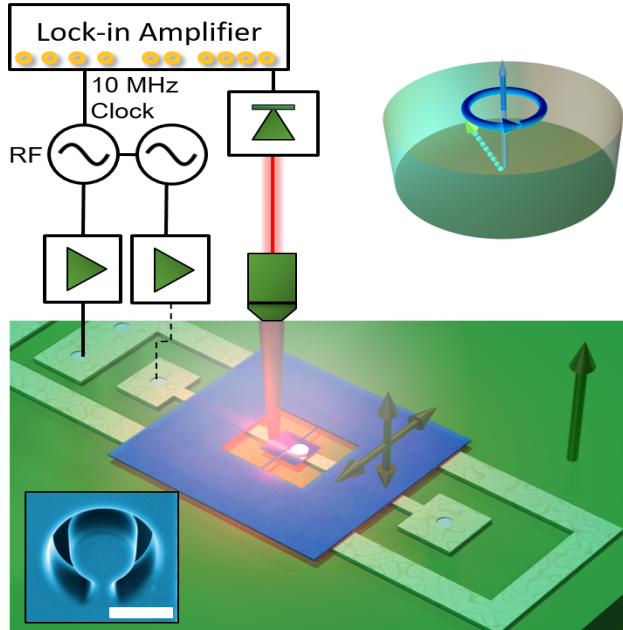


Figure C.2: Schematic of setup with extension of frequency bandwidth. A 3D rendering of a sample on top of TLs is presented. Utilizing signal generators and Mini-Circuits power amplifiers allows the bandwidth to increase to GHz ranges.

C.1.1 Setup details

The results presented in this thesis are obtained through measurements in three setups, with slight differences. The measurements are initiated with a conventional nanomechanical magnetometry with one coil producing a perpendicular RF field. The chamber contains a cooling system that allows the investigation of a sample at stable temperatures from approximately 3 K to room temperature. Because of limited space in the cold finger, we use an external Helmholtz configuration coil, with low bandwidth, to make an additional in-plane field for susceptibility harmonic investigations. Then a setup with two crossed coils was used, and finally we replaced the coils with TLs to extend the frequency

bandwidth.

In all the setups, the Michelson interferometry was used with a red laser, beam splitter, and long-distance objective to focus the laser spot on the mechanical device in the high vacuum regime. A lock-in technique was utilized to resolve the mechanical motion of the paddle sensitively. Before using Zurich Instruments, we used an SRS DSP lock-in amplifier (SR 830). From the internal source, a tone at the mechanical frequency to the RF was sent to the RF coil. Then, we separated the dc and RF signal from the PD readout. The RF signal returned as a lock-in input, from which, both amplitude and phase were used to determine the mechanical mode – movements of the paddle’s two side should be in an out-of phase in the torsional mode and in-phase in the flexural mode. The PD dc signal is very important too, since it can provide a big picture of the device. A significant breakthrough in our measurements was the use of a Zurich lock-in amplifier with many digital modules and features, such as scope, and a spectrum analyzer.

There are two possible ways for spatially rastering over the sample: changing the sample position in a fixed laser beam, or fixing the sample position and changing the beam position. We use the former case with piezo controls to adjust the sample position, since aligning the optics is more sensitive. Although a fixed sample position could overcome signal drifts usually caused by touching the chamber to optimize the sample position, the heating sources like laser heating or the local RF heating can also cause drifts. The laser optical power is adjusted to decrease the heating effect on the resonator. Typical values of 300 nW to 60 uW have been used. Then the reflected light comes to a photodetector, with a 125-MHz-free range (NewFocus 1801).

For dc field calibration, a Senis 3-axis Hall probe (HP) is used. One method is to perform the field calibration before and after taking measurements. We have the advantage of putting the HP as close as possible to the sample position in our measurements. Another method is to use a single-crystalline,

250nm-diameter yttrium iron garnet (YIG) sphere on top of TLs, where the sample supposed to place. Then, the corresponding fields are obtained from a frequency read-out via a vector network analyzer (VNA E5072A) based on a relationship between ferromagnetic resonance frequencies and corresponding applied magnetic fields. For a magnetic sphere, magnetic resonances have a known linear relationship with the magnetic field $\omega = \gamma\mu_0 H$ that is independent of demagnetizing factors. By considering $\gamma = 28.025$ GHz/T, the field axis is calibrated. The magnetic resonance calibration method provides a very accurate field mapping, however, it is limited to a specific high field range. The Kittel expression needs the uniform magnetization and our YIG sphere does not have uniform magnetization below ~ 40 kA/m, as shown in Appendix A, Section B.2.2.

In addition, with high RF signals (GHz range), shielding the chamber from noise is very important. To reduce the high frequency self-resonance of the chamber/TLs, some copper sheets have been employed. Interestingly, the position of copper sheets is very critical to reduce the main noises at 1.2, 1.58 and 2.5 GHz.

C.2 Torque sensor

We used three procedures to make torque sensors: in the first method, a Py disk was patterned via sputtering (electron beam deposition) through a stencil mask on top of a SiN membrane. Then, focused ion beam (FIB) milling was used to fabricate the torsional sensor (triple paddle) [43]. In the second method, electron beam lithography and a lift-off process were used to pattern an array of $1 \mu\text{m}$ and $2 \mu\text{m}$ diameter Py microdisks on nanomechanical torsional resonators [33].

The nanomechanical torsional resonators are patterned from a silicon-on-insulator substrate (Si device layer thickness = 300 nm, buried oxide thickness

= 1 μm) through electron beam lithography, reactive ion etching of the device layer, and release the sensors through buffered etching of the oxide layer. CO_2 critical point drying completed the process. In the third method, using FIB nano-manipulation, a single-crystalline YIG disk was cut and put on a pre-fabricated nanomechanical torsional resonator. More details about the mechanical sensor and fabrication with FIB are discussed in the following sections.

C.2.1 Mechanical and spin sensitivities

The sensor geometry is a torsional resonator consisting of a thin torsion rod (250 nm wide, torsion rod lengths ranged from 12 to 30 μm) with a square paddle at the center, designed sufficiently large enough to affix a mesoscopic sample (5.8 μm square). The sensor is operated at its fundamental mechanical torsional resonance mode, $f_{\text{mech}}=1.82$ MHz (COMSOL Multiphysics, a finite element program is used to determine the torsional resonance frequencies).

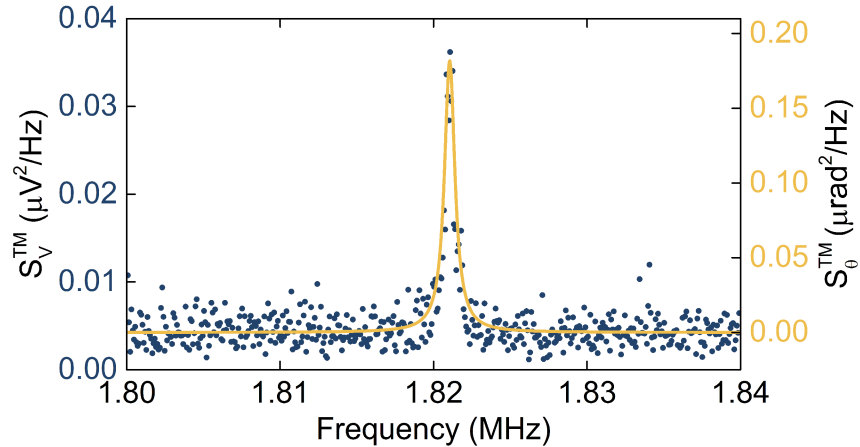


Figure C.3: Signal power spectral density from thermomechanical noise spectrum of the torque sensor supporting a YIG disk measured at room temperature, with no applied field. The area under the peak calibrates the angular displacement (right-side axis). thermal power spectral density, S_V^{TM} , was calibrated with the torque sensor deflection spectra, $S_X^{\text{TM}}(f)$. The measurement was taken using $40\mu\text{W}$ of laser power incident in the objective, with the sample in a vacuum of $\sim 10^{-4}$ mTorr. The mechanical quality factor is $Q=2890$.

The calibrated, thermomechanical angular-displacement noise spectrum is

shown in Figure C.3 (the calibration procedure is described in detail in [113]). The signal power spectral density, $S_V^{TM}(f)$, is related to the angular displacement, $S_\theta^{TM}(f)$, by $S_V^{TM}(f) = \alpha S_\theta^{TM}(f) + S_V^n$ where $\alpha^{1/2} = 0.41 \mu\text{V}/\mu\text{rad}$ is the responsivity factor and $S_V^n = 0.004 \mu\text{V}^2/\text{Hz}$ is the technical experimental noise [114] (constant over this frequency range). The torque sensitivity of the device is $3.5 \text{ aNm}/\text{Hz}^{1/2}$, based on a calculated torsional spring constant for the sensor of $\kappa_{tor} = 2.2 \times 10^{-11} \text{ Nm}/\text{rad}$.

The spin sensitivity is high in comparison with most implementations of inductive detection (and sensitivity comparable to the best state-of-the-art technique, superhigh frequency ESR using electromagnetic micro-resonators [115]). The torque on a single Bohr magneton, in a typical dither amplitude for modulated ESR, $H_2 = 100 \text{ A}/\text{m}$, is $1 \times 10^{-27} \text{ Nm}$. Existing nanomechanical torque sensors with zeptoNewton-meter (10^{-21} Nm) [116, 117] sensitivity are therefore capable of resolving 10^6 spins, or (for example) 10^7 classical spins precessing with a cone angle of 0.1 rad . The spin sensitivity in pulsed magnetic resonance applications, in which torque will be sampled stroboscopically after a programmable interval of free precession, will be less on account of the sampling duty cycle. A portion of the continuous-wave sensitivity may be recovered with higher amplitude H_2 torque-sampling pulses.

C.2.2 Fabrication a monocrystalline, mesoscopic YIG disk

To overcome the limitations and difficulties of lithographically patterning mesoscopic magnetic garnet structures, FIB was employed to sculpt a micromagnetic disk from a bulk YIG crystal. A nano-manipulation probe (housed within the FIB chamber) was then used to transfer the YIG disk onto the torque sensor. The source material is a $1 \text{ mm} \times 1 \text{ mm}$ chip diced from a commercial wafer of thick-film ($108 \mu\text{m}$) YIG grown by liquid phase epitaxy on gadolinium gallium

garnet [86]. A side of the die is mechanically polished to produce a sharp ninety-degree edge, and then coated with 5 nm of carbon to reduce charging effects during FIB milling.

Figure C.4 shows an intermediate result after the first three major steps of the milling procedure. In the first step, a trapezoidal back-trench (on the left in Figure C.4A) is milled, leaving a YIG lamella $3.5\mu\text{m}$ wide at the edge of the chip. The back-trench allows for the evacuation of sputtered material during subsequent milling steps. In the second step, the crystal is rotated ninety degrees, and a similar cavity milled $1\mu\text{m}$ from the other edge to create a through-trench. The result is a bridge of YIG suspended across the through-trench. The bridge is then thinned to $450 \pm 10\text{ nm}$ by fine polish-milling of the underside.

The third step of FIB processing defines a disk with a design radius of 650 nm, by milling a circular channel through the bridge with the ion beam at normal incidence to the crystal surface (figure C.4A). The final measured radius of the disk is $550 \pm 30\text{ nm}$, smaller than the design radius on account of the finite width of the ion beam. The resultant *magnetic* disk is smaller than the outside dimensions of the material structure, being encapsulated in a non-magnetic, ion-damaged ‘dead layer’ [118]. The magnetic damage from the initial FIB fabrication steps producing the suspended YIG bridge has been shown to be confined to a layer less than 40 nm thick [119]. The milling strategy minimizes but does not eliminate normal-incidence ion exposure of the final structure. A small normal-incidence dose occurs from the wings of the ion beam (shape approximately Gaussian) when the outline of the disk is defined, and again when brief ion imaging occurs during the specimen transfer to the torque sensor. Quantification of the ion damage is a topic of ongoing study. Here, our estimates of the final magnetic disk thickness (250 nm), and radius (490 nm), are based upon comparisons of the magnetic measurements with micromagnetic simulations.

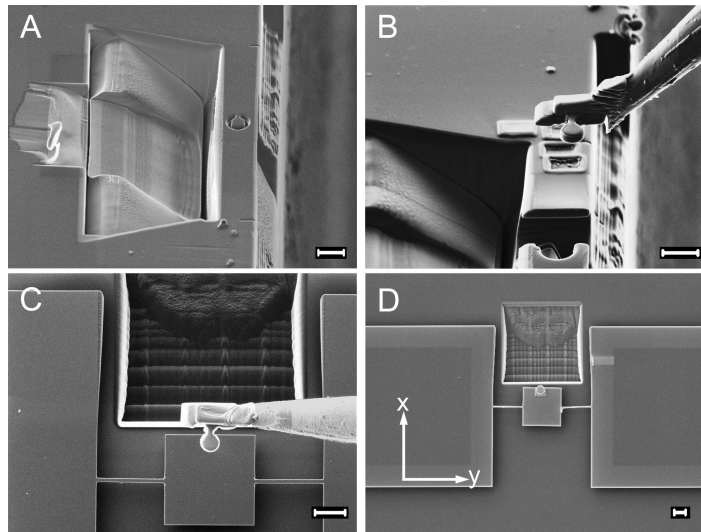


Figure C.4: Scanning electron images outlining the fabrication process of a nanomechanical torque sensor housing a single-crystal YIG micromagnetic disk. (A) The circular trench was defined in the thinned suspended YIG beam by three-dimensional FIB milling. (B) A nanomanipulation probe was attached to the section of the YIG beam (false-colored) adjacent to the disk and the section was removed for transfer to a prefabricated torsional resonator. (C) Top-down image during the approach of the YIG disk onto the resonator. (D) The completed torque sensor after the disk was bonded by electron beam-assisted platinum deposition and released from the nanomanipulation probe. All scale bars are $2\mu\text{m}$.

The only FIB modification to the prefabricated SOI device prior to attachment of the disk was the creation of a cavity in the silicon handle layer to ensure that the micro-manipulator did not contact the substrate during disk transfer. Electron-beam induced deposition of trimethyl (methylcyclopentadienyl)platinum(IV) precursor gas creates an organo-metallic weld that bonds the YIG structure to the manipulator. The tab on the edge of the disk enables this attachment without affecting the disk itself. The disk is released from the bar by three small cuts around the manipulator attachment site, and transported to the torque sensor (figure C.4B). The disk position in 3D is gauged using alternating ion and electron imaging from the two beam perspectives 54 degrees apart, until contact is made with the center paddle (figure C.4C). The net ion dose to specimen from this procedure is approximately 4^{15} ions/cm² (10 pA current, 20.13s image time, 5 frames, 0.0045 fraction of image area taken up by the disk). Once in contact, the disk is attached to the paddle with another platinum organometallic weld and separated from the tab, resulting in the completed device (figure C.4D).

C.3 Design of microwave printed circuit boards (Transmission Lines)

For generating orthogonal RF fields (in- and out-of-plane, \mathbf{H}_1 and \mathbf{H}_2 (and \mathbf{H}_3)) to the nanomechanical torque sensors, two separate planar TL circuits were patterned on the same FR-4 printed board. The printed circuit board layout is presented in Figure C.5a and the 3D rendering with the calculated fields are shown in Figure C.5b. The in-plane field is produced by the stripline at the board surface (brown, designated TL₁) and the rectangular loop (yellow, TL₂) generates the out-of-plane field components.

Each loop is connected to 50 Ohm TLs (top and bottom of the ground plane, green) and driven by separate RF power amplifiers (ENI 510L). The chip

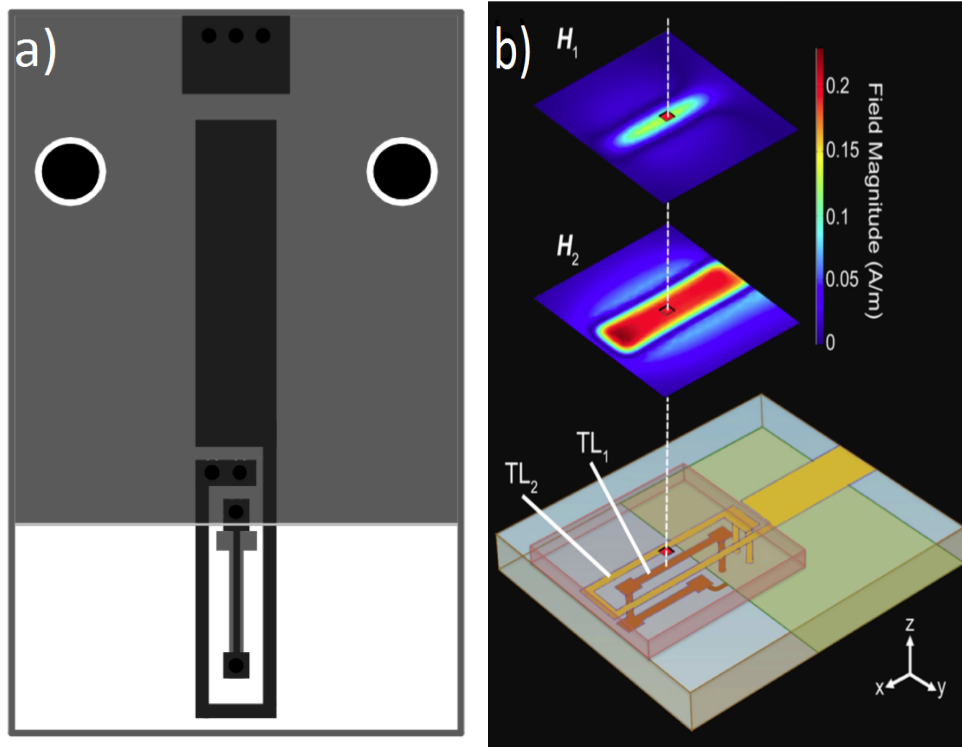


Figure C.5: Microwave TL geometry for generation of orthogonal RF magnetic fields. a) Transmission lines layout with PCB footprint of $1.7 \text{ cm} \times 3 \text{ cm}$. b) The loop (yellow) produces the out-of-plane RF field while the loop (brown) generates the in-plane component. The loops are driven by TL above and below the ground plane (green). Field strengths from TL_1 and TL_2 are shown in the color scale for a 1 mA current. The red square above TL_1 represents the torque sensor location. The sample substrate (transparent red) is $10 \text{ mm} \times 10 \text{ mm} \times 0.7 \text{ mm}$.

(transparent red block) holding the nanomechanical torque sensors is centered and mounted atop the loops (the torque sensors are located at the center of the chip shown as a $250 \times 250 \mu\text{m}^2$ red square). The calculated field magnitudes (using COMSOL Multiphysics), \mathbf{H}_1 and \mathbf{H}_2 , in the plane of the sensor are shown for 1 mA amplitude drive currents, which at the sensor location are approximately 0.13 A/m for \mathbf{H}_1 and 0.19 A/m for \mathbf{H}_2 . The symmetric loop design reduces mutual inductance and cross-coupling of the fields generated by each loop.

Figure C.6 shows in addition the simulated spatial profile of the in-plane RF field component from TL_1 and the out-of-plane component from TL_2 . With the present sample height of 0.7 mm above the microwave circuit board, positional accuracy of $\pm 100 \mu\text{m}$ is sufficient to ensure high directional accuracy of the RF fields. Considering the sample-board separation as a design variable, there is a trade-off between the accuracy of sample placement and the field strengths per unit current.

C.3.1 Transmission lines calibration

Zurich lock-in and RF amplifiers were used to drive the current through TMs (from 50 MHz to 500 MHz). We first characterize Zurich and ENIs (RF amplifiers) as functions of frequency to characterize TMs. The frequency spectra of Zurich internal generators were characterized for some amplitudes, as shown in Figure C.7. We directly connected the output (internal generator signal) to the input. In addition, low-amplitude drives were considered because of a limit on the input of the Zurich detectors (max of ± 3.5 V).

There was a tiny decrease in the output, around 4 % of the initial value for each response at the end of the frequency sweep, which is insignificant. However, for obtaining a uniform drive, a correction related to the drop function was considered in LabView programming.

We used two ENIs with a gain of 45 dBs to amplify the RF voltage corre-

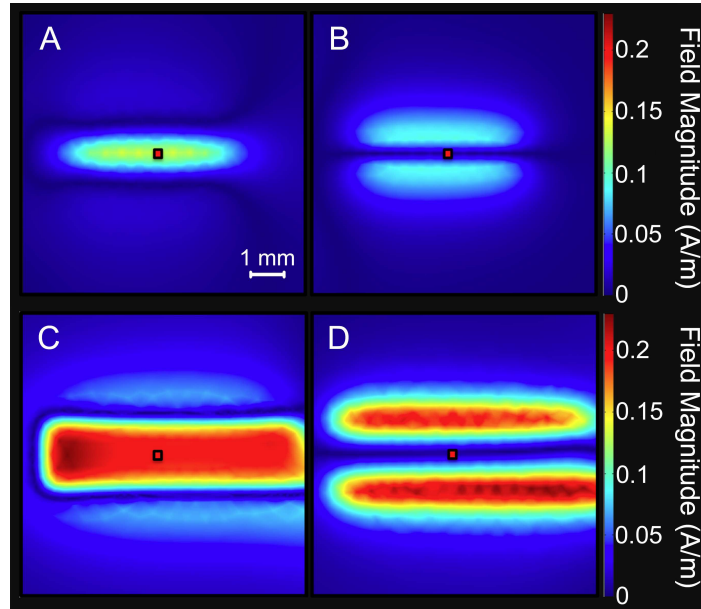


Figure C.6: Simulated RF field profiles to illustrate the variation of RF field strengths and directions if the sample placement is off-center. a), b): Out-of-plane, in-plane field strengths from the horizontal loop, for a 1 mA current. c), d): In-plane, out-of-plane fields strengths from the vertical loop, for a 1 mA current. Scale bar = 1 mm.

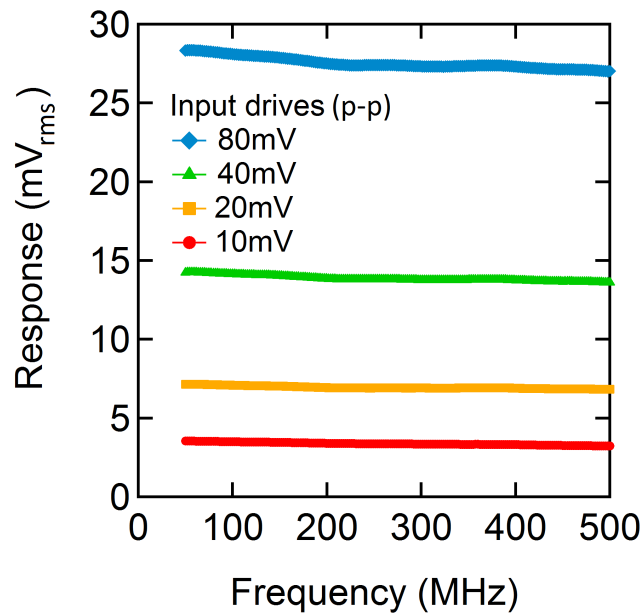


Figure C.7: Calibration of Zurich input versus frequency. Various amplitudes of input drive are examined to obtain the frequency characterization of Zurich internal signal generators. The output amplitude is presented in (rms) values, while the Zurich input is presented in peak-to-peak (p-p) voltage.

sponding to H_1 and H_2 . We drove each amplifier individually via Zurich input and read the frequency response through Zurich as well. Considering the input limitation, we adjusted the input voltage so that by applying the amplifiers, the output to the Zurich would be less than a one V_{rms} . The frequency of two identical ENIs are presented in Figure C.8. One of the amplifiers has a self-resonance at $f = 460$ MHz.

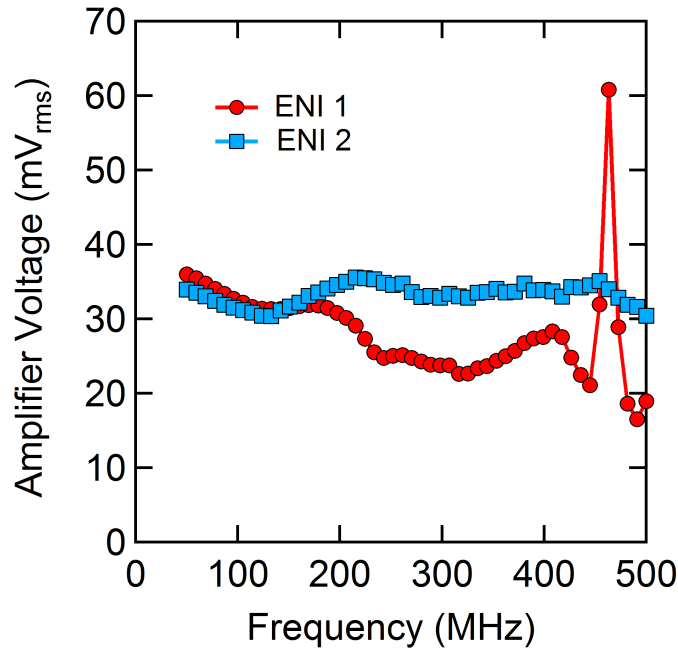


Figure C.8: Calibration of the ENI output versus frequency. The frequency responses are obtained by Zurich internal generators.

Next, we used a current probe, Tektronix CT1 with 1-GHz bandwidth to calibrate the RF fields. The current probe was placed as close as possible to the input terminal to measure the current through the lines. However, there is an experimental limit by the position of rigid connectors where the current exactly at the TLs could not be obtained. We used the Zurich Instrument and ENIs to set H_y and H_z lines at 80 mV_{p-p} and 125 mV_{p-p} , respectively, and the frequency is swept from 50 MHz to 500 MHz.

Figure C.9a shows each line field calibration versus frequency in the case where the other line is terminated. We performed some other tests for open end

and termination with long wire (10 ns). The configuration of the latter case is presented in Figure C.9c. The load of other line did not have a significant effect on the field calibration.

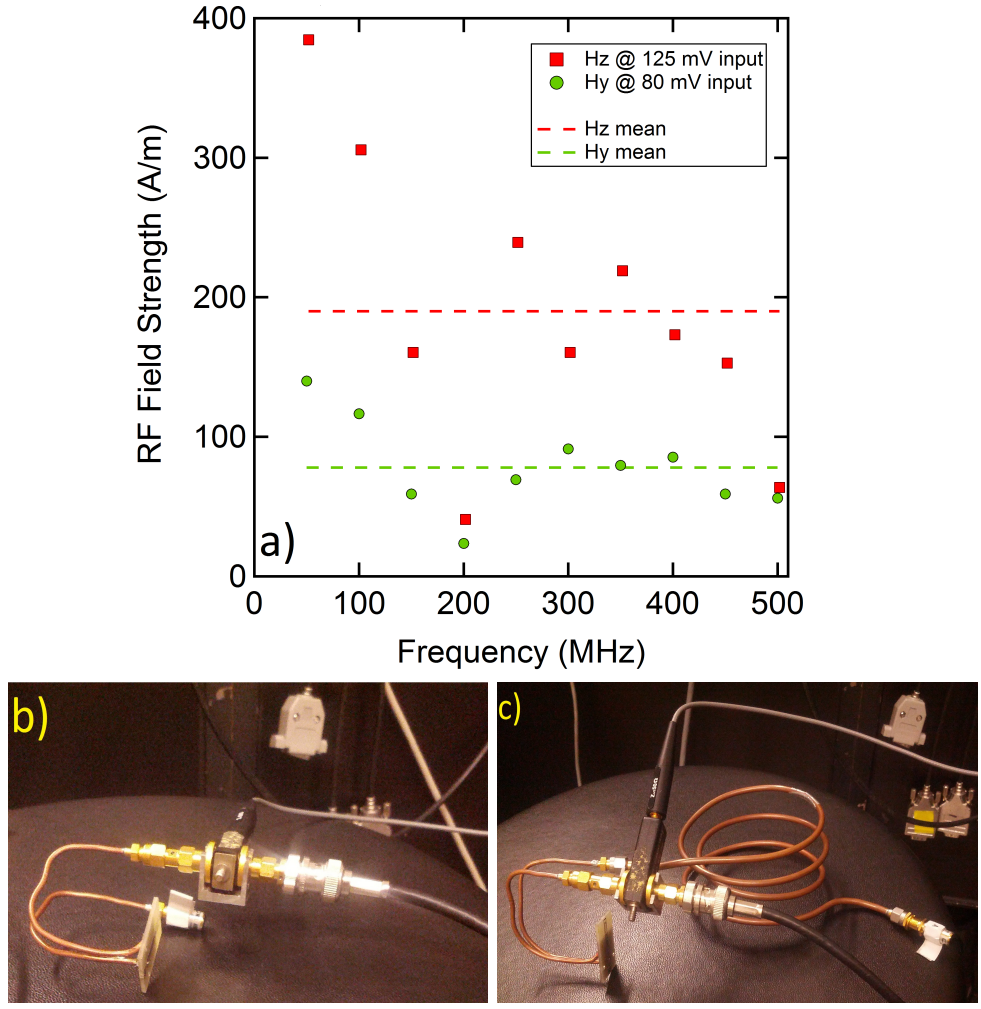


Figure C.9: Field calibration of TLs versus frequency. The field average values are $H_y = 78 \text{ A/m}$ and $H_z = 190 \text{ A/m}$. b) and c) The configurations for the current measurement for a terminated end and terminated with a longer wire (10 sec delay).

The field strengths are obtained from the current readout of the probe and the calculated ratios of 0.13 A/m for H_y and 0.19 A/m for H_z , for 1 mA amplitude drive currents.

C.3.2 Thermal investigations

The calibration by Zurich Instruments provides the limited bandwidth, so in order to cover the calibration for GHz frequency ranges, we use thermal imaging. In addition, we used higher bandwidth amplifiers (mini-circuits power amplifier). Figure C.10 shows the amplifier's gain over a frequency range of 300 MHz to 2.8 GHz. The gain is almost flat, 44.5 ± 2 dBm in the range of 500 MHz and 2.6 MHz. Beyond this range, there are sharp jumps in the gain characterization.

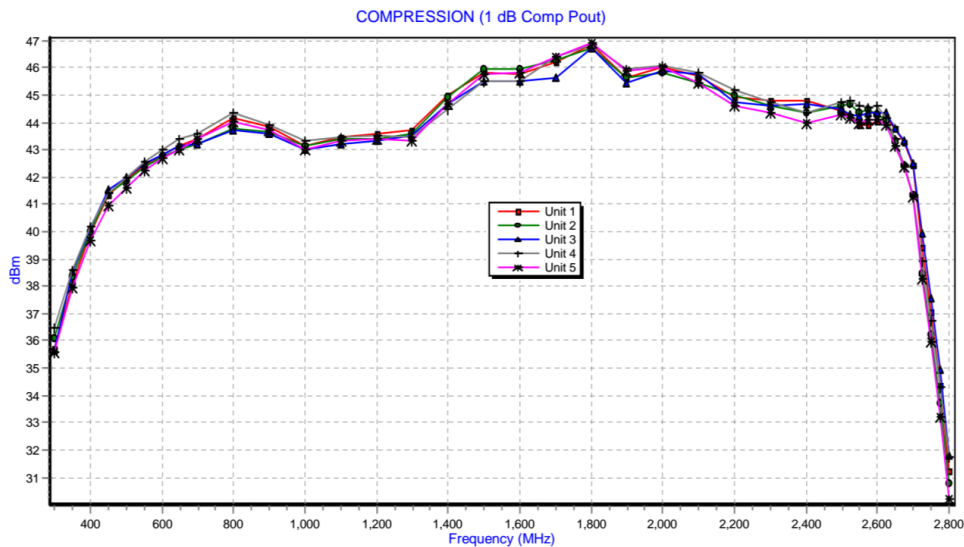


Figure C.10: The frequency-dependent gain of mini-circuits power amplifier. Taken from device datasheet.

It would be helpful to use thermal tests to investigate losses in the system. It looks like the current-carrying traces are the main source of heating and RF losses. We used a thermistor to measure the thermal effect of TLs heating. The thermistor was fixed in the place, close to TLs, by using a kapton tape wrapped it with semi-rigid wire to one of the posts in the chamber. The temperature was obtained by a direct readout of the thermistor voltage, and by transforming that value to Celsius degrees from a reference table. At each reading, we captured the transmitted power to the TLs through a Bird wattmeter that was placed after the amplifier. There was very little reflected power (towards the

amplifiers) in the measured cases. In Figure C.11a, at a constant amplitude drive (-10 dBm), the frequency was set with a couple of minutes wait time for reading out the power and temperature.

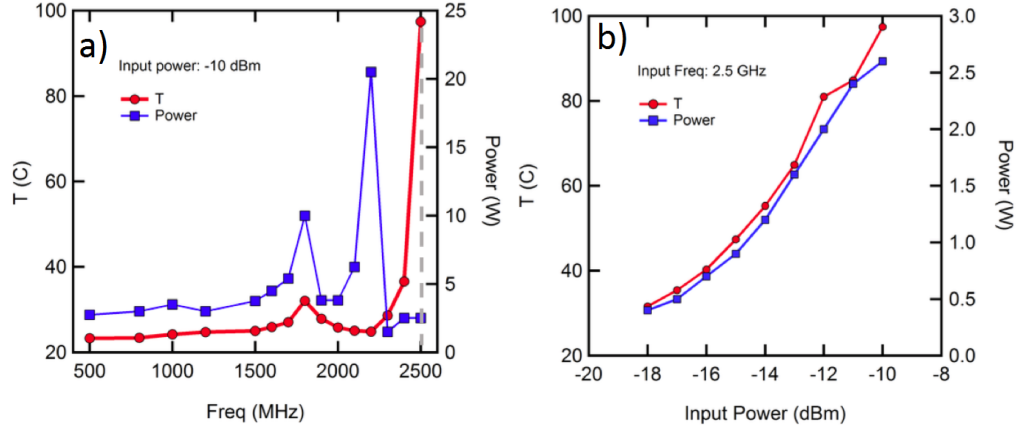


Figure C.11: Thermal investigation about working frequency range of TLs in vacuum. a) at a given input (-10 dBm), temperature of thermistor and transmitted power of the transmission lines. b) The temperature and transmitted power versus the input power are plotted at 2.5 GHz.

Above 2 GHz the temperature begins to rise rapidly, while the power drops. From measurements in air, it appears the trend is very similar to what happens with vacuum data. But the temperature did not jump higher than 100 °C and the additional jump in power appears at 1.8 GHz. The two peaks at 1.8 and 2.2 GHz tend to be internal resonance of TLs, at which the reflected power is very high. Higher frequency was not achievable because the wattmeter elements could not reach 2.8 GHz.

In addition, a parabolic relation between the temperature and input power was obtained. Figure C.11b shows the temperature and transmitted power as a function of input power at 2.5 GHz. The temperature changes slowly at a lower input drive, and varies more at a higher drive, e.g., by lowering the initial drive to half, $dT \approx -33$ °C.

On the other hand, we use an IR camera, Reed-R2100 with 0.7 mm resolution (minimum focus 20 cm, 3.3 mrad), to perform thermal scans. An Si chip is placed on top of the TLs and is held down with black electrical tape on each

side. The chip is nearly transparent at these wavelengths.

Figure C.12 shows the thermal scans for each line driven at -5 dBm and $f = 2.4$ GHz. The spatial sweeps show the temperature gradient. The H_z RF line heats up about 10 °C higher than the H_x line and it appears that there is more heat along the left side of the loop.

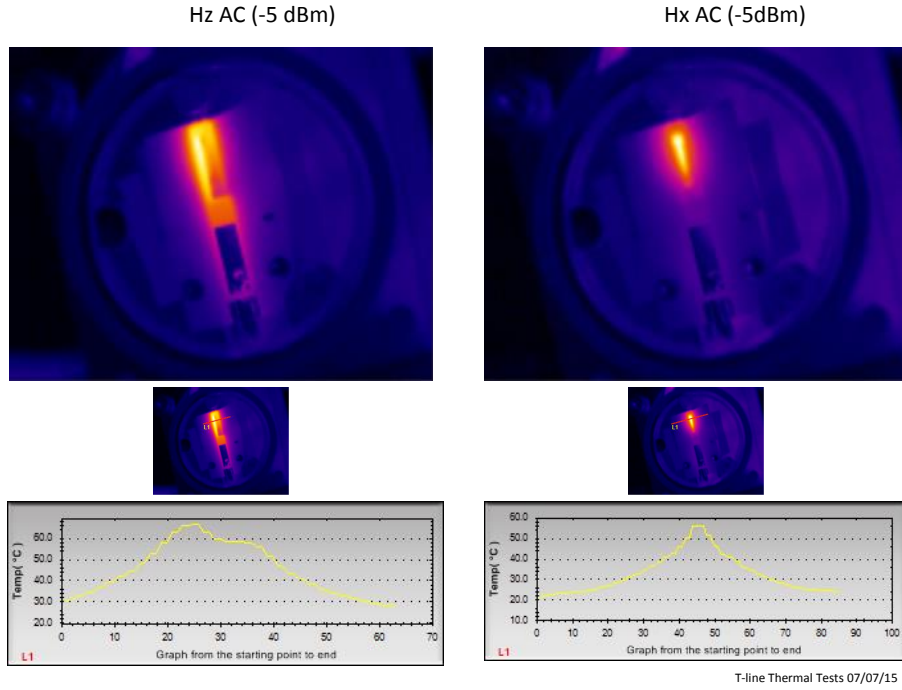


Figure C.12: Thermal scans of the transmission lines at $f = 2.4$ GHz via Fluke Ti32 with the standard lens.

C.4 VNA measurement

Vector network analyzer measurements are very straight forward. We connect the TLs input to the VNA, and then at the set power, the spectrum is obtained from 100 kHz to 8.5 GHz. We use VNA to characterize the TLs and also to obtain the field calibration, as well as a gyromagnetic ratio of YIG film. The details are presented in the following section.

C.4.1 TMs characterization

S12 and S21 are overlapped and has two self-resonance peaks at 42.6 MHz and 298 MHz, as shown in Figure C.13. The S11 has resonances at 4.36 and 6.42 GHz, while S22 has resonances at 4.42 and 6.67 GHz.

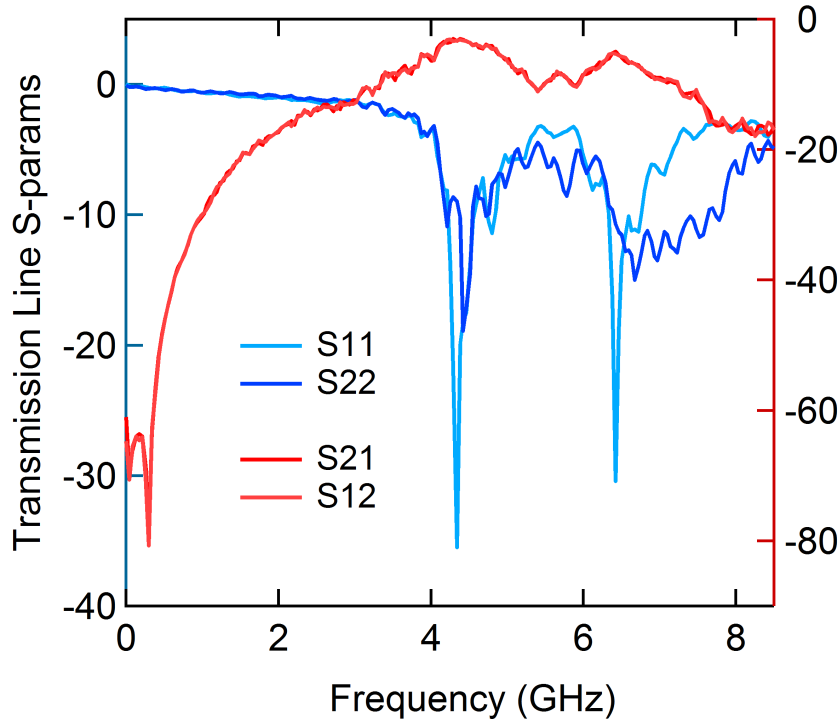


Figure C.13: Calibration of TMs via VNA E5072A. S11 and S22 are plotted on the left axis and S12/S21 on the right axis.

Although the frequency characterization of TMs did not show any self-resonance in 500 MHz-2.5 GHz range, connecting cables and the chamber itself can change the resonance spectrum.

C.4.2 Gyromagnetic ratios

The YIG, by virtue of having a very narrow ferromagnetic linewidth, is an ideal candidate to be used in the VNA measurements (S-parameters). A single-crystalline, 250 μ m-diameter YIG sphere is put on top of TMs and the S-parameters (S21) are directly read out via a VNA E5072A. The 1-axis HP

BGM-101 field sensor from Brockhaus with 0.1 mT resolution has been used to obtain the field values.

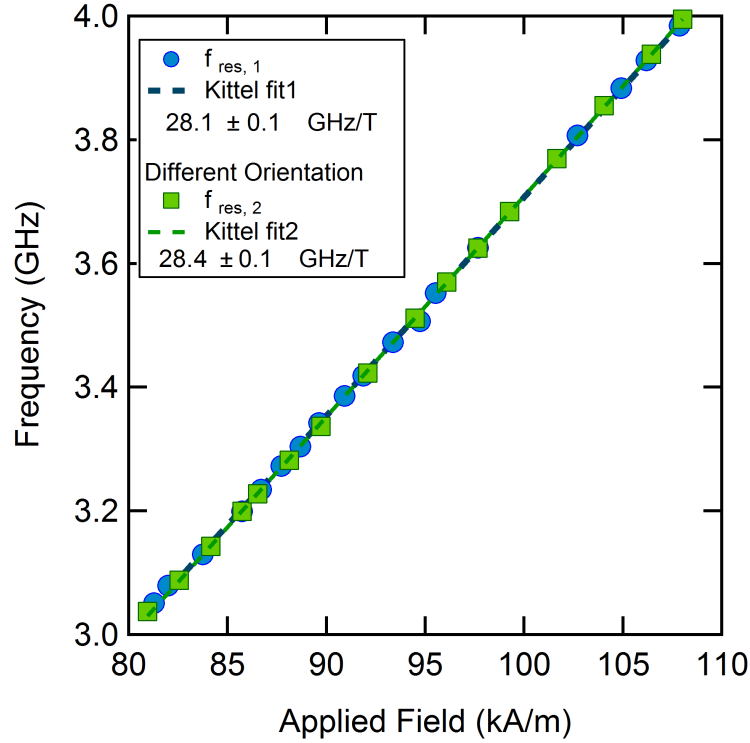


Figure C.14: Obtaining a gyromagnetic ratio in a 250- μm YIG sphere. Magnetic resonance frequencies are obtained in the presence of a permanent dc magnet, the position of which is changed manually. The sharp resonance at each field is fitted with a Gaussian function to obtain the exact resonance frequency, while the field is read out via a 1-axis HP. Two orientations are considered, and from the Kittel expression, the average gyromagnetic ratio of $\gamma = 28.3 \pm 0.1$ is obtained.

Two field orientations, in-plane and out-of-plane, are used to determine the gyromagnetic ratio in the YIG sphere. The magnetic resonance spectra are presented in Figure C.14. The accepted gyromagnetic ratio for the electron, $\gamma = 28.025$ GHz/T, is in the range of averaged experimental values, $\gamma = 28.3 \pm 0.1$ GHz/T.

For that reason, to obtain the field calibration, we use the YIG sphere instead of the sample on top of the TLs in the chamber. Although an observable signal exists even in the lower power of -50 dBm, the incident power of -20 dB is selected to drive RF fields in TLs. We measured the ferromagnetic resonance of

the YIG sphere by changing the magnetic dc bias. At each field step we sweep the frequency from 2 GHz to 8 GHz. We used the fundamental mode while the magnetization of the YIG is fully saturated in a perpendicular magnetic field. The corresponding fields are calculated from the analytical Kittel expression for a sphere and considering $\gamma = 28.025$ GHz/T.

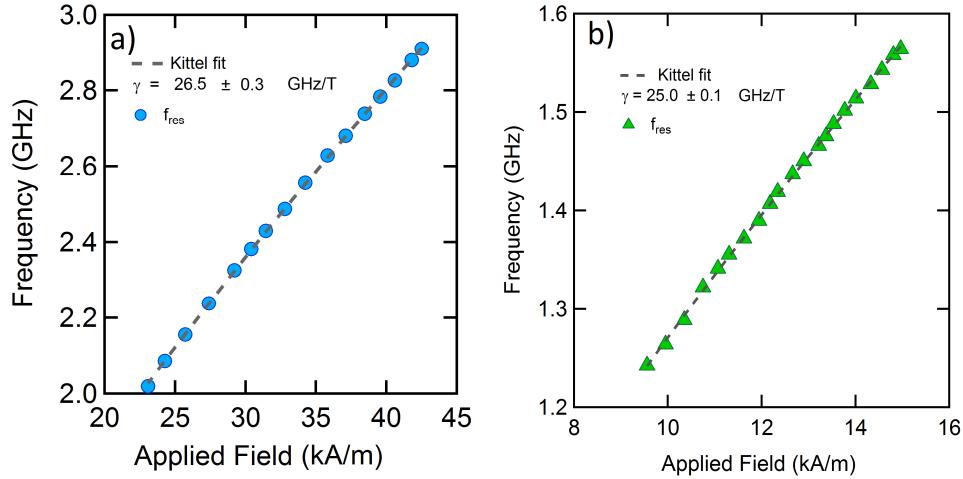


Figure C.15: Obtaining gyromagnetic ratio in pieces of original Shin-Etsu YIG wafer. a) and b) The magnetic resonance of two pieces, 5-mm and 10-mm squares, are presented with the Kittel fits.

An experimental reference for the gyromagnetic ratio value in the original YIG wafer was also measured with a couple of pieces of unmodified Shin-Etsu YIG. The magnetic resonance spectra for 5-mm and 10-mm squares of YIG are presented in Figure C.15. We put the substrates on top of the TLLs. In the various applied field (both the in-plane and out-of-plane direction) the resonance frequencies are obtained via VNA. From Kittel fits, two gyromagnetic ratios are obtained: 26.5 ± 0.3 GHz/T and 25.0 ± 0.1 GHz/T for 5-mm and 10-mm squares, respectively. One reason that both the values are smaller than the accepted value for the electron could be the 1% Bismuth doping of the wafer, as mentioned in the specs report.

In 1961, Van Vleck showed that in iron garnet materials there should be an effective g-factor, related to an effective gyromagnetic ratio. This effective value

could be lower than the accepted value for g-factor [120]. In addition, the ion doping could decrease the magnetization properties of the substrate by making some magnetically dead-layer [121, 122, 123]. However, more studies should be performed to learn about obtaining the gyromagnetic ratios in materials with substitute ions and confined structures.